

---

Electronic Thesis and Dissertation Repository

---

2-27-2020 2:00 PM

# A Micromechanics-based Multiscale Approach toward Continental Deformation, with Application to Ductile High-Strain Zones and Quartz Flow Laws

Xi Lu, *The University of Western Ontario*

Supervisor: Jiang, Dazhi, *The University of Western Ontario*

A thesis submitted in partial fulfillment of the requirements for the Doctor of Philosophy degree in Geology

© Xi Lu 2020

Follow this and additional works at: <https://ir.lib.uwo.ca/etd>



Part of the [Geology Commons](#), and the [Tectonics and Structure Commons](#)

---

## Recommended Citation

Lu, Xi, "A Micromechanics-based Multiscale Approach toward Continental Deformation, with Application to Ductile High-Strain Zones and Quartz Flow Laws" (2020). *Electronic Thesis and Dissertation Repository*. 6965.

<https://ir.lib.uwo.ca/etd/6965>

This Dissertation/Thesis is brought to you for free and open access by Scholarship@Western. It has been accepted for inclusion in Electronic Thesis and Dissertation Repository by an authorized administrator of Scholarship@Western. For more information, please contact [wlsadmin@uwo.ca](mailto:wlsadmin@uwo.ca).

## Abstract

Earth's lithosphere may be regarded as a composite material made of rheologically heterogeneous elements. The presence of these heterogeneous elements causes flow partitioning, making the deformation of Earth's lithosphere heterogeneous on all observation scales. Understanding the multiscale heterogeneous deformation and the overall rheology of the lithosphere is very important in structural geology and tectonics. The overall rheology of Earth's lithosphere on a given observation scale must be obtained from the properties of all constituents and may evolve during the deformation due to the fabric development. Both the problem of flow partitioning and characterization of the overall rheology are closely related and require a fully mechanical multiscale approach.

This thesis refines a micromechanics-based multiscale modeling approach called the self-consistent MultiOrder Power Law Approach (MOPLA). MOPLA treats the heterogeneous rock mass as a continuum of rheologically distinct elements. The rheological properties and the mechanical fields of the constituent elements and those of the composite material are computed by solving partitioning and homogenization equations self-consistently. The algorithm of MOPLA has been refined and implemented in MATLAB for high-performance computing. The micromechanical approach is used to investigate the deformation of ductile high-strain zones, advancing previous work on this subject to a full mechanical level.

This thesis considers a ductile high-strain zone as a flat heterogeneous inclusion embedded in the ductile lithosphere subjected to a tectonic deformation due to remote plate motion. The kinematic and the mechanical fields inside and outside the high-strain zone, including the finite strain accumulation in there, are solved by partitioning equations. The overall rheology of the high-strain zone is obtained by means of a self-consistent homogenization scheme.

Understanding the continental rheology requires an accurate quartz dislocation creep flow law. Despite decades of experimental studies, there are considerable discrepancies in quartz flow law parameters. This thesis proposes that the discrepancies could be explained by considering both the pressure effect on the activation enthalpy and the slip system dependence of the stress exponent. Two distinct dislocation creep flow laws corresponding to

two dominant slip systems are determined based on the current dataset of the creep experiments on quartz samples.

## Keywords

Micromechanics-based approach, Ductile high-strain zone, Quartz flow law, Continental rheology, Lithospheric multiscale deformation, Numerical modeling.

## Lay Summary

The Earth is a dynamic planet, and various parts of Earth interact. In response to the application of the deforming forces, Earth's lithosphere deforms by frictional slip along preexisting faults near the surface; at greater depth, it deforms predominantly by crystalline plasticity, leaving abundant geological records, like fabrics and structures during the geological history. Structural geology deals with the fabrics and structures from a regional to a submicroscopic scale to reconstruct the lithospheric deformation process and understand the mechanical properties (rheology) of the rocks in the lithosphere.

Rock masses in Earth's lithosphere are composed of many constituent elements, having distinct rheological properties. When the lithosphere is subjected to tectonic deformation, the mechanical and kinematic fields vary across the rheologically distinct elements because of the variations in rheology, leaving various fabrics and structures. The small-scale fabrics and structures can only relate to the relevant scale fields but not to the tectonic scale deformation process. In order to relate the small-scale features to the tectonic deformation, a multiscale approach is required.

On the other hand, as Earth's lithosphere is composed of many rheologically distinct elements, the overall rheology of the lithosphere must be obtained from the properties of all constituents. This process requires the knowledge of the rheological properties of all constituents, which are mainly based on high-temperature and high-pressure creep experiments on natural rocks or synthetic mineral aggregates, and a fully mechanical multiscale approach to help us obtain the overall rheology.

In fact, the multiscale deformation in Earth's lithosphere and the variation and evolution of the lithosphere rheology are closely related. Both require a fully mechanical multiscale approach combined with the observations from natural rocks and experiments. Recently a micromechanics-based self-consistent MultiOrder Power Law Approach (MOPLA) has been proposed to address the multiscale deformation in Earth's lithosphere and simulate the mechanical behavior of the lithosphere. This thesis applied this fully mechanical multiscale approach together with the high-quality data of creep experiments on wet quartzites and the geological records in natural rocks to investigate the multiscale deformation in Earth's lithosphere and the continental rheology.



## Co-Authorship Statement

Chapter 2 in this thesis is a co-authored manuscript with my supervisor, Dr. Dazhi Jiang and Dr. Mengmeng Qu, who was supervised by Dr. Dazhi Jiang. Dr. Qu wrote some part of the MATLAB code in this manuscript.

Chapter 4 in this thesis was published as a co-authored paper with my supervisor, Dr. Dazhi Jiang, entitled Quartz Flow Law Revisited: The Significance of Pressure Dependence of the Activation Enthalpy. In *Journal of Geophysical Research: Solid Earth*, 124(1), 241-256 (2019) (<https://doi.org/10.1029/2018JB016226>).

Chapter 5 in this thesis is a co-authored manuscript with my supervisor, Dr. Dazhi Jiang.

## Dedication

I dedicate this work to my parents for their love.

## Acknowledgments

First and foremost, I would like to thank my supervisor, Dr. Dazhi Jiang, for his support and guidance. At many stages of my graduate education, I benefited a lot from his advice and many discussions, particularly so when exploring new ideas. His enthusiasm, positive outlook, and confidence in my research inspired me and gave me confidence. Without his guidance and constant feedback, this Ph.D. would not have been achievable.

Many thanks to my committee members: Dr. Gerhard Pratt and Dr. Bob Linnen, for their insightful suggestions and comments on my research.

Special gratitude goes out to my colleague and my field assistants: Dr. Mengmeng Qu, Rui Yang, Kaitlyn Petkau, Ankit Bhandari, Dr. Tian Zhao, and Jun Shi for many discussions in my research and helping me with the fieldwork.

I am very grateful to my friends for their love and support. Notably, a very big thank you to my friend and my colleague Dr. Mengmeng Qu for the encouragement during my study and my life at Western and the guidance and help in many aspects of my research, like the programming and fieldwork, etc. Great thanks to my lovely members of the Ershilv band: Congxi Zhu, Yaozhi Li, and Rui Yang for their support.

Finally, I would like to say a heartfelt thank you to my Mum, Dad, Dr. Caiyu Zhang, and Dr. Keping Lu, for always loving me, believing in me and encouraging me. And my other family members for helping in whatever way they could during this challenging period. Especially, I would like to thank my Uncle Dr. Quanlin Hou, who is my first geology teacher and inspires me to become a geologist.

# Table of Contents

Abstract.....	ii
Lay Summary.....	iv
Co-Authorship Statement.....	v
Dedication.....	vi
Acknowledgments.....	vii
Table of Contents.....	viii
List of Tables.....	xi
List of Figures.....	xii
List of Appendices.....	xv
Chapter 1.....	1
1 General Introduction and Thesis Outline.....	1
1.1 Introduction.....	1
1.2 Thesis outline.....	9
1.3 References.....	12
Chapter 2.....	23
2 A MATLAB Package of the Self-consistent MultiOrder Power-Law Approach.....	23
2.1 Introduction.....	23
2.2 The classic Eshelby’s inclusion/inhomogeneity problem.....	24
2.3 Application of Eshelby’s solution to natural deformation in Earth’s lithosphere.....	30
2.3.1 Scale separation.....	30
2.3.2 Rheologically distinct elements with irregular shapes.....	31
2.3.3 Application to non-linear viscous materials.....	32
2.3.4 Heterogeneous matrix and homogenization.....	33
2.3.5 A multiscale strategy: inhomogeneities within inhomogeneities.....	38
2.4 MATLAB package of MOPLA.....	39
2.4.1 A brief summary of the algorithm for the self-consistent approach.....	39

2.4.2	A brief summary of the algorithm for the evolution of RDEs .....	42
2.4.3	Description of the MATLAB package.....	43
2.5	Verification and example.....	48
2.6	Conclusions.....	51
2.7	References.....	55
Chapter 3	.....	63
3	A Fully Mechanical Approach Toward High-Strain Zone Modeling Using the Generalized Eshelby Formalism .....	63
3.1	Introduction.....	63
3.2	A fully mechanical approach .....	68
3.3	Geometric simulation results and field observations.....	75
3.4	Stress distribution inside and outside the active high-strain zone .....	78
3.5	The strength of the large-scale high-strain zones .....	84
3.6	Conclusions.....	91
3.7	References.....	93
Chapter 4	.....	103
4	Quartz Flow Law Revisited: The Significance of Pressure Dependence of the Activation Enthalpy .....	103
4.1	Introduction.....	103
4.2	The choice of experimental data.....	109
4.2.1	Criteria of experimental data .....	109
4.2.2	Description of selected experiments .....	110
4.3	The determination of flow law parameters based on flow law 3.....	113
4.4	Remarks on flow law parameters.....	119
4.5	Quartz flow law derived from natural strain rate and stress estimates .....	121
4.6	Quartz flow law and continental strength.....	124
4.7	Conclusions.....	129
4.8	References.....	131

Chapter 5.....	145
5 Dislocation Creep Flow Laws of Wet Quartzite: The Significance of Pressure and Slip Systems .....	145
5.1 Introduction.....	145
5.2 Selection of experimental data.....	147
5.3 Two dislocation creep flow laws .....	148
5.4 Homogenized creep behavior in the transitional regime .....	156
5.5 Discussions .....	165
5.6 Conclusions.....	167
5.7 References.....	169
Chapter 6.....	177
6 Conclusions and Future Work.....	177
6.1 Conclusions.....	177
6.2 Future Work .....	179
6.3 References.....	181
Appendices.....	182
Curriculum Vitae .....	197

## List of Tables

Table 2.1 The input parameters of MATLAB function “MOPLA_primary.m” .....	45
Table 2.2 The output variables of MATLAB function “MOPLA_primary.m” .....	45
Table 2.3 The input parameters of MATLAB function “MOPLA_secondary.m” .....	46
Table 2.4 The output variables of MATLAB function “MOPLA_secondary.m” .....	47
Table 4.1 Experimentally determined flow law parameters reported by previous studies...	113
Table 5.1 Parameters of two distinct dislocation creep flow laws for wet quartzites.....	155

# List of Figures

Figure 1.1 The strength of the continental lithosphere based on the Yield Strength Envelope (YSE) .....	4
Figure 1.2 An illustration of Eshelby inclusion problem of an ellipsoidal elastic inhomogeneity in an infinite homogenous elastic matrix .....	6
Figure 1.3 A schematic illustration of a multiscale approach to natural deformation .....	7
Figure 2.1 Eshelby’s solution of the classic inclusion/inhomogeneity problem illustrated by a series of “virtual” transformations .....	26
Figure 2.2 A conceptual diagram to illustrate three different inclusion-matrix systems .....	35
Figure 2.3 A flowchart of the self-consistent MultiOrder Power-Law Approach (MOPLA) .....	41
Figure 2.4 An illustration of an ellipsoid and two distinct coordinates .....	44
Figure 2.5 The xyz coordinate and the inclined transpression model for the macroscale deformation of the Cascade Lake shear zone .....	50
Figure 2.6 The model predicted “lineation pattern” defined by the long axes of deformable fabric elements in RDEs (equal-area lower hemisphere projection) .....	52
Figure 2.7 The model predicted lineation pattern defined by the maximum principal finite strain axes in RDEs (equal-area lower hemisphere projection) .....	53
Figure 3.1 Three different previous shear zone models .....	65
Figure 3.2 Eshelby inclusion problem of an ellipsoidal inclusion in the matrix .....	69
Figure 3.3 A conceptual illustration of a crustal high-strain zone as a planar heterogeneous ellipsoidal inclusion embedded in a block of ductile lithosphere .....	71
Figure 3.4 A schematic diagram showing the shape and orientation of a planar ellipsoidal high-strain zone .....	72



Figure 3.5 A conceptual diagram showing the heterogeneous poly-element scenario and the self-consistent homogenization scheme.....	74
Figure 3.6 Equal-area lower hemisphere projections of the variation and evolution of the finite strain patterns in a sinistral transpressional zone.....	77
Figure 3.7 A geological map and field observations of the Shangdan Tectonic Zone, Qinling Orogenic Belt, China .....	79
Figure 3.8 The comparison of geometric results and field observations .....	80
Figure 3.9 The orientation of the maximum principal deviatoric stress ( $\sigma_1$ ) within the SAF and in its vicinity.....	83
Figure 3.10 A conceptual illustration of a planar heterogeneous poly-element high-strain zone embedded in a block of the ductile lithosphere and the self-consistent homogenization scheme.....	85
Figure 3.11 Geological maps and field observations in the mylonite zone at the northwest margin of the Grenville Front Tectonic Zone .....	87
Figure 3.12 Photomicrographs of the mylonitic granite and the banded mylonite.....	88
Figure 3.13 Plots of the homogenized viscosities of the quartz-mica aggregates versus the volume fraction of mica .....	90
Figure 4.1 Yield Strength Envelopes (YSE) for a wet quartzite crust based on flow laws with parameters derived from various experiments .....	105
Figure 4.2 Plot of strain rate versus differential stress for wet quartzite .....	107
Figure 4.3 Determination of the water fugacity exponent and the activation volume.....	116
Figure 4.4 Determination of the activation enthalpy .....	118
Figure 4.5 Plot of water fugacity exponent versus activation volume.....	122
Figure 4.6 The strength profile of our flow law compared with those based on other flow laws .....	126

Figure 5.1 Plots of normalized strain rate versus normalized stress for quartz creep experiments and the dislocation creep flow laws .....	151
Figure 5.2 Determination of the activation energy .....	152
Figure 5.3 Quartz c-axis fabrics and stress and strain rate data of eight general shear experimental runs.....	154
Figure 5.4 Deformation mechanism maps for quartzite .....	160
Figure 5.5 A conceptual diagram of the self-consistent homogenization approach.....	162
Figure 5.6 The strength profiles of the continental lithosphere using the two dislocation creep flow laws and the calculated bulk strengths of quartzite with varying contributions of prism <a> slip system .....	164

## List of Appendices

Appendix A The description of the functions in “ <i>Routines</i> ” in the MATLAB package of MOPLA.....	182
Appendix B Download link for the MATLAB package in Chapter 2.....	187
Appendix C Dataset of 20 creep experiments on quartz samples.....	188

## Chapter 1

### 1 General Introduction and Thesis Outline

#### 1.1 Introduction

The Earth is a dynamic planet. Various parts of Earth interact, producing earthquakes, volcanic eruptions and mountain building processes, etc. The rocks in Earth's lithosphere respond to the application of deforming forces, leaving a great number of geological records, like fabrics and structures, during the geologic history (e.g., Hobbs et al., 1976; Twiss and Moores, 1992). Structural geology and tectonics deal with the fabrics and structures spanning a wide range of characteristic lengths, from crystal lattice spacing to the size of lithospheric plates, to unravel the processes of the lithospheric deformation (e.g., Hobbs et al., 1976; Twiss and Moores, 1992; Passchier and Trouw, 2005). However, our direct field observations are always limited on the most easily accessible scales, typically from outcrops to hand samples and under microscopes. There is a significant intrinsic scale gap between the direct field observations and the tectonic processes across plate boundaries or in a mountain belt. Since Ramsay (1967), the Continuum Mechanics approach has been commonly used to understand the fabrics and structures with limited range of characteristic length scales and directly relate them to tectonic processes (e.g., Hobbs et al., 1976; Twiss and Moores, 1992; Pollard and Fletcher, 2005). Over the past five decades, a large number of theoretical models based on the classic Continuum Mechanics have been developed for a lot of specific structures (see a review in Jiang, 2014): the single-layer and multilayer folding theories (Johnson and Fletcher, 1994; Schmalholz and Podladchikov, 2000; Hudleston and Treagus, 2010; Schmalholz and Schmid, 2012); theories for the formation of pinch-and-swell structures (Smith, 1977; Schmalholz et al., 2008; Schmalholz and Fletcher, 2011); the geometrical/kinematic models for small ductile shear zones (Ramsay and Graham, 1970; Ramberg, 1975; see a review in Davis and Titus, 2011) and the mechanical model of Robin and Cruden (1994) for the tabular deformation zone; the Taylor-Bishop-Hill model (Lister and Paterson, 1979; Lister and Hobbs, 1980) and the viscoplastic self-consistent (VPSC) model (Molinari et al., 1987; Lebensohn and Tome, 1993) for the development of the crystallographic preferred orientation (CPO) fabrics in crystalline rocks. However,

each of the existing models can only deal with a specific structure with a certain characteristic length scale, because the classic Continuum Mechanics approach does not contain parameters with length scales to capture different characteristic scales. Rock masses in Earth's lithosphere are composed of a large number of rheologically distinct elements over a wide range of characteristics of lengths. The presence of the rheologically distinct elements in Earth's lithosphere commonly results in significant flow field partitioning (Lister and Williams, 1983). The partitioned stresses and strain rates vary across the heterogeneous elements, causing deformation pattern variations among heterogeneous elements (e.g., Lister and Williams, 1983; Ishii, 1992; Jiang, 1994 a, b; Jiang and White, 1995; Jiang and Williams, 1999; Hudleston, 1999; Goodwin and Tikoff, 2002; Jones et al., 2005; Jiang and Bentley, 2012; Jiang, 2014). Therefore, the small-scale structural or fabric features observed in the field are relevant to the partitioned flows at the relevant scales but cannot be directly related to the tectonic-scale deformation and the tectonic process. Many geologists have realized this problem but, none of the existing single-scale models can effectively address the multiscale heterogeneous deformation in Earth's lithosphere. A fully mechanical multiscale approach is necessary to relate the small-scale features in Earth's lithosphere to the tectonic-scale deformation process.

To apply a fully mechanical approach, we need to know the rheology of Earth's lithosphere, which is a very important and long-standing problem in structural geology and tectonics. It is commonly accepted that the rocks in Earth's lithosphere deform elastically and by frictional slip on preexisting fractures near the surface and predominantly by crystalline plasticity at greater depth (Nicolas and Poirier, 1976; Sibson, 1977; Brace and Kohlstedt, 1980; Kohlstedt et al., 1995; Mackwell et al., 1998; Jackson, 2002; Burov, 2011). So far, the current understanding of the rheology of the lithosphere at greater depth is mainly based on the laboratory high-temperature and high-pressure creep experiments on natural rocks or synthetic silicate aggregates (e.g., Heard and Carter, 1968; Chopra and Paterson, 1981; Caristan, 1982; Kirby and Kronenberg, 1984; Karato et al., 1986; Wilks and Carter, 1990; Luan and Paterson, 1992; Gleason and Tullis, 1995; Mackwell et al., 1998; Karato and Jung, 2003; Rybacki and Dresen, 2004; Rybacki et al., 2006;). The experimental data of stress, strain rate, grain size as well as

the deformation PT conditions are commonly fitted into flow laws (e.g., Dorn, 1955; Sherby and Burke, 1968; Sherby et al., 1970; Ashby, 1972; Kirby and Raleigh, 1973; Frost and Ashby, 1982; Ranalli, 1987). Since the 1970s, the concept of yield strength envelope (YSE), in which a vertical profile illustrates the maximum stress a rock can support with increasing depths according to the flow laws of the major rocks or mineral aggregates, has been extrapolated to represent the lithosphere strength (Fig.1.1; Goetze and Evans, 1979; Brace and Kohlstedt, 1980; Kirby, 1983; Kohlstedt et al., 1995; Burov, 2011). In the upper crust, the continental lithosphere strength is commonly represented by the frictional strength by Byerlee's law ( $\leq 15\text{km}$ ) and the strength of wet quartzites ( $15\text{km}\sim 30\text{km}$ ) (Gleason and Tullis, 1995). The lower crust is represented by the dry diabase (Mackwell et al., 1998) or undried granulite (Wilks and Carter, 1990) and the mantle by dry or wet olivine (Chopra and Paterson, 1981) (Fig.1.1). Therefore, accurate flow laws for major rocks or mineral aggregates, such as quartzite, are critical for the understanding of the lithosphere rheology. A rather unfortunate and embarrassing situation is that the flow laws determined from different creep experiments on a similar type of rock disagree considerably, leaving earth scientists ample room for speculation on the strength of the lithosphere. Furthermore, Earth's lithosphere is a heterogeneous polyphase material that consists of a larger number of rheologically distinct elements. The overall rheology of the heterogeneous polyphase rock masses in Earth's lithosphere must be obtained from the rheological properties of the constituent elements, their concentrations, and the geometric arrangement of the elements (e.g., Voigt, 1887; Reuss, 1929; Hill, 1963; Nemat-Nasser and Hori, 1999), all of which may evolve during the progressive deformation. It is perhaps oversimplified that using a simple flow law of a monophase mineral aggregate to represent the rheology of the lithosphere at a certain depth, like YSE. For instance, in the ductile continental crust, quartz is common and possibly strength-controlling mineral but the role of other phases like mica may also be significant (Kronenberg et al., 1990; Shea and Kronenberg, 1993; Tullis and Wenk, 1994; Tullis, 2002; Holyoke and Tullis, 2006; Montési, 2013).

In fact, the heterogeneous multiscale deformation in Earth's lithosphere and the overall rheology of Earth's lithosphere are closely related. Variations in rheology among the constituent elements of Earth's lithosphere cause significant flow partitioning and various

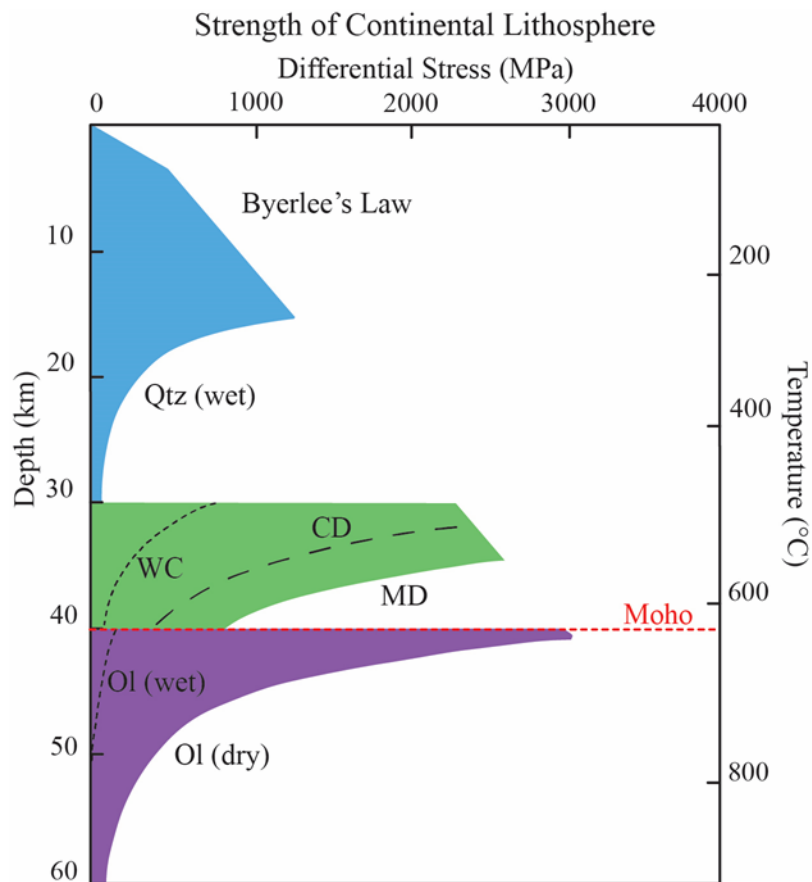


**Figure 1.1 The strength of the continental lithosphere based on the Yield Strength Envelope (YSE)**

The upper crust is represented by frictional strength by Byerlee's law in the brittle regime and wet quartz (Qtz) in the ductile regime. The lower crust is represented by dry diabase (MD) or undried granulite (WC). The mantle is represented by dry or wet olivine (Ol). The Moho is at 40 km, and the geothermal gradient corresponds to a surface heat flow of  $60 \text{ mWm}^{-2}$ . The representative strain rate is  $\dot{\epsilon} = 10^{-15} \text{ s}^{-1}$ . This figure is modified after Jackson (2002).

fabrics and structures in individual rheologically heterogeneous elements. The rheological properties of all constituent elements determine the overall rheology of Earth's lithosphere. The fabric development in Earth's lithosphere may also affect the rheology. The main objective of this thesis is to understand the heterogeneous multiscale deformation in Earth's lithosphere and the overall rheology of Earth's lithosphere. Both require a fully mechanical multiscale approach. Recently, a new micromechanics self-consistent MultiOrder Power-Law Approach (MOPLA, Jiang and Bentley, 2012; Jiang, 2014, 2016) is proposed to address the multiscale heterogeneous deformation in Earth's lithosphere and mechanical evolution of Earth's lithosphere during the progressive deformation. The backbone theory of MOPLA is the classic Eshelby (1957, 1959) inclusion problem, considering what is the elastic field inside an elastic inclusion embedded in an infinite homogeneous elastic matrix. Eshelby's pioneering work has led to the solution of a general elastic inhomogeneity embedded a homogenous matrix (Fig.1.2) (Mura, 1987), and then has been extended to general nonlinear, like power-law, viscous materials (Molinari et al., 1987; Lebensohn and Tomé, 1993; Jiang and Bentley, 2012; Jiang, 2013, 2014). Applying the extended Eshelby's formalisms for general power-law viscous materials to the multiscale lithospheric deformation led to the MOPLA. In MOPLA, each rheologically distinct element (RDE) in Earth's lithosphere is considered as an ellipsoidal inclusion embedded in a hypothetical Homogenous Equivalent Medium (HEM) subjected to the remote tectonic deformation (Fig.1.3a-d). The local mechanical fields, such as the stress, strain rate, and vorticity fields in each RDE, are partitioned from the far-field quantities caused by the tectonic-scale deformation. The partitioned mechanical fields, in turn, govern the small-scale fabric development in individual RDEs (Jiang, 2014) (Fig.1.3e-g). The macroscale mechanical fields in the lithosphere at every point are defined as the average of all local mechanical fields over a Representative Volume Element (RVE) that is a large enough volume, containing a representative assemblage of RDEs (Fig.1.3b, c). The overall rheology of Earth's lithosphere is represented by the rheology of HEM. The latter one can be obtained by means of a self-consistent homogenization scheme (Molinari et al., 1987; Lebensohn and Tomé, 1993; Jing, 2014) from the rheological properties of the constituent RDEs (Fig.1.3c, d). The numerical simulation of this new micromechanics



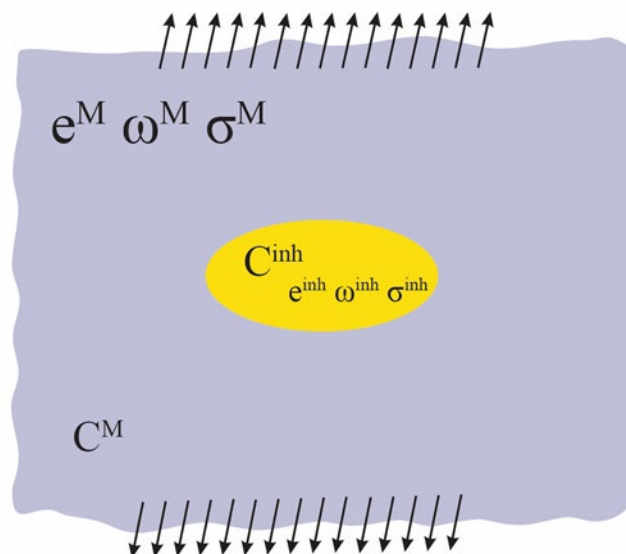


**Figure 1.2 An illustration of Eshelby inclusion problem of an ellipsoidal elastic inhomogeneity in an infinite homogenous elastic matrix**

$e$ ,  $\omega$ , and  $\sigma$  are the elastic strain, rotation, and Cauchy stress fields.  $C$  is the 4<sup>th</sup> order elastic stiffness tensor. The sub- or super-script “inh” and “M” stand for the properties in inhomogeneity and in matrix medium, respectively.

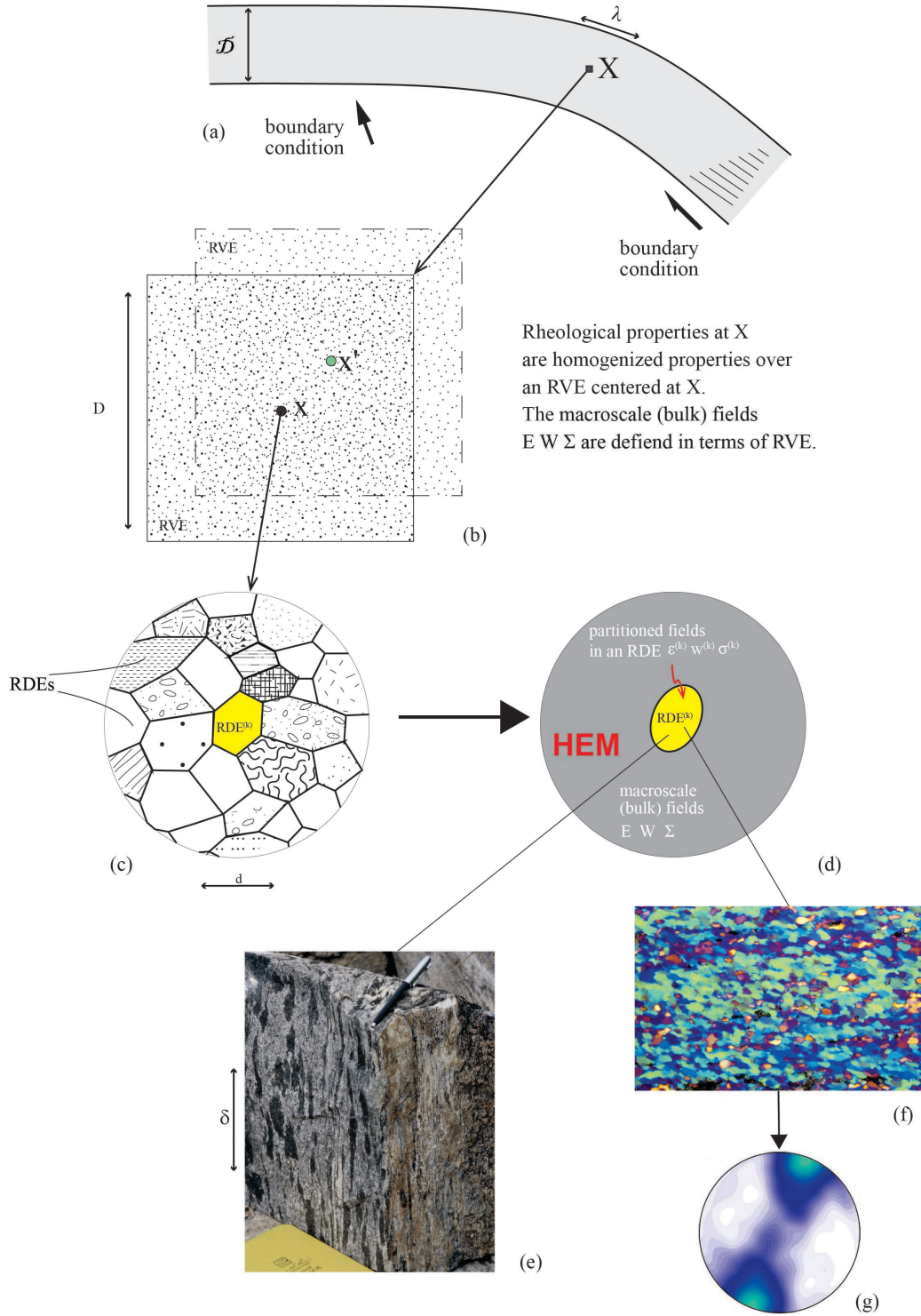


**Figure 1.3 A schematic illustration of a multiscale approach to natural deformation**

(a) The whole crustal deformation zone with a characteristic length of  $\mathcal{D}$  and the boundary conditions fluctuated at a scale of  $\lambda$ . The macroscale deformation of the zone at point X is defined in terms of a Representative Volume Element (RVE), centered at X, with a characteristic length of D in (b). D must be much smaller than the  $\mathcal{D}$  and the fluctuation length  $\lambda$  of the boundary loading.  $D \ll \mathcal{D}$  and  $D \ll \lambda$ . (c) The RVE is a large enough volume element that contains a representative assemblage of all Rheologically Distinct Elements (RDEs). The mean size of the RDEs is denoted by d ( $d \ll D$ ). The local fields are defined within individual RDEs. (d) Each RDE is considered as an ellipsoidal Eshelby inhomogeneity embedded in a hypothetical Homogeneous Equivalent Medium (HEM), whose rheological properties are represented by the homogenized properties over an RVE. The local fields in an RDE, called partitioned fields, govern (e) the structural and fabric elements observed on outcrops, (f) the microscopic shape fabrics, and (g) the lattice preferred orientation fabrics within the RDE. The structural or fabric feature has a characteristic length of  $\delta$  ( $\delta \ll d$ ). The absolute size of these characteristic lengths and the scale gaps between them depend on the nature of the deformation. This figure is modified after Qu (2018).

approach (MOPLA) can be realized using MATLAB scripts (more details below). This new approach allows the simulation of the overall rheology of Earth's lithosphere during the progressive deformation and the understanding of how the rheology variations in Earth's lithosphere control the multi-scale heterogeneous deformation.

Applying the micromechanical model to Earth's lithosphere necessitates the geological records to constrain the model inputs and test the model predictions. The deformation of Earth's lithosphere is characterized by localized deformation zones. Faults are commonly regarded as the expression of localized deformation in the brittle regime, whereas shear zones are the expression of localized strain in the ductile regime (e.g., Hobbs et al., 1976; Twiss and Moores, 1992). Localized deformation zones are fundamental structures in Earth's lithosphere, and govern the lithospheric deformation patterns, the formation of tectonic plate boundaries, the evolution of plate tectonics as well as the mechanical evolution of continental lithosphere (e.g., Zoback et al., 1987; Flesh et al., 2000; Hamner, 1988; Vauchez et al., 1998; Tommasi and Vauchez, 2001; Vauchez and Tommasi, 2003; Ben-Zion and Sammis, 2003; Gumiaux et al., 2004; Montési, 2013). Ancient ductile shear zones preserved abundant fabric data and petrological data on multiple scales; modern GPS data and geophysical data of active plate boundaries provide the information of plate motion, the velocity fields, the stress distribution, etc. These valuable data could help us to validate the new micromechanical model and understand the multi-scale deformation in Earth's lithosphere and the continental lithosphere rheology.

## 1.2 Thesis outline

This thesis aims to understand the heterogeneous multiscale deformation in Earth's lithosphere and the continental lithosphere rheology by applying a micromechanics-based self-consistent MultiOrder Power-Law Approach (MOPLA, Jiang and Bentley, 2012; Jiang, 2014, 2016) together with the high-quality data of creep experiments on quartz aggregates and the geological data from both ancient ductile shear zones and active plate boundaries. In order to achieve this main objective, this thesis made contributions to the following three key problems.

The theory and algorithm of MOPLA have been developed and well documented in Jiang (2014, 2016), and the algorithm has been written in the Mathcad package (Jiang, 2014).

However, the Mathcad package of MOPLA is not very efficient. MOPLA is a self-consistent approach, which requires a great number of iterative calculations, and each of them involves a large number of evaluations of the Eshelby tensors, the most time-consuming part of the whole calculation. Therefore, MOPLA requires a long computation time. Qu et al. (2016) developed an optimal scheme for numerical evaluations of Eshelby tensors. To improve the performance of the computation of MOPLA, Chapter 2 of this thesis refines the algorithm incorporating the work of Qu et al. (2016) and implements the algorithm in a MATLAB package. This effort will make it easier to widely apply MOPLA to various geological settings to address the multiscale deformation in Earth's lithosphere and the rheology of the lithosphere.

Crustal ductile high-strain zones accommodate most part of the tectonic deformation, leaving abundant fabrics in them and have a significant strong influence on the mechanical evolution of the continental lithosphere. In the past five decades, structural geologists dedicated to exploring the finite strain patterns inside a small-scale shear zone with clearly defined boundaries using single scale kinematic models (see reviews in Jiang and White, 1995; Jiang and Williams 1998; Davis and Titus 2011). Chapter 3 of this thesis takes a different approach to investigate the crustal-scale ductile high-strain zones. Chapter 3 considers a high-strain zone as a planar inhomogeneity embedded in the lithosphere undergoing tectonic-scale deformation and uses extended Eshelby's formalism to investigate the mechanical and kinematic fields inside the high-strain zone including the finite strain accumulation there. Therefore, the flow inside a high-strain zone is not a prescribed one, but the partitioned flow from the far-field plate motion. Because this approach is a complete mechanical one, it can address the problems associated with the mechanics of the high-strain zone system, like the stress distribution within a high-strain zone and that in its vicinity and the rheology of the high-strain zone. Investigating these problems will contribute to the understanding of the mechanics of the lithospheric deformation and the rheology of the continental lithosphere. This model has been applied to selected ancient and active high-strain zones to test it.

The dislocation flow law of wet quartzite is important to understand the rheology of the continental lithosphere as quartz is the most common and probably strength-controlling

mineral in the continental lithosphere. However, existing creep experiments have yielded very different quartz flow law parameters. Chapters 4 and 5 of this thesis demonstrate that the difference can be explained by considering the pressure effect on the activation enthalpy and the slip system dependence of the stress exponent. Two distinct dislocation creep flow laws for quartzites associated with different dominant slip systems are identified based on high-quality experimental data of wet quartzite together with related quartz c-axis fabrics. In both nature and experiments, the creep behavior of wet quartzite in the transitional regime, where both slip systems are significant, is common. Chapter 5 proposes two simple homogenized flow laws and also uses a micromechanics-based self-consistent homogenization approach (Jiang, 2014) to evaluate the bulk rheological properties in such a transitional flow regime.

### 1.3 References

- Ashby, M. F. (1972). A first report on deformation-mechanism maps. *Acta Metallurgica*, 20(7), 887-897. [https://doi.org/10.1016/0001-6160\(72\)90082-X](https://doi.org/10.1016/0001-6160(72)90082-X)
- Ben-Zion, Y., & Sammis, C. G. (2003). Characterization of fault zones. *Pure and Applied Geophysics*, 160(3-4), 677-715. <https://doi.org/10.1007/PL00012554>
- Behr, W. M., & Platt, J. P. (2014). Brittle faults are weak, yet the ductile middle crust is strong: Implications for lithospheric mechanics. *Geophysical Research Letters*, 41(22), 8067–8075. <https://doi.org/10.1002/2014GL061349>
- Brace, W. F., & Kohlstedt, D. L. (1980). Limits on lithospheric stress imposed by laboratory experiments. *Journal of Geophysical Research: Solid Earth*, 85(B11), 6248–6252. <https://doi.org/10.1029/JB085iB11p06248>
- Burov, E. B. (2011). Rheology and strength of the lithosphere. *Marine and Petroleum Geology*, 28(8), 1402–1443. <https://doi.org/10.1016/j.marpetgeo.2011.05.008>
- Caristan, Y. (1982). The transition from high temperature creep to fracture in Maryland diabase. *Journal of Geophysical Research: Solid Earth*, 87(B8), 6781–6790. <https://doi.org/10.1029/JB087iB08p06781>
- Chernak, L. J., Hirth, G., Selverstone, J., & Tullis, J. (2009). Effect of aqueous and carbonic fluids on the dislocation creep strength of quartz. *Journal of Geophysical Research: Solid Earth*, 114(B4). <https://doi.org/10.1029/2008JB005884>
- Chopra, P. N., & Paterson, M. S. (1981). The experimental deformation of dunite. *Tectonophysics*, 78(1–4), 453–473. [https://doi.org/10.1016/0040-1951\(81\)90024-X](https://doi.org/10.1016/0040-1951(81)90024-X)
- Davis, J. R., & Titus, S. J. (2011). Homogeneous steady deformation: A review of computational techniques. *Journal of Structural Geology*, 33(6), 1046-1062. <https://doi.org/10.1016/j.jsg.2011.03.001>

- Dorn, J. E. (1955). Some fundamental experiments on high temperature creep. *Journal of the Mechanics and Physics of Solids*, 3(2), 85–116. [https://doi.org/10.1016/0022-5096\(55\)90054-5](https://doi.org/10.1016/0022-5096(55)90054-5)
- Eshelby, J. D. (1957). The determination of the elastic field of an ellipsoidal inclusion and related problems. *Proceedings of the Royal Society of London. Series A. Mathematical and Physical Sciences*, 241(1226), 376-396.  
<https://doi.org/10.1098/rspa.1957.0133>
- Eshelby, J. D. (1959). The elastic field outside an ellipsoidal inclusion. *Proceedings of the Royal Society of London. Series A. Mathematical and Physical Sciences*, 252(1271), 561-569. <https://doi.org/10.1098/rspa.1959.0173>
- Eshelby, J. D., (1961). Elastic inclusions and inhomogeneities. In: Snedden, N.I., Hill, R. (Eds.), *Progress in Solid Mechanics*, vol. 2, pp. 89-104
- Farla, R. J. M., Karato, S. I., & Cai, Z. (2013). Role of orthopyroxene in rheological weakening of the lithosphere via dynamic recrystallization. *Proceedings of the National Academy of Sciences*, 110(41), 16355–16360.  
<https://doi.org/10.1073/pnas.1218335110>
- Flesch, L. M., Holt, W. E., Haines, A. J., & Shen-Tu, B. (2000). Dynamics of the Pacific-North American plate boundary in the western United States. *Science*, 287(5454), 834-836. <https://doi.org/10.1126/science.287.5454.834>
- Frost, H. J., & Ashby, M. F. (1982). *Deformation mechanism maps: the plasticity and creep of metals and ceramics*. Pergamon Press.
- Gleason, G. C., & Tullis, J. (1995). A flow law for dislocation creep of quartz aggregates determined with the molten salt cell. *Tectonophysics*, 247(1–4), 1–23.  
[https://doi.org/10.1016/0040-1951\(95\)00011-B](https://doi.org/10.1016/0040-1951(95)00011-B)
- Goetze, C., & Evans, B. (1979). Stress and temperature in the bending lithosphere as constrained by experimental rock mechanics. *Geophysical Journal*



*International*, 59(3), 463-478. <https://doi.org/10.1111/j.1365-246X.1979.tb02567.x>

- Goodwin, L. B., & Tikoff, B. (2002). Competency contrast, kinematics, and the development of foliations and lineations in the crust. *Journal of Structural Geology*, 24(6-7), 1065-1085. [https://doi.org/10.1016/S0191-8141\(01\)00092-X](https://doi.org/10.1016/S0191-8141(01)00092-X)
- Gumiaux, C., Judenherc, S., Brun, J. P., Gapais, D., Granet, M., & Poupinet, G. (2004). Restoration of lithosphere-scale wrenching from integrated structural and topographic data (Hercynian belt of western France). *Geology*, 32(4), 333-336. <https://doi.org/10.1130/G20134.2>
- Hanmer, S. (1988). Great Slave Lake Shear Zone, Canadian Shield: reconstructed vertical profile of a crustal-scale fault zone. *Tectonophysics*, 149(3), 245-264. [https://doi.org/10.1016/0040-1951\(88\)90176-X](https://doi.org/10.1016/0040-1951(88)90176-X)
- Heard, H. C., & Carter, N. L. (1968). Experimentally induced “natural” intragranular flow in quartz and quartzite. *American Journal of Science*. <https://doi.org/10.2475/ajs.266.1.1>
- Hill, R. (1965). A self-consistent mechanics of composite materials. *Journal of the Mechanics and Physics of Solids*, 13(4), 213-222. [https://doi.org/10.1016/0022-5096\(65\)90010-4](https://doi.org/10.1016/0022-5096(65)90010-4)
- Hobbs, B. E., Means, W. D., & Williams, P. F. (1976). *An outline of structural geology*. Wiley.
- Holyoke, C. W., & Kronenberg, A. K. (2013). Reversible water weakening of quartz. *Earth and Planetary Science Letters*, 374, 185–190. <https://doi.org/10.1016/j.epsl.2013.05.039>
- Holyoke, C. W., & Tullis, J. (2006). Mechanisms of weak phase interconnection and the effects of phase strength contrast on fabric development. *Journal of Structural Geology*, 28(4), 621–640. <https://doi.org/10.1016/j.jsg.2006.01.008>

- Hudleston, P. (1999). Strain compatibility and shear zones: is there a problem?. *Journal of Structural Geology*, 21(8-9), 923-932. [https://doi.org/10.1016/S0191-8141\(99\)00060-7](https://doi.org/10.1016/S0191-8141(99)00060-7)
- Hudleston, P. J., & Treagus, S. H. (2010). Information from folds: a review. *Journal of Structural Geology*, 32(12), 2042-2071. <https://doi.org/10.1016/j.jsg.2010.08.011>
- Huntington, K. W., & Klepeis, K. A. (2018). Challenges and opportunities for research in tectonics: Understanding deformation and the processes that link Earth systems, from geologic time to human time. A community vision document submitted to the US National Science Foundation.
- Ishii, K. (1992). Partitioning of non-coaxiality in deforming layered rock masses. *Tectonophysics*, 210, 33-43. [https://doi.org/10.1016/0040-1951\(92\)90126-Q](https://doi.org/10.1016/0040-1951(92)90126-Q)
- Jackson, J. (2002). Strength of the continental lithosphere: Time to abandon the jelly sandwich? *GSA Today*, 12(9), 4. [https://doi.org/10.1130/1052-5173\(2002\)012<0004:SOTCLT>2.0.CO;2](https://doi.org/10.1130/1052-5173(2002)012<0004:SOTCLT>2.0.CO;2)
- Jiang, D. (1994a). Vorticity determination, distribution, partitioning and the heterogeneity and non-steadiness of natural deformations. *Journal of Structural Geology*, 16(1), 121-130. [https://doi.org/10.1016/0191-8141\(94\)90023-X](https://doi.org/10.1016/0191-8141(94)90023-X)
- Jiang, D. (1994b). Flow variation in layered rocks subjected to bulk flow of various kinematic vorticities: theory and geological implications. *Journal of Structural Geology*, 16(8), 1159-1172. [https://doi.org/10.1016/0191-8141\(94\)90059-0](https://doi.org/10.1016/0191-8141(94)90059-0)
- Jiang, D. (2013). The motion of deformable ellipsoids in power-law viscous materials: Formulation and numerical implementation of a micromechanical approach applicable to flow partitioning and heterogeneous deformation in Earth's lithosphere. *Journal of Structural Geology*, 50, 22-34. <https://doi.org/10.1016/j.jsg.2012.06.011>

- Jiang, D. (2014). Structural geology meets micromechanics: A self-consistent model for the multiscale deformation and fabric development in Earth's ductile lithosphere. *Journal of Structural Geology*, 68, 247-272.  
<https://doi.org/10.1016/j.jsg.2014.05.020>
- Jiang, D. (2016). Viscous inclusions in anisotropic materials: Theoretical development and perspective applications. *Tectonophysics*, 693, 116-142.  
<https://doi.org/10.1016/j.tecto.2016.10.012>
- Jiang, D., & Bentley, C. (2012). A micromechanical approach for simulating multiscale fabrics in large-scale high-strain zones: Theory and application. *Journal of Geophysical Research: Solid Earth*, 117(B12).  
<https://doi.org/10.1029/2012JB009327>
- Jiang, D., & White, J. C. (1995). Kinematics of rock flow and the interpretation of geological structures, with particular reference to shear zones. *Journal of Structural Geology*, 17(9), 1249-1265. [https://doi.org/10.1016/0191-8141\(95\)00026-A](https://doi.org/10.1016/0191-8141(95)00026-A)
- Jiang, D., & Williams, P. F. (1999). A fundamental problem with the kinematic interpretation of geological structures. *Journal of Structural Geology*, 21(8-9), 933-937. [https://doi.org/10.1016/S0191-8141\(99\)00068-1](https://doi.org/10.1016/S0191-8141(99)00068-1)
- Johnson, A. M., & Fletcher, R. C. (1994). *Folding of viscous layers: mechanical analysis and interpretation of structures in deformed rock*.
- Jones, R. R., Holdsworth, R. E., McCaffrey, K. J., Clegg, P., & Tavarnelli, E. (2005). Scale dependence, strain compatibility and heterogeneity of three-dimensional deformation during mountain building: a discussion. *Journal of Structural Geology*, 27(7), 1190-1204. <https://doi.org/10.1016/j.jsg.2005.04.001>
- Karato, S. I., & Jung, H. (2003). Effects of pressure on high-temperature dislocation creep in olivine. *Philosophical Magazine*, 83(3), 401-414.  
<https://doi.org/10.1080/0141861021000025829>

- Karato, S. I., Paterson, M. S., & FitzGerald, J. D. (1986). Rheology of synthetic olivine aggregates: Influence of grain size and water. *Journal of Geophysical Research: Solid Earth*, *91*(B8), 8151-8176. <https://doi.org/10.1029/JB091iB08p08151>
- Kirby, S. H., & Kronenberg, A. K. (1984). Deformation of clinopyroxenite: Evidence for a transition in flow mechanisms and semibrittle behavior. *Journal of Geophysical Research: Solid Earth*, *89*(B5), 3177-3192. <https://doi.org/10.1029/JB089iB05p03177>
- Kirby, S. H. (1983). Rheology of the lithosphere. *Reviews of Geophysics*, *21*(6), 1458-1487. <https://doi.org/10.1029/RG021i006p01458>
- Kirby, S. H., & Raleigh, C. B. (1973). Mechanisms of high-temperature, solid-state flow in minerals and ceramics and their bearing on the creep behavior of the mantle. *Tectonophysics*, *19*(2), 165–194. [https://doi.org/10.1016/0040-1951\(73\)90038-3](https://doi.org/10.1016/0040-1951(73)90038-3)
- Koch, P. S., Christie, J. M., Ord, A., & George, R. P. (1989). Effect of water on the rheology of experimentally deformed quartzite. *Journal of Geophysical Research: Solid Earth*, *94*(B10), 13975–13996. <https://doi.org/10.1029/JB094iB10p13975>
- Kohlstedt, D. L., Evans, B., & Mackwell, S. J. (1995). Strength of the lithosphere: Constraints imposed by laboratory experiments. *Journal of Geophysical Research: Solid Earth*, *100*(B9), 17587–17602. <https://doi.org/10.1029/95JB01460>
- Kronenberg, A. K., Kirby, S. H., & Pinkston, J. (1990). Basal slip and mechanical anisotropy of biotite. *Journal of Geophysical Research: Solid Earth*, *95*(B12), 19257-19278. <https://doi.org/10.1029/JB095iB12p19257>
- Kronenberg, A. K., & Tullis, J. (1984). Flow strengths of quartz aggregates: Grain size and pressure effects due to hydrolytic weakening. *Journal of Geophysical Research: Solid Earth*, *89*(B6), 4281–4297. <https://doi.org/10.1029/JB089iB06p04281>

- Lebensohn, R. A., & Tomé, C. N. (1993). A self-consistent anisotropic approach for the simulation of plastic deformation and texture development of polycrystals: application to zirconium alloys. *Acta metallurgica et materialia*, 41(9), 2611-2624. [https://doi.org/10.1016/0956-7151\(93\)90130-K](https://doi.org/10.1016/0956-7151(93)90130-K).
- Lister, G. S., & Hobbs, B. E. (1980). The simulation of fabric development during plastic deformation and its application to quartzite: the influence of deformation history. *Journal of Structural Geology*, 2(3), 355-370. [https://doi.org/10.1016/0191-8141\(80\)90023-1](https://doi.org/10.1016/0191-8141(80)90023-1)
- Lister, G. S., & Williams, P. F. (1983). The partitioning of deformation in flowing rock masses. *Tectonophysics*, 92(1-3), 1-33. [https://doi.org/10.1016/0040-1951\(83\)90083-5](https://doi.org/10.1016/0040-1951(83)90083-5)
- Lister, G. S., & Paterson, M. S. (1979). The simulation of fabric development during plastic deformation and its application to quartzite: fabric transitions. *Journal of Structural Geology*, 1(2), 99-115. [https://doi.org/10.1016/0191-8141\(79\)90047-6](https://doi.org/10.1016/0191-8141(79)90047-6)
- Luan, F. C., & Paterson, M. S. (1992). Preparation and deformation of synthetic aggregates of quartz. *Journal of Geophysical Research: Solid Earth*, 97(B1), 301-320. <https://doi.org/10.1029/91JB01748>
- Mackwell, S. J., Zimmerman, M. E., & Kohlstedt, D. L. (1998). High-temperature deformation of dry diabase with application to tectonics on Venus. *Journal of Geophysical Research: Solid Earth*, 103(B1), 975-984. <https://doi.org/10.1029/97JB02671>
- Molinari, A., Canova, G. R., & Ahzi, S. (1987). A self-consistent approach of the large deformation polycrystal viscoplasticity. *Acta Metallurgica*, 35(12), 2983-2994. [https://doi.org/10.1016/0001-6160\(87\)90297-5](https://doi.org/10.1016/0001-6160(87)90297-5)
- Montési, L. G. J. (2013). Fabric development as the key for forming ductile shear zones and enabling plate tectonics. *Journal of Structural Geology*, 50, 254-266. <https://doi.org/10.1016/j.jsg.2012.12.011>

- Moores, E. M., & Twiss, R. J. (1995). *Tectonics*. W.H. Freeman and Company, New York.
- Nemat-Nasser, S., Hori, M., 1999. *Micromechanics: Overall Properties of Heterogeneous Materials*. Second revised edition. Elsevier.
- Nicolas, A., & Poirier, J. P. (1976). *Crystalline plasticity and solid state flow in metamorphic rocks*. John Wiley & Sons.
- Post, A. D., Tullis, J., & Yund, R. A. (1996). Effects of chemical environment on dislocation creep of quartzite. *Journal of Geophysical Research: Solid Earth*, 101(B10), 22143–22155. <https://doi.org/10.1029/96JB01926>
- Qu, M., Jiang, D., & Lu, L. X. (2016). An optimal scheme for numerical evaluation of Eshelby tensors and its implementation in a MATLAB package for simulating the motion of viscous ellipsoids in slow flows. *Computers & geosciences*, 96, 98-108. <https://doi.org/10.1016/j.cageo.2016.08.005>
- Qu, M. (2018). Analysis and Tectonic Synthesis of the Multiscale Structures along the Shangdan Tectonic Zone in the Qinling Orogenic Belt, China. Electronic Thesis and Dissertation Repository. 5383. <https://ir.lib.uwo.ca/etd/5383>
- Ramberg, H. (1975). Particle paths, displacement and progressive strain applicable to rocks. *Tectonophysics*, 28(1-2), 1-37. [https://doi.org/10.1016/0040-1951\(75\)90058-X](https://doi.org/10.1016/0040-1951(75)90058-X)
- Ramsay, J. G., & Graham, R. H. (1970). Strain variation in shear belts. *Canadian Journal of Earth Sciences*, 7(3), 786-813. <https://doi.org/10.1139/e70-078>
- Ramsay, J. G. (1967). *Folding and fracturing of rocks*. Mc Graw Hill Book Company
- Ranalli, G. (1987). *Rheology of the Earth: Deformation and Flow Processes in Geophysics and Geodynamics*. Boston: Allen & Unwin.

- Reuss, A. (1929). Berechnung der fließgrenze von mischkristallen auf grund der plastizitätsbedingung für einkristalle. *ZAMM-Journal of Applied Mathematics and Mechanics/Zeitschrift für Angewandte Mathematik und Mechanik*, 9(1), 49-58.
- Robin, P. Y. F., & Cruden, A. R. (1994). Strain and vorticity patterns in ideally ductile transpression zones. *Journal of Structural Geology*, 16(4), 447-466.  
[https://doi.org/10.1016/0191-8141\(94\)90090-6](https://doi.org/10.1016/0191-8141(94)90090-6)
- Rutter, E. H., & Brodie, K. H. (2004). Experimental intracrystalline plastic flow in hot-pressed synthetic quartzite prepared from Brazilian quartz crystals. *Journal of Structural Geology*, 26(2), 259-270. [https://doi.org/10.1016/S0191-8141\(03\)00096-8](https://doi.org/10.1016/S0191-8141(03)00096-8)
- Rybacki, E., & Dresen, G. (2004). Deformation mechanism maps for feldspar rocks. *Tectonophysics*, 382(3-4), 173-187. <https://doi.org/10.1016/j.tecto.2004.01.006>
- Rybacki, E., Gottschalk, M., Wirth, R., & Dresen, G. (2006). Influence of water fugacity and activation volume on the flow properties of fine-grained anorthite aggregates. *Journal of Geophysical Research: Solid Earth*, 111(B3).  
<https://doi.org/10.1029/2005JB003663>
- Schmalholz, S. M., & Fletcher, R. C. (2011). The exponential flow law applied to necking and folding of a ductile layer. *Geophysical Journal International*, 184(1), 83-89. <https://doi.org/10.1111/j.1365-246X.2010.04846.x>
- Schmalholz, S. M., Schmid, D. W., & Fletcher, R. C. (2008). Evolution of pinch-and-swell structures in a power-law layer. *Journal of Structural Geology*, 30(5), 649-663. <https://doi.org/10.1016/j.jsg.2008.01.002>
- Schmalholz, S. M., & Podladchikov, Y. Y. (2000). Finite amplitude folding: transition from exponential to layer length controlled growth. *Earth and Planetary Science Letters*, 179(2), 363-377. [https://doi.org/10.1016/S0012-821X\(00\)00116-3](https://doi.org/10.1016/S0012-821X(00)00116-3)

- Schmalholz, S. M., & Schmid, D. W. (2012). Folding in power-law viscous multi-layers. *Phil. Trans. R. Soc. A*, 370(1665), 1798-1826. <https://doi.org/10.1098/rsta.2011.0421>
- Shea, W. T., & Kronenberg, A. K. (1993). Strength and anisotropy of foliated rocks with varied mica contents. *Journal of Structural Geology*, 15(9–10), 1097–1121. [https://doi.org/10.1016/0191-8141\(93\)90158-7](https://doi.org/10.1016/0191-8141(93)90158-7)
- Sherby, O. D., & Burke, P. M. (1968). Mechanical behavior of crystalline solids at elevated temperature. *Progress in Materials Science*, 13, 323–390. [https://doi.org/10.1016/0079-6425\(68\)90024-8](https://doi.org/10.1016/0079-6425(68)90024-8)
- Sherby, O. D., Robbins, J. L., & Goldberg, A. (1970). Calculation of activation volumes for self-diffusion and creep at high temperature. *Journal of Applied Physics*, 41(10), 3961–3968. <https://doi.org/10.1063/1.1658396>
- Sibson, R. H. (1977). Fault rocks and fault mechanisms. *Journal of the Geological Society*, 133(3), 191–213. <https://doi.org/10.1144/gsjgs.133.3.0191>
- Tullis, J. (2002). Deformation of Granitic Rocks: Experimental Studies and Natural Examples. *Reviews in Mineralogy and Geochemistry*, 51(1), 51–95. <https://doi.org/10.2138/gsrmg.51.1.51>
- Tullis, J., & Wenk, H. R. (1994). Effect of muscovite on the strength and lattice preferred orientations of experimentally deformed quartz aggregates. *Materials Science and Engineering: A*, 175(1-2), 209-220. [https://doi.org/10.1016/0921-5093\(94\)91060-X](https://doi.org/10.1016/0921-5093(94)91060-X)
- Twiss, R.J., & Moores, E.M. (1992). *Structural Geology*. W.H. Freeman and Company, New York.
- Passchier, C. W., & Trouw, R. A. (2005). *Microtectonics*. Springer Science & Business Media.
- Pollard, D. D., & Fletcher, R.C. (2005). *Fundamentals of Structural Geology*. Cambridge University Press.



- Wilks, K. R., & Carter, N. L. (1990). Rheology of some continental lower crustal rocks. *Tectonophysics*, 182(1–2), 57–77. [https://doi.org/10.1016/0040-1951\(90\)90342-6](https://doi.org/10.1016/0040-1951(90)90342-6)
- Vaucher, A., & Tommasi, A. (2003). Wrench faults down to the asthenosphere: Geological and geophysical evidence and thermomechanical effects. *Geological Society, London, Special Publications*, 210(1), 15-34. <https://doi.org/10.1144/GSL.SP.2003.210.01.02>
- Vaucher, A., Tommasi, A., & Barruol, G. (1998). Rheological heterogeneity, mechanical anisotropy and deformation of the continental lithosphere. *Tectonophysics*, 296(1), 61-86. [https://doi.org/10.1016/S0040-1951\(98\)00137-1](https://doi.org/10.1016/S0040-1951(98)00137-1)
- Voigt, W. (1887). *Theoretische studien über die elasticitätsverhältnisse der krystalle*. in der Dieterichschen Buchhandlung.
- Zoback, M. D., Zoback, M. L., Mount, V. S., Suppe, J., Eaton, J. P., Healy, J. H., ... & Wong, I. G. (1987). New evidence on the state of stress of the San Andreas fault system. *Science*, 238(4830), 1105-1111. <https://doi.org/10.1126/science.238.4830.1105>

## Chapter 2

### 2 A MATLAB Package of the Self-consistent MultiOrder Power-Law Approach

#### 2.1 Introduction

The Earth's lithosphere has abundant structures and fabrics due to tectonic deformation. These structures and fabrics cover a vast range of scales, from the shape and crystallographic-preferred orientations of mineral crystals, which must be examined in thin sections, to outcrop larger scale features like faults, folds, and ductile high-strain zones (e.g., Twiss and Moores, 1992; Pollard and Fletcher, 2005; Passchier and Trouw, 2006). Structural geologists study the structures and fabrics in order to reconstruct the lithospheric deformation processes and to understand the rheology of Earth's lithosphere. The theoretical framework for this effort has been mainly on single-scale continuum mechanics (see Jiang 2014, 2016, for more discussion). However, Earth's lithosphere is made of rheologically heterogeneous elements on any given scale, leading to significant flow field partitioning (Lister and Williams, 1983). The single-scale approach is incapable of making a rigorous connection between small-scale features with the tectonic-scale deformation boundary conditions. Many geologists have recognized that flow partitioning is the key to relate the heterogeneous small-scale structures and fabrics to the tectonic deformations (e.g., Lister and Williams, 1983; Jiang, 1994a, b; Jiang and White, 1995; Jiang and Williams, 1999; Hudleston, 1999; Goodwin and Tikoff, 2002; Jones et al., 2005). In order to understand the deformation in rheologically heterogeneous elements, a multiscale approach is necessary, and such an approach must be based on complete mechanics principles (Jiang and Bentley, 2012; Jiang 2013, 2014, 2016).

Recently, a micromechanics-based self-consistent MultiOrder Power-Law Approach (MOPLA, Jiang and Bentley, 2012; Jiang, 2014, 2016) has been developed to address the flow partitioning problem and then investigate the multiscale deformation and fabric development in the heterogeneous lithosphere. *MultiOrder* refers to the approach of embedding rheologically distinct higher-order elements in a lower-order element to simulate the multiscale nature of deformation, and *Power-Law* means that the rheology of all elements is power-law viscous (Jiang 2014). So far, MOPLA has been widely applied

to many geological settings to understand the development of small-scale ductile shear zones from rheologically weak domains (Xiang and Jiang, 2013), the lineation variation in Cascade Lake shear zone in the east Sierra Nevada of California (Jiang and Bentley, 2012; Jiang, 2014), the formation of micafish porphyroclasts (Chen et al., 2014), the pressure variations among rheologically heterogeneous elements (Jiang and Bhandari, 2018), and the formation of L-tectonite (Yang et al., 2019).

The theory and algorithms of MOPLA have been well documented in Jiang (2014, 2016), and related computation is implemented in MathCad (Jiang, 2014). The MathCad application is user-friendly but at the cost of computational efficiency. In this work, I provide a more refined algorithm of MOPLA and implement it in MATLAB.

Specifically, MOPLA is computationally intensive because it requires a large number of iterative calculations, and each iteration round involves a large number of evaluations of 4<sup>th</sup> order Eshelby tensor, which is the most time-consuming part in the calculation. Therefore, the bottleneck of the MOPLA computation boils down to the evaluation of Eshelby tensors. Qu et al. (2016) developed an optimal scheme to evaluate Eshelby tensors efficiently. In this work, I refined the algorithm of MOPLA by distinguishing the macroscale fields from the remote fields and developed the MATLAB package for MOPLA incorporating the work of Qu et al. (2016) and using the Parallel Computing Toolbox in MATLAB so that the computation of MOPLA becomes more efficient (more details see below).

To facilitate the description of the new package, I first review the backbone theory of MOPLA and summarize the important equations used in this package. Then, I describe the structure of the MATLAB package. Finally, this package is validated by applying it to the Cascade Lake shear zone in the east Sierra Nevada of California (Jiang and Bentley, 2012; Jiang, 2014). This application also serves as an example to show how to use the MATLAB package.

## 2.2 The classic Eshelby's inclusion/inhomogeneity problem

The backbone theory of MOPLA is the remarkable work of Eshelby's (1957) inclusion solution. The classic Eshelby's inclusion/inhomogeneity problem deals with an infinite

homogenous elastic solid with sub-volume  $\Omega$  in it (Fig.2.1a). The material inside  $\Omega$  is called *inclusion* if it has identical elastic properties as the surrounding material, or *inhomogeneity* if the domain has distinct elastic properties; The material outside  $\Omega$  is called *matrix*. The inclusion  $\Omega$  in the solid that undergoes a uniform strain field will cause stress and strain in the solid. Eshelby (1957,1959,1961) solved that the elastic fields both in the inclusion and matrix elegantly through a series of ‘virtual’ transformations (Fig.2.1). If we remove the inclusion  $\Omega$  from the surrounding matrix, the inclusion tends to deform to  $\Omega^*$  and undergo a uniform strain  $\mathbf{e}^*$ , which is called eigenstrain, to reach a stress-free state (Fig.2.1b). The infinite solid with a hole remains stress and strain-free. Apply surface traction on  $\Omega^*$  to deform it back to the original shape  $\Omega$ , then place the inclusion back to the void and remove the surface traction. The interaction between the matrix and inclusion leads to the equilibrated constrained state of the inclusion, which differs from the initial state by a strain field  $\mathbf{e}^c$  and a rotation field  $\boldsymbol{\omega}^c$  (Fig. 2.1c). If the inclusion is an ellipsoid, the constrained stress and elastic fields (strain and rotation) within the inclusion are uniform (Eshelby, 1957, p. 384, his Eq.3.5). The constrained strain field,  $\mathbf{e}^c$ , and rotation,  $\boldsymbol{\omega}^c$ , in the ellipsoid are related to the eigenstrain  $\mathbf{e}^*$  by two 4<sup>th</sup> order tensors:

$$\mathbf{e}^c = \mathbf{S} : \mathbf{e}^* ; \quad \boldsymbol{\omega}^c = \mathbf{\Pi} : \mathbf{e}^* \quad (2.1)$$

where  $\mathbf{S}$  and  $\mathbf{\Pi}$  are the symmetric and anti-symmetric Eshelby tensors for the interior points, respectively. The sign “:” stands for the double-index contraction of two tensors. As the elastic fields are uniform in an ellipsoidal inclusion, both  $\mathbf{S}$  and  $\mathbf{\Pi}$  for are constant quantities inside the inclusion.

Now, let us consider an inhomogeneity having distinct elastic properties from the matrix embedded in an infinite matrix medium subjected to a uniform remote deformation. Eshelby (1957) proposed that an inhomogeneity can always be replaced by a unique ‘equivalent inclusion’ with the proper eigenstrain field so that the stress state inside the inclusion is the same as when the inhomogeneity is present. Then the deformation inside an inhomogeneity is treated as a superposition of the applied remote deformation and a perturbation deformation caused by the equivalent inclusion. Eshelby’s approach enables

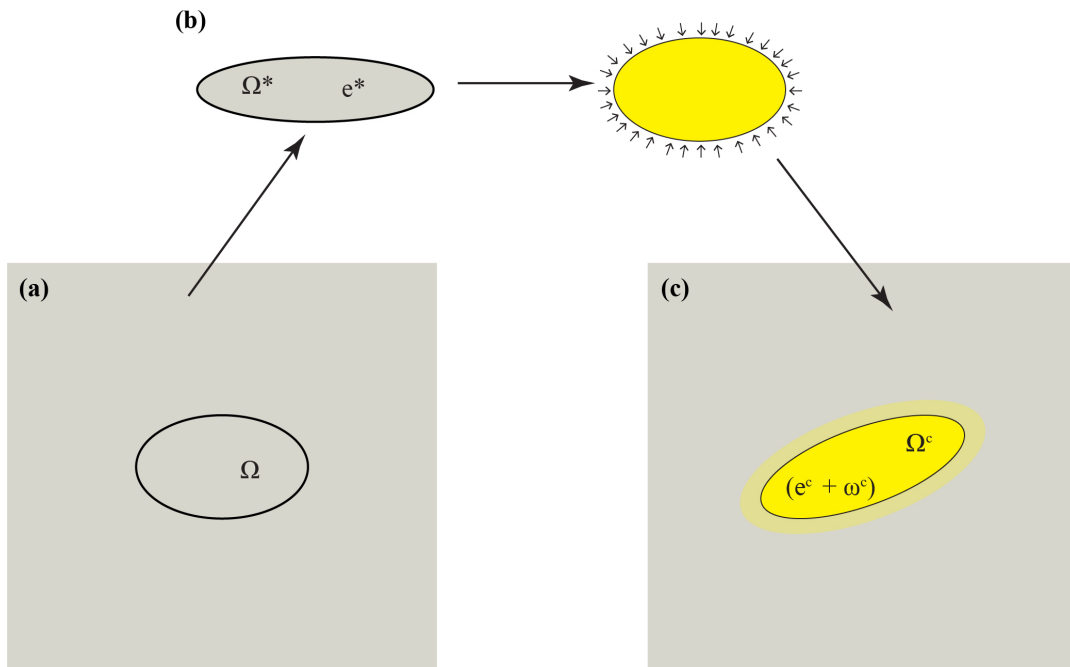


**Figure 2.1 Eshelby's solution of the classic inclusion/inhomogeneity problem illustrated by a series of "virtual" transformations**

(a) A homogeneous infinite elastic material with a region  $\Omega$ , called inclusion, in it. If the inclusion were cut out, the matrix would remain stress and strain free. (b) Remove the inclusion from the matrix. The eigenstrain  $e^*$  transforms  $\Omega$  to  $\Omega^*$ . The transformed  $\Omega^*$  state with a strain of  $e^*$  corresponds to the stress-free state of the inclusion. To fit back the inclusion to the matrix, surface traction is applied to  $\Omega^*$  to deform it back to the shape of  $\Omega$ . Then place the inclusion back to the matrix with a void. (c) The final equilibrated state of the inclusion. Both inclusion and matrix will undergo an elastic field. The inclusion will deform and rotate to  $\Omega^C$  state. The strain and rotation within the inclusion are  $e^C$  and  $\omega^C$ .

the flow fields inside a general elastic inhomogeneity to be related to the remote flow field (Mura, 1987) and has been formulated in Jiang (2013):

$$\mathbf{e}^{\text{inh}} = \mathbf{A} : \mathbf{e}^{\text{M}}, \quad \mathbf{A} = \left[ \mathbf{J}^s + \mathbf{S} (\mathbf{C}_{\text{M}}^{-1} : \mathbf{C}_{\text{inh}} - \mathbf{J}^s) \right]^{-1} \quad (2.2a)$$

$$\boldsymbol{\omega}^{\text{inh}} = \boldsymbol{\omega}^{\text{M}} + \boldsymbol{\Pi} : \mathbf{S}^{-1} : (\mathbf{A} - \mathbf{J}^s) \mathbf{e}^{\text{M}} \quad (2.2b)$$

$$\boldsymbol{\sigma}^{\text{inh}} = \mathbf{B} : \boldsymbol{\sigma}^{\text{M}}, \quad \mathbf{B} = \mathbf{C}_{\text{inh}} : \mathbf{A} : \mathbf{C}_{\text{M}}^{-1} \quad (2.2c)$$

where  $\mathbf{e}$ ,  $\boldsymbol{\omega}$ , and  $\boldsymbol{\sigma}$  are the elastic strain, rotation, and Cauchy stress fields;  $\mathbf{C}$  is the 4<sup>th</sup> order elastic stiffness tensor. The sub- or super-script ‘inh’ and ‘M’ stand for the properties in inhomogeneity and in matrix medium, respectively.  $\mathbf{A}$  and  $\mathbf{B}$  are respectively the 4<sup>th</sup> order strain partitioning and stress partition tensors.  $\mathbf{J}^s$  is the 4<sup>th</sup> order symmetric identity tensor (more details see below). As the inhomogeneity is viewed as an equivalent inclusion, I will simply use ‘inclusions’ to represent both inhomogeneities or inclusions hereafter.

Viscous materials are commonly assumed incompressible. In order to extend Eshelby’s formalism to incompressible viscous materials, one can either adopt a “penalty approach” (Lebensohn and Tome, 1993) or use the incompressibility as an additional kinematic condition. As the first approach has some major drawbacks as discussed in Jiang (2016), we follow the latter one. To do so, the Cauchy stress field must be decomposed into a deviatoric part and a pressure part (e.g., Spencer, 1980). The rheology equation of an incompressible viscous material is associated with the deviatoric stress only. In this situation, Eshelby’s solution for linear viscous materials is expressed as:

$$\boldsymbol{\varepsilon} = \mathbf{A} : \mathbf{E}, \quad \mathbf{A} = \left[ \mathbf{J}^s + \mathbf{S} (\mathbf{C}_{\text{M}}^{-1} : \mathbf{C}_{\text{E}} - \mathbf{J}^s) \right]^{-1} \quad (2.3a)$$

$$\mathbf{w} = \mathbf{W} + \boldsymbol{\Pi} : \mathbf{S}^{-1} : (\boldsymbol{\varepsilon} - \mathbf{E}) \quad (2.3b)$$

$$\boldsymbol{\sigma} = \mathbf{B} : \boldsymbol{\Sigma}, \quad \mathbf{B} = \mathbf{C}_{\text{E}} : \mathbf{A} : \mathbf{C}_{\text{M}}^{-1} \quad (2.3c)$$

where  $\boldsymbol{\varepsilon}$ ,  $\boldsymbol{\sigma}$ , and  $\boldsymbol{w}$  are respectively the strain rate, deviatoric stress, and vorticity inside the inclusion; the corresponding uppercase symbols  $\mathbf{E}$ ,  $\boldsymbol{\Sigma}$ , and  $\mathbf{W}$  represent the equivalent quantities in the remote field.  $\mathbf{C}$  with sub-script ‘‘M’’ and ‘‘E’’ stand for the viscous stiffness tensors in inclusion or in the matrix and  $\mathbf{A}$  is called the strain-rate partitioning tensor now.

Clearly, Eshelby’s solution requires the evaluation of  $\mathbf{S}$  and  $\boldsymbol{\Pi}$ . The expressions of  $\mathbf{S}$  and  $\boldsymbol{\Pi}$  for isotropic elastic materials are expressed in terms of elliptical integrals (Eshelby, 1957; Mura, 1987, P.77-84). One can also use these expressions and set the Poisson’s ratio  $\nu = 0.5$  to get  $\mathbf{S}^v$  and  $\boldsymbol{\Pi}^v$  for isotropic viscous materials, which are commonly assumed incompressible (Bilby et al., 1975; Bilby and Kolbuszewski, 1977). In fact,  $\boldsymbol{\Pi}^v$  and  $\boldsymbol{\Pi}|_{\nu=0.5}$  are indeed equal, but  $\mathbf{S}^v$  and  $\mathbf{S}|_{\nu=0.5}$  are equal for off-diagonal components only. The components of  $\mathbf{S}$  and  $\mathbf{S}^v$  are and those of  $\boldsymbol{\Pi}$  and  $\boldsymbol{\Pi}^v$  have the following relations (Jiang, 2016):

$$S_{ijkl}^v = S_{ijkl}|_{\nu=0.5} - \frac{1}{3}(S_{ii11} + S_{ii22} + S_{ii33})|_{\nu=0.5} \quad (\text{no sum}) \quad (2.4a)$$

$$\Pi_{ijkl}^v \equiv \Pi_{ijkl}|_{\nu=0.5} \quad (2.4b)$$

where the superscript ‘v’ stands for incompressible viscous material. The evaluation of Eshelby tensors for isotropic materials is realized by the MATLAB files ‘*SnPI\_poisson.m*’ and ‘*SnPI\_vis.m*’ (Appendix A). For general elastic or general incompressible viscous materials,  $\mathbf{S}$  and  $\boldsymbol{\Pi}$  or  $\mathbf{S}^v$  and  $\boldsymbol{\Pi}^v$  are expressed in terms of a Green’s interaction 4<sup>th</sup> order tensor  $\mathbf{T}$  or  $\mathbf{T}^v$  (Jiang, 2013, 2014):

$$\mathbf{S} = \mathbf{J}^s : \mathbf{T} : \mathbf{C}; \quad \boldsymbol{\Pi} = \mathbf{J}^a : \mathbf{T} : \mathbf{C} \quad (\text{compressible materials}) \quad (2.5a)$$

$$\mathbf{S}^v = \mathbf{J}^d : \mathbf{T}^v : \mathbf{C}; \quad \boldsymbol{\Pi}^v = \mathbf{J}^a : \mathbf{T}^v : \mathbf{C} \quad (\text{incompressible materials}) \quad (2.5b)$$

where  $\mathbf{J}^s$ ,  $\mathbf{J}^a$  and  $\mathbf{J}^d$  are 4<sup>th</sup> order symmetric identity, anti-symmetric identity, and deviatoric identity tensors defined in terms of the Kronecker delta  $\delta_{ij} = \begin{cases} 1 & i = j \\ 0 & i \neq j \end{cases}$ :

$$J_{ijkl}^s = \frac{1}{2}(\delta_{ik}\delta_{jl} + \delta_{jk}\delta_{il}), J_{ijkl}^a = \frac{1}{2}(\delta_{ik}\delta_{jl} - \delta_{jk}\delta_{il}), J_{ijkl}^d = J_{ijkl}^s - \frac{1}{3}\delta_{ij}\delta_{kl} \quad (2.6)$$

According to Eq.2.5, the evaluation of Eshelby tensors for general materials ( $\mathbf{S}$  and  $\mathbf{\Pi}$  or  $\mathbf{S}^v$  and  $\mathbf{\Pi}^v$ ) boils down to the calculation of  $\mathbf{T}$  or  $\mathbf{T}^v$ , which can be expressed in following integrals (Lebensohn et al., 1998; Jiang, 2014, 2016):

$$T_{ijkl} = \frac{a_1 a_2 a_3}{2\pi} \int_0^\pi \int_0^\pi A_{ik}^{-1} z_j z_l \rho^{-3} \sin \phi d\phi d\theta \quad (\text{compressible materials}) \quad (2.7a)$$

$$T_{ijkl}^v = \frac{a_1 a_2 a_3}{2\pi} \int_0^\pi \int_0^\pi \widehat{A}_{ik} z_j z_l \rho^{-3} \sin \phi d\phi d\theta \quad (\text{incompressible materials}) \quad (2.7b)$$

where  $a_i$  ( $i=1,2,3$ ) are the three semi-axes of the ellipsoidal inclusion, unit vector  $\mathbf{z}$  is

$$\text{expressed in terms of spherical angles by } \mathbf{z} = \begin{pmatrix} \cos \theta \sin \phi \\ \sin \theta \sin \phi \\ \cos \phi \end{pmatrix},$$

$\rho = \sqrt{(a_1 z_1)^2 + (a_2 z_2)^2 + (a_3 z_3)^2}$ , and  $A_{ik} = C_{ijkl}^M z_j z_l$  is the Christoffel stiffness tensor (e.g.,

$$\text{Barnett, 1972; Walker, 1993). } \widehat{A}_{ik} \text{ is constructed from } A_{ik} \text{ as: } \begin{pmatrix} \widehat{\mathbf{A}} & \boldsymbol{\zeta} \\ \boldsymbol{\zeta}^T & \lambda \end{pmatrix} = \begin{pmatrix} \mathbf{A} & \mathbf{z} \\ \mathbf{z}^T & 0 \end{pmatrix}^{-1}.$$

Jiang (2014) in his Mathcad scripts used a product Gaussian quadrature to get the numerical integrations, which is very time-consuming, especially for the elongated or flattened ellipsoid. Qu et al., (2016) provided an optimal scheme to numerically evaluate the integral (Eq2.7b) using a product Gaussian quadrature or a Lebedev quadrature depending on the shape of the ellipsoid. In order to save computational time, part of the numerical integration of Eq.2.7b has been written in C language and compiled using MATLAB built-in *mex* function and the Microsoft C++ 2015 compiler by Qu et al. (2016). This package incorporated the work of Qu et al. (2016) and extended it to compressible material (Eq.2.7a). The numerical integrations for general compressible/incompressible materials (Eq.7) are realized in MATLAB files ‘*Tfunction.m*’ and ‘*Tfunction\_AGLQ.m*’ (Appendix A). Above Eshelby’s formalism is for



compressible materials, to get the corresponding equations for incompressible materials, one can replace  $\mathbf{S}$ ,  $\mathbf{\Pi}$  and  $\mathbf{J}^s$  in Eqs.2.3 and 2.4 with  $\mathbf{S}^v$ ,  $\mathbf{\Pi}^v$ , and  $\mathbf{J}^d$ .

## 2.3 Application of Eshelby's solution to natural deformation in Earth's lithosphere

Earth's lithosphere is made of a large number of rheologically distinct elements (RDEs). In Eshelby's sense, each rheologically distinct element is regarded as an Eshelby inclusion. Applying Eshelby's solution for the inclusion/inhomogeneity problem to natural deformation allows us to quantitatively evaluate the partitioned flow fields inside each rheologically distinct element from the remote tectonic flow. The partitioned flow fields, in turn, can be used to investigate the small-scale structures and fabrics. This is the backbone of MOPLA. However, to apply the Eshelby's solution (Eq.2.3) to heterogeneous Earth's lithosphere the following aspects need to be addressed: first, the lithosphere is not an infinite medium; second, in nature, the rheologically distinct elements have irregular shapes, not perfect ellipsoids; third, the rock masses in Earth's lithosphere are generally non-linear, and commonly considered as power-law materials; last, the rock masses are heterogeneous poly-element materials. This section discusses the above problems one by one as well as the strategy to address the multiscale deformation.

### 2.3.1 Scale separation

As Earth's lithosphere is not an infinite medium, but Eshelby's solution is for the inclusions embedded in an infinite matrix. To apply Eshelby's solution to Earth's lithosphere, the condition of scale separation (Zaoui, 2002; Qu and Cherkaoui, 2006; Jiang, 2014) must be satisfied. Let us consider a crustal deformation caused by a tectonic loading (Fig.1.3) as an example to explain this concept. The whole crustal deformation zone has a characteristic length of  $\mathcal{D}$ , and the remote tectonic loading has a fluctuation length of  $\lambda$  (Fig.1.3a). The statistically homogeneous macroscale fields ('regional' or 'bulk' strain rate  $\mathbf{E}$ , vorticity  $\mathbf{W}$ , and stress  $\mathbf{\Sigma}$ ) of the zone are defined in terms of a Representative Volume Element (RVE) at every point  $X$ , with a characteristic length of  $D$  (Fig.1.3b). The RVE is a large enough volume element containing a representative assemblage of all Rheologically Distinct Elements (RDEs) with an average size of  $d$  (Fig.1.3c). The partitioned fields ('local' strain rate  $\boldsymbol{\varepsilon}$ , vorticity  $\mathbf{w}$  and stress  $\boldsymbol{\sigma}$ ) are

defined within individual RDEs. The condition of scale separation requires that the mean size of RDEs must be much smaller than the size of RVE ( $d \ll D$ ) which itself must be much smaller the size of the whole crustal deformation ( $D \ll \mathcal{D}$ ) and the fluctuation length of the boundary loading ( $D \ll \lambda$ ). In such a case, the size of each RDE is inappreciable compared to its distance from the deformation boundary, so the boundary effects on RDEs can be ignored. With this condition, each RDE in Earth's lithosphere can be regarded as an Eshelby inclusion embedded in an infinite matrix. Applying Eshelby's solutions, the partitioned fields within an RDE can be solved. That, in turn, governs the smaller-scaled structural and fabric elements there, with a characteristic length of  $\delta$  ( $\delta \ll d$ ). (Fig.1.3e-g). The scale separation must be satisfied; however, the absolute size of the characteristic lengths and the scale gaps between them depend on the nature of the deformation.

### 2.3.2 Rheologically distinct elements with irregular shapes

Eshelby approved that the stress and flow fields inside ellipsoidal inclusions are uniform; however, in nature, the rheologically distinct elements have irregular shapes. For the inclusions with irregular shapes, Eshelby's solutions (Eqs.2.3) are considered as the approximations of average fields inside the inclusions. Although this a practical method, it seems working well. A larger member of works have been done to apply Eshelby's solution to the real materials considered individual grains with irregular shapes in a polycrystalline material as ellipsoidal inclusions embedded in the polycrystalline medium (Budiansky and Mangasarian, 1960; Mura, 1987, p.421-433; Lebensohn and Tome, 1993; Molinari, 2002). In addition, the rigid or deformable clasts, dislocations, stacking faults, cracks, weakened zones, and other discontinuities can also be treated as 'ellipsoids' in the literature (e.g., Ramsay, 1967; Dunnet, 1969; Gay, 1968; Ghosh and Ramberg, 1976; Mura, 1987, p.15-20, 240-379; Rudnicki, 1977; Ježek et al., 1996; Healy et al., 2006; Exner and Dabrowski, 2010). Therefore, in MOPLA, the rheologically distinct elements with irregular shapes are viewed as ellipsoidal inclusions. This assumption allows the application of Eshelby's solutions to real materials.

### 2.3.3 Application to non-linear viscous materials

The rock mass in Earth's lithosphere is commonly regarded as a power-law viscous material, where the strain rate  $\boldsymbol{\varepsilon}$  is related to the deviatoric stress  $\boldsymbol{\sigma}$  to the power of  $n$  ( $>1$ ), called the stress exponent (e.g., Kohlstedt et al., 1995; Tullis, 2002). The constitutive relation for a general non-linear material, including power-law material, can be written as:

$$\sigma_{ij} = f_{ij}(\varepsilon_{kl}) \quad \text{or} \quad \varepsilon_{ij} = g_{ij}(\sigma_{kl}) \quad (2.8a)$$

or in pseudo-linear forms:

$$\boldsymbol{\sigma} = \mathbf{C}^{\text{sec}} \boldsymbol{\varepsilon} \quad \text{or} \quad \boldsymbol{\varepsilon} = \mathbf{M}^{\text{sec}} \boldsymbol{\sigma} \quad (2.8b)$$

where  $\mathbf{C}^{\text{sec}}$  and  $\mathbf{M}^{\text{sec}}$  (inverse of each other) are respectively the 4<sup>th</sup> order secant stiffness (or viscosity) and secant compliance tensors. Both tensors depend on the current state of stress or strain rate. For non-linear viscous materials, there is no exact Eshelby's solution, like Eqs.2.3. To extend the Eshelby's solution to a non-linear material one needs to approximately express the constitutive equation for non-linear materials in a linear form by a variety of linearization approaches (e.g., Hutchinson, 1976; Molinari et al., 1987; Lebensohn and Tome, 1993; Masson et al., 2000; Lebensohn et al., 2003, 2004; Jiang, 2014):

$$\boldsymbol{\varepsilon} = \widehat{\mathbf{M}} : \boldsymbol{\sigma} + \boldsymbol{\varepsilon}^0 \quad \text{or} \quad \boldsymbol{\sigma} = \widehat{\mathbf{C}} : \boldsymbol{\varepsilon} + \boldsymbol{\sigma}^0 \quad (2.9)$$

where the  $\widehat{\mathbf{C}}$  and  $\widehat{\mathbf{M}}$  are respectively the linearized viscous stiffness and linearized viscous compliance;  $\boldsymbol{\varepsilon}^0$  and  $\boldsymbol{\sigma}^0$  are the pre-strain-rate and pre-stress terms. Then Eshelby's formalism (Eq.2.3) can be rewritten as (Jiang, 2014):

$$\boldsymbol{\varepsilon}^{(k)} = \widehat{\mathbf{A}}^{(k)} : \mathbf{E} + \widehat{\boldsymbol{\alpha}}^{(k)} ; \quad (2.10a)$$

$$\mathbf{w}^{(k)} = \mathbf{W} + \boldsymbol{\Pi}^{(k)} : \mathbf{S}^{(k)-1} : (\boldsymbol{\varepsilon}^{(k)} - \mathbf{E}) \quad (2.10b)$$

$$\boldsymbol{\sigma}^{(k)} = \widehat{\mathbf{B}}^{(k)} : \boldsymbol{\Sigma} + \widehat{\boldsymbol{\beta}}^{(k)} \quad (2.10c)$$

In Eq.2.10,  $\widehat{\mathbf{A}}^{(k)}$  and  $\widehat{\mathbf{a}}^{(k)}$  are 4<sup>th</sup>-order and second-order strain-rate partitioning tensors,  $\widehat{\mathbf{B}}^{(k)}$  and  $\widehat{\mathbf{\beta}}^{(k)}$  4<sup>th</sup>-order and second-order stress partitioning tensors defined in terms of  $\mathbf{H}$  and  $\widehat{\mathbf{H}}$ :

$$\widehat{\mathbf{A}}^{(k)} = \left( \mathbf{H}^{(k)} + \widehat{\mathbf{C}}^{(k)} \right)^{-1} : \left( \mathbf{H}^{(k)} + \widehat{\mathbf{C}}_{\mathbf{M}} \right); \quad \widehat{\mathbf{a}}^{(k)} = \left( \mathbf{H}^{(k)} + \widehat{\mathbf{C}}^{(k)} \right)^{-1} : \left( \boldsymbol{\Sigma}^0 - \boldsymbol{\sigma}^{0(k)} \right) \quad (2.11a)$$

$$\widehat{\mathbf{B}}^{(k)} = \left( \widehat{\mathbf{M}}^{(k)} + \widehat{\mathbf{H}}^{(k)} \right)^{-1} : \left( \widehat{\mathbf{M}}_{\mathbf{M}} + \widehat{\mathbf{H}}^{(k)} \right); \quad \widehat{\mathbf{\beta}}^{(k)} = \left( \widehat{\mathbf{M}}^{(k)} + \widehat{\mathbf{H}}^{(k)} \right)^{-1} : \left( \mathbf{E}^0 - \boldsymbol{\varepsilon}^{0(k)} \right) \quad (2.11b)$$

where  $\mathbf{H} = \widehat{\mathbf{C}}_{\mathbf{M}} : (\mathbf{S}^{-1} - \mathbf{J}^s)$  is called the Hill's constraint tensor (Qu and Cherkaoui, 2006, p.90, 315) and  $\widehat{\mathbf{H}} = (\mathbf{S}^{-1} - \mathbf{J}^s)^{-1} : \widehat{\mathbf{M}}_{\mathbf{M}}$ , the inverse of  $\mathbf{H}$ , is also known as the interaction tensor (Lenbsohn and Tomé, 1993).

In this MATLAB Package, the well-known tangent linearization (Hutchinson, 1976; Molinari et al., 1987; Lebensohn and Tomé, 1993) is adopted:

$$\boldsymbol{\sigma} = \mathbf{C}^{\text{tan}} \boldsymbol{\varepsilon} + \boldsymbol{\sigma}^0; \quad \boldsymbol{\varepsilon} = \mathbf{M}^{\text{tan}} \boldsymbol{\sigma} + \boldsymbol{\varepsilon}^0 \quad (2.12a)$$

$$\mathbf{M}^{\text{tan}} = n \mathbf{M}^{\text{sec}}; \quad \mathbf{C}^{\text{tan}} = \frac{1}{n} \mathbf{C}^{\text{sec}} \quad (2.12b)$$

where  $\mathbf{C}^{\text{tan}}$  and  $\mathbf{M}^{\text{tan}}$  (inverse of each other) are respectively the tangent stiffness (or viscosity) and tangent compliance tensors, which linearly related the stress and strain rate in the vicinity of  $\boldsymbol{\sigma}^0$  and  $\boldsymbol{\varepsilon}^0$ .

### 2.3.4 Heterogeneous matrix and homogenization

Earth's lithosphere is made of a large number of constituents with distinct rheological properties, different shapes, and orientations, so Earth's lithosphere is a heterogenous poly-element material. In order to apply the extended Eshelby formalisms to the heterogenous poly-element lithosphere, the concept of Homogenous Equivalent Medium (HEM) is applied. Consider a Representative Volume Element (RVE) composed of a large number of rheologically distinct elements (RDEs), then the macroscale field

properties (stress, strain-rate, and vorticity) at every point are defined as the average properties over the RVE. Each element is treated as an Eshelby inclusion embedded in an idealized HEM whose rheological properties are obtained from the overall rheological properties of the RVE (Fig.2.2e). In micromechanics, the procedure to evaluate the overall rheological properties of the composite material from the rheological properties of its constituent elements is called homogenization. Several efficient homogenization approaches are proposed (e.g., Mori and Tanaka, 1973; Molinari et al., 1987; Mura, 1987; Lebensohn and Tome, 1993; Nemat-Nasser and Hori, 1999; Qu and Cherkaoui, 2006).

If the inclusions in the composite material (Fig.2.2b) are so far apart from each other that their interactions can be neglected, this system can be considered as dilute inclusions in a groundmass. The rheology of the HEM is simply represented by the matrix rheology. Given a remote loading ( $\mathbf{L} = \mathbf{E} + \mathbf{W}$ ), the macroscale stress in the matrix is calculated by the constitutive equation ( $\mathbf{\Sigma} = \mathbf{C}_m : \mathbf{E}$ ). As the shapes, orientations, and the rheological properties of all inclusions are known, the partitioned flow and stress fields ( $\mathbf{e}^{(k)}$ ,  $\mathbf{w}^{(k)}$  and  $\mathbf{\sigma}^{(k)}$ ) inside individual inclusions can be obtained by the Eshelby's solution (Eqs.2.12 and 2.13).

As the inclusion volume fraction increases, the interaction among inclusions becomes significant. Consider a composite material with a large number of RDEs subjected to a strain rate  $\mathbf{E}$ ; homogenization approach is required to find suitable choices of the homogeneous reference medium with macroscale response defined by:

$$\mathbf{\Sigma} = \bar{\mathbf{C}} : \mathbf{E} + \mathbf{\Sigma}^0 \text{ or } \mathbf{E} = \bar{\mathbf{M}} : \mathbf{\Sigma} + \mathbf{E}^0 \quad (2.13)$$

where  $\bar{\mathbf{C}}$  and  $\bar{\mathbf{M}}$  are the macroscale linear-form of homogenized stiffness and compliance tensors defined at  $\mathbf{E}$ ;  $\mathbf{\Sigma}^0$  and  $\mathbf{E}^0$  are the back-extrapolated terms.  $\bar{\mathbf{C}}$ ,  $\bar{\mathbf{M}}$ ,  $\mathbf{\Sigma}^0$  and  $\mathbf{E}^0$  are uniform.

The homogenization scheme is characterized by choice of the homogenous reference medium. Consider a composite material with RDEs embedded in a connected matrix (Fig.2.2c), Mori-Tanaka method (Mori and Tanaka, 1973; Molinari and Mercier, 2004; Mercier and Molinari, 2009) is adopted to capture the overall rheology. Each element is

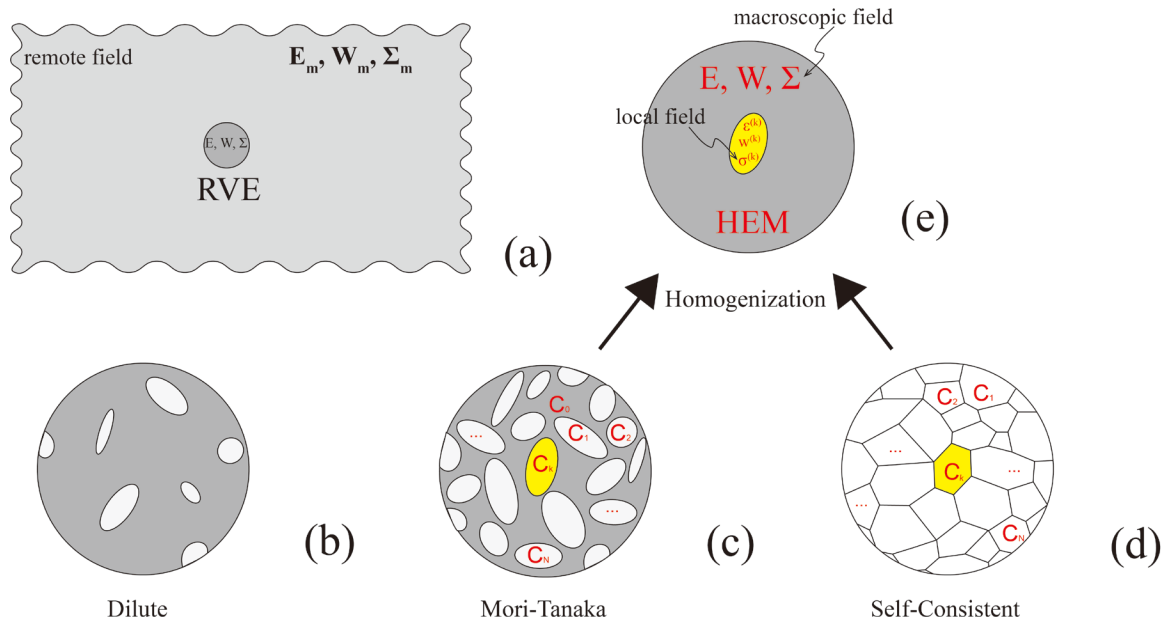


**Figure 2.2 A conceptual diagram to illustrate three different inclusion-matrix systems**

(a) An infinite composite medium subjected to a remote field (strain rate  $E_m$ , vorticity  $W_m$  and deviatoric stress  $\Sigma_m$ ) in the infinity. The corresponding macroscale fields ( $E$ ,  $W$  and  $\Sigma$ ) at every point are defined over a Representative Volume Element (RVE) (b) The dilute situation where the volume fraction of the inclusion is low and the inclusions are far apart away from each other. In this scenario, the overall rheology is simply represented by the matrix rheology. (c) A composited material with more inclusions embedded in a connected matrix. The matrix phase ( $C_0$ ) is adopted as a reference medium to solve the partitioned fields ( $\epsilon^{(k)}$ ,  $w^{(k)}$  and  $\sigma^{(k)}$ ) for individual inclusions. The overall rheology is obtained by the Mori-Tanaka approach. (d) A poly-element composite material without a distinct matrix phase in it. Each element is reviewed as an inclusion embedded in the rest of inclusions. In this scenario, Homogenous Equivalent Medium (HEM) in (e) is adopted as a reference medium, which has the macroscale response of the material ( $E$ ,  $W$  and  $\Sigma$ ) and whose rheology is obtained by means of a self-consistent scheme from the properties of all the constituent elements in an RVE. This figure is modified after Qu et al. (2016).

considered as an inclusion surrounded by a reference medium, which is the matrix material with remaining inclusions in it. For a heterogeneous poly-phase aggregate without matrix (Fig.2.2d), the overall rheology can be obtained by the self-consistent scheme (Molinari et al., 1987; Lebensohn et al., 2003, 2004; Molinari and Mercier, 2004; Mercier and Molinari, 2009). In the self-consistent scheme, each element can be viewed as an inclusion embedded in the HEM made of the remaining RDEs. Although the choices of the reference medium in the two cases are different, in either case, each element is regarded as an inclusion embedded in the reference medium subjected at infinity to the remote strain rate  $\mathbf{E}_m$  (*a priori* different with  $\mathbf{E}$ ), which is the average strain rate in the reference medium. The macroscale response of the reference medium is represented by (Molinari, 2002):

$$\boldsymbol{\Sigma}_m = \bar{\mathbf{C}} : \mathbf{E}_m + \boldsymbol{\Sigma}^0, \quad \boldsymbol{\Sigma} = \bar{\mathbf{C}} : \mathbf{E} + \boldsymbol{\Sigma}^0 \quad (2.14)$$

where  $\boldsymbol{\Sigma}_m$  is the average stress in the reference medium resulting from  $\mathbf{E}_m$ ;  $\boldsymbol{\Sigma}$  is the macroscale stress due to the applied strain rate  $\mathbf{E}$ .

Consider an RVE consist of  $N$  different elements labeled as  $k$  ( $k = 0, 1, \dots, N$ ;  $k = 0$  represents the connected matrix phase if there is one). The average flow fields  $\boldsymbol{\varepsilon}^{(k)}$ ,  $\mathbf{w}^{(k)}$  and  $\boldsymbol{\sigma}^{(k)}$  in each element are related to remote flow fields  $\mathbf{E}_m$ ,  $\mathbf{W}_m$  and  $\boldsymbol{\Sigma}_m$  in the matrix material by the following equations:

$$\boldsymbol{\varepsilon}^{(k)} - \mathbf{E}_m = -\widehat{\mathbf{H}}^{(k)} : (\boldsymbol{\sigma}^{(k)} - \boldsymbol{\Sigma}_m) \quad (2.15a)$$

$$\mathbf{w}^{(k)} - \mathbf{W}_m = \boldsymbol{\Pi}^{(k)} : \mathbf{S}^{(k)-1} : (\boldsymbol{\varepsilon}^{(k)} - \mathbf{E}_m) \quad (2.15b)$$

$$\widehat{\mathbf{H}}^{(k)} = (\mathbf{S}^{(k)-1} - \mathbf{J}^s)^{-1} : \mathbf{M}_M \quad (2.15c)$$

where  $\widehat{\mathbf{H}}$  is evaluated at  $\mathbf{E}_m$ , or by the strain rate and stress partitioning equations:

$$\boldsymbol{\varepsilon}^{(k)} = \widehat{\mathbf{A}}^{(k)} : \mathbf{E}_m + \widehat{\boldsymbol{\alpha}}^{(k)} \quad (2.16a)$$

$$\boldsymbol{\sigma}^{(k)} = \widehat{\mathbf{B}}^{(k)} : \boldsymbol{\Sigma}_m + \widehat{\boldsymbol{\beta}}^{(k)} \quad (2.16b)$$

The macroscale field quantities at any point in the homogenous reference medium are defined as the volume average over the RVE:

$$\boldsymbol{\Sigma}(\mathbf{x}) = \frac{1}{V} \int_V \boldsymbol{\sigma}(\mathbf{x}) dV = \langle \boldsymbol{\sigma} \rangle \quad (2.17a)$$

$$\mathbf{E}(\mathbf{x}) = \frac{1}{V} \int_V \boldsymbol{\varepsilon}(\mathbf{x}) dV = \langle \boldsymbol{\varepsilon} \rangle \quad (2.17b)$$

$$\mathbf{W}(\mathbf{x}) = \frac{1}{V} \int_V \mathbf{w}(\mathbf{x}) dV = \langle \mathbf{w} \rangle \quad (2.17c)$$

where  $V$  is the volume of the RVE and  $\langle \bullet \rangle$  stands for the volume averaging operation over the RVE. Imposing the consistency condition on Eq.2.15b and Eqs.2.16 gives:

$$\mathbf{E}_m = \langle \widehat{\mathbf{A}}^{(k)} \rangle^{-1} : \mathbf{E} - \langle \widehat{\mathbf{A}}^{(k)} \rangle^{-1} : \langle \widehat{\boldsymbol{\alpha}}^{(k)} \rangle \quad (2.18a)$$

$$\boldsymbol{\Sigma}_m = \langle \widehat{\mathbf{B}}^{(k)} \rangle^{-1} : \boldsymbol{\Sigma} - \langle \widehat{\mathbf{B}}^{(k)} \rangle^{-1} : \langle \widehat{\boldsymbol{\beta}}^{(k)} \rangle \quad (2.18b)$$

$$\mathbf{W}_m = \mathbf{W} - \langle \boldsymbol{\Pi}^{(k)} : \mathbf{S}^{(k-1)} \rangle : (\mathbf{E} - \mathbf{E}_m) \quad (2.18c)$$

Combining the nonlinear response of each element ( $\boldsymbol{\sigma}^{(k)} = \widehat{\mathbf{C}}^{(k)} : \boldsymbol{\varepsilon}^{(k)} + \boldsymbol{\sigma}^{0(k)}$ ) with the strain-rate partitioning equation (Eq.2.16a) and imposing the stress consistency

$\langle \boldsymbol{\sigma}^{(k)} \rangle = \boldsymbol{\Sigma}$  condition leads to  $\boldsymbol{\Sigma} = \langle \widehat{\mathbf{C}}^{(k)} : \widehat{\mathbf{A}}^{(k)} \rangle : \mathbf{E}_m + \langle \widehat{\mathbf{C}}^{(k)} : \widehat{\boldsymbol{\alpha}}^{(k)} + \boldsymbol{\sigma}^{0(k)} \rangle$ . Then substitute

the matrix strain rate  $\mathbf{E}_m$  with the applied strain rate  $\mathbf{E}$  using (Eq.2.18a), we have the following expressions for the linear-form of homogenized stiffness and back-extrapolated term:



$$\begin{aligned}
\bar{\mathbf{C}} &= \left\langle \widehat{\mathbf{C}}^{(k)} : \widehat{\mathbf{A}}^{(k)} \right\rangle : \left\langle \widehat{\mathbf{A}}^{(k)} \right\rangle^{-1} \\
\boldsymbol{\Sigma}^0 &= \left\langle \widehat{\mathbf{C}}^{(k)} : \widehat{\mathbf{a}}^{(k)} + \boldsymbol{\sigma}^{0(k)} \right\rangle - \left\langle \widehat{\mathbf{C}}^{(k)} : \widehat{\mathbf{A}}^{(k)} \right\rangle : \left\langle \widehat{\mathbf{A}}^{(k)} \right\rangle^{-1} : \left\langle \widehat{\mathbf{a}}^{(k)} \right\rangle
\end{aligned} \tag{2.19}$$

Similarly, combining the linearized response of each element ( $\boldsymbol{\varepsilon}^{(k)} = \widehat{\mathbf{M}}^{(k)} : \boldsymbol{\sigma}^{(k)} + \boldsymbol{\varepsilon}^{0(k)}$ ), with stress partitioning equation (Eq.2.16b) and imposing the strain rate consistency condition  $\left\langle \boldsymbol{\varepsilon}^{(k)} \right\rangle = \mathbf{E}$  yield  $\mathbf{E} = \left\langle \widehat{\mathbf{M}}^{(k)} : \widehat{\mathbf{B}}^{(k)} \right\rangle : \boldsymbol{\Sigma}_m + \left\langle \widehat{\mathbf{M}}^{(k)} : \widehat{\boldsymbol{\beta}}^{(k)} + \boldsymbol{\varepsilon}^{0(k)} \right\rangle$ . Then substitute the matrix stress  $\boldsymbol{\Sigma}_m$  with  $\boldsymbol{\Sigma}$  using (Eq.2.18b), we can obtain the following expressions for the linear-form of homogenized compliance and back-extrapolated term:

$$\begin{aligned}
\bar{\mathbf{M}} &= \left\langle \widehat{\mathbf{M}}^{(k)} : \widehat{\mathbf{B}}^{(k)} \right\rangle : \left\langle \widehat{\mathbf{B}}^{(k)} \right\rangle^{-1} \\
\mathbf{E}^0 &= \left\langle \widehat{\mathbf{M}}^{(k)} : \widehat{\boldsymbol{\beta}}^{(k)} + \boldsymbol{\varepsilon}^{0(k)} \right\rangle - \left\langle \widehat{\mathbf{M}}^{(k)} : \widehat{\mathbf{B}}^{(k)} \right\rangle : \left\langle \widehat{\mathbf{B}}^{(k)} \right\rangle^{-1} : \left\langle \widehat{\boldsymbol{\beta}}^{(k)} \right\rangle
\end{aligned} \tag{2.20}$$

Note, the above partitioning equations (Eqs.2.15 and 2.16) and homogenization equations (Eqs.2.19 and 2.20) are valid for both the Mori-Tanaka and the self-consistent schemes. These two schemes are distinguished by choice of the reference medium with a connected matrix in the Mori-Tanaka method and a conceptual Homogenous Equivalent Medium (HEM) in the Self-consistent approach. Nevertheless, they can be formulated in the same way. In MOPLA, the self-consistent approach is adopted.

### 2.3.5 A multiscale strategy: inhomogeneities within inhomogeneities

As discussed in the introduction, the observed small-scale structures and fabrics can only be related to the fields at the relevant scale but not the tectonic-scale deformation. To address the multiscale deformation, a concept of ‘inhomogeneities within inhomogeneities’ is proposed by Jiang and Bentley (2012) and Jiang (2014). Structural and fabric elements are considered as high-order (usually smaller size) RDEs within lower-order (usually larger size) RDEs (Jiang and Bentley, 2012). For a deformation process caused by tectonic loading or displacements, the tectonic-scale deformation is partitioned into lower-order RDEs. Then the partitioned fields in a lower-order RDE will

determine the fabric development and deformation pattern within it, which are commonly defined by the shapes and orientations of the higher-order RDEs in it. If the RDEs are treated as ellipsoidal inclusions, the extended Eshelby's solutions can be used to construct the multiscale approach. Especially, let's consider an RVE composed of a large number of lower-order RDEs, then each lower-order RDE is regarded as an Eshelby ellipsoidal inclusion embedded in the rest of lower-order RDEs. Within each lower-order RDE, there are a few dilute higher-order RDEs (structural and fabric elements) in a groundmass. First, one can solve the partitioned fields within each lower-order RDEs self-consistently using the partitioning (Eqs.2.15 and 2.16) and homogenization (Eqs.2.19 or 2.20) equations. Then, the obtained fields in individual lower-order RDEs are used as boundary conditions to investigate the fields in each higher-order RDEs and the fabric development at the higher-order-RDE level by using the partitioning equations (Eq.2.10). By using this rather straightforward multiscale strategy, one can relate the structural and fabric elements to tectonic-scale deformation. So far, the backbone theory of MOPLA, Eshelby's inclusion/inhomogeneity problem, and the major assumptions and strategies used to apply Eshelby's solutions to heterogeneous multiscale deformation in Earth's lithosphere are introduced. In the next section, I will describe the MATLAB package of MOPLA.

## 2.4 MATLAB package of MOPLA

### 2.4.1 A brief summary of the algorithm for the self-consistent approach

Once the imposed flow field and the initial setup of all lower-order RDEs, including the shape, the orientation, the rheological properties, are known, the instantaneous partitioned fields in individual lower-order RDEs can be solved self-consistently. The imposed flow is given by a velocity gradient tensor  $\mathbf{L}$ , which can be decomposed into the strain rate tensor  $\mathbf{E} = \frac{1}{2}(\mathbf{L} + \mathbf{L}^T)$ , and the velocity tensor  $\mathbf{W} = \frac{1}{2}(\mathbf{L} - \mathbf{L}^T)$ . The initial state of an RDE at the initial time  $t_0$  is defined by its shape, orientation, and rheological properties (the effective viscosity  $\eta_{eff}$  and the stress exponent  $n$ ). Because of power-law rheology, the effective viscosity of an RDE must be defined at a reference strain-rate state, such as

the state of  $\mathbf{E}$  and updated in every incremental state. During the deformation, all RDEs may deform and rotate, so one also needs to update the shape and orientation of an RDE in every incremental state (more details see below).

To get the instantaneous fields in an RDE from the remote fields using the partitioning equations, one must know the homogenized compliance (or stiffness) of HEM, which depends on the instantaneous rheological properties of the constituent RDEs. However, the homogenized compliance (or stiffness) of HEM is unknown until the partitioned stress (or strain rate) fields in all RDEs are known. Therefore, a self-consistent approach is necessary by which one can solve the partitioned fields in the constituent RDEs and the homogenized compliance (or stiffness) of HEM simultaneously. The self-consistent approach is achieved by two iterative loops (Jiang, 2014). Fig.2.3 briefly illustrates the procedures of the two iterative loops. Note, as discussed in section 2.4.3, the remote deviatoric stress field  $\Sigma_m$  resulting from  $\mathbf{E}_m$  is different from the macroscale deviatoric stress  $\Sigma$  due to the imposed  $\mathbf{E}$ . The remote field properties and the macroscale field properties were not distinguished in Jiang (2014) but are distinguished in this MATLAB package. The outer iterative loop starts with the initial guesses of  $\overline{\mathbf{M}}_{\text{initial}}$ ,  $\mathbf{E}_{\text{initial}}^0$  and  $\Sigma_m$ , assuming  $\Sigma_m = \Sigma$ . Then for every RDE, the inner iterative loop is launched to calculate the partitioned fields ( $\sigma^{(k)}$  and  $\epsilon^{(k)}$ ) using the partitioning equations (Eqs.2.15 and 2.16) and update the rheological properties until the output rheological properties coincide with the output ones within a specified tolerance. If this condition is satisfied, the partitioned

stress of an RDE must satisfy:  $\frac{\|\sigma_{\text{current}}^{(k)} - \sigma_{\text{last}}^{(k)}\|}{\|\sigma_{\text{last}}^{(k)}\|} < \text{tolerance}$ . As the above computation

repeats in every RDEs, to save computational time, these computations are carried out simultaneously in this package by using the MATLAB built-in Parallel Computing Toolbox. Then the instantaneous rheological properties of all RDEs can be used to update the homogenized properties of HEM  $\overline{\mathbf{M}}$  and  $\mathbf{E}^0$  (Eq.2.20), the macroscale stress  $\Sigma$ , and the remote stress  $\Sigma_m$  (Eq.2.18b), which are used to execute the new round of outer iteration. The outer iterative loop terminates when the output  $\overline{\mathbf{M}}$  and  $\mathbf{E}^0$  coincide with

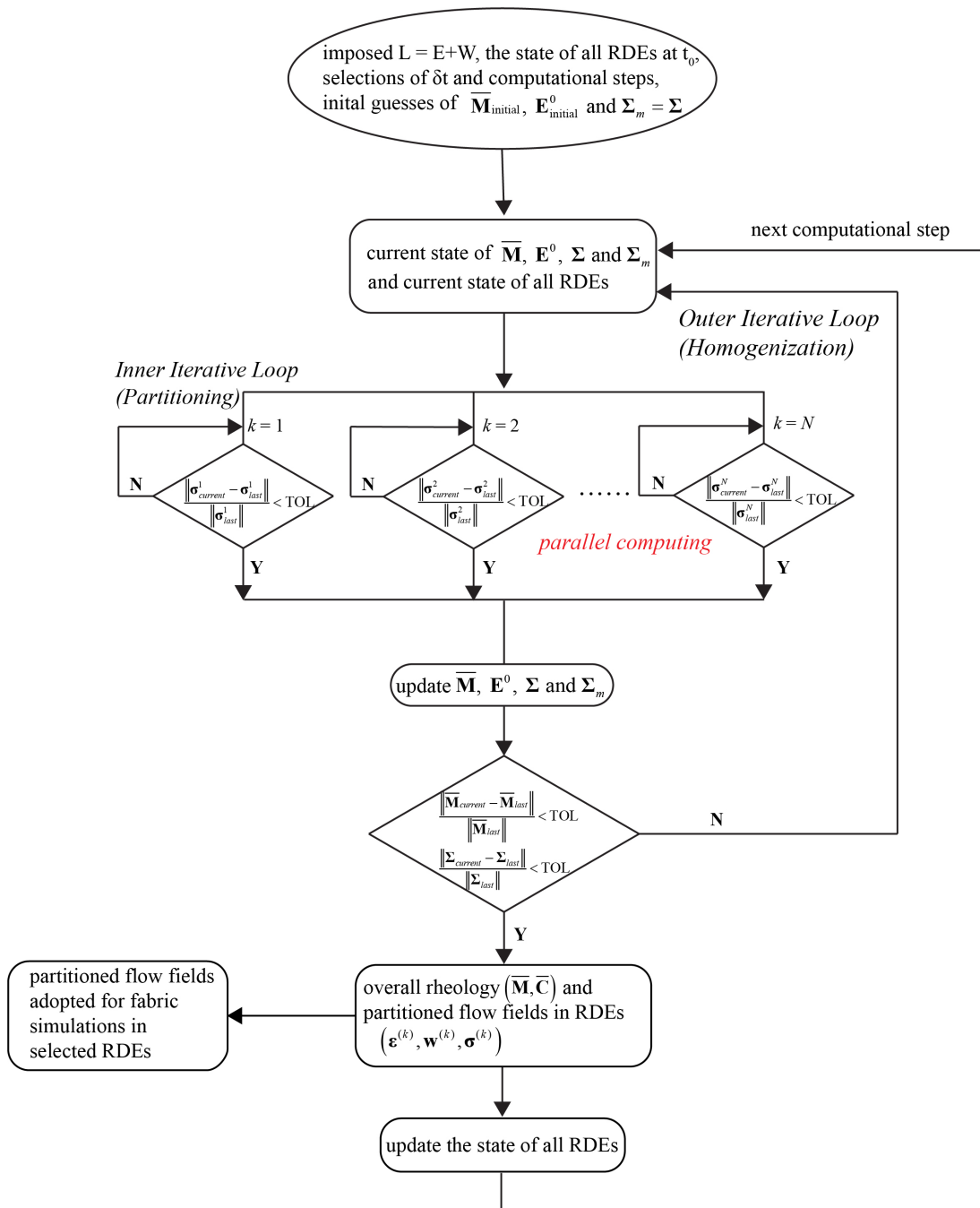


**Figure 2.3 A flowchart of the self-consistent MultiOrder Power-Law Approach (MOPLA)**

the input ones within a tolerance:  $\frac{\|\bar{\mathbf{M}}_{current} - \bar{\mathbf{M}}_{last}\|}{\|\bar{\mathbf{M}}_{last}\|} < \text{tolerance}$ , and the macroscale stress

also satisfies:  $\frac{\|\Sigma_{current} - \Sigma_{last}\|}{\|\Sigma_{last}\|} < \text{tolerance}$ . When both loops are complete, the self-

consistent computation for one computational step is done.

## 2.4.2 A brief summary of the algorithm for the evolution of RDEs

At the time  $t$ , the shape of an RDE is defined by the lengths of its 3 semi-axes ( $a_1$ ,  $a_2$ , and  $a_3$ ), which is expressed in a vector form:  $\mathbf{a} = \begin{pmatrix} a_1 \\ a_2 \\ a_3 \end{pmatrix}$ . The orientation is defined

by a coordinate system  $x'_1x'_2x'_3$  with 3 axes fixed to 3 semi-axes of the ellipsoid (Fig.2.4).

Let the unit vectors parallel to the axes of the global coordinate  $x_1x_2x_3$  be, respectively,  $\mathbf{e}_1$ ,  $\mathbf{e}_2$ , and  $\mathbf{e}_3$ , and those parallel to the axes of the coordinate system  $x'_1x'_2x'_3$  be  $\mathbf{e}'_1$ ,  $\mathbf{e}'_2$ ,

and  $\mathbf{e}'_3$ . Then the orientation is represented by a matrix,  $\mathbf{Q} = \begin{pmatrix} \mathbf{e}'_1{}^T \\ \mathbf{e}'_2{}^T \\ \mathbf{e}'_3{}^T \end{pmatrix}$  in  $x_1x_2x_3$  system,

which can also be defined by a set of 3 spherical angles (Jiang, 2007a, b, 2012, 2013).

Once the remote flow fields in the matrix ( $\mathbf{E}_m$  and  $\mathbf{W}_m$ ) known, the strain rate  $\boldsymbol{\varepsilon}$  and vorticity  $\mathbf{w}$  inside an RDE are calculated using Eqs.2.15. The shape and orientation evolution with time of an RDE is governed by the set of equations (Jiang, 2012):

$$\frac{d\mathbf{a}}{dt} = \hat{\boldsymbol{\varepsilon}}\mathbf{a}, \quad \hat{\boldsymbol{\varepsilon}}_{ij} = \text{diag}(\varepsilon_{ij}) = \begin{cases} 0 & \text{if } i \neq j \\ \varepsilon_{ij} & \text{if } i = j \end{cases} \quad \text{and} \quad \mathbf{a} = \begin{pmatrix} a_1 \\ a_2 \\ a_3 \end{pmatrix} \quad (2.21a)$$

$$\frac{d\mathbf{Q}}{dt} = -\bar{\boldsymbol{\Theta}}\mathbf{Q} \quad (2.21b)$$

In the above equation,  $\bar{\Theta}$  represents the angular velocity, defined by (Jiang, 2007b, 2012, 2013):

$$\bar{\Theta} = \mathbf{w} - \mathbf{w}' \quad (2.22)$$

where  $\mathbf{w}'$  is the vorticity of the RDE measured relative to the reference tracking the RDE's three semi-axes. The components of  $\mathbf{w}'$  expressed in the RDE's own coordinate axes are (Goddard and Miller, 1967; Bilby and Kolbuszewski, 1977; Jiang 2012, 2013):

$$w_{ij}' = \begin{cases} \frac{a_i^2 + a_j^2}{a_i^2 - a_j^2} \varepsilon_{ij} & a_i \neq a_j \\ w_{ij} & a_i = a_j \end{cases} \quad (2.23)$$

The evolution of the shape and orientation of an RDE for one computational step (Eq.2.21) can be solved numerically using a combination of Runge-Kutta method and Rodrigues rotation approximation (Jiang, 2014). Repeating this procedure for as many steps as necessary, the history of the RDEs is completely tracked to any large finite strains.

When the system achieves large finite strains, the RDEs may be too elongated or flattened so that boudinage may develop. To account for the development of boudinage, we set a threshold for the ratios of the lengths of the axes (long axis/intermediate axis and intermediate axis/short). Once the ratios of the lengths of the axes exceed the threshold, we will set the length of the longer axis to its half.

### 2.4.3 Description of the MATLAB package

The algorithm of MOPLA has been written in a MATLAB package generally. This package contains the following two main MATLAB functions called '*MOPLA\_primary.m*' and '*MOPLA\_secondary.m*'.

'*MOPLA\_primaty.m*' considers a poly-phase rock mass composed of  $N$  rheologically distinct elements (RDEs) subjected to tectonic displacement. This function is for the simulation of the overall mechanical behavior of the heterogeneous rock mass as well as

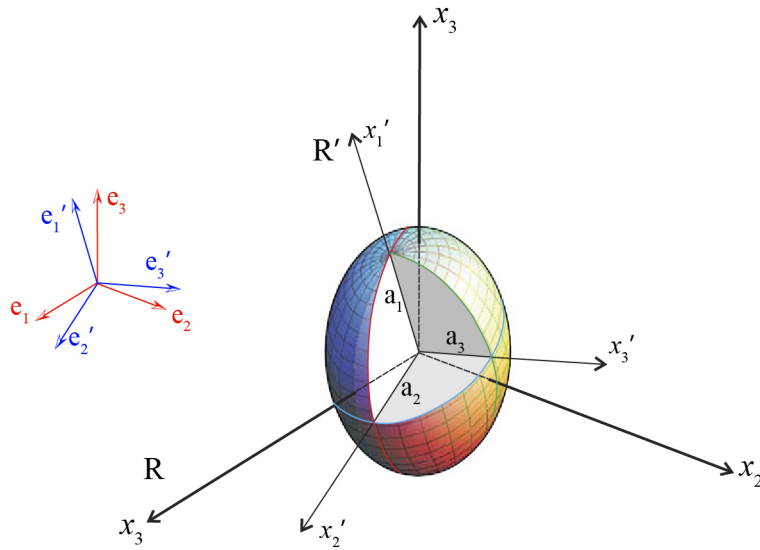


**Figure 2.4 An illustration of an ellipsoid and two distinct coordinates**

**The global coordinate  $x_1x_2x_3$  with base unit vectors  $e_i$  and the coordinate system  $x'_1x'_2x'_3$  with base unit vectors  $e'_i$  parallel to the three semi axes of an ellipsoid. This figure is modified after Jiang (2012).**

the shape and orientation evolution of all rheologically distinct elements. The input parameters are listed in Table 2.1:

**Table 2.1 The input parameters of MATLAB function “MOPLA\_primary.m”**

<i>L</i>	Imposed macroscale velocity gradient tensor, a 3-by-3 matrix.
<i>n</i>	The number of rheologically distinct elements (RDEs).
<i>a</i>	The initial three semi-axes of RDEs ( $a_1 > a_2 > a_3$ ; $a_3 = 1$ ), a 3-by-3 matrix.
<i>q</i>	The initial orientations of RDEs as transformation matrix, a 3-by-3-by- <i>n</i> matrix.
<i>eta</i>	The effective viscosities of RDEs defined at the initial state, such as the imposed macroscale strain-rate state, a 1-by- <i>n</i> vector.
<i>Ne</i>	The stress exponents of RDEs, a 1-by- <i>n</i> vector.
<i>steps</i>	The total computational steps.
<i>tincr</i>	The time increment of each computational step; the choice of <i>tincr</i> must ensure that each computational step represents an infinitesimal deformation.

The output variables are in Table 2.2:

**Table 2.2 The output variables of MATLAB function “MOPLA\_primary.m”**

<i>C_bar_evl</i>	The evolution with time of the homogeneous macroscale stiffness tensor of the heterogeneous rock mass, a 3-by-3-by-3-by-3-by- <i>steps</i> matrix.
<i>S_bar_evl</i>	The evolution with time of the macroscale deviatoric stress tensor due to the imposed macroscale strain rate, a 3-by-3-by- <i>steps</i> matrix.
<i>Q_evl</i>	The orientation evolution of all RDEs with time, a 3-by-3-by- <i>n</i> -by- <i>steps</i> matrix.
<i>A_evl</i>	The shape evolution of all RDEs with time, a 3-by- <i>n</i> -by- <i>steps</i> matrix.

‘MOPLA\_secondary.m’ considers a poly-phase rock mass composed of *N* primary (lower-order) RDEs subjected to tectonic displacement. In each primary RDE, there are



some secondary (higher-order) inclusions, which are the observed structural and fabric elements in the geology scenario. I assume that each primary RDE is isotropic, and secondary inclusions are so far apart from each other that they are considered as dilute inclusions in a groundmass. This function allows us to simulate the overall mechanical behavior of the heterogeneous rock mass, and to track the shape and orientation evolution of all primary and secondary inclusions. Therefore, one can investigate the fabric development at the observed structural and fabric-element level. The input parameters are in Table 2.3:

**Table 2.3 The input parameters of MATLAB function “MOPLA\_secondary.m”**

<i>L</i>	Imposed macroscale velocity gradient tensor, a 3-by-3 matrix.
<i>n</i>	The number of primary RDEs.
<i>a</i>	The initial three semi-axes of primary RDEs ( $a_1 > a_2 > a_3$ ; $a_3 = 1$ ), a 3-by-3 matrix.
<i>q</i>	The initial orientations of primary RDEs, a 3-by-3-by- <i>n</i> matrix.
<i>eta</i>	The effective viscosities of primary RDEs defined at the initial state, such as the imposed macroscale strain-rate state, a 1-by- <i>n</i> vector.
<i>Ne</i>	The stress exponents of primary RDEs, a 1-by- <i>n</i> vector.
<i>ns</i>	The number of secondary inclusions in each primary RDE.
<i>ak</i>	The initial three semi-axes of secondary inclusions, a 3-by- <i>n</i> -by- <i>ns</i> matrix.
<i>qk</i>	The initial orientation of secondary inclusions, a 3-by-3-by- <i>n</i> -by- <i>ns</i> matrix
<i>etak</i>	The effective viscosities of secondary inclusions defined at the initial state, such as the imposed macroscale strain-rate state, a <i>ns</i> -by- <i>n</i> matrix.
<i>Nk</i>	The stress exponents of secondary inclusions, a <i>ns</i> -by- <i>n</i> matrix.
<i>steps</i>	The total computational steps.
<i>tincr</i>	The time increment of each computational step; the choice of <i>tincr</i> must ensure that each computational step represents an infinitesimal deformation.

The output variables are in Table 2.4:

**Table 2.4 The output variables of MATLAB function “MOPLA\_secondary.m”**

<i>C_bar_evl</i>	The evolution with time of the homogeneous macroscale stiffness tensor of the heterogeneous rock mass, a 3-by-3-by-3-by-3-by-steps matrix.
<i>S_bar_evl</i>	The evolution with time of the macroscale deviatoric stress tensor due to the imposed macroscale strain rate, a 3-by-3-by-steps matrix.
<i>Q_evl</i>	The orientation evolution of all primary RDEs with time, a 3-by-3-by-n-by-steps matrix.
<i>A_evl</i>	The shape evolution of all primary RDEs with time, a 3-by-n-by-steps matrix.
<i>Qk_evl</i>	The orientation evolution of all secondary inclusions with time, a 3-by-3-by-n-by-steps matrix.
<i>Ak_evl</i>	The shape evolution of all secondary inclusions with time, a 3-by-n-by-steps matrix.

Beside the two main functions, there is a folder called *Routines*. This folder contains the functions called in two main functions or the example that we will discuss later. Please add this folder and the subfolders within it to the MATLAB path before running the main functions. The functions in this folder could be divided into four groups: *Common Tensor Operations*, *Eshelby Tensors and Green Interaction Tensor*, *Evolution of the Inhomogeneities*, and *Visualization*. The subfolder ‘*Common Tensor Operations*’ contains the basic tensor operations which are involved in the calculation of MOPLA but not defined in MATLAB. The subfolder ‘*Eshelby Tensors and Green Interaction Tensor*’ contains the functions for the evaluation of Eshelby tensors for different kinds of materials, which is required in Eshelby’s solution. The subfolder ‘*the Evolution of the Inhomogeneities*’ contains the functions to generate the initial shape and orientation of the RDEs and track the shape and orientation evolution of RDEs. The ‘*Visualization*’ subfolder contains the functions to plot the orientations of three semi-axes of an ellipsoidal in an equal area stereonet and plot the length of the three semi-axes of an

ellipsoidal in a Flinn diagram. The description of these functions in detail is in Appendix A. The MATLAB package is available in Appendix B.

## 2.5 Verification and example

This MATLAB package is applied to fabric development in the Cascade Lake shear zone in the eastern Sierra Nevada of California (Jiang and Bentley, 2012; Jiang, 2014) as verification and an example as well, showing how to use this package. Please add the whole folder to the MATLAB path, and one can directly run the executable MATLAB file '*Example.m*'.

The Cascade shear zone is a dextral transpressional deformation zone. Within the shear zone, a variation pattern in lineation plunge is observed on outcrops (Jiang and Bentley, 2012; Jiang, 2014). The variation pattern in lineation plunge in Cascade Lake shear zone is interpreted as the result of flow partitioning (Jiang and Bentley, 2012). The lineations are regarded as microscale structures developed, responding to partitioned flows in many RDEs throughout the Cascade shear zone (Jiang and Bentley, 2012). The development of the lineations can be modeled by MOPLA.

I use an RVE composed of 200 primary RDEs to represent the poly-phase rock masses in the Cascade Lake shear zone as Jiang (2014). At the initial state, the 200 RDEs are uniform randomly oriented with random shapes: (long axis: intermediate axis: short axis) 10-1:10-1:1. This shape variability covers a wide variety of bodies from nearly spherical (1:1:1) to pancake-like (10:10:1) to cigar-like ones (10:1:1). In Cascade Lake shear zone, there are around 60% felsic metavolcanic rocks in volume. Hence 120 of the 200 RDEs are assigned a relative effective viscosity of 1 and the remaining 80 RDEs varying between 1 and 10 at the macroscale strain-rate state. All RDEs are assumed to be power-law viscous and isotropic, with stress exponents between 2 and 4.

In order to investigate the fabric development at the higher-order fabric-element level, two hypotheses are tested (Jiang, 2014): the lineations were either defined by the preferred orientations of deformable objects or reflected the geometry of the finite strain fields in RDEs. I put two randomly oriented secondary inclusions within each primary RDE to test these two hypotheses, respectively. I assume that each primary inclusion is

isotropic, and the secondary inclusions are regarded as dilute inclusions in a groundmass. To test the first hypothesis, the first secondary inclusion is set to be one time stronger than its hosting RDE because lineation is more likely to develop in a rheologically strong element under a macroscale simple-shear-dominated flow (Yang et al., 2019). This secondary inclusion is assumed to have the same shape variability. The stress exponent of this secondary inclusion is simply set to 3. Then the orientation of the long axes of the first secondary inclusion should represent the plunge of the lineation. To test the second hypothesis, the second secondary inclusion must have a spherical shape (1:1:1) and the same viscosity and stress exponent as its hosting RDE, so that the geometry of this secondary inclusion after deformation reflects the geometry of the finite strain field in its hosting RDE. Then the orientation of the long axes of the second secondary inclusion should represent the plunge of the lineation.

For the macroscale flow field, a homogeneous kinematic model for an inclined tabular zone undergoing horizontal convergence but without along-strike stretching is used (Jiang, 2014). As shown in Fig.2.5,  $xyz$  coordinate is used to define the macroscale flow field, where the x-axis is parallel to the strike of the shear zone, the y-axis perpendicular to the shear zone boundary with +y in the dip direction of the shear zone, and the z-axis is parallel to the dip line of the shear zone with +z pointing upward. The boundary convergence velocity  $v$  is oblique to the strike of the shear zone.  $\alpha$  is the convergence angle, which is measured from the +x direction to the oblique convergence velocity  $v$ . If the oblique convergence is sinistral,  $\alpha$  is less than  $90^\circ$ ; if the oblique convergence is dextral,  $\alpha$  is more than  $90^\circ$  (Fig.2.5).  $\beta$  the dip angle of the shear zone. In the coordinate shown in Fig. 2.5, the velocity gradient is expressed as:

$$\mathbf{L} = \begin{pmatrix} 0 & -\cos \alpha & 0 \\ 0 & -\sin \alpha \sin \beta & 0 \\ 0 & \sin \alpha \cos \beta & \sin \alpha \sin \beta \end{pmatrix} \varepsilon_v, \text{ where } \varepsilon_v \text{ is the average rate of deformation of the}$$

zone defined by the ratio of the convergence rate and the active zone thickness. As the fabric development is a final product of the progressive deformation and does not relate to the rate of the deformation,  $\varepsilon_v$  can be simply set to 1. For the Cascade Lake shear zone,  $\beta$  is set to  $70^\circ$ . The convergence angle  $\alpha$  is varying from  $0^\circ$  to  $30^\circ$ . The time



increment of each computational step is  $\delta t = 0.01$  to ensure that each computational step represents an infinitesimal deformation. Fig.2.6 shows the model predicted lineation pattern defined by the long axes of deformable fabric elements in RDEs for convergence angle varying from  $0^\circ$  to  $30^\circ$ . Fig.2.7 is the model predicted lineation pattern defined by the maximum principle finite strain axes in RDEs for convergence angle varying from  $0^\circ$  to  $30^\circ$ . Both are the equal-area lower hemisphere projection. This simulation reproduces the modeling results of Jiang (2014), suggesting that this MATLAB package is verified (Figs.2.6 and 2.7). In Fig.2.6, at high convergence angle ( $\alpha = 15^\circ - 30^\circ$ ) and high bulk strain (computational steps  $>500$  steps), the lineations defined by the long axes of the deformable fabric elements are more concentrated near the z-axis than the prediction of Jiang (2014, Fig.10). In Fig.2.7, at a high convergence angle ( $\alpha = 20^\circ - 30^\circ$ ), the lineations defined by the maximum principle finite strain axes are broader than the prediction of Jiang (2014, Fig.11). The slight differences are due to the following reasons: First, the initial states of the RDEs in Jiang (2014) and this study are randomly generated to ensure the variability of the RDEs. Although the initial states of the RDEs in the two studies were generated following the same procedure, they are not identical. Second, the remote field and the imposed macroscale field are distinguished in this package but not in Jiang (2014). Third, different quadrature methods are used in the two studies to numerically evaluate the Eshelby tensors. Jiang (2014) adopted the Gauss-Legendre Quadrature with 20 nodes to calculate the Eshelby tensors, whereas an optimal scheme for numerical evaluation of Eshelby tensors, combining the Gauss-Legendre Quadrature and the Lebedev Quadrature (Qu et al., 2016), is used in this package.

## 2.6 Conclusions

This work provides a more refined algorithm of MOPLA by distinguishing the remote flow fields and the macroscale flow fields and implements the algorithm in MATLAB, a powerful and popular software. This work also incorporates the optimal scheme of Qu et al. (2016) to evaluate the Eshelby tensors numerically and uses the MATLAB built-in Parallel Computing Toolbox for high-performance computing. The backbone theory of MOPLA and the important equations in the algorithm are well summarized in this work. Then I explained the structure of this MATLAB package and applied this package to

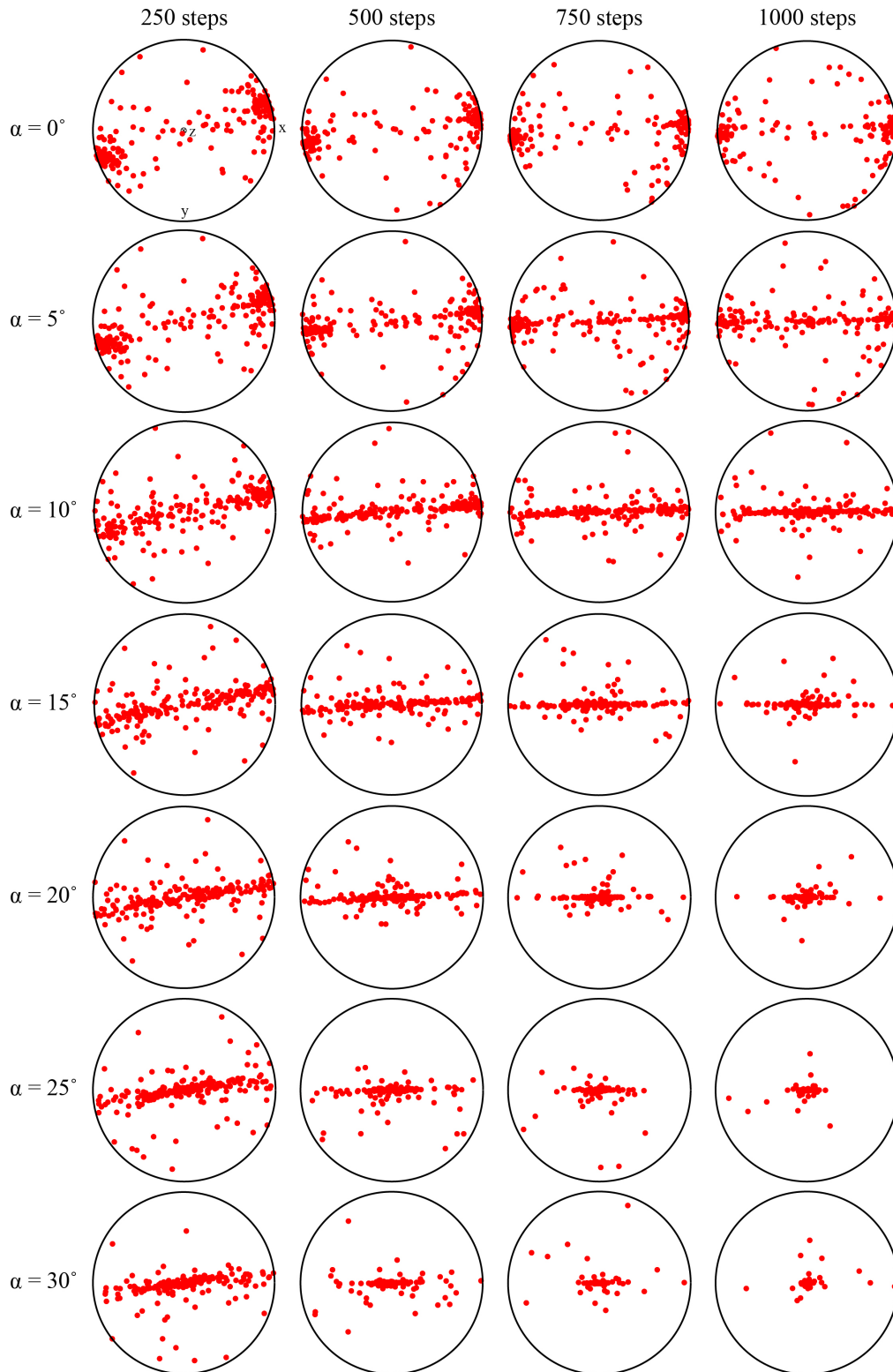


**Figure 2.6** The model predicted “lineation pattern” defined by the long axes of deformable fabric elements in RDEs (equal-area lower hemisphere projection)

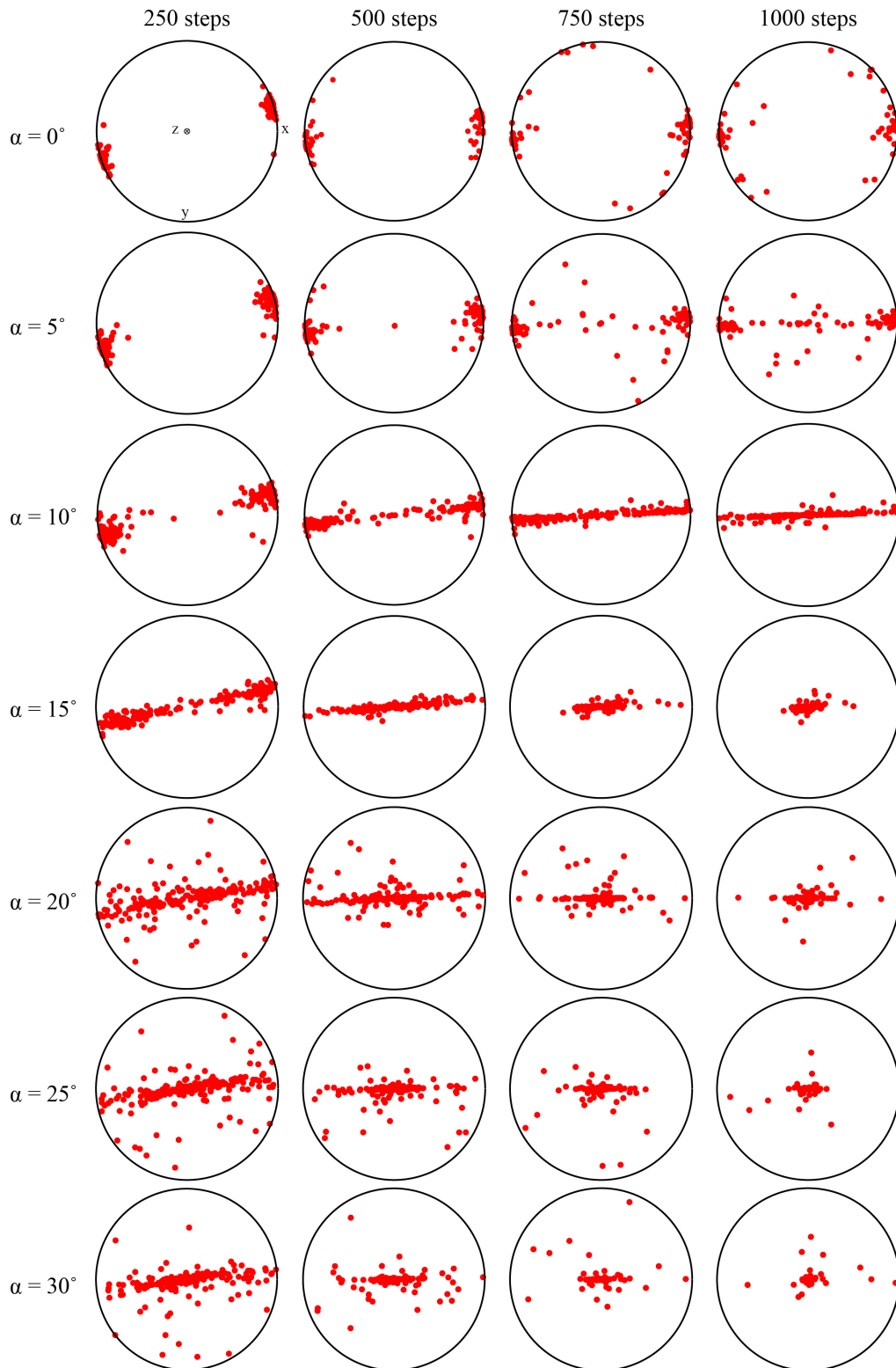


**Figure 2.7** The model predicted lineation pattern defined by the maximum principal finite strain axes in RDEs (equal-area lower hemisphere projection)



fabric development in Cascade Lake shear zone as a verification. This application is also a sample to show how to use this MATLAB package.

## 2.7 References

- Barnett, D. M. (1972). The precise evaluation of derivatives of the anisotropic elastic Green's functions. *Physica status solidi (b)*, 49(2), 741-748.  
<https://doi.org/10.1002/pssb.2220490238>
- Bilby, B. A., Eshelby, J. D., & Kundu, A. K. (1975). The change of shape of a viscous ellipsoidal region embedded in a slowly deforming matrix having a different viscosity. *Tectonophysics*, 28(4), 265-274. [https://doi.org/10.1016/0040-1951\(75\)90041-4](https://doi.org/10.1016/0040-1951(75)90041-4)
- Bilby, B. A., & Kolbuszewski, M. L. (1977). The finite deformation of an inhomogeneity in two-dimensional slow viscous incompressible flow. *Proceedings of the Royal Society of London. A. Mathematical and Physical Sciences*, 355(1682), 335-353.  
<https://doi.org/10.1098/rspa.1977.0101>
- Budiansky, B., & Mangasarian, O. L. (1960). Plastic stress concentration at a circular hole in an infinite sheet subjected to equal biaxial tension. *Journal of Applied Mechanics*, 27(1), 59-64. <https://doi.org/10.1115/1.3643935>
- Chen, Y., Jiang, D., Zhu, G., & Xiang, B. (2014). The formation of micafish: a modeling investigation based on micromechanics. *Journal of Structural Geology*, 68, 300-315. <https://doi.org/10.1016/j.jsg.2013.12.005>
- Dunnet, D. (1969). A technique of finite strain analysis using elliptical particles. *Tectonophysics*, 7(2), 117-136. [https://doi.org/10.1016/0040-1951\(69\)90002-X](https://doi.org/10.1016/0040-1951(69)90002-X)
- Eshelby, J. D. (1957). The determination of the elastic field of an ellipsoidal inclusion, and related problems. *Proceedings of the Royal Society of London. Series A. Mathematical and Physical Sciences*, 241(1226), 376-396.  
<https://doi.org/10.1098/rspa.1957.0133>

- Eshelby, J. D. (1959). The elastic field outside an ellipsoidal inclusion. *Proceedings of the Royal Society of London. Series A. Mathematical and Physical Sciences*, 252(1271), 561-569. <https://doi.org/10.1098/rspa.1959.0173>
- Eshelby, J.D., 1961. Elastic inclusions and inhomogeneities. In: Snedden, N.I., Hill, R. (Eds.), *Progress in Solid Mechanics*, vol. 2, pp. 89-104
- Exner, U., & Dabrowski, M. (2010). Monoclinic and triclinic 3D flanking structures around elliptical cracks. *Journal of Structural Geology*, 32(12), 2009-2021. <https://doi.org/10.1016/j.jsg.2010.08.002>
- Gay, N. C. (1968). Pure shear and simple shear deformation of inhomogeneous viscous fluids. 1. Theory. *Tectonophysics*, 5(3), 211-234. [https://doi.org/10.1016/0040-1951\(68\)90065-6](https://doi.org/10.1016/0040-1951(68)90065-6)
- Ghosh, S. K., & Ramberg, H. (1976). Reorientation of inclusions by combination of pure shear and simple shear. *Tectonophysics*, 34(1-2), 1-70. [https://doi.org/10.1016/0040-1951\(76\)90176-1](https://doi.org/10.1016/0040-1951(76)90176-1)
- Goddard, J. D., & Miller, C. (1967). Nonlinear effects in the rheology of dilute suspensions. *Journal of Fluid Mechanics*, 28(4), 657-673. <https://doi.org/10.1017/S0022112067002381>
- Goodwin, L. B., & Tikoff, B. (2002). Competency contrast, kinematics, and the development of foliations and lineations in the crust. *Journal of Structural Geology*, 24(6-7), 1065-1085. [https://doi.org/10.1016/S0191-8141\(01\)00092-X](https://doi.org/10.1016/S0191-8141(01)00092-X)
- Healy, D., Jones, R. R., & Holdsworth, R. E. (2006). New insights into the development of brittle shear fractures from a 3-D numerical model of microcrack interaction. *Earth and Planetary Science Letters*, 249(1-2), 14-28. <https://doi.org/10.1016/j.epsl.2006.06.041>
- Hill, R. (1965). A self-consistent mechanics of composite materials. *Journal of the Mechanics and Physics of Solids*, 13(4), 213-222. [https://doi.org/10.1016/0022-5096\(65\)90010-4](https://doi.org/10.1016/0022-5096(65)90010-4)

- Hudleston, P. (1999). Strain compatibility and shear zones: is there a problem?. *Journal of Structural Geology*, 21(8-9), 923-932. [https://doi.org/10.1016/S0191-8141\(99\)00060-7](https://doi.org/10.1016/S0191-8141(99)00060-7)
- Hutchinson, J. W. (1976). Bounds and self-consistent estimates for creep of polycrystalline materials. *Proceedings of the Royal Society of London. A. Mathematical and Physical Sciences*, 348(1652), 101-127. <https://doi.org/10.1098/rspa.1976.0027>
- Ježek, J., Schulmann, K., & Segeth, K. (1996). Fabric evolution of rigid inclusions during mixed coaxial and simple shear flows. *Tectonophysics*, 257(2-4), 203-221. [https://doi.org/10.1016/0040-1951\(95\)00133-6](https://doi.org/10.1016/0040-1951(95)00133-6)
- Jiang, D. (1994). Vorticity determination, distribution, partitioning and the heterogeneity and non-steadiness of natural deformations. *Journal of Structural Geology*, 16(1), 121-130. [https://doi.org/10.1016/0191-8141\(94\)90023-X](https://doi.org/10.1016/0191-8141(94)90023-X)
- Jiang, D. (1994). Flow variation in layered rocks subjected to bulk flow of various kinematic vorticities: theory and geological implications. *Journal of Structural Geology*, 16(8), 1159-1172. [https://doi.org/10.1016/0191-8141\(94\)90059-0](https://doi.org/10.1016/0191-8141(94)90059-0)
- Jiang, D. (2007a). Numerical modeling of the motion of deformable ellipsoidal objects in slow viscous flows. *Journal of Structural Geology*, 29(3), 435-452. <https://doi.org/10.1016/j.jsg.2006.09.009>
- Jiang, D. (2007b). Numerical modeling of the motion of rigid ellipsoidal objects in slow viscous flows: a new approach. *Journal of Structural Geology*, 29(2), 189-200. <https://doi.org/10.1016/j.jsg.2006.09.010>
- Jiang, D. (2012). A general approach for modeling the motion of rigid and deformable ellipsoids in ductile flows. *Computers & geosciences*, 38(1), 52-61. <https://doi.org/10.1016/j.cageo.2011.05.002>
- Jiang, D. (2013). The motion of deformable ellipsoids in power-law viscous materials: Formulation and numerical implementation of a micromechanical approach

applicable to flow partitioning and heterogeneous deformation in Earth's lithosphere. *Journal of structural geology*, 50, 22-34.

<https://doi.org/10.1016/j.jsg.2012.06.011>

Jiang, D. (2014). Structural geology meets micromechanics: A self-consistent model for the multiscale deformation and fabric development in Earth's ductile lithosphere. *Journal of Structural Geology*, 68, 247-272.

<https://doi.org/10.1016/j.jsg.2014.05.020>

Jiang, D. (2016). Viscous inclusions in anisotropic materials: Theoretical development and perspective applications. *Tectonophysics*, 693, 116-142.

<https://doi.org/10.1016/j.tecto.2016.10.012>

Jiang, D., & Bentley, C. (2012). A micromechanical approach for simulating multiscale fabrics in large-scale high-strain zones: Theory and application. *Journal of Geophysical Research: Solid Earth*, 117(B12).

<https://doi.org/10.1029/2012JB009327>

Jiang, D., & Bhandari, A. (2018). Pressure variations among rheologically heterogeneous elements in Earth's lithosphere: A micromechanics investigation. *Earth and Planetary Science Letters*, 498, 397-407.

<https://doi.org/10.1016/j.epsl.2018.07.010>

Jiang, D., & White, J. C. (1995). Kinematics of rock flow and the interpretation of geological structures, with particular reference to shear zones. *Journal of Structural Geology*, 17(9), 1249-1265. [https://doi.org/10.1016/0191-8141\(95\)00026-A](https://doi.org/10.1016/0191-8141(95)00026-A)

[https://doi.org/10.1016/0191-8141\(95\)00026-A](https://doi.org/10.1016/0191-8141(95)00026-A)

Jiang, D., & Williams, P. F. (1999). A fundamental problem with the kinematic interpretation of geological structures. *Journal of Structural Geology*, 21(8-9), 933-937. [https://doi.org/10.1016/S0191-8141\(99\)00068-1](https://doi.org/10.1016/S0191-8141(99)00068-1)

[https://doi.org/10.1016/S0191-8141\(99\)00068-1](https://doi.org/10.1016/S0191-8141(99)00068-1)

Jones, R. R., Holdsworth, R. E., Clegg, P., McCaffrey, K., & Tavarnelli, E. (2004). Inclined transpression. *Journal of Structural Geology*, 26(8), 1531-1548.

<https://doi.org/10.1016/j.jsg.2004.01.004>

- Jones, R. R., Holdsworth, R. E., McCaffrey, K. J., Clegg, P., & Tavarnelli, E. (2005). Scale dependence, strain compatibility and heterogeneity of three-dimensional deformation during mountain building: a discussion. *Journal of Structural Geology*, 27(7), 1190-1204. <https://doi.org/10.1016/j.jsg.2005.04.001>
- Kohlstedt, D. L., Evans, B., & Mackwell, S. J. (1995). Strength of the lithosphere: Constraints imposed by laboratory experiments. *Journal of Geophysical Research: Solid Earth*, 100(B9), 17587–17602. <https://doi.org/10.1029/95JB01460>
- Lebensohn, R. A., Dawson, P. R., Kern, H. M., & Wenk, H. R. (2003). Heterogeneous deformation and texture development in halite polycrystals: comparison of different modeling approaches and experimental data. *Tectonophysics*, 370(1-4), 287-311. [https://doi.org/10.1016/S0040-1951\(03\)00192-6](https://doi.org/10.1016/S0040-1951(03)00192-6)
- Lebensohn, R. A., & Tomé, C. N. (1993). A self-consistent anisotropic approach for the simulation of plastic deformation and texture development of polycrystals: application to zirconium alloys. *Acta metallurgica et materialia*, 41(9), 2611-2624. [https://doi.org/10.1016/0956-7151\(93\)90130-K](https://doi.org/10.1016/0956-7151(93)90130-K).
- Lebensohn, R. A., Tomé, C. N., & Maudlin, P. J. (2004). A self-consistent formulation for the prediction of the anisotropic behavior of viscoplastic polycrystals with voids. *Journal of the Mechanics and Physics of Solids*, 52(2), 249-278. [https://doi.org/10.1016/S0022-5096\(03\)00114-5](https://doi.org/10.1016/S0022-5096(03)00114-5)
- Lebensohn, R. A., Turner, P. A., Signorelli, J. W., Canova, G. R., & Tomé, C. N. (1998). Calculation of intergranular stresses based on a large-strain viscoplastic self-consistent polycrystal model. *Modelling and Simulation in Materials Science and Engineering*, 6(4), 447.
- Lister, G. S., & Williams, P. F. (1983). The partitioning of deformation in flowing rock masses. *Tectonophysics*, 92(1-3), 1-33. [https://doi.org/10.1016/0040-1951\(83\)90083-5](https://doi.org/10.1016/0040-1951(83)90083-5)
- Masson, R., Bornert, M., Suquet, P., & Zaoui, A. (2000). An affine formulation for the prediction of the effective properties of nonlinear composites and

polycrystals. *Journal of the Mechanics and Physics of Solids*, 48(6-7), 1203-1227.  
[https://doi.org/10.1016/S0022-5096\(99\)00071-X](https://doi.org/10.1016/S0022-5096(99)00071-X)

Mercier, S., & Molinari, A. (2009). Homogenization of elastic–viscoplastic heterogeneous materials: Self-consistent and Mori-Tanaka schemes. *International Journal of Plasticity*, 25(6), 1024-1048.

<https://doi.org/10.1016/j.ijplas.2008.08.006>

Molinari, A. (2002). Averaging models for heterogeneous viscoplastic and elastic viscoplastic materials. *Journal of Engineering Materials and Technology*, 124(1), 62-70. <https://doi.org/10.1115/1.1421052>

Molinari, A., Canova, G. R., & Ahzi, S. (1987). A self-consistent approach of the large deformation polycrystal viscoplasticity. *Acta Metallurgica*, 35(12), 2983-2994.

[https://doi.org/10.1016/0001-6160\(87\)90297-5](https://doi.org/10.1016/0001-6160(87)90297-5)

Molinari, A., & Mercier, S. (2004). Homogenization of viscoplastic materials. In *IUTAM Symposium on Multiscale Modeling and Characterization of Elastic-Inelastic Behavior of Engineering Materials* (pp. 113-124). Springer, Dordrecht.

Mori, T., & Tanaka, K. (1973). Average stress in matrix and average elastic energy of materials with misfitting inclusions. *Acta metallurgica*, 21(5), 571-574.

Mura, T., 1987. *Micromechanics of Defects in Solids*. Martinus Nijhoff Publishers, Dordrecht/Boston/Lancaster. [https://doi.org/10.1016/0001-6160\(73\)90064-3](https://doi.org/10.1016/0001-6160(73)90064-3)

Nemat-Nasser, S., Hori, M., 1999. *Micromechanics: Overall Properties of Heterogeneous Materials*. Second revised edition. Elsevier.

Passchier, C. W., Mancktelow, N. S., & Grasemann, B. (2005). Flow perturbations: a tool to study and characterize heterogeneous deformation. *Journal of Structural Geology*, 27(6), 1011-1026. <https://doi.org/10.1016/j.jsg.2005.01.016>

Passchier, C. W., & Trouw, R. A. (2005). *Microtectonics*. Springer Science & Business Media.

- Pollard, D.D., & Fletcher, R.C. (2005). *Fundamentals of Structural Geology*. Cambridge University Press.
- Qu, J., & Cherkaoui, M. (2006). *Fundamentals of micromechanics of solids* (pp. 226-240). Hoboken: Wiley.
- Qu, M., Jiang, D., & Lu, L. X. (2016). An optimal scheme for numerical evaluation of Eshelby tensors and its implementation in a MATLAB package for simulating the motion of viscous ellipsoids in slow flows. *Computers & geosciences*, 96, 98-108. <https://doi.org/10.1016/j.cageo.2016.08.005>
- Ramsay, J. G. (1967). Folding and fracturing of rocks. *Mc Graw Hill Book Company*
- Rudnicki, J. W. (1977). The inception of faulting in a rock mass with a weakened zone. *Journal of Geophysical Research*, 82(5), 844-854. <https://doi.org/10.1029/JB082i005p00844>
- Spencer, A.J.M., 1980. Continuum Mechanics. Longman, London.
- Tullis, J. (2002). Deformation of granitic rocks: experimental studies and natural examples. *Reviews in Mineralogy and Geochemistry*, 51(1), 51-95. <https://doi.org/10.2138/gsrmg.51.1.51>
- Twiss, R.J., & Moores, E.M. (1992). *Structural Geology*. W.H. Freeman and Company, New York.
- Walker, K. P. (1993). Fourier integral representation of the Green function for an anisotropic elastic half-space. *Proceedings of the Royal Society of London. Series A: Mathematical and Physical Sciences*, 443(1918), 367-389. <https://doi.org/10.1098/rspa.1993.0151>
- Xiang, B., & Jiang, D. (2013). Small-scale ductile shear zones as transposed rheologically weak domains: A numerical modeling investigation and practical application. *Journal of Structural Geology*, 54, 184-198. <https://doi.org/10.1016/j.jsg.2013.06.003>



- Yang, R., Jiang, D., & Lu, L. X. (2019). Constrictional strain and linear fabrics as a result of deformation partitioning: a multiscale modeling investigation and tectonic significance. *Tectonics*. <https://doi.org/10.1029/2019TC005490>
- Zaoui, A. (2002). Continuum micromechanics: survey. *Journal of Engineering Mechanics*, 128(8), 808-816.

## Chapter 3

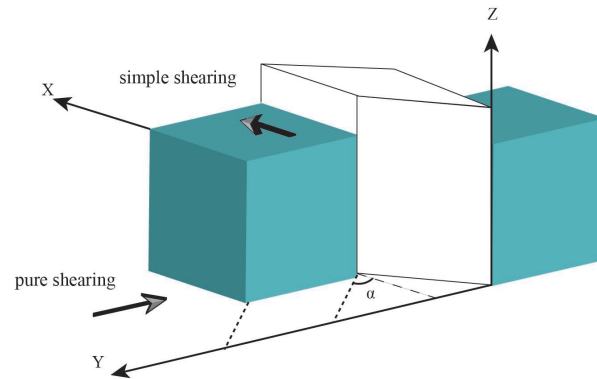
### 3 A Fully Mechanical Approach Toward High-Strain Zone Modeling Using the Generalized Eshelby Formalism

#### 3.1 Introduction

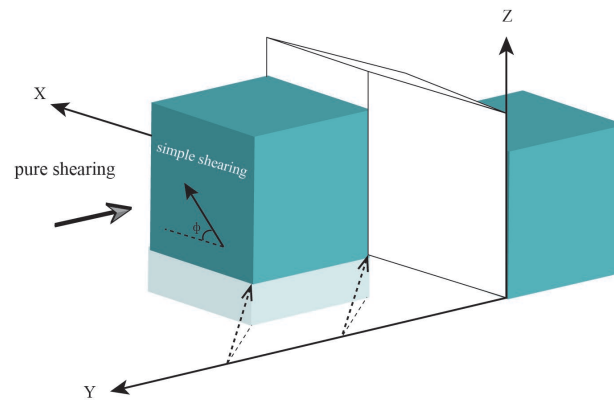
The deformation of Earth's lithosphere is characterized by localized high-strain zones, instead of distributed deformation (e.g., Twiss and Mooress, 1992; Poirier, 1980). Ductile high-strain zones manifest themselves in multiple scales (Poirier, 1980), including small-scale structures and tectonic-scale structures that form major tectonic boundaries (Hamner, 1988; Vauchez and Tommasi, 2003; Gumiaux et al., 2004; Montési, 2013).

Once the tectonic-scale ductile high-strain zones are established, they may remain for a long time and have a strong influence on the mechanical evolution of Earth's continental lithosphere (Vauchez et al., 1998; Tommasi and Vauchez, 2001; Ben-Zion and Sammis, 2003).

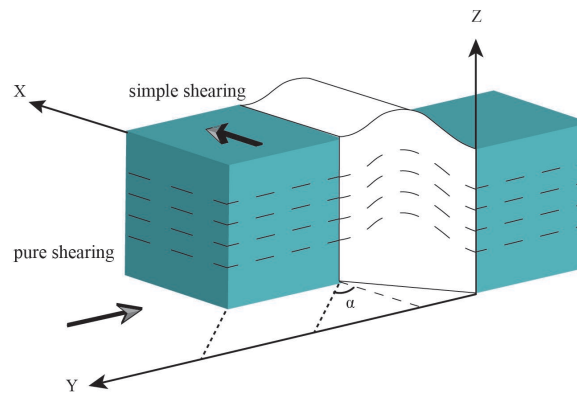
In the past five decades, there have been a great number of kinematic models that relate the progressive deformation and finite strain pattern in a ductile high-strain zone to the movement of its boundaries (see reviews in Jiang and White, 1995; Jiang and Williams 1998; Davis and Titus 2011). Ramsay and Graham (1970) presented the first kinematic shear zone model in terms of the finite strain approach, in which the shear zone is bounded by two parallel and rigid walls extending infinitely. The progressive deformation in the zone is simple shearing. Ramberg (1975) considered more general two-dimensional shear zone deformation as a combination of pure shearing and simple shearing using the rate of deformation approach. Sanderson and Marchini (1984, Fig.3.1a) considered a special type of three-dimensional deformation, which they referred to as transpression, in terms of finite strain formulation. Their model describes a vertical tabular zone bounded by two rigid walls obliquely converging toward each other. The convergent component is accommodated by a homogeneous and strike-length constant but vertically stretching pure shearing, whereas the strike-slip (or trans-) component is accommodated by a homogeneous simple shearing. The strain compatibility between the deforming zone and the country rocks is violated, and the boundaries of the zone are discontinuous (e.g., Schwerdtner, 1989). As pointed out by Robin and Cruden (1994), the



(a) Sanderson and Marchini (1984)



(b) Lin et al. (1998); Jiang and Williams (1998)



(c) Robin and Cruden (1994)

**Figure 3.1 Three different previous shear zone models**

**(a) The “transpression” kinematic model of Sanderson and Marchini (1984). This model describes a vertical tabular zone bounded by two obliquely converging rigid walls. The strike-length constant. The shortening across the zone is compensated by the vertical thickening to conserve volume. The material within the zone can freely slip along the two rigid walls. (b) The “triclinic” kinematic model (Lin et al., 1998; Jiang and Williams, 1998). In this model, the shearing direction for the trans-component is oblique to the principal stretching directions of the boundaries. (3) The mechanical model of “Robin and Cruden, 1994”. The deformation in this model is analyzed based on the extrusional flow of a Newtonian viscous fluid compressed between two rigid walls with a simple shearing motion parallel to the walls.**

transpression in Sanderson and Marchini (1984) is different from the original meaning of the term coined by Harland (1971) which stands for the boundary condition of oblique convergence only (see Jiang and Williams, 1998; Yang et al., 2019 for more discussion on this). The oblique convergence between two parallel-sided blocks, the transpression in the sense of Harland (1970), is not necessarily accommodated by the homogeneous deformation in the sense of Sanderson and Marchini (1984).

In the finite strain approach, it matters how the order of simple-shear and pure-shear components is applied. In reality, both simple and pure shearing act simultaneously, although with variable relative magnitudes if the progressive deformation is non-steady. Fossen and Tikoff (1993) and Tikoff and Teyssier (1994) reformulated Sanderson and Marchini's model in terms of the rate of deformation following Ramberg's approach. Other transpression models have also been published (e.g., Simpson and De Paor, 1993; Jones and Tanner, 1995; Krantz, 1995; Teyssier et al., 1995), some models have been extended to include all possible three-dimensional monoclinic deformation with an added component of extrusion (Jones et al., 1997; Fossen and Tikoff, 1998; Passchier, 1998). These models, like that of Sanderson and Marchini (1984), have a monoclinic symmetry where the shearing direction is parallel to one of the principal directions of the pure-shearing component (Jiang and Williams, 1998). Monoclinic models predict either a strike-parallel or a dip-parallel lineation pattern. However, over time geologists recognized that lineations in sub-vertical shear zones might vary between strike-parallel or dip-parallel (e.g., Hudleston et al., 1988; Robin and Cruden, 1994; Goodwin and Williams, 1996; Lin et al., 1998), which cannot be explained by traditional monoclinic models. Lin et al. (1998; Fig.3.1b) first presented a triclinic kinematic model in terms of the rate of deformation. Jones and Holdsworth (1998) presented a similar model in the finite strain form. In such triclinic models, the shearing direction for the trans-component is oblique to the principal stretching directions of the boundaries. Despite the different deformation paths included in particular models, in essence, these kinematic models are generated in a similar way and can be summarized in a unified model of Jiang and Williams (1998). Fernández and Díaz-Azpiroz (2009) proposed the so-called more general model, which is the rotation of Jiang and Williams (1998).

Robin and Cruden (1994) took a different approach. They developed a mechanical model of transpression (Fig.3.1c) by combining Jaeger's (1964, p.140-143) analytical solution for extrusional flow of a Newtonian viscous fluid compressed between two rigid parallel walls with a simple shearing motion parallel to the walls. Dutton (1997) investigated the finite strain geometry of Robin and Cruden's model. So far, the series of work forms the basis to explore the finite strain patterns and the rotation and strain paths of fabrics in a shear zone.

In all kinematic models, a homogeneous and constant flow field (or deformation path) must be defined *a priori* for the shear zone, so that the finite strain evolution with time can be solved. The latter is then compared with natural fabric geometries. This may be justified in small-scale (centimeters- to meters-scales) Ramsay-type shear zones in homogeneous rocks with clearly defined boundaries. In crustal-scale ductile high-strain zones, the rocks are heterogeneous and anisotropic due to the ongoing development of fabrics. More importantly, the high-strain zone rocks interact with the country rock. During the deformation, the high-strain zones may deform and rotate unless they are well developed and form the plate boundaries, then their shapes and orientations may remain unchanged. In the course of a high-strain zone development, its orientation and geometry with respect to the geological setting and its rheological properties change with time. As a result, the flow field within the high-strain zone changes with time. It becomes impractical to assign a flow field for such a high-strain zone.

This work takes a different approach in this paper. This work considers a high-strain zone as a planar heterogeneous inclusion embedded in the lithosphere undergoing tectonic-scale deformation. This work uses Eshelby's formulation to investigate the mechanical and kinematic fields inside the high-strain zone, including the finite strain accumulation there. Therefore, the flow inside a high-strain zone is the partitioned flow of the tectonic scale deformation due to far-field plate motion. Because our approach is a complete mechanical one, it can address the problems associated with the mechanics of the high-strain zone system, such as the stress distribution and the rheology of the high-strain zone. As high-strain zones are rheologically weak and the fundamental structures that accommodate a large number of deformations within Earth's lithosphere and, in turn,

influence the lithospheric deformation processes, the mechanical evolution of the lithosphere as well as the continental rheology. Therefore, investigating the mechanics of the high-strain zone system is crucial. It will help us to understand the mechanics of the lithospheric deformation and describe the rheology of the continental lithosphere.

To constrain the model inputs and test the geometric results deduced by model, this work applies this model to an ancient crustal high-strain zone, the Shangdan Tectonic Zone in Qinling Orogenic Belt, where abundant fabrics are preserved. This work also discusses the stress distribution in the active deformation zone and its vicinity and the strength of the large-scale high-strain zone by applying this model to the San Andreas Fault in Central California and the strength of the high-strain zone by applying it to mylonite zones at the northwest margin of the Grenville Front Tectonic Zone.

### 3.2 A fully mechanical approach

This work presents a new high-strain zone model based on the classical Eshelby inclusion problem. Eshelby (1957, 1959) provided an elegant approach to solve the elastic fields inside and outside an ellipsoidal inclusion embedded in an infinite homogenous elastic matrix. The Eshelby solutions have been extended to general nonlinear viscous materials with a linearization approach (Molinari et al., 1987; Lebensohn and Tomé, 1993; Jiang, 2013, 2014, 2016; Fig.3.2). In this model, the ductile lithosphere subjected to plate motion is considered as an infinite power-law viscous material. A crustal ductile high-strain zone is considered as a planar heterogeneous inclusion, with three semi-axes being  $a_1 > a_2 \gg a_3$  embedded in the lithospheric matrix (Fig.3.3). An internal coordinate,  $x'y'z'$ , with three axes  $x'$ ,  $y'$  and  $z'$  respectively parallel to the three semi-axes  $a_1$ ,  $a_2$  and  $a_3$ , is adopted (Fig.3.4). The mechanical and kinematic fields inside the high-strain zone are defined in the internal coordinate. While, the plate motion and the mechanical and kinematic fields outside and adjacent to the high-strain zone are defined in the external right-hand coordinate  $xyz$ , with the x-axis parallel to the strike of the high-strain zone and the z-axis

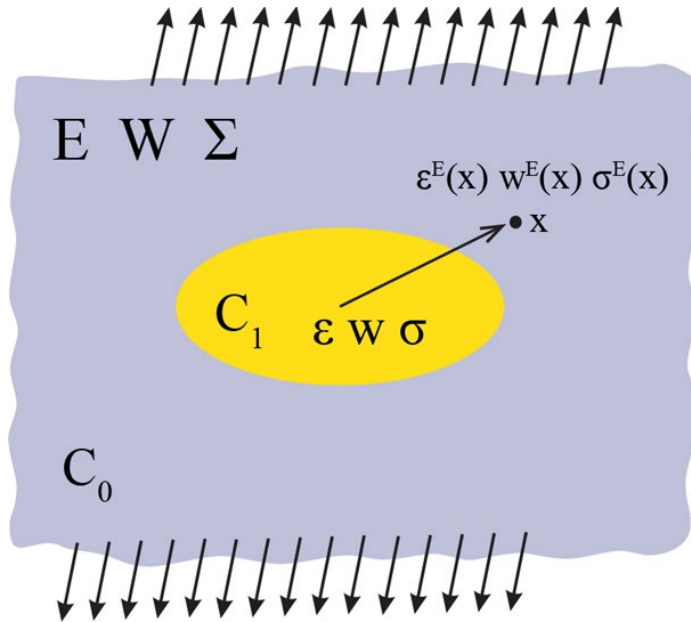


**Figure 3.2 Eshelby inclusion problem of an ellipsoidal inclusion in the matrix**

$C_0$  and  $C_1$  are the 4<sup>th</sup> order viscous stiffnesses of the inclusion and the matrix. The lowercase uppercase letter  $E$ ,  $\Sigma$ , and  $W$  stand for the strain-rate, stress, and vorticity fields in the matrix. The constant fields inside an RDE are denoted by corresponding lowercase letters  $\epsilon$ ,  $\sigma$ , and  $w$ . The mechanical fields outside the inclusion vary with the position vector  $x$  and are expressed by  $\epsilon^E(x)$ ,  $w^E(x)$  and  $\sigma^E(x)$ . This figure is modified after Jiang and Bhandari (2018).



vertical (Fig.3.4). The kinematic and mechanical fields inside an inclusion are related to the far-field quantities by the following set of partitioning equations (Jiang 2014):

$$\boldsymbol{\varepsilon} - \mathbf{E} = [\mathbf{J}^d - \mathbf{S}^{-1}]^{-1} : \mathbf{C}_0^{-1} : (\boldsymbol{\sigma} - \boldsymbol{\Sigma}) \quad (3.1a)$$

$$\mathbf{w} - \mathbf{W} = \mathbf{\Pi} : \mathbf{S}^{-1} : (\boldsymbol{\varepsilon} - \mathbf{E}) \quad (3.1b)$$

The lowercase letters  $\boldsymbol{\varepsilon}$ ,  $\boldsymbol{\sigma}$ , and  $\mathbf{w}$  represent, respectively, the strain-rate, stress, and vorticity tensors inside an inclusion; uppercase  $\mathbf{E}$ ,  $\boldsymbol{\Sigma}$ , and  $\mathbf{W}$  stand for the corresponding far-field quantities (Fig.3.2).  $\mathbf{C}_0$  is the 4<sup>th</sup> order viscous stiffnesses of the matrix.  $\mathbf{S}$  and  $\mathbf{\Pi}$  are 4<sup>th</sup> order Eshelby tensors for interior points with the former being symmetric and latter antisymmetric.  $\mathbf{J}^d$  is the 4<sup>th</sup> order deviatoric identity tensor defined by the Kronecker delta  $\delta_{ij} = \begin{cases} 1 & i = j \\ 0 & i \neq j \end{cases}$  (Jiang, 2014):  $J_{ijkl}^d = \frac{1}{2}(\delta_{ik}\delta_{jl} + \delta_{jk}\delta_{il}) - \frac{1}{3}\delta_{ij}\delta_{kl}$ .

The far-field fields are determined by the plate motion. With known far-field fields, the partitioned fields inside the high-strain zone can be obtained by the numerical computation using Eq.3.1 (Jiang 2012, 2013, 2014). Then the finite strain pattern inside the high-strain zone can be investigated from the flow fields inside the high-strain zone using the relation between the flow and finite strain (Jiang, 2010):

$$\begin{aligned} \mathbf{F}^i(\delta t) &= \exp(\mathbf{I}^i \delta t) \\ \mathbf{F}(t) &= \mathbf{F}^{\left(\frac{t}{\delta t}\right)} \mathbf{F}^{\left(\frac{t}{\delta t}-1\right)} \dots \mathbf{F}^{(2)} \mathbf{F}^{(1)} \end{aligned} \quad (3.2)$$

where  $\mathbf{F}^i$  and  $\mathbf{I}^i (= \boldsymbol{\varepsilon}^i + \mathbf{w}^i)$  are the incremental position gradient and the flow inside the high-strain zone for  $i^{\text{th}}$  computational step.  $\delta t$  is incremental time for each computational step.  $\mathbf{F}(t)$  is the position gradient for the deformation over a computation time of  $t$ .

The kinematic fields outside the high-strain zone are given by following two partitioning equations (Jiang 2016):

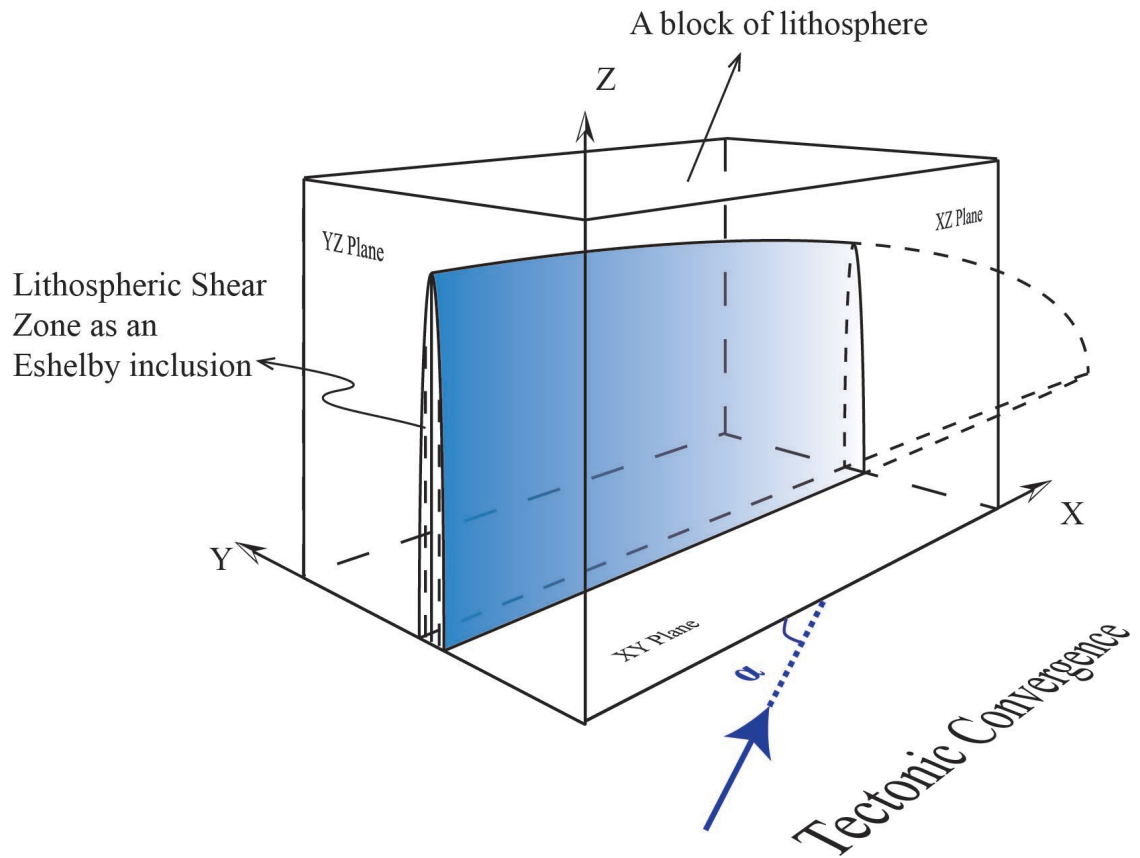


**Figure 3.3 A conceptual illustration of a crustal high-strain zone as a planar heterogeneous ellipsoidal inclusion embedded in a block of ductile lithosphere**

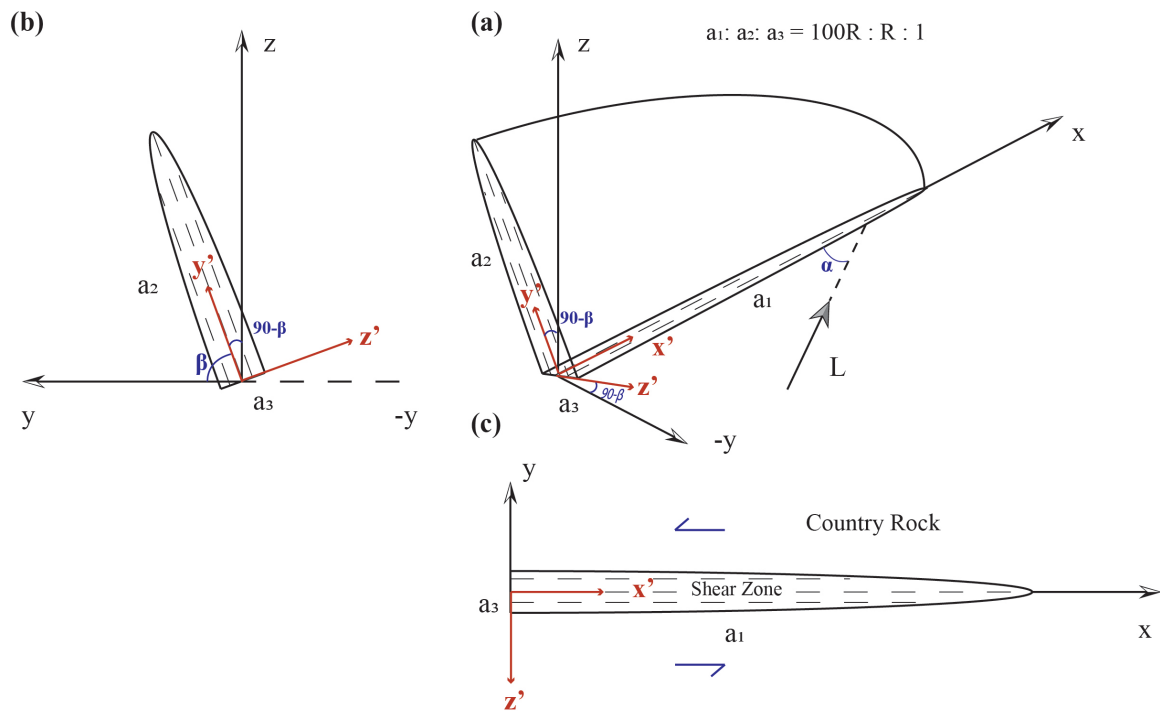


**Figure 3.4** A schematic diagram showing the shape and orientation of a planar ellipsoidal high-strain zone

(a) A three-dimensional view of the planar high-strain zone with three semi-axes  $a_1$ ,  $a_2$ , and  $a_3$ .  $a_1 : a_2 : a_3 = 100R : R : 1$ , where  $R$  is the shape parameter. A global coordinate  $xyz$  and an internal coordinate,  $x'y'z'$ , with three axes  $x'$ ,  $y'$  and  $z'$  respectively parallel to the three semi-axes  $a_1$ ,  $a_2$  and  $a_3$ , are adopted.  $L$  is the far-field flow due to the plate motion.  $\alpha$  is the convergence angle.  $\beta$  is the dip angle of the high-strain zone. (b) The cross-section of  $yz$ -plane. (c) The cross-section of the  $xy$ -plane.

$$\boldsymbol{\varepsilon}^E(\mathbf{x}) = \mathbf{E} + \mathbf{S}^E(\mathbf{x}) : \mathbf{S}^{-1} : (\boldsymbol{\varepsilon} - \mathbf{E}) \quad (3.3a)$$

$$\mathbf{w}^E(\mathbf{x}) = \mathbf{W} + \boldsymbol{\Pi}^E(\mathbf{x}) : \mathbf{S}^{-1} : (\boldsymbol{\varepsilon} - \mathbf{E}) \quad (3.3b)$$

where the superscript “ $E$ ” stands for the exterior field quantities.  $\mathbf{S}^E(\mathbf{x})$  and  $\boldsymbol{\Pi}^E(\mathbf{x})$  are the Eshelby tensors for exterior points, and both depend on location. Once the strain rate fields outside the high-strain zone are obtained, the corresponding stress fields can be calculated using the constitutive relation:

$$\boldsymbol{\sigma}^E(\mathbf{x}) = \mathbf{C}_0 : \boldsymbol{\varepsilon}^E(\mathbf{x}) \quad (3.4)$$

Earth’s lithosphere is a rheologically heterogeneous poly-element material. In order to apply the extended Eshelby’s solutions to Earth’s lithosphere, this work borrowed the concept of Homogeneous Equivalent Medium (HEM) (Molinari et al., 1987; Lebensohn and Tomé, 1993). The heterogeneous rock mass composed of a large number of “rheologically distinct elements” (RDEs) is replaced by a hypothetical HEM whose rheological properties are obtained by means of self-consistent homogenization from the effective properties of all RDEs contained in “Representative Volume Element” (RVE) (Molinari et al., 1987; Lebensohn and Tomé, 1993; Jiang, 2014) (Fig. 5.5). Therefore, the country rock (matrix) is regarded as an isotropic power-law viscous material with a stress exponent of  $n_0$ . The viscous stiffness tensor of country rock can be expressed in terms of the effective viscosity  $\eta_0$ :

$$\mathbf{C}_0 = 2\eta_0 \mathbf{J}^d \quad (3.5)$$

Rock within the high-strain zone is also a power-law viscous material with a stress exponent of  $n_1$ . As foliation is well developed in the high-strain zone, the material inside high-strain zone is considered as a transversely isotropic material, having two distinct effective viscosities:  $\eta_1^s$  being the viscosity for shearing along the foliation (parallel to the  $a_1a_2$  plane of the inhomogeneity) and  $\eta_1^n$  for shearing that does not activate the foliation slip. Clearly  $\eta_1^s < \eta_1^n$  and the degree of anisotropy for the material can be defined as (Chen et al., 2014):

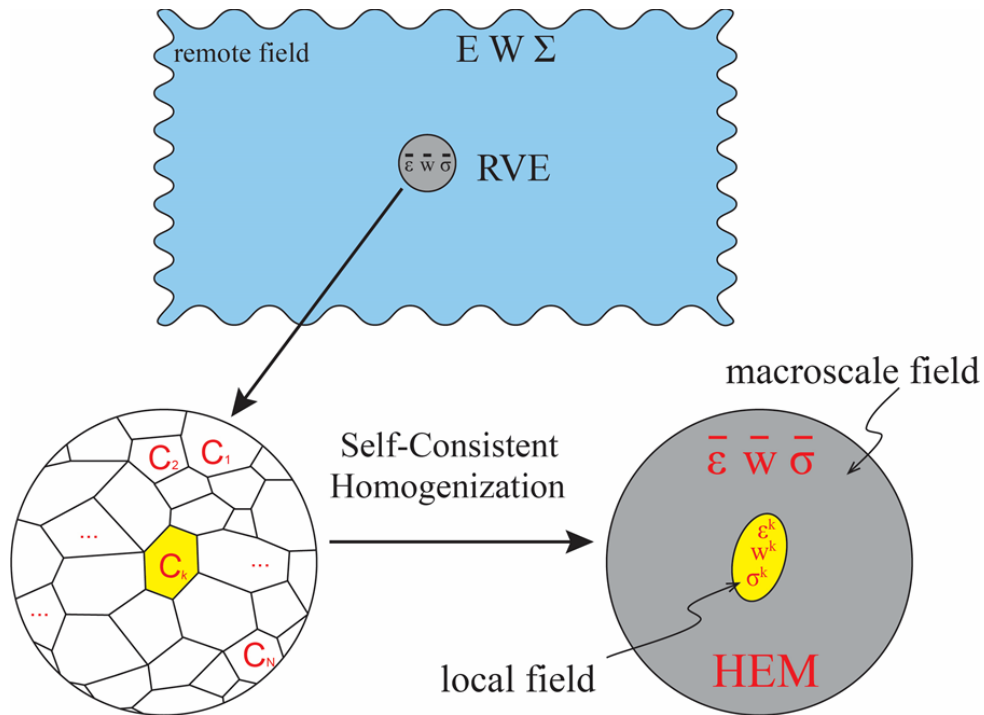


**Figure 3.5** A conceptual diagram showing the heterogeneous poly-element scenario and the self-consistent homogenization scheme

**(a)** An infinite poly-element composite material subjected to the remote field with strain rate  $E$ , vorticity  $W$ , and the deviatoric stress  $\Sigma$ . The macroscale fields ( $\bar{\epsilon}$ ,  $\bar{w}$ , and  $\bar{\sigma}$ ) defined, at every point, in terms of the Representative Volume Element (RVE). **(b)** An RVE is a large enough element consisting of a representative assemblage of Rheologically Distinct Elements (RDEs). **(c)** Each RDE is reviewed as an ellipsoid embedded in a Homogeneous Equivalent Medium (HEM) whose rheology is the “average” from the rheological properties of all constituent elements in the RVE. The overall rheology of HEM is obtained by means of a self-consistent homogenization scheme from the properties of the constituents.

$$m = \frac{\eta_1^n}{\eta_1^s} \quad (3.6)$$

The viscosity ratio between the viscosity of the matrix and that of the ellipsoid is defined as:

$$r = \frac{\eta_1^n}{\eta_0} \quad (3.7)$$

The anisotropic viscous stiffness tensor for the material inside the high-strain zone can be expressed in terms of the viscosity ratio  $r$ , the degree of anisotropy  $m$  as well as the viscosity of matrix  $\mu_0$  (Jiang, 2016):

$$\mathbf{C}_{ijkl}^1 = 2r\eta_0 \begin{pmatrix} J_{11kl}^d & J_{12kl}^d & \frac{1}{m} J_{13kl}^d \\ J_{21kl}^d & J_{22kl}^d & \frac{1}{m} J_{23kl}^d \\ \frac{1}{m} J_{31kl}^d & \frac{1}{m} J_{32kl}^d & J_{33kl}^d \end{pmatrix} \quad (3.8)$$

where  $C_{ijkl}^1$  and  $J_{ijkl}^d$  represent, respectively, the components of the ellipsoid viscosity tensor  $\mathbf{C}_1$  and the 4<sup>th</sup> order identity tensor  $\mathbf{J}^d$ .

Numerical calculation in this paper using Eqs.3.1-3, and the calculation of self-consistent homogenization are realized using MATLAB scripts, the algorithms for which are in the literature (Jiang, 2010; Jiang and Bentley, 2012; Jiang, 2014, 2016; Qu et al., 2016) and in Chapter 2 of this thesis.

### 3.3 Geometric simulation results and field observations

Once the far-field flow, which is determined by the plate motion and the state of the high-strain zone (the shape, orientation, and rheological properties) as well as the rheology of the country rock are known, the finite strain pattern and fabrics inside a high-strain zone can be obtained using Eq.3.1 and the method in Jiang (2010). Once the high-strain zone established, it retains its shape and orientation for a long time. This work assumes that the computation starts when the high-strain zone is already established, so the shape and

orientation of the high-strain zone remain unchanged during the computational time. As shown in Fig.3.4, the shape of the high-strain zone is defined as  $a_1 : a_2 : a_3 = 100R : R : 1$ , where  $R$  is a shape parameter. The strike of the high-strain zone is parallel to x-axis and  $\beta$  is the dip angle. Because only the viscosity ratio  $r$  between the country rocks and the high-strain zone influences the development of the fabrics, not the absolute viscosities, the viscosity of country rocks  $\eta_0$  is simply set to 1. In a power-law material, the viscous stiffness tensor (or viscosity) is not a material constant but depends on the current strain rate (or stress) state. Therefore, the viscosity ratio  $r$  between the power-law matrix (country rocks) and the power-law ellipsoid (high-strain zone) is not a constant either and changes during the deformation. For simplicity, the stress exponents for both country rocks  $n_0$  and the high-strain zone  $n_1$  are set to 1. Then the viscosity ratio  $r$  is constant. This work considers a sinistral oblique converging plate motion in the reference model. In  $xyz$  coordinate, as shown in Figs.5.3 and 5.4, the far-field flow derived from the plate

motion is  $L = \begin{pmatrix} 0 & \cos \alpha & 0 \\ 0 & -\sin \alpha & 0 \\ 0 & 0 & \sin \alpha \end{pmatrix} \varepsilon_v$ , where  $\alpha$  is the convergence angle,  $\varepsilon_v$  the average

rate of deformation of the high-strain zone. As the fabric formation is the final product of progressive deformation and irrelevant to the absolute deformation rate,  $\varepsilon_v$  is simply set to 1. The reference model considers a high-strain zone with a shape parameter of  $R = 20$ , a viscosity ratio of  $r = 10^{-2}$ , and an anisotropy degree of  $m = 1$ , indicating the high-strain zone is isotropic. The time step for computation is  $\delta t = 0.02$  that ensure every step corresponds to an infinitesimal increment of deformation (Jiang, 2014). The total computational time is 100 steps. A series of simulation runs are performed varying convergence angle  $\alpha$  progressively from  $0^\circ$  to  $90^\circ$ , dip angle  $\beta$  from  $90^\circ$  to  $40^\circ$ . Over a total computation time  $t$ , the finite strain patterns based on the reference model are shown in Fig.3.6. The lineations are represented by the maximum principal strain axes, and the poles to the foliations are represented by the minimum principal strain axes. As finite strain increases, the foliations converge to nearly parallel to the high-strain zone boundaries regardless of convergence angle and dip angle. For a vertical high-strain zone ( $\beta = 90^\circ$ ), at large finite strains, the lineations are strike-parallel when  $\alpha$  is small

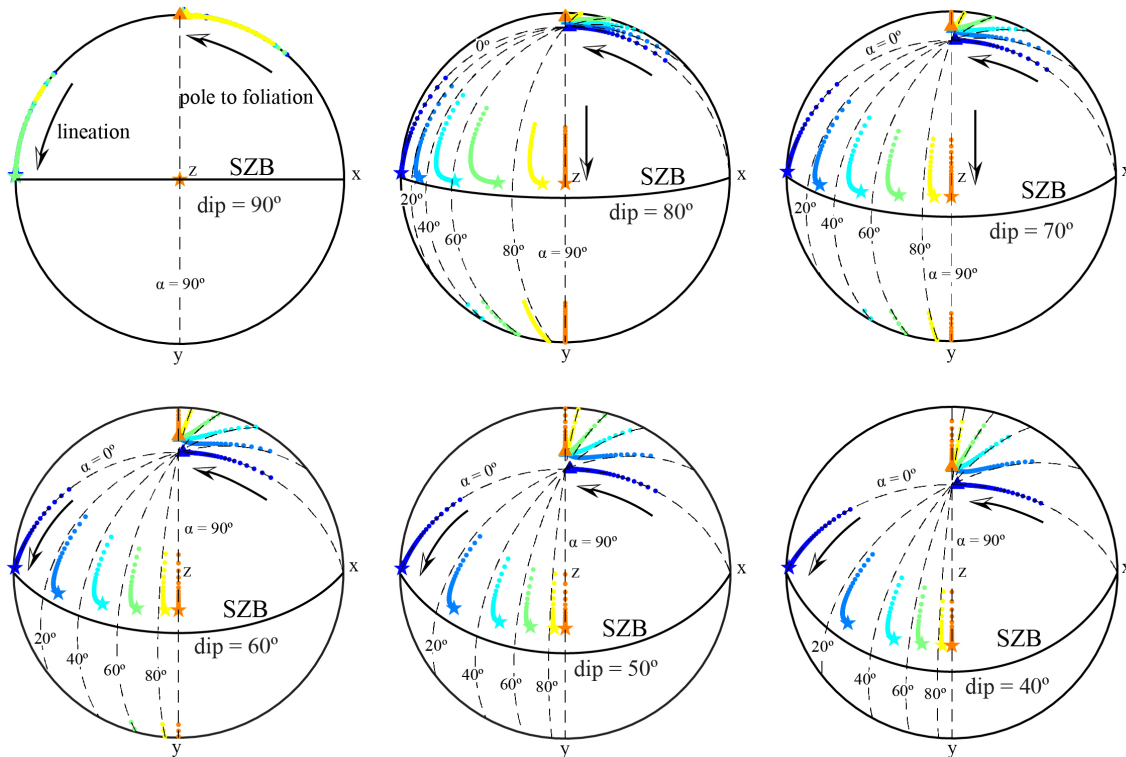


**Figure 3.6 Equal-area lower hemisphere projections of the variation and evolution of the finite strain patterns in a sinistral transpressional zone**

The lineations are represented by the maximum principal strain axes (stars), and the poles to the foliations are represented by the minimum principal strain axes (triangles). As strain increases, the fabrics rotate along with the arrows.  $\alpha$  is the convergence angle and  $\beta$  is the dip angle. The black line represents the high-strain zone boundary (see text for more details).



( $\alpha \leq 60^\circ$ ) and vertical when  $\alpha$  is very large ( $\alpha > 60^\circ$ ). For an oblique high-strain zone ( $\beta \neq 90^\circ$ ), at large finite strains, the lineations are from the strike-parallel to nearly dip-parallel as  $\alpha$  increasing progressively from  $0^\circ$  to  $90^\circ$ . Simulation runs with various shape parameters  $R$ , viscosity ratios  $r$ , and anisotropy degrees  $m$  are performed as well. The simulation results show that the finite strain pattern is insensitive to these parameters.

This model has been applied to an ancient high-strain zone, Shangdan Tectonic Zone in Qinling Orogenic Belt. The Qinling Orogenic Belt extends nearly 2500 km from west to east across central China (Fig.3.7a; Dong et al., 2011). The Qinling Orogenic Belt is formed by the convergence and collision between north and south China blocks (e.g., Dong et al., 2011; Dong and Santosh, 2016). It is divided into the south Qinling and the north Qinling by Shangdan Suture Zone (or Shangdan Tectonic Zone) (Fig.3.7a; Meng and Zhang, 2000). The Shangdan Tectonic Zone is defined by the discontinuously exposed Danfeng Complex that consists of ophiolitic mélangé (Dong et al., 2011; Dong and Santosh, 2016). From Danfeng area to Shangnan area, well-developed lineations, sub-vertical foliations, and sinistral shear-sense indicators are observed along the Shangdan Tectonic Zone (Figs.3.7c and d). The poles to the foliations and the lineations in this area are plotted in Fig.3.7b, and the average dip angle of the foliations is  $\sim 70^\circ$ . In this area, the Shangdan Tectonic Zone is regarded as a highly flatten inclusion with a dip angle of  $70^\circ$  subjected to a sinistral oblique converging plate motion. The simulation results when  $\beta = 70^\circ$  and  $\alpha = 5 \sim 20^\circ$  are consistent with the fabrics observed in the field (Fig.3.8). So, there must be a large component of shearing in this area, and the convergence angle  $\alpha$  of the plate motion is constrained between  $5^\circ$  to  $20^\circ$ . Comparing the geometric results deduced from the model and the field observations in Shangdan Tectonic Zone allows us to constrain the plate motion during the deformation time in this area and validate this model as well.

### 3.4 Stress distribution inside and outside the active high-strain zone

As this model is a complete mechanical one, it allows not only the simulation of the finite strain pattern within a high-strain zone but also the investigation of the stress distribution

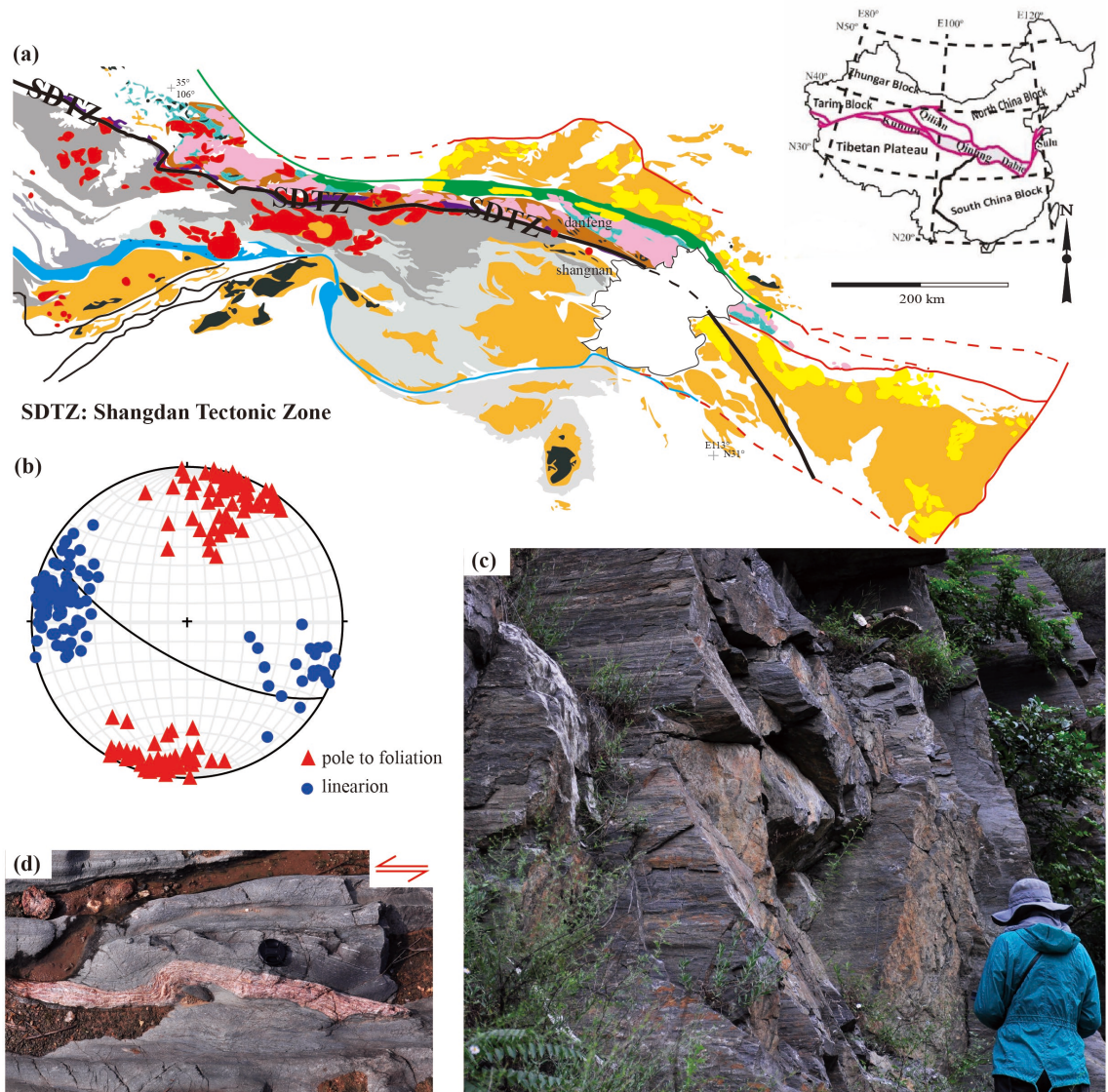


**Figure 3.7 A geological map and field observations of the Shangdan Tectonic Zone, Qinling Orogenic Belt, China**

(a) A geological map showing the location and the main structures and geological domains of the Qinling Orogenic Belt and its adjacent areas (modified after Dong and Santosh, 2016). (c) and (d) Field photos showing the well-developed lineations, sub-vertical foliations, and sinistral shear-sense indicators along the Shangdan Tectonic Zone from Danfeng area to Shangnan area. (b) Equal-area lower-hemisphere plots of the fabric data in this area. Red triangles are the poles to the foliations and the blue dots are the lineations.

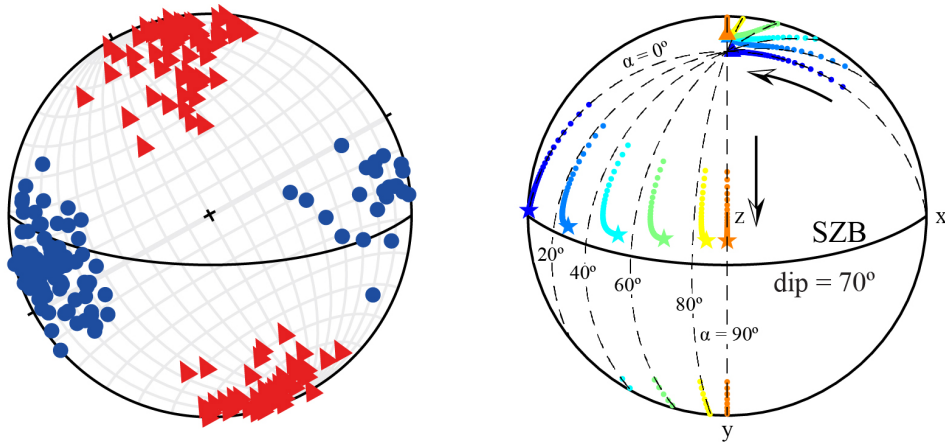


**Figure 3.8 The comparison of geometric results and field observations**

**(a) Equal-area lower-hemisphere plots of the fabric data collected along Shangdan Tectonic Zone from the Danfeng area to the Shangnan area. Red triangles represent the poles to the foliations and the blue dots stand for the lineations. (b) Equal-area lower-hemisphere plots of the variation and evolution of finite-strain-related lineations and poles to the foliations in a sinistral transpressional zone when dip angle  $\beta = 70^\circ$  and the convergence angle  $\alpha$  varies from  $0^\circ$  to  $90^\circ$ . The simulation results when  $\beta = 70^\circ$  and  $\alpha = 5 \sim 20^\circ$  are consistent with the fabric observations.**

inside and outside an active high-strain zone. The relative plate motion between the North American and Pacific Plates is N35°W at a rate of  $48 \pm 1$  mm/yr (DeMets et al., 1990) that leads to dextral oblique converging. The San Andreas Fault (SAF) is a major fault in the plate boundary and in central California. The SAF is nearly vertical ( $\beta = 90^\circ$ ) and oriented at N40°W, giving a convergence angle  $\alpha \sim 5^\circ$ . The SAF is a pure right-lateral strike-slip fault that accommodates hundreds of kilometers displacement along it (Zoback et al., 1987). The direction of maximum horizontal compression in the SAF is expected to be 30° to 45° from the vertical fault plane based on the traditional mechanical model (e.g., Jaeger and Cook, 1969). However, there is clear evidence that both the SAF and the adjacent diffused region (over 200km) together accommodated the plate motion (Teyssier et al., 1995; Titus et al. 2012). The orientation of young thrust faults and upright folds and borehole breakouts in the diffused zone suggests that the direction of the maximum principal deviatoric stress ( $\sigma_1$ ) is between 78° to 84° to the SAF (Mount and Suppe, 1987; Zoback et al., 1987; Jones, 1988; Townend and Zoback, 2004). It is a long-standing geological problem of how the stress distributes in the vicinity of the SAF and how to account for the widespread thrust faults and upright folds perpendicular to the SAF. Zoback et al. (1987) used a simple model for elastic material to show that the fault normal stress field is consistent with the plate motion as long as the fault is extremely weak in the shear direction. They also suggested that through the entire lithosphere not only in brittle crust, localized high-strain zones and faults may reorient tectonic stresses that results in the thrust faults and upright folds perpendicular to the SAF.

In order to investigate the stress distribution in the vicinity of SAF in the ductile region, we consider the SAF in the ductile region as a vertical highly flatten inclusion with a shape parameter of  $R = 20$ , subjected to a dextral oblique converging with a convergence angle of  $\alpha = 5^\circ$ . The stress distribution inside and adjacent to the SAF can be solved by Eshelby's solutions for the interior and exterior fields (Eqs.3.1 and 3.2). The viscosity varies by two to three orders of magnitude over the western United States, with low viscosity along the SAF and high viscosity in the country rocks (Flesch et al., 2000). The SAF is weak with respect to strike-slip probably due to rheological anisotropy (Gilbert et al., 1994; Flesch et al., 2000). This work assumes that the stress exponents for the SAF

$n_1$  and country rocks  $n_0$  are 1, and the viscosity of country rocks  $\eta_0$  is 1. The viscosity ratio between the SAF and the country rocks is set to  $r = 10^{-2}$  and  $r = 10^{-3}$ . The anisotropy degree is set to  $m = 1$  for isotropic situation, and  $m = 10$ , indicating that  $\eta_1^s$  of the SAF is one order of magnitude lower than  $\eta_1^n$ .

The orientations of the maximum principal deviatoric stress ( $\sigma_1$ ) within the SAF and in its vicinity are plotted in Fig.3.9. When  $r = 10^{-2}$  and  $m = 1$ , the exterior stresses do not rotate too much (Fig.3.9a). The exterior stress becomes nearly perpendicular to the SAF in its vicinity, if the viscosity ratio between the SAF and the country rocks is decreased by one order of magnitude (Fig.3.9c) or the anisotropy of the SAF is increased by one order of magnitude (Fig.3.9b) or both (Fig.3.9d). The results in Figs.3.9b and c are identical, indicating that the ratio between the viscosity of the SAF for shearing along the foliation  $\eta_1^s$  and the viscosity of country rocks  $\eta_0$  determines the orientation of the exterior stress. Simulation runs with varied shape parameter  $R$  are performed; the orientation of the exterior stress is insensitive to the shape parameter  $R$  as long as the three semi-axes satisfy  $a_1 \gg a_2 > a_3$ . We also notice that although the exterior stress rotates to nearly perpendicular when the SAF is weak along the foliation, the exterior stress resumes about one characteristic length away from the SAF.

To conclude, the plate motion ultimately determines the stress field and deformation pattern. The presence of the large weak zones, including faults in the brittle region and high-strain zones in the ductile region, alters the stress field and deformation pattern adjacent to the weak zones. However, in the ductile region, plate oblique convergence and the presence of the weak SAF can account for a narrow band of stress rotation; it cannot explain the widespread thrust faults and upright folds perpendicular to the SAF. Additional factors, including basal tractions and buoyancy forces due to horizontal variation in gravitational potential energy (GPE; Flesch et al., 2000), may affect the stress orientation in the western United States.

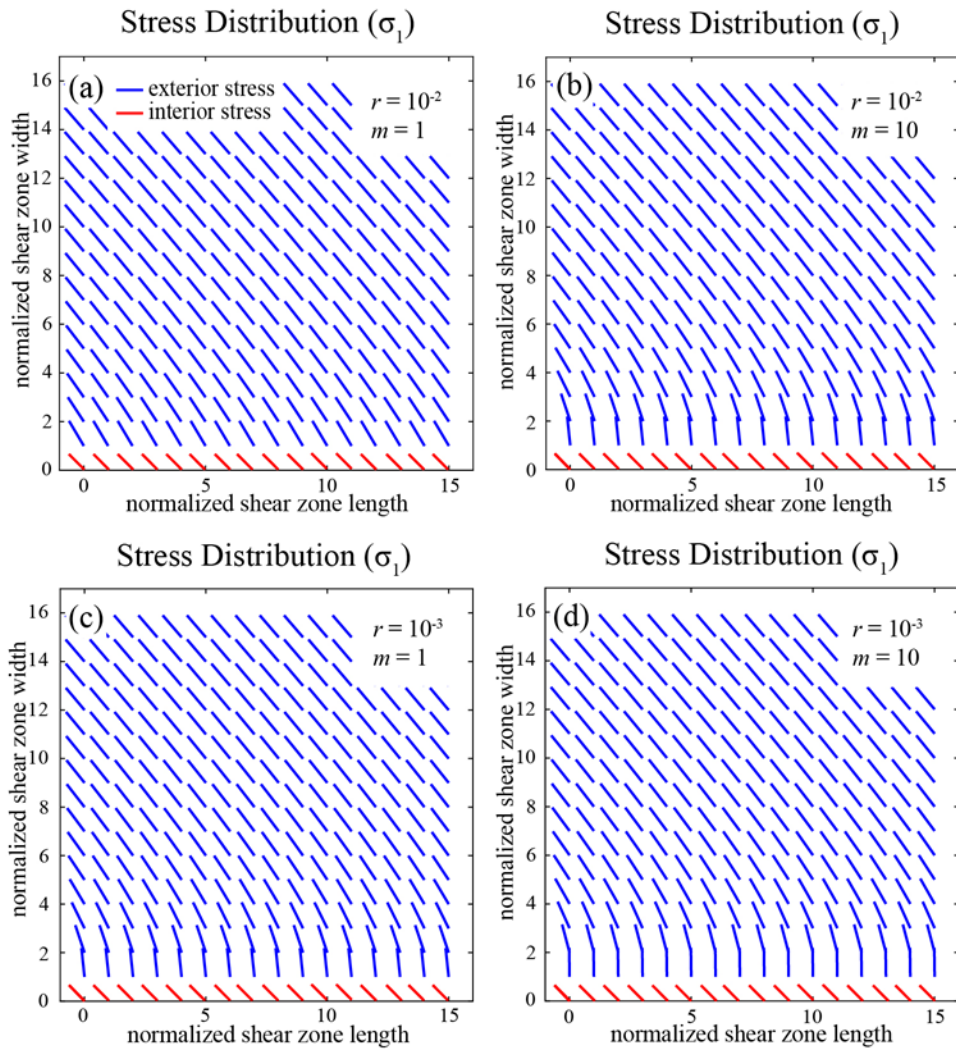


**Figure 3.9** The orientation of the maximum principal deviatoric stress ( $\sigma_1$ ) within the SAF and in its vicinity

The red bar represents the interior stress field, and the blue bar is the exterior stress field. The simulation results when (a)  $r = 10^{-2}$  and  $m = 1$ ; (b)  $r = 10^{-2}$  and  $m = 10$ ; (c)  $r = 10^{-3}$  and  $m = 1$ ; (d)  $r = 10^{-3}$  and  $m = 10$ . For more details, see the text.

### 3.5 The strength of the large-scale high-strain zones

As Earth's deformation in the ductile region is characterized by localized high-strain zones (e.g., Poirier, 1980; Twiss and Moores, 1992; Passchier and Trouw, 2005), the strength of the large-scale high-strain zone is the key to understand the continental strength. The strength of the quartz aggregates in a quartz-bearing mylonite zone has commonly been used to represent the strength of the mylonite zone and, in turn, to constrain the continental lithosphere strength (Behr & Platt, 2014; Kohlstedt et al., 1995). However, the roles of other minerals, like mica, and the anisotropy due to the development of fabrics have a strong influence in the strength of the high-strain zones (Kronenberg et al., 1990; Shea and Kronenberg, 1993; Tullis and Wenk, 1994; Tullis, 2002; Holyoke and Tullis, 2006; Montési, 2013). It is oversimplified to use the strength of quartz aggregates to represent the high-strain zone strength. The large-scale high-strain zone is composed of a lot of rheologically distinct elements (Fig.3.10). Therefore, the overall strength of the high-strain zone must be obtained from the rheological properties of the constituents. To account distinct rheological properties and the preferred orientation development of the constituent elements, the self-consistent homogenization approach (Molinari et al., 1987; Lebensohn and Tomé, 1993; Jiang 2014, 2016; Fig.3.10) is required to obtain the overall rheology of the high-strain zone.

I applied the self-consistent homogenization approach to the mylonite zones at the northwest margin of the Grenville Front Tectonic Zone to investigate the strength of the high-strain zone. The Grenville Front Tectonic Zone (GFTZ) is a NE-trending deformation belt at the northwest front of the Grenville Orogen (Wynne-Edwards, 1972; Davidson, 1984). GFTZ is a thrust zone formed during the Grenvillian Orogeny (LaTour 1981; Haggart et al., 1993; Rivers, 2008). Compositional layering transposition foliations, lineations, and tight-to-isoclinal folds are observed in GFTZ (Li, 2012, Ph.D. thesis). At the northwest margin of the GFTZ, the NE-striking mylonite zones are well exposed (Fig.3.11b). In the banded mylonite zone (Fig.3.11c), rocks are highly deformed, and fabrics are characterized by NE-striking and steeply dipping transposition foliations and SE-plunging lineations (Fig.3.11e). Thin sections from the banded mylonite show that the rocks are metasediment, and the main minerals are quartz, mica and feldspar



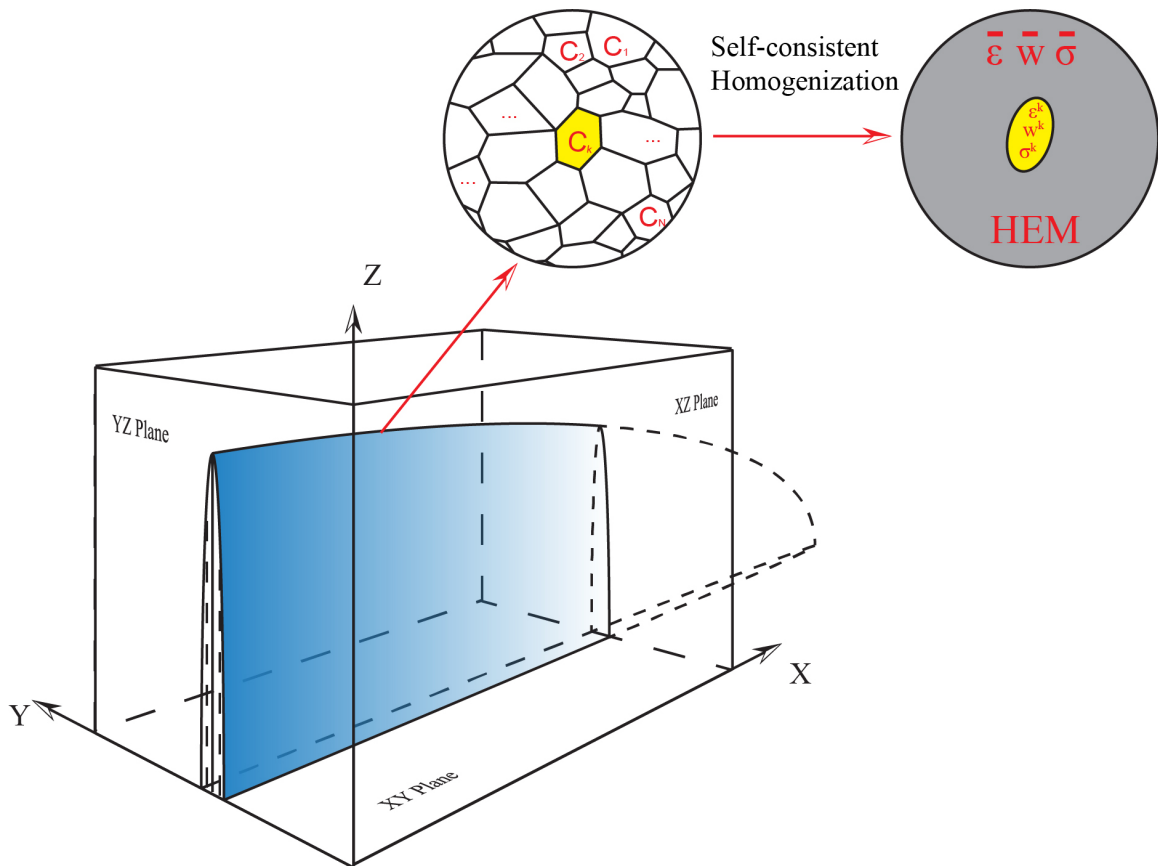
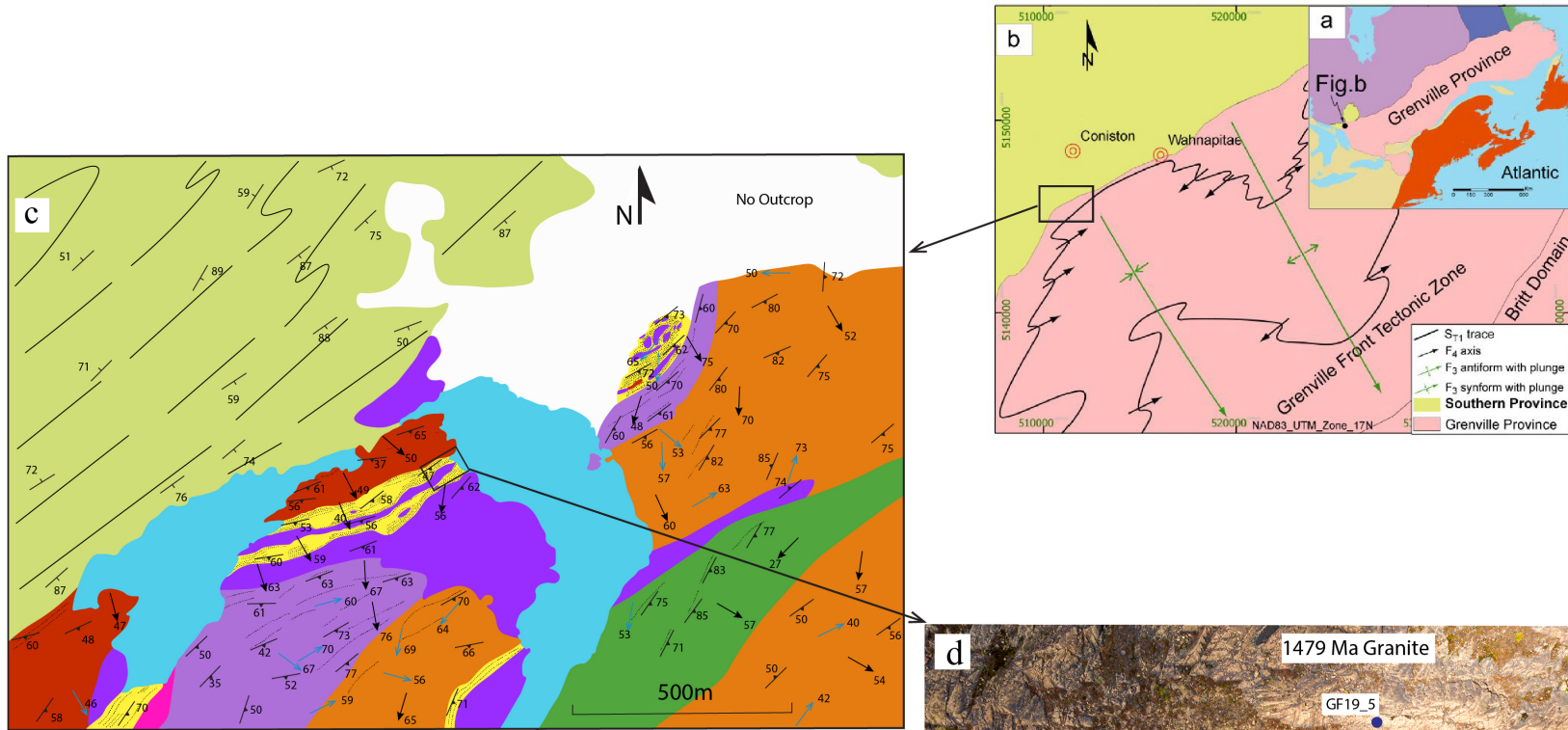


**Figure 3.10** A conceptual illustration of a planar heterogeneous poly-element high-strain zone embedded in a block of the ductile lithosphere and the self-consistent homogenization scheme





- Mississagi metasandstone
- 1464 Ma megacrystic granite
- Migmatitic gneiss
- Foliation
- Banded mylonite
- Nipissing diabase
- Amphibolite
- Lineation
- 1479 Ma granite
- Nipissing diabase with pegmatite
- Bedding
- Fold axis

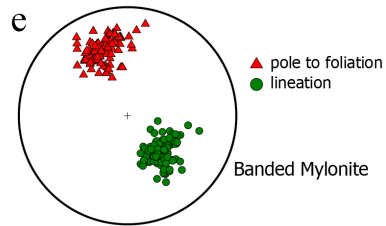


**Figure 3.11 Geological maps and field observations in the mylonite zone at the northwest margin of the Grenville Front Tectonic Zone**

**(a)** A regional geological map showing the location of the area in **(b)** with respect to the whole Grenville Province (modified after Li, 2012). The area in **(c)** is located at the northwest margin of the Grenville Front Tectonic Zone. The upper left part of this study area is covered by Mississagi metasediments with sedimentary beds. The lower right part is highly deformed. NE-striking and steeply dipping transposition foliations, SE-plunging lineations, and tight-to-isoclinal folds are observed in the lower right part of the map. **(d)** A field photo showing the banded mylonite, mylonitic 1479 Ma granite, and the undeformed diabase, as well as the sample (S08, S11, GF19\_3, and GF19\_5) locations. **(e)** Equal-area lower-hemisphere projection of the fabric data in banded mylonite zone. Red triangles are the poles to the foliations and the green dots are the lineations.

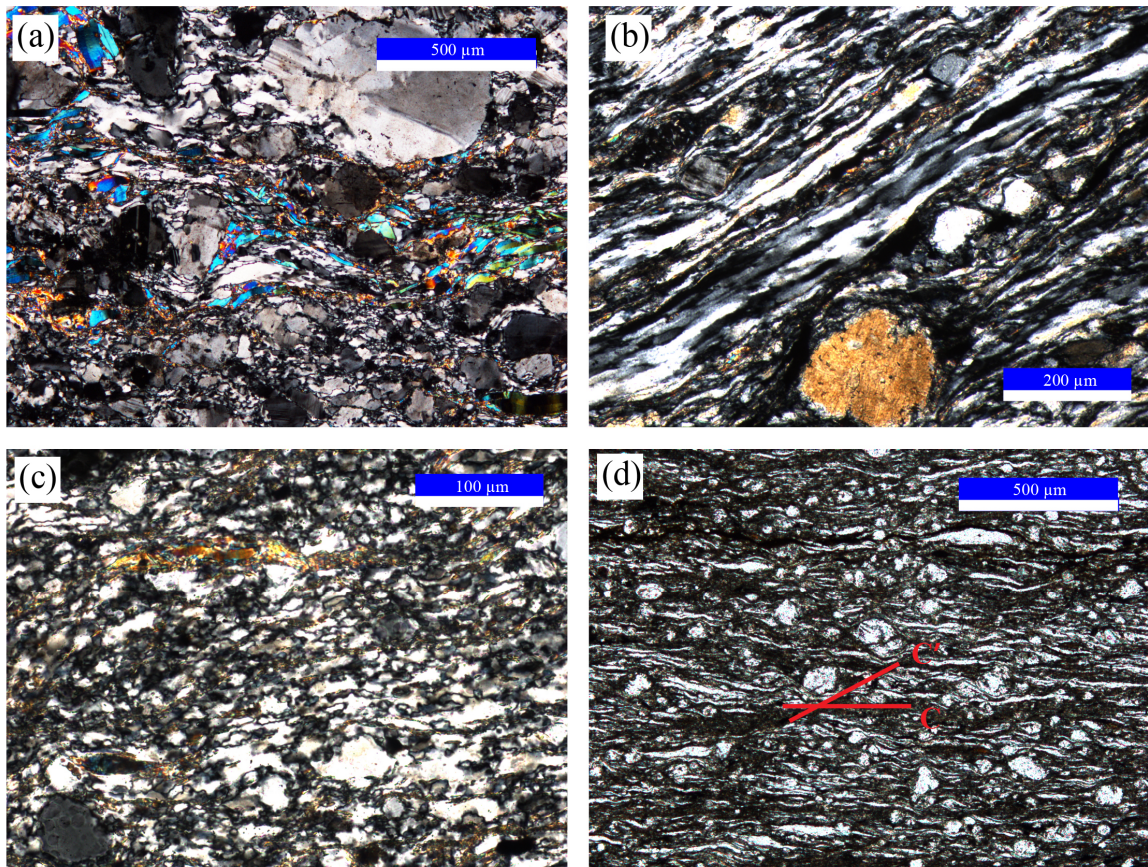


**Figure 3.12 Photomicrographs of the mylonitic granite and the banded mylonite**

**(a) Sample GF19\_5:** The mylonite 1479 Ma granite with feldspar porphyroclasts (bottom left) in quartz and mica grains. The quartz grains are deformed by SGR recrystallization. **(b) Sample S08:** Quartz ribbons with SGR recrystallized quartz grains. Feldspar porphyroclasts are surrounded by quartz grains. **(c) Sample GF19\_3:** SGR recrystallized quartz grains. (a)-(c) are under cross-polarized light. **(d) Sample S11:** Microstructures in banded mylonite under plain polarized light showing C'-type shear band and C-foliation. This thin section is parallel to the stretching lineation and perpendicular to the foliation, viewed toward the northeast. It shows top-to-the-left shear sense. The light elongated grains are quartz grains, and the dark area is mica. (b)-(d) are all collected from banded mylonite with varied volume fractions of mica.



(Fig.3.12). Feldspar porphyroclasts are in a matrix of quartz and mica grains. Subgrain rotation recrystallization of quartz grains is observed in the thin sections, indicating the deformation temperature was between 400°C to 500°C (Stipp et al., 2002). Mica grains are aligned parallel to the foliation. The volume fraction of mica grains varies from sample to sample (Fig.3.12). As the feldspar porphyroclasts are far apart from each other and the volume fraction of feldspar is relatively low, this work simply assumes that the rheology of the high-strain zone is represented by the rheology of the quartz-mica aggregates.

Consider an RVE composed of 500 quartz and mica grains (RDEs) with random shapes (Fig.3.10). The volume fractions of quartz grains and mica grains are denoted by  $c_q$  and  $c_m$ , and  $c_q + c_m = 1$ . This work further assumes that the quartz grains are rheologically isotropic, randomly orientated, and the mica grains are transversely isotropic with two distinct effective viscosities:  $\eta_{mica}^s$  being the viscosity for shearing along the basal cleavage and  $\eta_{mica}^n$  for shearing without the activation of basal slip. If the basal cleavage planes of mica grains are aligned parallel to the foliations of the high-strain zone, the high-strain zone is also transversely isotropic, having two distinct effective viscosities  $\bar{\eta}^s$  and  $\bar{\eta}^n$ . The effective viscosity of quartz  $\eta_{quartz}$  and the viscosity of mica for shearing along basal slip  $\eta_{mica}^s$  can be obtained using the flow laws (Kronenberg et al., 1990; Lu and Jiang, 2019) in terms of strain rate invariant and deviatoric stress invariant (Ranalli, 1987, p.70) at a reference P-T condition and a reference strain rate. We obtained  $\eta_{quartz} = 1.87 \times 10^{13} \text{ MPa} \cdot \text{s}$  and  $\eta_{mica}^s = 4.61 \times 10^{12} \text{ MPa} \cdot \text{s}$  for a P-T condition of 450°C and 405 MPa and a strain rate of  $\dot{\epsilon} = 10^{-12} \text{ s}^{-1}$ . If the anisotropic degree of mica is set to

$$m = \frac{\eta_{mica}^n}{\eta_{mica}^s} = 10, \text{ we have } \eta_{quartz} : \eta_{mica}^s : \eta_{mica}^n = 4 : 1 : 10 .$$

Fig.3.13 shows the homogenized rheological properties of the high-strain zone ( $\bar{\eta}^s$  and  $\bar{\eta}^n$ ), normalized to  $\eta_{mica}^s$ , obtained by the self-consistent approach. If there is no mica

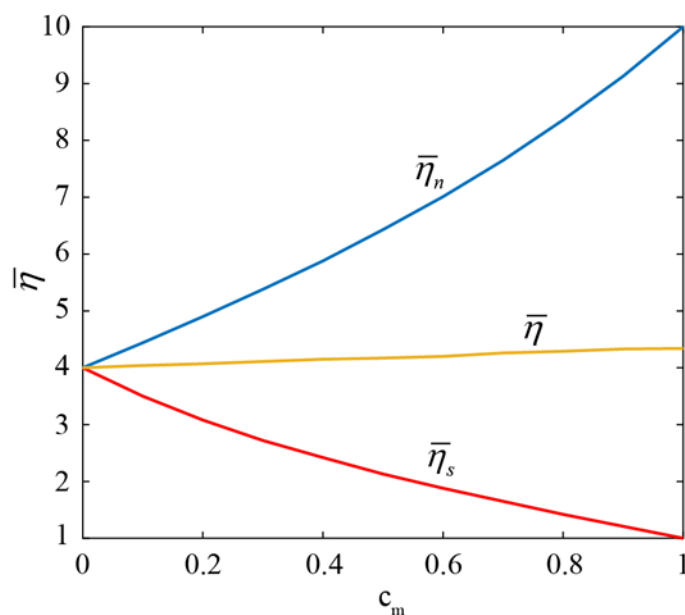


**Figure 3.13 Plots of the homogenized viscosities of the quartz-mica aggregates versus the volume fraction of mica**

A reference P-T condition of 450°C and 405 MPa and a reference strain rate of  $\dot{\varepsilon} = 10^{-12} \text{ s}^{-1}$  are used. Quartz grains are isotropic and randomly orientated, and they follow the flow law of Lu and Jiang (2019). The mica grains are transversely anisotropic with an anisotropic degree of 10. The slip along the basal cleavage follows the flow law of Kronenberg et al. (1990). When mica grains are randomly orientated, the whole aggregates is also isotropic. The yellow line represents the homogenized viscosity  $\bar{\eta}$  of quartz-mica aggregates in this situation. There is another situation where the aggregates become anisotropic due to the development of foliation defined by the alignment of the mica basal cleavage planes. Then blue and red lines represent, respectively, the homogenized viscosity without active the slip along the foliation  $\bar{\eta}_n$  and the one shearing along the foliation  $\bar{\eta}_s$ .  $c_m$  is the volume fraction of mica grains.

grain ( $c_m = 0$ ), the high-strain zone is isotropic, and the homogenized effective viscosity of the high-strain zone is equal to  $\eta_{quartz}$ . As the volume fraction of mica  $c_m$  increases, the high-strain zone becomes anisotropic due to the development of foliation defined by the alignment of the mica basal cleavage planes and  $\bar{\eta}^s$  decreases from 4 to 1 and  $\bar{\eta}^s$  increases from 4 to 10. If the mica grains are randomly orientated, then the high-strain zone is isotropic, and the homogenized effective viscosity of high-strain zone increases from 4 to 4.34 as  $c_m$  increases. Adding weak minerals, like mica, in the high-strain zone will decrease its strength. Especially, if the rocks in the high-strain zones are anisotropic due to the development of the foliation defined by the alignment of the anisotropic minerals, the high-strain zone becomes extremely weak with respect to shearing along the foliation plane.

### 3.6 Conclusions

This work considers the large-scale high-strain zone as a heterogeneous and highly flattened inclusion embedded in the ductile lithosphere and applies the extended nonlinear Eshelby solutions to the continental lithosphere with self-consistent homogenization approach.

The Eshelby's solutions on inclusions for interior and exterior fields allow us to investigate the geometries inside the high-strain zone, the stress distribution within and in the vicinity of the high-strain zone. The self-consistent homogenization approach helps to obtain the overall strength of the high-strain zone from the properties of the constituents.

This new micromechanical-based high-strain zone model has been applied to the Shangdan Tectonic Zone in Qinling Orogenic belt, where well-developed sub-vertical foliations, shallowing dipping lineations, and sinistral shear sense indicators are observed. Comparing the geometries deduced from this model with the field observation in Shangdan Tectonic Zone, we validate this model and constrain the convergence angle of the plate motion in this area to  $5^\circ \sim 20^\circ$ .

The application to the San Andreas Fault in Central California helps to verify this model and to understand the stress distribution within and in the vicinity of a high-strain zone in the ductile region. The plate motion between the North America and Pacific Plates ultimately determines the stress field. The presence of the weak SAF in the ductile region can account for a narrow band of stress rotation; it cannot explain the widespread thrust faults and upright folds perpendicular to the SAF. Additional factors like the forces caused by horizontal variation in gravitational potential energy may affect the stress orientation in the western United States.

The application to the mylonite zone in the Grenville Front Tectonic Zone quantitatively demonstrates that the presence of weak minerals, like mica, and the rheological anisotropy due to the development of fabrics in the high-strain zone significantly weaken the high-strain zone with respect to shearing along the foliation plane. Simply using the strength of the quartz aggregates to represent the high-strain zone strength or even to constrain the strength of the continental lithosphere is oversimplified. A more rigorous homogenization approach is required to obtain the overall rheology of the high-strain zone from the properties, concentrations, and the geometric arrangement of the constituents.

### 3.7 References

- Behr, W. M., & Platt, J. P. (2014). Brittle faults are weak, yet the ductile middle crust is strong: Implications for lithospheric mechanics. *Geophysical Research Letters*, *41*(22), 8067–8075. <https://doi.org/10.1002/2014GL061349>
- Ben-Zion, Y., & Sammis, C. G. (2003). Characterization of fault zones. *Pure and Applied Geophysics*, *160*(3-4), 677-715. <https://doi.org/10.1007/PL00012554>
- Chen, Y., Jiang, D., Zhu, G., & Xiang, B. (2014). The formation of micafish: a modeling investigation based on micromechanics. *Journal of Structural Geology*, *68*, 300-315. <https://doi.org/10.1016/j.jsg.2013.12.005>
- Davidson, A., 1984. Tectonic boundaries within the Grenville Province of the Canadian Shield. *Journal of Geodynamics* *1* (3-5), 433-444. [https://doi.org/10.1016/0264-3707\(84\)90018-8](https://doi.org/10.1016/0264-3707(84)90018-8)
- Davis, J. R., & Titus, S. J. (2011). Homogeneous steady deformation: A review of computational techniques. *Journal of Structural Geology*, *33*(6), 1046-1062. <https://doi.org/10.1016/j.jsg.2011.03.001>
- DeMets, C., Gordon, R. G., Argus, D. F., & Stein, S. (1994). Effect of recent revisions to the geomagnetic reversal time scale on estimates of current plate motions. *Geophysical research letters*, *21*(20), 2191-2194. <https://doi.org/10.1029/94GL02118>
- Dong, Y., Zhang, G., Neubauer, F., Liu, X., Genser, J., & Hauzenberger, C. (2011). Tectonic evolution of the Qinling orogen, China: review and synthesis. *Journal of Asian Earth Sciences*, *41*(3), 213-237. <https://doi.org/10.1016/j.jseaes.2011.03.002>
- Dong, Y., & Santosh, M. (2016). Tectonic architecture and multiple orogeny of the Qinling Orogenic Belt, Central China. *Gondwana Research*, *29*(1), 1-40. <https://doi.org/10.1016/j.gr.2015.06.009>



- Dutton, B. J. (1997). Finite strains in transpression zones with no boundary slip. *Journal of Structural Geology*, 19(9), 1189-1200. [https://doi.org/10.1016/S0191-8141\(97\)00043-6](https://doi.org/10.1016/S0191-8141(97)00043-6)
- Eshelby, J. D. (1957). The determination of the elastic field of an ellipsoidal inclusion, and related problems. *Proceedings of the Royal Society of London. Series A. Mathematical and Physical Sciences*, 241(1226), 376-396. <https://doi.org/10.1098/rspa.1957.0133>
- Eshelby, J. D. (1959). The elastic field outside an ellipsoidal inclusion. *Proceedings of the Royal Society of London. Series A. Mathematical and Physical Sciences*, 252(1271), 561-569. <https://doi.org/10.1098/rspa.1959.0173>
- Fernández, C., & Díaz-Azpiroz, M. (2009). Triclinic transpression zones with inclined extrusion. *Journal of Structural Geology*, 31(10), 1255-1269. <https://doi.org/10.1016/j.jsg.2009.07.001>
- Flesch, L. M., Holt, W. E., Haines, A. J., & Shen-Tu, B. (2000). Dynamics of the Pacific-North American plate boundary in the western United States. *Science*, 287(5454), 834-836. <https://doi.org/10.1126/science.287.5454.834>
- Fletcher, R. C., & Pollard, D. D. (1999). Can we understand structural and tectonic processes and their products without appeal to a complete mechanics? *Journal of Structural Geology*, 21(8), 1071-1088. [https://doi.org/10.1016/S0191-8141\(99\)00056-5](https://doi.org/10.1016/S0191-8141(99)00056-5)
- Fossen, H., & Tikoff, B. (1993). The deformation matrix for simultaneous simple shearing, pure shearing and volume change, and its application to transpression-transension tectonics. *Journal of Structural Geology*, 15(3-5), 413-422. [https://doi.org/10.1016/0191-8141\(93\)90137-Y](https://doi.org/10.1016/0191-8141(93)90137-Y)

- Fossen, H., & Tikoff, B. (1998). Extended models of transpression and transtension, and application to tectonic settings. *Geological Society, London, Special Publications*, 135(1), 15-33. <https://doi.org/10.1144/GSL.SP.1998.135.01.02>
- Gilbert, L. E., Scholz, C. H., & Beavan, J. (1994). Strain localization along the San Andreas fault: consequences for loading mechanisms. *Journal of Geophysical Research: Solid Earth*, 99(B12), 23975-23984. <https://doi.org/10.1029/94JB01558>
- Goodwin, L. B., & Williams, P. F. (1996). Deformation path partitioning within a transpressive shear zone, Marble Cove, Newfoundland. *Journal of Structural Geology*, 18(8), 975-990. [https://doi.org/10.1016/0191-8141\(96\)00015-6](https://doi.org/10.1016/0191-8141(96)00015-6)
- Gumiaux, C., Judenherc, S., Brun, J. P., Gapais, D., Granet, M., & Poupinet, G. (2004). Restoration of lithosphere-scale wrenching from integrated structural and tomographic data (Hercynian belt of western France). *Geology*, 32(4), 333-336. <https://doi.org/10.1130/G20134.2>
- Haggart, M. J., Jamieson, R. A., Reynolds, P. H., Krogh, T. E., Beaumont, C., Culshaw, N. G., 1993. Last gasp of the Grenville Orogeny: thermochronology of the Grenville Front tectonic zone near Killarney, Ontario. *The Journal of Geology* 101 (5), 575-589. <https://doi.org/10.1086/648250>
- Hanmer, S. (1988). Great Slave Lake Shear Zone, Canadian Shield: reconstructed vertical profile of a crustal-scale fault zone. *Tectonophysics*, 149(3), 245-264. [https://doi.org/10.1016/0040-1951\(88\)90176-X](https://doi.org/10.1016/0040-1951(88)90176-X)
- Harland, W. B. (1971). Tectonic transpression in caledonian Spitsbergen. *Geological Magazine*, 108(1), 27-41. <https://doi.org/10.1017/S0016756800050937>
- Hobbs, B. E., & Ord, A. (2014). *Structural geology: the mechanics of deforming metamorphic rocks*. Elsevier.

- Holyoke, C. W., & Tullis, J. (2006). Mechanisms of weak phase interconnection and the effects of phase strength contrast on fabric development. *Journal of Structural Geology*, 28(4), 621–640. <https://doi.org/10.1016/j.jsg.2006.01.008>
- Hudleston, P. J., Schultz-Ela, D., & Southwick, D. L. (1988). Transpression in an Archean greenstone belt, northern Minnesota. *Canadian Journal of Earth Sciences*, 25(7), 1060-1068. <https://doi.org/10.1139/e88-103>
- Jaeger, J. C., 1962. *Elasticity, Fracture and Flow*, John Wiley & Sons. New York.
- Jaeger, J. C., & Cook, N. G. (1969). *Fundamentals of rock mechanics*, Methuen & Co. Ltd., London, 513.
- Jiang, D., & Williams, P. F. (1998). High-strain zones: a unified model. *Journal of Structural Geology*, 20(8), 1105-1120. [https://doi.org/10.1016/S0191-8141\(98\)00025-X](https://doi.org/10.1016/S0191-8141(98)00025-X)
- Jiang, D. (2010). Flow and finite deformation of surface elements in three dimensional homogeneous progressive deformations. *Tectonophysics*, 487(1), 85-99  
<https://doi.org/10.1016/j.tecto.2010.03.011>
- Jiang, D. (2012). A general approach for modeling the motion of rigid and deformable ellipsoids in ductile flows. *Computers & geosciences*, 38(1), 52-61.  
<https://doi.org/10.1016/j.cageo.2011.05.002>
- Jiang, D. (2013). The motion of deformable ellipsoids in power-law viscous materials: Formulation and numerical implementation of a micromechanical approach applicable to flow partitioning and heterogeneous deformation in Earth's lithosphere. *Journal of structural geology*, 50, 22-34.  
<https://doi.org/10.1016/j.jsg.2012.06.011>
- Jiang, D. (2014). Structural geology meets micromechanics: A self-consistent model for the multiscale deformation and fabric development in Earth's ductile

lithosphere. *Journal of Structural Geology*, 68, 247-272.

<https://doi.org/10.1016/j.jsg.2014.05.020>

Jiang, D. (2016). Viscous inclusions in anisotropic materials: Theoretical development and perspective applications. *Tectonophysics*, 693, 116-142.

<https://doi.org/10.1016/j.tecto.2016.10.012>

Jones, L. M. (1988). Focal mechanisms and the state of stress on the San Andreas fault in southern California. *Journal of Geophysical Research: Solid Earth*, 93(B8), 8869-8891. <https://doi.org/10.1029/JB093iB08p08869>

Jones, R. R., & Holdsworth, R. E. (1998). Oblique simple shear in transpression zones. *Geological Society, London, Special Publications*, 135(1), 35-40.

<https://doi.org/10.1144/GSL.SP.1998.135.01.03>

Jones, R. R., Holdsworth, R. E., & Bailey, W. (1997). Lateral extrusion in transpression zones: the importance of boundary conditions. *Journal of Structural Geology*, 19(9), 1201-1217. [https://doi.org/10.1016/S0191-8141\(97\)00034-5](https://doi.org/10.1016/S0191-8141(97)00034-5)

Kohlstedt, D. L., Evans, B., & Mackwell, S. J. (1995). Strength of the lithosphere: Constraints imposed by laboratory experiments. *Journal of Geophysical Research: Solid Earth*, 100(B9), 17587-17602.

<https://doi.org/10.1029/95JB01460>

Kronenberg, A. K., Kirby, S. H., & Pinkston, J. (1990). Basal slip and mechanical anisotropy of biotite. *Journal of Geophysical Research: Solid Earth*, 95(B12), 19257-19278. <https://doi.org/10.1029/JB095iB12p19257>

Kronenberg, A. K., Kirby, S. H., & Pinkston, J. (1990). Basal slip and mechanical anisotropy of biotite. *Journal of Geophysical Research: Solid Earth*, 95(B12), 19257-19278. <https://doi.org/10.1029/JB095iB12p19257>

La Tour, T. E., 1981. Significance of folds and mylonites at the Grenville Front in Ontario: Summary. *Geological Society of America Bulletin* 92 (7), 411-413.

- Lebensohn, R. A., & Tomé, C. N. (1993). A self-consistent anisotropic approach for the simulation of plastic deformation and texture development of polycrystals: application to zirconium alloys. *Acta metallurgica et materialia*, 41(9), 2611-2624. [https://doi.org/10.1016/0956-7151\(93\)90130-K](https://doi.org/10.1016/0956-7151(93)90130-K).
- Li, C. (2012). An Investigation of Deformation Structures and Their Tectonic Significance Across the Grenville Front Tectonic Zone in the Vicinity of Sudbury, Ontario, Canada. *Electronic Thesis and Dissertation Repository*. Paper 464.
- Lin, S., Jiang, D., & Williams, P. F. (1998). Transpression (or transtension) zones of triclinic symmetry: natural example and theoretical modelling. *Geological Society, London, Special Publications*, 135(1), 41-57. <https://doi.org/10.1144/GSL.SP.1998.135.01.04>
- Lu, L. X., & Jiang, D. (2019). Quartz Flow Law Revisited: The Significance of Pressure Dependence of the Activation Enthalpy. *Journal of Geophysical Research: Solid Earth*, 124(1), 241-256. <https://doi.org/10.1029/2018JB016226>
- Meng, Q. R., & Zhang, G. W. (2000). Geologic framework and tectonic evolution of the Qinling orogen, central China. *Tectonophysics*, 323(3-4), 183-196. [https://doi.org/10.1016/S0040-1951\(00\)00106-2](https://doi.org/10.1016/S0040-1951(00)00106-2)
- Mercier, S., & Molinari, A. (2009). Homogenization of elastic–viscoplastic heterogeneous materials: Self-consistent and Mori-Tanaka schemes. *International Journal of Plasticity*, 25(6), 1024-1048. <https://doi.org/10.1016/j.ijplas.2008.08.006>
- Molinari, A., Canova, G. R., & Ahzi, S. (1987). A self-consistent approach of the large deformation polycrystal viscoplasticity. *Acta Metallurgica*, 35(12), 2983-2994. [https://doi.org/10.1016/0001-6160\(87\)90297-5](https://doi.org/10.1016/0001-6160(87)90297-5)

- Montési, L. G. (2013). Fabric development as the key for forming ductile shear zones and enabling plate tectonics. *Journal of Structural Geology*, 50, 254-266.  
<https://doi.org/10.1016/j.jsg.2012.12.011>
- Mori, T., & Tanaka, K. (1973). Average stress in matrix and average elastic energy of materials with misfitting inclusions. *Acta metallurgica*, 21(5), 571-574.  
[https://doi.org/10.1016/0001-6160\(73\)90064-3](https://doi.org/10.1016/0001-6160(73)90064-3)
- Mount, V. S., & Suppe, J. (1987). State of stress near the San Andreas fault: Implications for wrench tectonics. *Geology*, 15(12), 1143-1146. [https://doi.org/10.1130/0091-7613\(1987\)15<1143:SOSNTS>2.0.CO;2](https://doi.org/10.1130/0091-7613(1987)15<1143:SOSNTS>2.0.CO;2)
- Wynne-Edwards, H. R., 1972. The Grenville Province. In: Price, R. A., Douglas, R. J. W. (Eds.), Variations in tectonic styles in Canada. Geological Association of Canada Special Paper, 11, 263-334.
- Passchier, C. W., & Trouw, R. A. (2005). *Microtectonics*. Springer Science & Business Media.
- Passchier, C. W. (1998). Monoclinic model shear zones. *Journal of Structural Geology*, 20(8), 1121-1137. [https://doi.org/10.1016/S0191-8141\(98\)00046-7](https://doi.org/10.1016/S0191-8141(98)00046-7)
- Poirier, J. P. (1980). Shear localization and shear instability in materials in the ductile field. *Journal of Structural Geology*, 2(1-2), 135-142.  
[https://doi.org/10.1016/0191-8141\(80\)90043-7](https://doi.org/10.1016/0191-8141(80)90043-7)
- Ramberg, H. (1975). Particle paths, displacement and progressive strain applicable to rocks. *Tectonophysics*, 28(1-2), 1-37. [https://doi.org/10.1016/0040-1951\(75\)90058-X](https://doi.org/10.1016/0040-1951(75)90058-X)
- Ramsay, J. G., & Graham, R. H. (1970). Strain variation in shear belts. *Canadian Journal of Earth Sciences*, 7(3), 786-813. <https://doi.org/10.1139/e70-078>

- Ranalli, G. (1987). *Rheology of the Earth: Deformation and Flow Processes in Geophysics and Geodynamics*. Boston: Allen & Unwin.
- Rivers, T., 2008. Assembly and preservation of lower, mid, and upper orogenic crust in the Grenville Province—Implications for the evolution of large hot long-duration orogens. *Precambrian Research* 167, 237-259.  
<https://doi.org/10.1016/j.precamres.2008.08.005>
- Robin, P. Y. F., & Cruden, A. R. (1994). Strain and vorticity patterns in ideally ductile transpression zones. *Journal of Structural Geology*, 16(4), 447-466.  
[https://doi.org/10.1016/0191-8141\(94\)90090-6](https://doi.org/10.1016/0191-8141(94)90090-6)
- Sanderson, D. J., & Marchini, W. R. D. (1984). Transpression. *Journal of Structural Geology*, 6(5), 449-458. [https://doi.org/10.1016/0191-8141\(84\)90058-0](https://doi.org/10.1016/0191-8141(84)90058-0)
- Schwerdtner, W. M. (1989). The solid-body tilt of deformed paleohorizontal planes: application to an Archean transpression zone, southern Canadian Shield. *Journal of Structural Geology*, 11(8), 1021-1027. [https://doi.org/10.1016/0191-8141\(89\)90052-7](https://doi.org/10.1016/0191-8141(89)90052-7)
- Shea, W. T., & Kronenberg, A. K. (1993). Strength and anisotropy of foliated rocks with varied mica contents. *Journal of Structural Geology*, 15(9–10), 1097–1121.  
[https://doi.org/10.1016/0191-8141\(93\)90158-7](https://doi.org/10.1016/0191-8141(93)90158-7)
- Simpson, C., & De Paor, D. G. (1993). Strain and kinematic analysis in general shear zones. *Journal of Structural Geology*, 15(1), 1-20. [https://doi.org/10.1016/0191-8141\(93\)90075-L](https://doi.org/10.1016/0191-8141(93)90075-L)
- Stipp, M., StuÈnitz, H., Heilbronner, R., & Schmid, S. M. (2002). The eastern Tonale fault zone: a ‘natural laboratory’ for crystal plastic deformation of quartz over a temperature range from 250 to 700 C. *Journal of Structural Geology*, 24(12), 1861-1884. [https://doi.org/10.1016/S0191-8141\(02\)00035-4](https://doi.org/10.1016/S0191-8141(02)00035-4)

- Teyssier, C., Tikoff, B., & Markley, M. (1995). Oblique plate motion and continental tectonics. *Geology*, 23(5), 447-450. [https://doi.org/10.1130/0091-7613\(1995\)023<0447:OPMACT>2.3.CO;2](https://doi.org/10.1130/0091-7613(1995)023<0447:OPMACT>2.3.CO;2)
- Tikoff, B., & Teyssier, C. (1994). Strain modeling of displacement-field partitioning in transpressional orogens. *Journal of Structural Geology*, 16(11), 1575-1588. [https://doi.org/10.1016/0191-8141\(94\)90034-5](https://doi.org/10.1016/0191-8141(94)90034-5)
- Titus, S. J., Dyson, M., DeMets, C., Tikoff, B., Rolandone, F., & Bürgmann, R. (2011). Geologic versus geodetic deformation adjacent to the San Andreas fault, central California. *Geological Society of America Bulletin*, 123(5-6), 794-820. <https://doi.org/10.1130/B30150.1>
- Tommasi, A., & Vauchez, A. (2001). Continental rifting parallel to ancient collisional belts: an effect of the mechanical anisotropy of the lithospheric mantle. *Earth and Planetary Science Letters*, 185(1), 199-210. [https://doi.org/10.1016/S0012-821X\(00\)00350-2](https://doi.org/10.1016/S0012-821X(00)00350-2)
- Townend, J., & Zoback, M. D. (2004). Regional tectonic stress near the San Andreas fault in central and southern California. *Geophysical Research Letters*, 31(15). <https://doi.org/10.1029/2003GL018918>
- Tullis, J. (2002). Deformation of Granitic Rocks: Experimental Studies and Natural Examples. *Reviews in Mineralogy and Geochemistry*, 51(1), 51-95. <https://doi.org/10.2138/gsrmg.51.1.51>
- Tullis, J., & Wenk, H. R. (1994). Effect of muscovite on the strength and lattice preferred orientations of experimentally deformed quartz aggregates. *Materials Science and Engineering: A*, 175(1-2), 209-220. [https://doi.org/10.1016/0921-5093\(94\)91060-X](https://doi.org/10.1016/0921-5093(94)91060-X)
- Twiss, R. J., & Moores, E. M. (2007). *Structural Geology*. © WH Freeman and Company.



- Vauchez, A., & Tommasi, A. (2003). Wrench faults down to the asthenosphere: Geological and geophysical evidence and thermomechanical effects. *Geological Society, London, Special Publications*, 210(1), 15-34.  
<https://doi.org/10.1144/GSL.SP.2003.210.01.02>
- Vauchez, A., Tommasi, A., & Barruol, G. (1998). Rheological heterogeneity, mechanical anisotropy and deformation of the continental lithosphere. *Tectonophysics*, 296(1), 61-86. [https://doi.org/10.1016/S0040-1951\(98\)00137-1](https://doi.org/10.1016/S0040-1951(98)00137-1)
- Zoback, M. D., Zoback, M. L., Mount, V. S., Suppe, J., Eaton, J. P., Healy, J. H., ... & Wong, I. G. (1987). New evidence on the state of stress of the San Andreas fault system. *Science*, 238(4830), 1105-1111.  
<https://doi.org/10.1126/science.238.4830.1105>

## Chapter 4

### 4 Quartz Flow Law Revisited: The Significance of Pressure Dependence of the Activation Enthalpy

#### 4.1 Introduction

Earth's lithosphere deforms elastically and by frictional slip on preexisting fractures and discontinuities near the surface. At greater depth, with increasing temperature and pressure, the lithosphere deforms predominantly by crystalline plasticity (Nicolas and Poirier, 1976; Sibson, 1977; Brace and Kohlstedt, 1980; Kohlstedt et al., 1995; Mackwell et al., 1998; Jackson, 2002; Burov, 2011). Although still with a considerable degree of uncertainty, our current understanding of the rheology of the ductile lithosphere is based on laboratory high-temperature and high-pressure creep experiments on natural rocks or synthetic silicate aggregates (e.g., Heard and Carter, 1968; Chopra and Paterson, 1981; Shelton and Tullis, 1981; Caristan, 1982; Kirby and Kronenberg, 1984; Karato et al., 1986; Wilks and Carter, 1990; Hirth and Tullis, 1992; Luan and Paterson, 1992; Gleason and Tullis, 1995; Mackwell et al., 1998; Karato and Jung, 2003; Rybacki and Dresen, 2004; Rybacki et al., 2006). The experimental data are commonly fitted into a power-law relationship between strain rate and differential stress, referred to as a *flow law* (Dorn, 1955; Sherby and Burke, 1968; Ashby, 1972; Kirby and Raleigh, 1973; Frost and Ashby, 1982; Ranalli, 1987). For the dislocation creep of a polycrystal aggregate, the traditional flow law (referred to as flow law 1 below) is:

$$\dot{\epsilon} = \mathbb{A} \exp\left(-\frac{\mathbb{Q}}{RT}\right) \sigma^{\mathbb{m}} \quad (4.1)$$

where  $\dot{\epsilon}$  is the strain rate,  $\mathbb{A}$  the pre-exponential parameter,  $\mathbb{Q}$  the activation energy,  $R$  the universal gas constant,  $T$  the absolute temperature,  $\sigma$  the differential stress, and  $\mathbb{m}$  the stress exponent. The parameters ( $\mathbb{A}$ ,  $\mathbb{Q}$ , and  $\mathbb{m}$ ) are determined from laboratory deformation experiments. So far, great efforts have been made to determine flow law parameters for many rock types and monophase aggregates and the results have been used in the construction of the yield strength envelope (YSE) of the lithosphere (Brace and Kohlstedt, 1980; Kirby, 1983; Kohlstedt et al., 1995; Mackwell et al., 1998; Burov,

2011) and in geodynamic modeling on different scales and under different geological settings (e.g., Goetze and Evans, 1979; Ranalli, 1987; Beaumont et al., 2004; Jamieson et al., 2004; Wightman et al., 2006; Karato, 2008; Hudleston and Treagus, 2010; Schmalholz and Fletcher, 2011; Schmalholz and Schmid, 2012; Farla et al., 2013; Montési, 2013; Behr and Platt, 2014). Unfortunately, a major problem with using flow laws is that different experiments on a similar type of rock (such as quartzite) may yield significantly varied flow law parameters, leading to great uncertainties for the strength of the lithosphere based on that rock type (Burov and Diament, 1995; Maggi et al., 2000; Jackson, 2002; Watts and Burov, 2003; Burov and Watts, 2006). For instance, a flow law of quartz aggregates is commonly used to represent the rheology of the continental crust (Kohlstedt et al., 1995; Behr and Platt, 2014) in recognition that quartz is a common and possibly strength-controlling mineral, although the role of other phases like mica may also be significant (Kronenberg et al., 1990; Shea and Kronenberg, 1993; Tullis and Wenk, 1994; Tullis, 2002; Holyoke and Tullis, 2006; Montési, 2013). Fig.4.1 plots the YSE based on flow law 1 for quartz with parameters determined from different experiments. The crustal strength (differential stress) predicted by these quartz flow laws can vary by more than an order of magnitude.

A major cause of the difference in quartz flow law parameters is recognized to be ‘hydrolytic weakening’ (Griggs and Blacic, 1964, 1965; Griggs, 1967). Hydrolytic weakening has also been firmly established for many other silicate minerals including olivine and feldspar (e.g., Tullis and Yund, 1980; Mei and Kohlstedt, 2000; Rybacki et al., 2006; Karato, 2008). But despite a large number of experiments, the precise mechanism of ‘hydrolytic weakening’ on quartz creep is still not fully understood (Jaoul et al., 1984; Kronenberg and Tullis, 1984; Ord and Hobbs, 1986; Koch et al., 1989; Paterson, 1989; Tullis and Yund, 1989; Kronenberg, 1994; Post et al., 1996; Chernak et al., 2009; Holyoke and Kronenberg, 2013). Progress has been made rather phenomenologically by incorporating a water fugacity term to flow law 1 to get the following expression (e.g., Paterson, 1989; Kohlstedt et al., 1995; Post et al., 1996) which will be referred to as flow law 2 in this chapter:

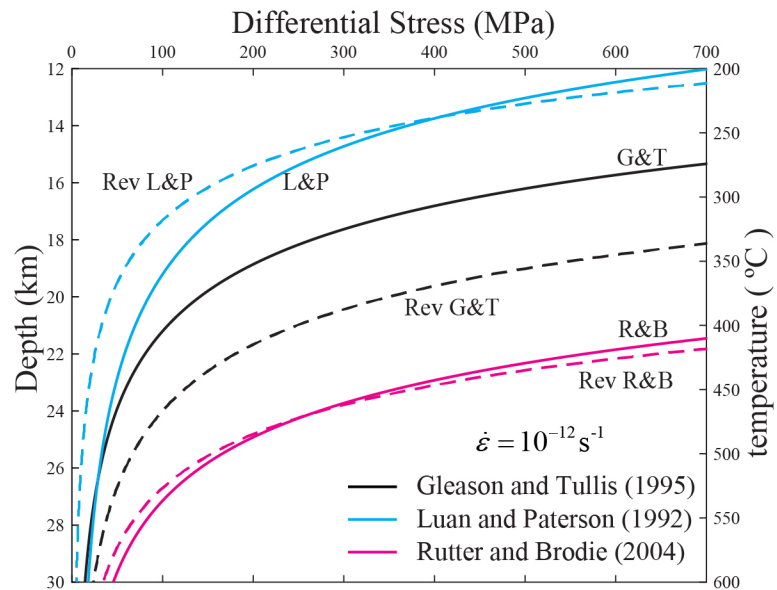


**Figure 4.1 Yield Strength Envelopes (YSE) for a wet quartzite crust based on flow laws with parameters derived from various experiments**

**A geothermal gradient of 20°C/km and a strain rate of  $10^{-12} \text{ s}^{-1}$  are used. G&T: Gleason and Tullis (1995), L&P: Luan and Paterson (1992), R&B: Rutter and Brodie (2004). Solid lines are based on flow law 1. Dashed lines are based on flow law 2. The Rev G&T and Rev L&P are based on Fukuda and Shimizu, (2017). Significant discrepancies exist among different experiments.**

$$\dot{\epsilon} = A' f_w^m \exp\left(-\frac{Q}{RT}\right) \sigma^m \quad (4.2)$$

where  $f_w$  is the water fugacity and  $m$  the water fugacity exponent. This approach simply replaces the pre-exponential term,  $A$ , in flow law 1, by a power-law term of the water fugacity, i.e.  $A = A' f_w^m$  (Kohlstedt et al., 1995; Rutter and Brodie, 2004; Fukuda and Shimizu, 2017). The water fugacity in an experimental run can be determined using the state equation of water (Pitzer and Sterner, 1994) when the partial pressure of water is known. Many attempts have been made to determine  $m$  (Gleason and Tullis, 1995; Kohlstedt et al., 1995; Post et al., 1996; Chernak et al., 2009; Holyoke and Kronenberg, 2013). Kohlstedt et al. (1995) argued that consideration of  $f_w$  with flow law 2 could explain the difference between the flow law of Gleason and Tullis (1995) for Black Hill quartzites and that of Luan and Paterson (1992) for silicic acid origin synthetic specimens. However, this argument is valid only if the effect on flow law due to  $Q$  difference between Gleason and Tullis (1995) and Luan and Paterson (1992) is insignificant compared to the effect of  $f_w$ . This is not the case except for the high temperature conditions considered by Kohlstedt et al. (1995, their Fig.5). As Kohlstedt et al. themselves (1995, their Fig.9) showed, when extrapolated to lower temperature conditions, the difference between the flow laws of Gleason and Tullis (1995) and Luan and Paterson (1992) remains significant even when  $f_w$  is incorporated (Fig.4.2). This is because the exponential term in which  $Q$  occurs,  $\exp\left(-\frac{Q}{RT}\right)$ , has a big effect on the

flow law. The effect due to a difference in  $Q$  can be expressed as

$$\frac{\delta \left[ \exp\left(-\frac{Q}{RT}\right) \right]}{\exp\left(-\frac{Q}{RT}\right)} = -\frac{\delta Q}{RT}. \text{ At extremely high temperatures, such as that considered by}$$

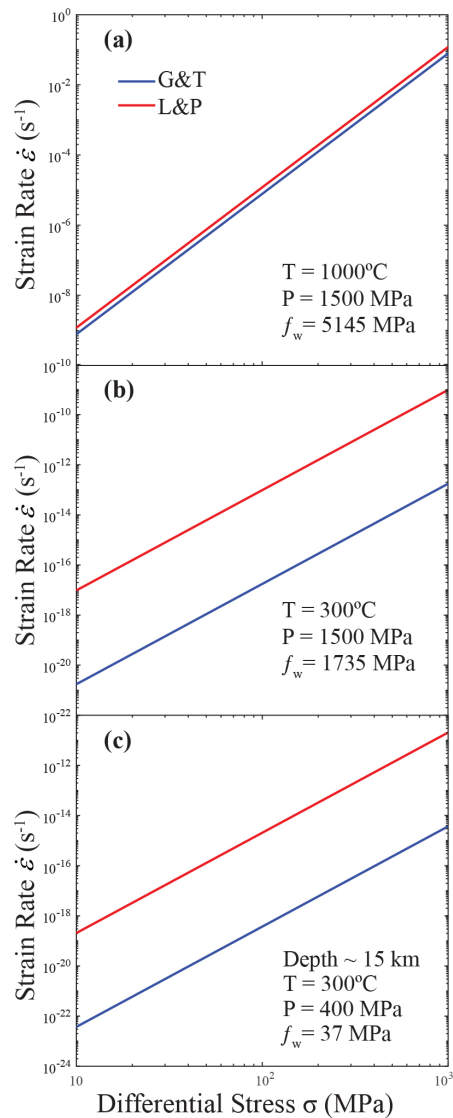


**Figure 4.2 Plot of strain rate versus differential stress for wet quartzite**

**a):** The plot of Kohlstedt et al. (1995) at a temperature of 1000°C and under 1500 MPa confining pressure, showing ‘stunning’ consistency between Gleason and Tullis (1995) and Luan and Paterson (1992) in terms of flow law 2. A water fugacity exponent of 1 was used. **b):** The plot at a temperature of 300°C under 1500 MPa. **c):** The same plot at 300°C and 400 MPa. It is clear that the consistency between the two experiments disappears at low-temperature conditions.

Kohlstedt et al. (1995),  $-\frac{\delta Q}{RT} \rightarrow 0$  leading to  $\frac{\delta \left[ \exp\left(-\frac{Q}{RT}\right) \right]}{\exp\left(-\frac{Q}{RT}\right)} \approx 0$ . At lower

temperatures however,  $\frac{|\delta Q|}{RT}$  is larger and the difference  $\delta Q$  results in a more significant discrepancy in the flow laws with parameters derived from different experiments (Fig.4.1).

The  $Q$  values determined from experiments are indeed quite different with  $Q = 152$  kJ/mol in Luan and Paterson (1992),  $Q = 223$  kJ/mol in Gleason and Tullis (1995), and  $Q = 242$  kJ/mol in Rutter and Brodie (2004). Fukuda and Shimizu (2017) attribute this difference to the activation of different dislocation slip systems. While it is plausible that each slip system has a unique activation energy, as many slip systems have been active in any one of these experiments the  $Q$  value in the flow law must be related to all active slip systems. As there is no evidence supporting any systematic difference in the activated slip systems among these experiments, we are unconvinced by the explanation of Fukuda and Shimizu (2017). The experimental runs of Gleason and Tullis (1995) were under 1.5 GPa confining pressure, 1.2 GPa higher than the experimental runs of Luan and Paterson (1992) and Rutter and Brodie (2004). We suspect that the pressure effect through the activation volume may be responsible for the observed differences in  $Q$  and the variations in quartz flow law. To account for this effect, the appropriate flow law is of the following form (Sherby et al., 1970; Frost and Ashby, 1982), called flow law 3 in this paper:

$$\dot{\epsilon} = Af_w^m \exp\left(-\frac{Q+PV}{RT}\right) \sigma^n \quad (4.3)$$

where  $V$ ,  $Q$ ,  $P$ , are respectively the activation volume, the activation energy, and the pressure. The  $Q + PV$  term is collectively the activation enthalpy  $H (= Q + PV)$ . Note the different fonts used in flow law 3 from those used in flow laws 1 and 2 are intentional, as

$A$ ,  $Q$ ,  $m$ ,  $A'$  and  $m$  in flow laws 1 and 2, and  $A$ ,  $Q$ ,  $V$ ,  $m$ , and  $n$  in flow law 3 may be distinct quantities (see below).

It is commonly assumed that, for deformation in the crust, the  $PV$  term is negligible because the pressure is relatively low and hence  $Q \approx H$  is justified (as in flow laws 1 and 2). However, the big difference in confining pressure used in different experiments means that, even for a rather modest estimate of the activation volume, say  $V = 15 \text{ cm}^3/\text{mol}$  (for comparison, the activation volumes for olivine is  $14 \sim 24 \text{ cm}^3/\text{mol}$ , Karato and Jung, 2003, and  $24 \sim 38 \text{ cm}^3/\text{mol}$  for anorthite, Rybacki et al., 2006), the  $PV$  term in flow law 3 may account for over 10% variation in  $Q$ , which could already explain the difference in  $Q$  between Gleason and Tullis (1995) and Luan and Paterson (1992).

In what follows, we critically re-examine published high-quality experimental data on quartz creep in terms of flow law 3 and refit the data from experimental runs that are interpreted to represent steady-state dislocation creep in regimes 2 and 3 (Hirth and Tullis, 1992). We obtain a consistent set of flow law parameters ( $A$ ,  $Q$ ,  $V$ ,  $m$ , and  $n$ ) and show that the apparent inconsistencies among existing experiments can be better explained. We compare our refined flow law with other studies and discuss its implications for continental lithosphere strength.

## 4.2 The choice of experimental data

### 4.2.1 Criteria of experimental data

There are many creep experiments on quartz aggregates. We mainly use the experimental data of Gleason and Tullis (1995) for Black Hill quartzite samples (the runs with no melt) and the data of Luan and Paterson (1992) for silicic acid origin synthetic specimens to constrain the parameters in terms of flow law 3. We also discuss the results of Rutter and Brodie (2004) for synthetic ultrafine-grained Brazilian quartzite. The reasons for our choice are as follows. First, the measurements of the differential stress must be accurate. Most experiments on quartz aggregates in the 1980s (Parrish et al., 1976; Kronenberg and Tullis, 1984; Koch et al., 1989) were carried out in Griggs-type deformation apparatus with solid-confining media. The strength of the solid-confining media used in these



experiments leads to overestimated strengths of quartz aggregates (Gleason and Tullis, 1993, 1995; Holyoke and Kronenberg, 2010). Even with the correction proposed by Holyoke and Kronenberg (2010), the flow stress values still have significant errors ( $\pm 30$  MPa). We also exclude the data of Stipp and Tullis (2003) because the flow stress, in their experiment, was taken as the average over a large strain interval and thus producing great errors ( $\pm 16 \sim \pm 40$  MPa). Second, for our purpose, we require that the data are collected in a steady-state creep regime. Phenomenologically, a steady-state creep regime must exhibit a flat stress-strain curve. In the dislocation climb accommodated regimes (regimes 2 and 3 of Hirth and Tullis, 1992), a steady-state flow is achieved by  $\sim 5\%$  strain under experimental conditions; however, in recrystallization accommodated regime (regime 1 of Hirth and Tullis, 1992), a steady-state flow requires that a steady-state microstructure of dynamically recrystallized grains is established, which is realized only at large strains. We do not use experimental runs (Parrish et al., 1976; Shelton and Tullis, 1981; Kronenberg and Tullis, 1984; Koch et al., 1989; Post et al., 1996; Holyoke and Kronenberg, 2013) which had not reached the steady-state flow by the end of deformation (some may even involve semi-brittle deformation). Finally, for the experimental runs that are used in this paper, we ensure that the samples were deformed by dislocation creep as much as we can possibly tell from the papers. Although other mechanisms are also important in nature, we are most concerned with a dislocation creep flow law that can be extrapolated to natural conditions. Stress-strain rate relations derived from mixed deformation mechanisms are more difficult to extrapolate to natural conditions. Experimental runs (e.g., silica gel origin specimens in Luan and Paterson, 1992; Rutter and Brodie, 2004) that are believed to contain a significant component of grain boundary sliding and its accommodating mechanisms are not used, although the dominant deformation mechanism is still believed to be dislocation creep.

#### 4.2.2 Description of selected experiments

Based on the criteria above, we mainly rely on Gleason and Tullis (1995), Luan and Paterson (1992), and Rutter and Brodie (2004). Each of these experiments is described briefly: Gleason and Tullis (1995) performed a creep experiment on the Black Hill

quartzites (BHQ) at  $\sim 1.5$  GPa confining pressure in the Griggs-type apparatus with the molten salt cell (MSC). BHQ is a natural quartzite with an average grain size of  $100 \mu\text{m}$ . The authors reported results for regimes 2 and 3 dislocation creep, where the steady-state flow was achieved under experimental conditions. Fitting the data to flow law 1, they obtained  $m = 4.0 \pm 0.9$ , and  $Q = 223 \pm 56$  kJ/mol. Holyoke and Kronenberg (2010) pointed out that the measured differential stresses in Griggs-type apparatus with MSC were greater than those measured in gas apparatus and suggested a correction to the differential stresses of Gleason and Tullis (1995) using a simple linear calibration ( $\sigma_{\text{Gas apparatus}} = 0.73 \times \sigma_{\text{GriggsMSC}} \pm 10 \text{MPa}$ ). This correction does not change the values of  $m$  and  $Q$  significantly but does change the pre-exponential parameter  $A$  from  $1.1 \times 10^{-4} \text{MPa}^{-m} \text{s}^{-1}$  to  $5.1 \times 10^{-4} \text{MPa}^{-m} \text{s}^{-1}$  (Holyoke and Kronenberg, 2010).

Luan and Paterson (1992) performed a creep experiment at 300 MPa confining pressure on three synthetic quartz aggregates made from hot-pressing techniques from natural quartz powder, precipitated silica gel, and silicic acid in gas-apparatus. Only data from their silicic acid origin specimens are used here because only these samples underwent steady-state dislocation creep. The silicic acid origin specimen has an average grain size of around  $20 \sim 30 \mu\text{m}$ . It contains a total water content less than 0.1 wt%, corresponding to a minimum specific volume of  $0.004 \text{m}^3 \text{kg}^{-1}$ , in an initial porosity of 1%, which gives a maximum pore pressure of around 150 MPa assuming the ideal-gas behavior of water. Considering that the porosity may have decreased during deformation due to the differential stress contribution to the pressure and the development of shape preferred orientations, the actual water pore pressure should be between 150 MPa and the ambient pressure. The microstructures show a strong crystallographic preferred orientation; however, the serrated grain boundaries and the recrystallized grains are rare. Therefore, we interpret the deformation mechanism to be dominated by regime 2 dislocation creep (Hirth and Tullis, 1992). The experimental runs on silicic acid origin specimens gave a value of  $4.0 \pm 0.8$  for  $m$ , and  $152 \pm 71$  kJ/mol for  $Q$ . For the stress exponent  $m$ , Luan and Paterson (1992) used data from ‘upward strain-rate stepping runs’ only, to ensure the use of steady-state results. Fukuda and Shimizu (2017) used *all* of Luan and Paterson (1992)

experimental runs (see Fukuda and Shimizu 2017, their Fig.A1) and obtained a lower value  $m \approx 3$ . In this paper, we adopt the value of  $m = 4.0 \pm 0.8$  reported by Luan and Paterson (1992) and do not consider Fukuda and Shimizu's (2017) recalculation because of concerns of their use of non-steady-state results. Results from natural quartz origin samples and silica gel origin samples in Luan and Paterson (1992) are not used because the natural quartz origin specimens deformed in a brittle-ductile transitional manner, characterized by the pronounced maximum in the stress-strain curve, or showed continuing strain hardening and the silica gel origin specimens contained a higher content of impurities and potential partial melting during the deformation, producing a great component of grain boundary sliding.

Rutter and Brodie (2004) performed a creep experiment on the synthetic ultrafine-grained quartzite prepared from clear Brazilian quartz powder with added water. The samples displayed rapid grain-growth to  $12 \sim 20 \mu\text{m}$  during hot-pressing at 1473 K and then were deformed in gas-apparatus at confining pressure of 300 MPa and temperature from 1273 K to 1473 K. The authors estimated that the water pore pressure was up to 300 MPa during compaction (see their Fig.3), assuming 0.6 wt% water absorbed in a final porosity of 1.25%. Transmission electron image of the interior of the grain showing well-developed dislocation creep microstructures indicates that the samples were deformed by intracrystalline dislocation creep. However, lower strain areas show rectangular grains with aligned grain boundaries suggesting an important component of grain boundary sliding although the deformation is dominated by intracrystalline dislocation creep. An empirical flow law was obtained with a lower value of  $2.97 \pm 0.29$  for  $m$ , and a rather higher  $Q$  of  $242 \pm 24 \text{ kJ/mol}$ . The authors also revised the pre-exponential parameter accordingly, using  $A = A' f_w^m$  and a value of 1 for  $m$  following Kohlstedt et al. (1995) and Hirth et al. (2001). Because there may be a great component of grain boundary sliding in the experiment of Rutter and Brodie (2004), we do not use their data to determine the parameters in flow law 3. However, we will discuss their results in Section 4.4.

The flow law parameters based on flow law 1 determined from these three sets of data are summarized in Table 4.1.

**Table 4.1 Experimentally determined flow law parameters reported by previous studies**

	$m$	$Q$ (kJ/mol)	$\ln A$ (MPa <sup>-<math>m</math></sup> ms <sup>-1</sup> )
Gleason and Tullis, (1995) (BHQ with no melt)	$4 \pm 0.9$	$223 \pm 56$	$-9.12 \pm 4.61$ $-7.58^a$
Luan and Paterson, (1992) (Silicic Acid origin)	$4 \pm 0.8$	$152 \pm 71$	$-18.24^b$
Rutter and Brodie, (2004) (Synthetic Ultrafine-grained quartzite)	$2.97 \pm 0.29$	$242 \pm 24$	$-5.64 \pm 0.90$ $-11.35^c$

<sup>a</sup> The pre-exponential parameter is corrected following the calibration of Holyoke and Kronenberg (2010).

<sup>b</sup> Luan and Paterson (1992) did not report the pre-exponential parameter. The pre-exponential parameter is calculated by substituting their stress exponent and activation energy into flow law 1. The averaged value is used here.

<sup>c</sup> The pre-exponential parameter is revised by assuming  $A = A' f_w^{mm}$  and  $mm = 1$ .

### 4.3 The determination of flow law parameters based on flow law 3

To determine  $n$  in flow law 3, constant  $T$ ,  $P$ , and  $f_w$  tests are required because

$$n = \left( \frac{\partial \ln \dot{\epsilon}}{\partial \ln \sigma} \right)_{T,P,f_w}. \text{ For the same set of samples used in a series of experimental runs, } f_w$$

itself is a function of  $P$  and  $T$  only. Therefore, constant  $P$  and  $T$  also implies constant  $f_w$

(i.e.,  $n = \left( \frac{\partial \ln \dot{\epsilon}}{\partial \ln \sigma} \right)_{T,P,f} = \left( \frac{\partial \ln \dot{\epsilon}}{\partial \ln \sigma} \right)_{T,P}$ ). As previous experiments were indeed carried out under constant  $T$  and  $P$  (Luan and Paterson, 1992; Gleason and Tullis, 1995), previously determined stress exponent  $m$  is, therefore, still valid in flow law 3. We thus adopt the stress exponent  $m = 4.0 \pm 0.9$  for the BHQ (Gleason and Tullis, 1995) and  $m = 4.0 \pm 0.8$  for the silicic acid origin sample (Luan and Paterson, 1992) because microstructures from these two sets of samples suggest they were deformed by steady-state regimes 2 and 3 dislocation creep.

To determine  $m$ , we first express  $m$  in terms of  $f_w$ ,  $\sigma$  and  $P$  by taking the natural logarithm of both sides of Eq.4.3 first and then taking the full derivative with respect to the variables  $f_w$ ,  $\sigma$ , and  $P$  to get:

$$m = -n \left( \frac{\partial \ln \sigma}{\partial \ln f_w} \right)_{T,\dot{\epsilon}} + \frac{V}{RT} \left( \frac{\partial P}{\partial \ln f_w} \right)_{T,\dot{\epsilon}} \quad (4.4)$$

Clearly,  $m$  and  $V$  are not independent. Because the evaluation of both  $\left( \frac{\partial \ln \sigma}{\partial \ln f_w} \right)_{T,\dot{\epsilon}}$  and

$\left( \frac{\partial P}{\partial \ln f_w} \right)_{T,\dot{\epsilon}}$  requires two experimental runs, a minimum of three sets of  $P$  and  $f_w$

stepping experimental runs at constant  $\dot{\epsilon}$  and  $T$  are required to solve  $m$  and  $V$  simultaneously with Eq.4.4. Because the experiments of Gleason and Tullis (1995) and Luan and Paterson (1992) were conducted under a constant  $P$ , and the data were collected over a  $f_w$  range too small to allow any accurate determination of  $m$  and  $V$ , we have to search for other  $P$  and  $f_w$  stepping experiments. We were able to identify three  $f_w$  stepping experimental runs on novaculite samples of Kronenberg and Tullis (1984). Although these experimental runs do not satisfy all the above criteria stated in Section 4.2, they are suitable for  $m$  and  $V$  determination as they were carried out under constant  $T$  and  $\dot{\epsilon}$  and over a large  $P$  range, equivalent to a large  $f_w$  range. The experimental runs of

Kronenberg and Tullis (1984) were carried in Griggs-type apparatus with solid-confining media from 820 MPa to 1590 MPa (see their Fig.3). The flow stresses are determined at 20% strain and have been corrected following the calibration of Holyoke and Kronenberg (2010) for solid salt (SSA) assemblies ( $\sigma_{\text{Gas apparatus}} = 0.73 \times \sigma_{\text{GriggsSSA}} - 48 \text{MPa} \pm 30 \text{MPa}$ ). Other  $f_w$  stepping experimental runs (Chernak et al., 2009; Holyoke and Kronenberg, 2013; Kronenberg and Tullis, 1984; Post et al., 1996) are excluded either because they involved semi-brittle deformation, or they did not achieve a steady-state flow by the end of the runs. We use the iterative linear regression method of Karato and Jung (2003) to solve for the values of  $m$  and  $V$ . The iteration starts with an initial guess of  $V$ . Plotting  $\left( \frac{PV}{RT} - n \ln \sigma \right)$  versus  $\ln f_w$  yields an initial  $m$ . By plotting  $\left( n \ln \sigma + m \ln f_w \right)$  versus  $P$ , using the initial  $m$ , the slope then gives an updated  $V$  which is used for the next round of iteration. The iteration continues until the current  $V$  and  $m$  coincide with their values in last round within a specific tolerance. With the three sets of data, we obtain  $m = 2.7$  and  $V = 35.3 \text{ cm}^3/\text{mol}$  (Fig.4.3). Because there are only three sets of data, the uncertainties with  $m$  and  $V$  cannot be determined. We will discuss this point in Section 4.4.

Once  $V$  is determined,  $Q$  can be determined by obtaining  $H$  first, using constant  $\sigma$ ,  $P$ ,  $f_w$ , and  $T$  stepping tests:

$$H = Q + PV = \frac{1}{R} \left( \frac{\partial \ln \dot{\epsilon}}{\partial (1/T)} \right)_{P, f_w, \sigma} \quad (4.5)$$

As past experiments (Luan and Paterson, 1992; Gleason and Tullis, 1995) were performed under constant  $\dot{\epsilon}$  and  $P$  and varying  $T$  conditions.  $\sigma$  and  $f_w$  were varied from one run to another with the varied  $T$ . To make use of the data collected from constant  $\dot{\epsilon}$  and  $P$  and  $T$  stepping runs, the constant-strain rate ( $\dot{\epsilon}_e$ ) is converted to a reference strain rate ( $\dot{\epsilon}_r$ ) corresponding to a common reference stress ( $\sigma_r$ ) and reference water fugacity ( $f_r$ ) using

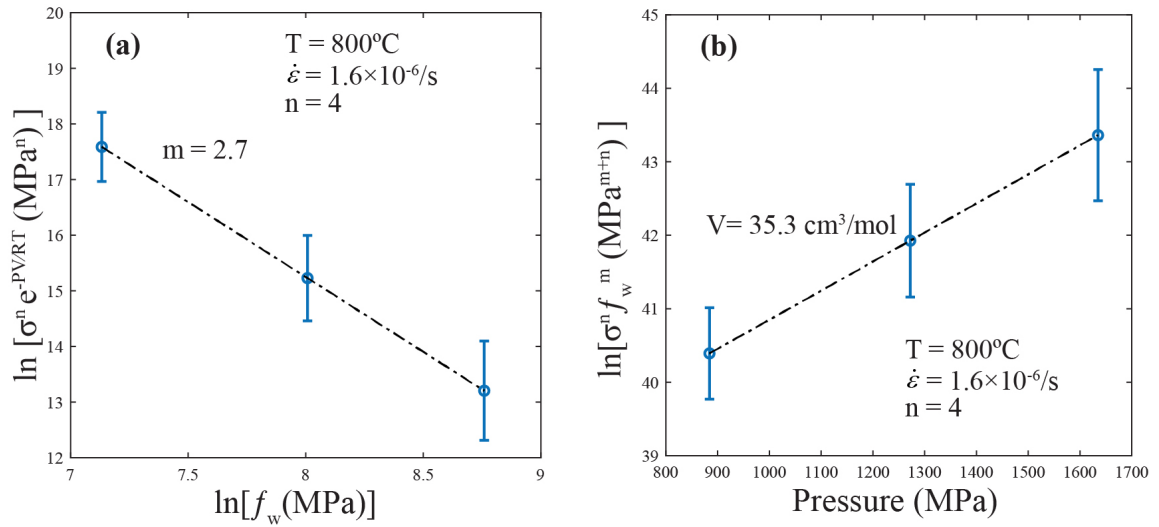


**Figure 4.3 Determination of the water fugacity exponent and the activation volume**

**a):** Plot of  $\ln\left(\sigma^n e^{-\frac{PV}{RT}}\right)$  versus  $\ln f_w$ . The slope gives  $m = 2.7$ . **b):** Plot of  $\ln(\sigma^n f_w^m)$

versus pressure. The slope gives the activation volume  $V = 35.3 \text{ cm}^3/\text{mol}$ . Data are from wet novaculite samples of Kronenberg and Tullis (1984). The  $m$  and  $V$  are determined by an iterative linear regression method (see text for more details).

$\dot{\epsilon} = \dot{\epsilon}_e \left( \frac{\sigma_r}{\sigma_e} \right)^n \left( \frac{f_r}{f_e} \right)^m$ , which is the form of flow law 3 normalized against a reference state.

Plotting the natural logarithm of the reference strain rate  $\ln \dot{\epsilon}_r$  versus  $1/T$ , the slope gives the value of  $H$ .

Luan and Paterson (1992) reported an initial water pore pressure of 150 MPa corresponding to a  $f_w$  of 144 MPa at 1300 K. Considering that the porosity likely decreases during deformation, the actual water pore pressure may be up to 400 MPa, if the contribution of the deviatoric stress to the pressure is considered (with  $P = P_{con} + \frac{\sigma_{diff}}{3}$ ). This implies that the maximum  $f_w$  may be up to 482 MPa at 1300 K. As no accurate measurement in water pore pressure is available, we use a water pore pressure of  $275 \pm 125$  MPa to calculate  $f_w$  for their test runs. Gleason and Tullis (1995) assumed that the water pore pressure is equal to the ambient pressure. We also make the correction to incorporate the deviatoric stress contribution to the ambient pressure.  $H$  is determined by linear regression for experimental results of Gleason and Tullis (1995) and Luan and Paterson (1992) (Fig.4.4). Assuming that the measurements in  $T$  and  $\dot{\epsilon}$  in Gleason and Tullis (1995) and Luan and Paterson (1992) are accurate (no errors of these measurements were provided in their papers), the uncertainty in  $H$  arises from the uncertainties in  $n$ ,  $\sigma$ ,  $f_w$ , and  $m$ , and can be expressed as

$$\delta H = RT \left( \ln \sigma \cdot \delta n + \frac{n}{\sigma} \cdot \delta \sigma + \ln f \cdot \delta m + \frac{m}{f} \cdot \delta f \right).$$

Since  $\delta m$  is unknown, the errors thus

represent a minimum estimate as  $\delta H \geq RT \left( \ln \sigma \cdot \delta n + \frac{n}{\sigma} \cdot \delta \sigma + \frac{m}{f} \cdot \delta f \right)$ . Using  $V = 35.3$

$\text{cm}^3/\text{mol}$  determined above, we obtain  $Q = 127$  kJ/mol for Gleason and Tullis (1995) and  $Q = 137$  kJ/mol for Luan and Paterson (1992), or  $Q = 132 \pm 5$  kJ/mol. Substituting the parameters  $n$ ,  $m$ ,  $V$  and  $Q$  into flow law 3, the pre-exponential parameter  $A$  is determined.



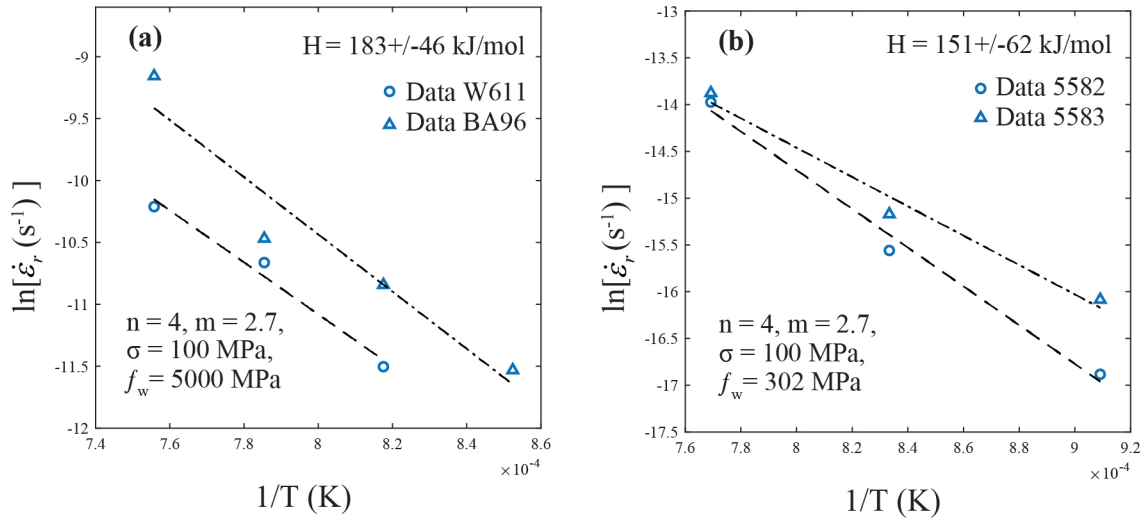


**Figure 4.4 Determination of the activation enthalpy**

Plot of  $\ln(\dot{\epsilon}_r)$  versus  $1/T$  to determine the activation enthalpy. a): Plot for data from samples W-611 and BA-96 of Gleason and Tullis (1995). The strain rates were calculated by converting experimental strain rates to those under a reference stress of 100 MPa and water fugacity of 5000 MPa using  $n = 4$  and  $m = 2.7$ . The converted strain rates are then plotted versus inverse absolute temperatures. The averaged activation enthalpy is  $H = 183 \pm 46 \text{ kJ/mol}$ . b): Plot for data from samples 5582 and 5583 of Luan and Paterson (1992). The reference stress was 100 MPa and reference water fugacity 302 MPa (corresponding to a pore pressure of 275 MPa and 1300 K). Stress and water fugacity exponents are the same as above. The averaged activation enthalpy is  $H = 151 \pm 62 \text{ kJ/mol}$ . The uncertainty in  $H$  represents a minimum estimate of  $\delta H$ , arising from the uncertainties in  $n$ ,  $\sigma$ , and  $f_w$ .

Using the data of Gleason and Tullis (1995) and Luan and Paterson (1992), we obtain the pre-exponential parameter  $A = (6.0 \pm 5.0) \times 10^{-15} \text{ MPa}^{-n-m} \text{ s}^{-1}$ . To summarize, we obtain a consistent flow law of the following:

$$\dot{\epsilon} = 6.0 \times 10^{-15} f_w^{2.7} \exp\left(-\frac{132000 + 35.3P}{RT}\right) \sigma^4 \quad (4.6)$$

where the  $f_w$ ,  $P$  and  $\sigma$  are in MPa.

#### 4.4 Remarks on flow law parameters

Gleason and Tullis (1995) and Luan and Paterson (1992) both obtained a similar stress exponent ( $m = 4.0 \pm 0.9$  and  $m = 4.0 \pm 0.8$  respectively) for regimes 2 and 3 dislocation creep. We have adopted this result as we justified above. Rutter and Brodie (2004) obtained a lower value of 2.97 for the ultrafine-grained synthetic quartzite. Luan and Paterson (1992) also got a lower  $m$  of 2.3 for their silica gel origin specimen. As Luan and Paterson (1992) and Rutter and Brodie (2004) both pointed out, these lower values are likely due to an important component of grain boundary sliding mechanism. Grain boundary sliding (GBS) must be associated with accommodating rate-controlling processes (Gifkins, 1976) including diffusion along grain boundaries ( $\dot{\epsilon} \propto \sigma$ , Frost and Ashby, 1982) and the dislocation movement localized near grain boundaries – the so-called ‘mantle’ ( $\dot{\epsilon} \propto \sigma^2$ , Mukherjee, 1971; Ashby and Verrall, 1973). Significant activity of such mechanisms is expected to cause a reduction of the overall stress exponent. As grain boundary sliding and its accommodating processes are sensitive to the grain size, the above interpretation is consistent with the ultrafine-grained synthetic quartzite (12 ~ 20  $\mu\text{m}$ ) of Rutter and Brodie (2004), for which a lower stress exponent (of 2.97) was obtained. However, the lower stress exponent (of 2.3) of Luan and Paterson (1992) was obtained for silica gel origin specimens with a larger average grain size around 80  $\mu\text{m}$ . Luan and Paterson (1992) attributed the lower stress exponent to the high impurity content in these specimens, which may have facilitated more grain boundary mechanisms.

Previous works (Gleason and Tullis, 1995; Kohlstedt et al., 1995; Post et al., 1996; Chernak et al., 2009; Holyoke and Kronenberg, 2013) have underestimated  $m$  because the activation volume  $V$  was not considered. Strictly speaking,  $m$  is not a constant as it also a continuous function of  $P$  and  $T$  (Eq.4.4). However, from 10 km depth to 30 km depth, the  $\frac{V}{RT} \left( \frac{\partial P}{\partial \ln f_w} \right)$  term decreases slightly from 1.95 to 1.79, assuming a thermal gradient of 20°C/km and  $V = 35.3 \text{ cm}^3/\text{mol}$ . Thus,  $m$  is practically a constant under such crustal P-T conditions.

We obtain  $V = 35.3 \text{ cm}^3/\text{mol}$  for wet quartzite based on three sets of experiment runs that are available. Future studies are needed to refine this value. However, this value is reasonable from a theoretical point of view. The rate of dislocation creep is ultimately diffusion controlled. The total activation volume is the sum of the activation volume for point defect formation ( $V_f$ ) and that for point defect migration ( $V_m$ ) corresponding locally to shearing or dilatation. They can be related to the pressure dependence of the melting temperature  $T_m$ , the activation energy  $Q$ , the Young's modulus  $E$ , bulk modulus  $K$ , and shear modulus  $G$  and their pressure sensitivity by (Béjina et al., 2003):

$$V_f = \frac{Q}{T_m} \frac{dT_m}{dP}$$

$$V_m = E \left( \frac{1}{G} \frac{dG}{dP} - \frac{1}{K} \right) \text{ or } V_m = E \left( \frac{1}{K} \frac{dK}{dP} - \frac{1}{K} \right)$$

Using the pressure sensitivity of  $T_m$  for  $\beta$ -quartz given by Swamy et al. (1994) and  $Q = 132 \text{ kJ/mol}$  (this study), the activation volume for defect formation is estimated to be  $V_f \approx 18 \text{ cm}^3/\text{mol}$ . Using the elastic constants of natural quartz and their pressure derivatives of Heyliger et al. (2003), Ji et al. (2018), and Levy et al. (2000),  $V_m \approx 1 \sim 7 \text{ cm}^3/\text{mol}$ . Therefore, the activation volume for dry quartzite is around  $V \approx 19 \sim 25 \text{ cm}^3/\text{mol}$ . The activation volume for 'wet' quartzite is expected to be larger because of the contribution from the dissolution of OH in mineral structure (Karato and Jung, 2003). Thus, the

estimated  $V = 35.3 \text{ cm}^3/\text{mol}$  is reasonable for ‘wet’ quartzite. In addition, our estimate is also consistent with the activation volumes of other silicate minerals. Karato and Jung (2003) reported an activation volume of  $14 \text{ cm}^3/\text{mol}$  and  $24 \text{ cm}^3/\text{mol}$  for ‘dry’ and ‘wet’ olivine respectively; Rybacki et al. (2006) reported an activation volume of  $24 \text{ cm}^3/\text{mol}$  and  $38 \text{ cm}^3/\text{mol}$  for the anorthite under ‘dry’ and ‘wet’ conditions. The uncertainty in  $V$  will also lead to an uncertainty in  $m$  (Fig.4.5). For instance, an uncertainty of  $\pm 10 \text{ cm}^3/\text{mol}$  in  $V$  will result in an uncertainty of  $\pm 0.5$  in  $m$ .

#### 4.5 Quartz flow law derived from natural strain rate and stress estimates

The great difference among flow law parameters from different experiments has motivated Hirth et al. (2001) to obtain a “better” set of flow law parameters from natural quartz-rich mylonites from the Ruby Gap duplex in terms of flow law 2. As their empirical flow law continues to be applied in many recent studies (e.g., Behr and Platt, 2011; 2014), we wish to comment on their approach.

Hirth et al. (2001) adopted a stress exponent  $n$  of 4. They regarded the difference in the pre-exponential term  $A$  (Table 4.1) between Luan and Paterson (1992) and Gleason and Tullis (1995) as being solely due to  $f_w$  variation between the two experiments, as Kohlstedt et al. (1995) have proposed. They then proceeded to determine  $n$  and  $A'$ . They disregarded experimentally-determined  $Q$  from Gleason and Tullis (1995) and Luan and Paterson (1992) and relied entirely on fitting strain rate and stress ( $\dot{\epsilon}$  and  $\sigma$ ) estimates from the Ruby Gap mylonites to determine  $Q$ . We show that the large uncertainties associated with such estimates mean that determining  $Q$  from them is not practical. Hirth et al. (2001) estimated  $\dot{\epsilon}$  of the natural mylonites from the Ruby Gap duplex by two methods. The first was to use a very rough estimate of the finite strain ( $\epsilon$ , Shimamoto and Ikeda, 1976; Fry, 1979) divided by the deformation time ( $t$ ) estimated from geochronology. This ignored the significant role of vorticity (the rotational component of the velocity field) history which determines the efficiency of finite strain accumulation (e.g., Means et al., 1980; Jiang 2010; Kuiper and Jiang, 2010). The finite strains in no

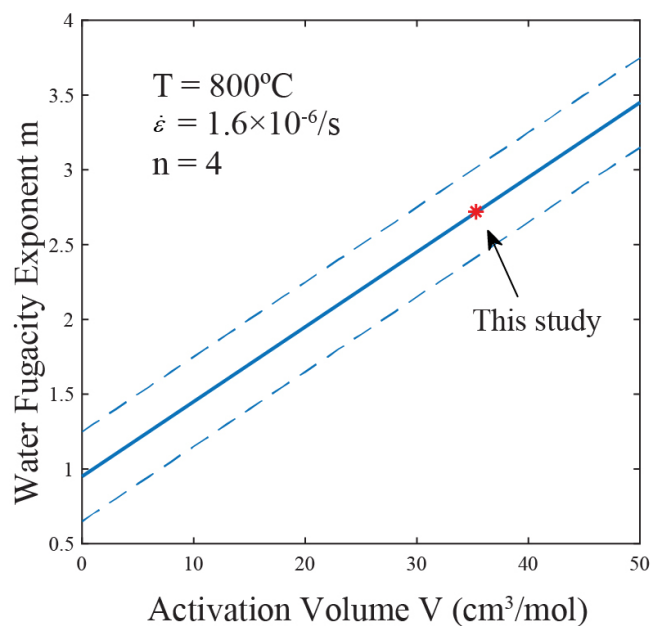


**Figure 4.5** Plot of water fugacity exponent versus activation volume

$V$  is parameterized in a range of  $0 \sim 50 \text{ cm}^3/\text{mol}$ .  $m$  increases with increasing  $V$ . The dashed lines represent the uncertainties in  $m$  arising from the uncertainties in  $n$  and  $\sigma$ . The red star represents our result of  $m = 2.7$  and  $V = 35.3 \text{ cm}^3/\text{mol}$ .

mylonites are known to have been produced by coaxial progressive deformations (zero vorticity) and assuming such a path will underestimate the strain rate by an unknown factor. The time  $t$  during which the mylonite zone was active is also hard to determine accurately as the authors themselves acknowledged. Based on geochronology, the Ruby Gap duplex deformation lasted  $\sim 30$  Ma, but the mylonite zone might have been active only for a portion of the entire deformation history.

The second method Hirth et al. (2001) used to estimate  $\dot{\epsilon}$  was to use  $\dot{\gamma} = \frac{v}{d}$ , where  $\dot{\gamma}$  is the average shear strain rate,  $v$  the boundary displacement rate and  $d$  the active thickness of the shear zone (e.g., Sibson, 1977; White and Mawer, 1991). They adopted a  $v = 1.5$  km/millions (1.5 mm/yr) which is an order of magnitude slower than other geological and current GPS observations on crustal scale zones (e.g., Sutherland et al., 2006; McGill et al., 2013 and below). They used the present total mylonite thickness (1–2 km) for  $d$ . But it is possible that the thickness of *active* deformation at any moment in the lifespan of the shear zone might have been only a fraction of the final thickness. Hirth et al. (2001) obtained  $\dot{\epsilon}$  of  $10^{-15} \sim 5 \times 10^{-14} \text{ s}^{-1}$  for the Ruby Gap duplex. Considering the above arguments, their  $\dot{\epsilon}$  is likely underestimated significantly. As we will show in the next section, many lines of evidence suggest that  $\dot{\epsilon}$  for natural shear zones are most likely in the range between  $10^{-13}$  to  $10^{-11} \text{ s}^{-1}$  and we believe the Ruby Gap duplex mylonites are not inconsistent with this range.

The  $\sigma$  estimate in Earth's lithosphere is also associated with large uncertainties. The recrystallized grainsize for the Ruby Gap duplex mylonites is between 20 and 40  $\mu\text{m}$ . This corresponds to a range of  $\sigma$  between 60 to 100 MPa based on the piezometer of Twiss (1977) according to Hirth et al. (2001). The same grainsize range would correspond to  $\sigma$  of 26 to 46 MPa based on the piezometer of Stipp and Tullis (2003) with a systematic correction following Holyoke and Kronenberg (2010). If one considers other piezometric formulations (e.g., Austin and Evans, 2007, 2009; Shimizu, 2008, 2012), the stress range is even larger as we will discuss in the next section.

Hirth et al. (2001) obtained  $Q = 135 \pm 15$  kJ/mol. If we consider the above ranges in strain rate ( $\dot{\epsilon} = 10^{-13} \sim 10^{-11} \text{ s}^{-1}$ ) and stress estimates ( $\sigma = 26 \sim 100 \text{ MPa}$ ), assume that the values of  $A'$  and  $m$  determined by Hirth et al. (2001) are accurate, and ignore any error in the temperature estimate, the range for  $Q$  will be from 77 to 125 kJ/mol.

The main point we try to make in this section is that estimates based on natural mylonites cannot be used to construct a more accurate flow law. Stress, strain rate, temperature and pressure conditions are far better constrained in high-quality experiments than in natural mylonites.

We have used a different approach in this paper. We rely on well-selected experimental sets and seek to explain the large discrepancy among experiments on the basis of more established understanding of the pressure effect on the crystalline plasticity of silicates (Karato and Jung, 2003; Rybacki et al., 2006; Karato, 2008). It is important to note that although both  $f_w$  and  $PV$  affect the flow law significantly through pressure, their effects are in opposite directions. For a given  $\dot{\epsilon}$ ,  $f_w$  increases with increasing pressure, thus causing a decrease in  $\sigma$ . In contrast, the term  $\exp\left(-\frac{Q+PV}{RT}\right)$  decreases with increasing pressure as  $V$  is always positive, which leads to an increase in  $\sigma$ . Therefore, both  $f_w$  and  $PV$  must be considered in a flow law (Eq.4.3). This leads to our flow law (Eq.4.6) which explains the large discrepancy in  $Q$  among experiments. Since the  $PV$  term is ignored in flow law 2, it is not possible to account for the observed differences in previous experiments by calibrating its parameters.

## 4.6 Quartz flow law and continental strength

To use the flow law determined in this study to consider the continental strength, one must first select a bulk  $\dot{\epsilon}$ . We first follow up the discussion on strain rate in the last section and give a general  $\dot{\epsilon}$  estimate based on natural data. Recent studies based on geology and GPS measurements have constrained the slip rate along the Alpine fault to be between 23 to 27 mm/yr (Norris and Cooper, 2000; Sutherland et al., 2006). The slip

rate along the San Andreas Fault is constrained between 5.7 to 35 mm/yr (Titus et al., 2005; Fialko, 2006; van Der Woerd et al., 2006; McGill et al., 2013; Heermance and Yule, 2017). The thicknesses of exhumed mylonites vary from 0.2 km to more than 3.5 km, but most mylonite zones are under 2 km (e.g., Davis et al., 1986; Schulz and Evans, 2000; Norris and Cooper, 2003; Brown et al., 2012). It is unclear if this thickness range that we observe today can represent the *active* thickness at the time of deformation. If it does and with the assumption that the GPS slip rate data represent long-term rates, then it gives a  $\dot{\epsilon}$  range for natural mylonites roughly between  $10^{-13}$  to  $10^{-11} \text{ s}^{-1}$ . The Global Strain Rate Map shows that the second invariants of  $\dot{\epsilon}$  estimated from geodetically determined surface velocity fields along major fault systems are around  $10^{-14} \text{ s}^{-1}$  (Kreemer et al., 2014), which is an estimate for the time-averaged bulk strain rate over an orogen. The  $\dot{\epsilon}$  of a localized high-strain zone within the *active* thickness during the *active* time is certainly higher than average (Fagereng and Biggs, 2018). Therefore, we regard the range between  $10^{-13}$  to  $10^{-11} \text{ s}^{-1}$  as a best representative of the strain rate in natural shear zones and will use  $10^{-12 \pm 1} \text{ s}^{-1}$  in our consideration of the continental strength below.

The strength profiles based on the wet quartz flow law determined in this paper and those of previous works (Luan and Paterson, 1992; Gleason and Tullis, 1995; Rutter and Brodie, 2004) are plotted in Fig.4.6 for a geothermal gradient of  $20^\circ\text{C}/\text{km}$  and a representative strain rate of  $10^{-12} \text{ s}^{-1}$ . We assume the water partial pressure equals to lithostatic pressure. The shaded region covers the strain rate range between  $10^{-13}$  to  $10^{-11} \text{ s}^{-1}$  for our flow law. Note the flow laws of Gleason and Tullis (1995) and Luan and Paterson (1992) are based on flow law 1 (Eq.4.1) without the fugacity term. We have also calculated the differential stresses, using various piezometers (Stipp and Tullis, 2003; Austin and Evans, 2007, 2009; Shimizu, 2008, 2012; Cross et al., 2017; Heilbronner and Kilian, 2017), for many natural zones using the data of Behr and Platt (2014) and Stipp et al. (2010) on quartz grain size, deformation pressure and temperature. The stress estimates vary greatly depending on piezometers adopted (Fig.4.6).



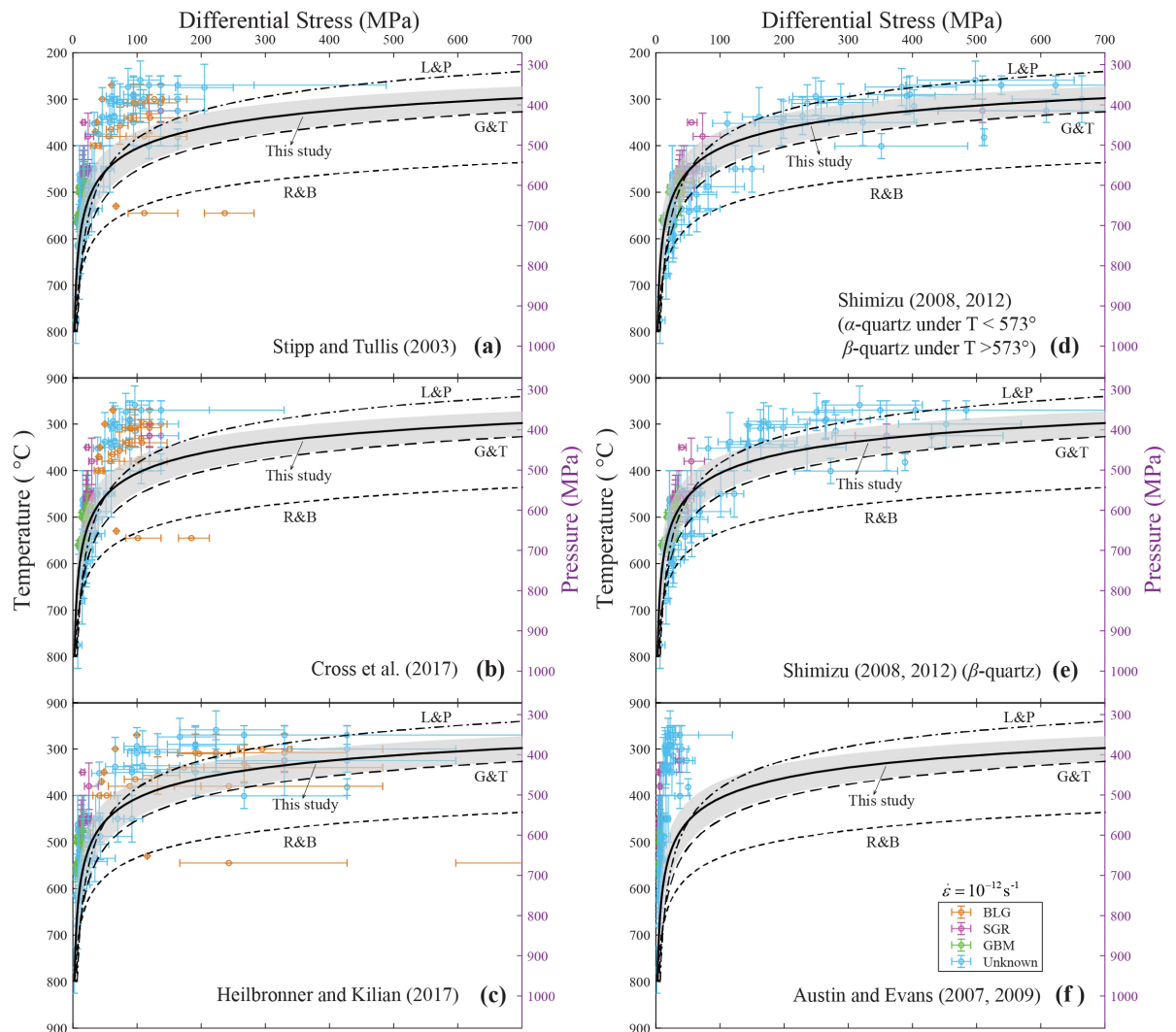


**Figure 4.6** The strength profile of our flow law compared with those based on other flow laws

A geothermal gradient of  $20^{\circ}\text{C}/\text{km}$  and strain rate of  $10^{-12}\text{s}^{-1}$  are used. The shaded region covers the strain rate range between  $10^{-13}$  to  $10^{-11}\text{s}^{-1}$  for our flow law. Estimated differential stresses and deformation pressure and temperature conditions of some natural mylonites are also plotted. The pressure and temperature data and the quartz grainsize distributions are from Behr and Platt (2014) and Stipp et al. (2010). We have calculated the differential stresses using different piezometric methods: (a) Stipp and Tullis (2003), (b) Cross et al. (2017), (c)

**Heilbronner and Kilian (2017), (d) Shimizu (2008, 2012) with  $\alpha$ - and  $\beta$ -quartz used respectively for low and high temperatures, (e) Shimizu (2008, 2012) for  $\beta$ -quartz, and (f) Austin and Evens (2007, 2009).**

The piezometric relation of Twiss (1977),  $d_s = B\sigma^{-\lambda}$ , where  $d_s$  is the average steady-state grain size,  $B$  and  $\lambda$  are empirically determined based on creep experiments (e.g., Christie et al., 1980 ; Mercier et al., 1977) has been widely applied on natural mylonites to infer the paleostress (e.g., White, 1979; Ord and Christie, 1984; Dunlap et al., 1997; Zulauf, 2001; Behr and Platt, 2011; Kidder et al., 2012). Stipp and Tullis (2003) did a careful laboratory calibration for this piezometric relation with coaxial compression experiments on BHQ in a Griggs apparatus with MSC. The grain size was analyzed using computer integrated polarization microscopy. Cross et al. (2017) used electron backscatter diffraction (EBSD) image to separate recrystallized grains from relict grains and further refined the piezometer of Stipp and Tullis (2003). The stress estimates based on Stipp and Tullis (2003) are plotted in Fig.4.6a and those based on Cross et al. (2017) in Fig.4.6b. In both Figs.6a and b, we have corrected the stress term of Stipp and Tullis (2003) and Cross et al. (2017) to account for the frictional effect of the confining medium following Holyoke and Kronenberg (2010). Stress estimates from Cross et al (2017) are slightly lower than those from Stipp and Tullis (2003). Heilbronner and Kilian (2017) conducted non-coaxial (general shear) experiments on BHQ in a Griggs apparatus with a solid-medium. They claimed that non-coaxial set up enabled accurate flow stress determination (Richter et al., 2016) and the EBSD imaging allowed more accurate recrystallized grain size measurement. The piezometer of Heilbronner and Kilian (2017) yields significantly higher stresses than the piezometer of Stipp and Tullis (2003) (Fig.4.6c).

Shimizu (2008, 2012) developed a piezometer for dynamically recrystallized grain size achieved by subgrain rotation and grain boundary migration mechanisms. At higher temperatures where  $\beta$ -quartz is appropriate, the stress estimates based on Shimizu's model agree well with the experiment data of Stipp and Tullis (2003). At lower temperatures where  $\alpha$ -quartz is applied, Shimizu's model yields considerably higher

stresses than the piezometer of Stipp and Tullis (2003). The stress estimates based on Shimizu (2008, 2012) with  $\alpha$ - and  $\beta$ -quartz used respectively for low and high temperatures are plotted in Fig.4.6d. As the creep experiments used in this paper are all in the  $\beta$ -quartz stability field, our flow law and other flow laws used in Fig.4.6 are strictly applicable for  $\beta$ -quartz. Furthermore, quartz piezometers have not always distinguished  $\alpha$ - and  $\beta$ -quartz. Therefore, there is additional uncertainty about how stress estimates based on Shimizu's  $\alpha$ -quartz model are interpreted. The stress estimates based on  $\beta$ -quartz, regardless of temperature, are plotted in Fig.4.6e.

Austin and Evans (2007, 2009) proposed the so-called “paleowattmeter” model, which considers the balance between grain size reduction and grain growth. The grain size reduction is driven by mechanical work done to the grain, and the rate of grain growth is assumed to follow the kinetic law of static grain growth. For quartz aggregates, the paleowattmeter predicts consistently lower stresses than other piezometers (Fig.4.6f). Note data associated with bulging recrystallization (BLG) are excluded in Figs.6d-f because the models of Shimizu (2008, 2012) and Austin and Evans (2007, 2009) do not apply to BLG.

The difference in stress estimates based on these piezometers is significant (Fig.4.6). We believe the predictions of paleowattmeter are too low (Fig.4.6f). Coaxial experiment calibrations (Stipp and Tullis, 2003; Cross et al., 2017) (Figs.4.6a and b) appear to generate stresses below flow law predictions for temperature below 500°C. The reason for the great difference between coaxial experiment calibration (Figs.4.6a and b) and non-coaxial (general shear) experiment calibration (Fig.4.6c) is yet to be clarified. It is possible the friction correction on stress for coaxial experiments is overdone. Stress estimates based on non-coaxial experiment calibrations (Heilbronner and Kilian, 2017) (Fig.4.6c) are in better agreement with our flow law prediction and also with the stress estimates based on Shimizu (2008, 2012) (Figs.4.6d and e). We are reluctant to draw any conclusion on the agreement between stress estimates and our flow law prediction in Figs.4.6c-e, because of uncertainties associated with piezometers and the choice of strain

rate. There are also uncertainties arising from the fact that natural samples were collected from regions with geothermal gradients varying from 10°C/km to 40°C/km or with unknown geothermal gradients. The geothermal gradient of 20°C/km used in Fig.4.6 is a simplification. Our purpose here is not to resolve the stress and strength of the crust, but to present our flow law in the context of current knowledge and uncertainties of continental strength in order to facilitate further investigation on the subject.

Furthermore, it is perhaps also an oversimplification to use a simple flow law of wet quartzite to represent the rheology of the continental lithosphere as the latter is composed of polyphase rocks whose overall rheology depends on the rheological properties of the constituents, their concentrations, and their geometric arrangement, all of which change during progressive deformation (e.g., Tullis, 2002; Montési, 2013; Jiang, 2014, 2016).

## 4.7 Conclusions

We have demonstrated that the pressure dependence of the activation enthalpy through the activation volume is the key to reconcile the great difference in flow laws derived from existing experiments.

We critically evaluated existing high-quality experimental data on quartz creep and used them to obtain a best-fit flow law for quartz aggregates under regime 2 and regime 3

dislocation creep:  $\dot{\epsilon} = 6.0 \times 10^{-15} f_w^{2.7} \exp\left(-\frac{132000 + 35.3P}{RT}\right) \sigma^4$ . The water fugacity

exponent and the activation volume are interrelated. The errors associated with them are unknown due to limited experiment data. The obtained active volume is comparable with other silicate minerals and reasonable from theoretical arguments. The new flow law can well explain the difference between previous flow laws with parameters determined in Gleason and Tullis (1995) and Luan and Paterson (1992).

Stress and strain rate estimates from natural mylonites have far greater uncertainties than well-controlled laboratory creep experiments. It is unrealistic to expect that such estimates can allow determination of flow law parameters better than well-controlled experiments.

Crustal scale ductile shear zones likely flow at a strain rate between  $10^{-13} \text{ s}^{-1}$  and  $10^{-11} \text{ s}^{-1}$  based on exhumed mylonite zone thickness and slip rates derived from geological and modern GPS observations. This strain rate range corresponds to a lithosphere strength profile which, based on our flow law, is broadly consistent with piezometric data based on Heilbronner and Kilian (2017) and Shimizu (2008, 2012).

## 4.8 References

- Ashby, M. F. (1972). A first report on deformation-mechanism maps. *Acta Metallurgica*, 20(7), 887-897. [https://doi.org/10.1016/0001-6160\(72\)90082-X](https://doi.org/10.1016/0001-6160(72)90082-X)
- Ashby, M. F., & Verrall, R. A. (1973). Diffusion-accommodated flow and superplasticity. *Acta Metallurgica*, 21(2), 149–163. [https://doi.org/10.1016/0001-6160\(73\)90057-6](https://doi.org/10.1016/0001-6160(73)90057-6)
- Austin, N., & Evans, B. (2007). Paleowattmeters: A scaling relation for dynamically recrystallized grain size. *Geology*, 35(4), 343. <https://doi.org/10.1130/G23244A.1>
- Austin, N., & Evans, B. (2009). The kinetics of microstructural evolution during deformation of calcite. *Journal of Geophysical Research: Solid Earth*, 114(B9). <https://doi.org/10.1029/2008JB006138>
- Beaumont, C., Jamieson, R. A., Nguyen, M. H., & Medvedev, S. (2004). Crustal channel flows: 1. Numerical models with applications to the tectonics of the Himalayan-Tibetan orogen. *Journal of Geophysical Research: Solid Earth*, 109(B6), 1–29. <https://doi.org/10.1029/2003JB002809>
- Behr, W. M., & Platt, J. P. (2011). A naturally constrained stress profile through the middle crust in an extensional terrane. *Earth and Planetary Science Letters*, 303(3–4), 181–192. <https://doi.org/10.1016/j.epsl.2010.11.044>
- Behr, W. M., & Platt, J. P. (2014). Brittle faults are weak, yet the ductile middle crust is strong: Implications for lithospheric mechanics. *Geophysical Research Letters*, 41(22), 8067–8075. <https://doi.org/10.1002/2014GL061349>
- Béjina, F., Jaoul, O., & Liebermann, R. C. (2003). Diffusion in minerals at high pressure: a review. *Physics of the Earth and Planetary Interiors*, 139(1–2), 3–20. [https://doi.org/10.1016/S0031-9201\(03\)00140-7](https://doi.org/10.1016/S0031-9201(03)00140-7)
- Brace, W. F., & Kohlstedt, D. L. (1980). Limits on lithospheric stress imposed by laboratory experiments. *Journal of Geophysical Research: Solid Earth*, 85(B11),

6248–6252. <https://doi.org/10.1029/JB085iB11p06248>

- Brown, S. R., Gibson, H. D., Andrews, G. D. M., Thorkelson, D. J., Marshall, D. D., Vervoort, J. D., & Rayner, N. (2012). New constraints on Eocene extension within the Canadian Cordillera and identification of Phanerozoic protoliths for footwall gneisses of the Okanagan Valley shear zone. *Lithosphere*, *4*(4), 354–377. <https://doi.org/10.1130/L199.1>
- Burov, E. B. (2011). Rheology and strength of the lithosphere. *Marine and Petroleum Geology*, *28*(8), 1402–1443. <https://doi.org/10.1016/j.marpetgeo.2011.05.008>
- Burov, E. B., & Diament, M. (1995). The effective elastic thickness ( $T_e$ ) of continental lithosphere: What does it really mean? *Journal of Geophysical Research: Solid Earth*, *100*(B3), 3905–3927. <https://doi.org/10.1029/94JB02770>
- Burov, E. B., & Watts, A. B. (2006). The long-term strength of continental lithosphere: “jelly sandwich” or “crème brûlée”? *GSA Today*, *16*(1), 4. [https://doi.org/10.1130/1052-5173\(2006\)016<4:TLTSOC>2.0.CO;2](https://doi.org/10.1130/1052-5173(2006)016<4:TLTSOC>2.0.CO;2)
- Caristan, Y. (1982). The transition from high temperature creep to fracture in Maryland diabase. *Journal of Geophysical Research: Solid Earth*, *87*(B8), 6781–6790. <https://doi.org/10.1029/JB087iB08p06781>
- Chernak, L. J., Hirth, G., Selverstone, J., & Tullis, J. (2009). Effect of aqueous and carbonic fluids on the dislocation creep strength of quartz. *Journal of Geophysical Research: Solid Earth*, *114*(B4). <https://doi.org/10.1029/2008JB005884>
- Christie, J. M., Ord, A., & Koch, P. S. (1980). Relationship between recrystallized grain size and flow stress in experimentally deformed quartzite. *Eos*, *61*, 377.
- Chopra, P. N., & Paterson, M. S. (1981). The experimental deformation of dunite. *Tectonophysics*, *78*(1–4), 453–473. [https://doi.org/10.1016/0040-1951\(81\)90024-X](https://doi.org/10.1016/0040-1951(81)90024-X)
- Cross, A. J., Prior, D. J., Stipp, M., & Kidder, S. (2017). The recrystallized grain size piezometer for quartz: An EBSD-based calibration. *Geophysical Research*

- Letters*, 44(13), 6667-6674. <https://doi.org/10.1002/2017GL073836>
- Davis, G. A., Lister, G. S., & Reynolds, S. J. (1986). Structural evolution of the Whipple and South mountains shear zones, southwestern United States. *Geology*, 14(1), 7–10. [https://doi.org/10.1130/0091-7613\(1986\)14<7:SEOTWA>2.0.CO;2](https://doi.org/10.1130/0091-7613(1986)14<7:SEOTWA>2.0.CO;2)
- Dorn, J. E. (1955). Some fundamental experiments on high temperature creep. *Journal of the Mechanics and Physics of Solids*, 3(2), 85–116. [https://doi.org/10.1016/0022-5096\(55\)90054-5](https://doi.org/10.1016/0022-5096(55)90054-5)
- Dunlap, W. J., Hirth, G., & Teyssier, C. (1997). Thermomechanical evolution of a ductile duplex. *Tectonics*, 16(6), 983-1000. <https://doi.org/10.1029/97TC00614>
- Fagereng, Å., & Biggs, J. (2018). New perspectives on ‘geological strain rates’ calculated from both naturally deformed and actively deforming rocks. *Journal of Structural Geology*. <https://doi.org/10.1016/j.jsg.2018.10.004>
- Farla, R. J. M., Karato, S. I., & Cai, Z. (2013). Role of orthopyroxene in rheological weakening of the lithosphere via dynamic recrystallization. *Proceedings of the National Academy of Sciences*, 110(41), 16355–16360. <https://doi.org/10.1073/pnas.1218335110>
- Fialko, Y. (2006). Interseismic strain accumulation and the earthquake potential on the southern San Andreas fault system. *Nature*, 441(7096), 968–971. <https://doi.org/10.1038/nature04797>
- Frost, H. J., & Ashby, M. F. (1982). *Deformation mechanism maps: the plasticity and creep of metals and ceramics*. Pergamon Press.
- Fry, N. (1979). Random point distributions and strain measurement in rocks. *Tectonophysics*, 60(1–2), 89–105. [https://doi.org/10.1016/0040-1951\(79\)90135-5](https://doi.org/10.1016/0040-1951(79)90135-5)
- Fukuda, J., & Shimizu, I. (2017). Theoretical derivation of flow laws for quartz dislocation creep: Comparisons with experimental creep data and extrapolation to natural conditions using water fugacity corrections. *Journal of Geophysical*



- Research: Solid Earth*, 122(8), 5956–5971. <https://doi.org/10.1002/2016JB013798>
- Gifkins, R. C. (1976). Grain-Boundary Sliding and its Accommodation During Creep and Superplasticity. *Metallurgical Transactions A*, 7A, 1225–1232.  
<https://doi.org/10.1007/BF02656607>
- Gleason, G. C., & Tullis, J. (1993). Improving flow laws and piezometers for quartz and feldspar aggregates. *Geophysical Research Letters*, 20(19), 2111–2114.  
<https://doi.org/10.1029/93GL02236>
- Gleason, G. C., & Tullis, J. (1995). A flow law for dislocation creep of quartz aggregates determined with the molten salt cell. *Tectonophysics*, 247(1–4), 1–23.  
[https://doi.org/10.1016/0040-1951\(95\)00011-B](https://doi.org/10.1016/0040-1951(95)00011-B)
- Goetze, C., & Evans, B. (1979). Stress and temperature in the bending lithosphere as constrained by experimental rock mechanics. *Geophysical Journal International*, 59(3), 463–478. <https://doi.org/10.1111/j.1365-246X.1979.tb02567.x>
- Griggs, D. (1967). Hydrolytic weakening of quartz and other silicates. *Geophysical Journal International*, 14(1–4), 19–31. <https://doi.org/10.1111/j.1365-246X.1967.tb06218.x>
- Griggs, D. T., & Blacic, J. D. (1964). The strength of quartz in the ductile regime. *EOS. Trans. Am. Geophys. Union*, 45, 102–103.
- Griggs, D. T., & Blacic, J. D. (1965). Quartz: Anomalous Weakness of Synthetic Crystals. *Science*, 147(3655), 292–295.  
<https://doi.org/10.1126/science.147.3655.292>
- Heard, H. C., & Carter, N. L. (1968). Experimentally induced “natural” intragranular flow in quartz and quartzite. *American Journal of Science*.  
<https://doi.org/10.2475/ajs.266.1.1>
- Heermance, R. V., & Yule, D. (2017). Holocene slip rates along the San Andreas Fault System in the San Geronio Pass and implications for large earthquakes in southern

- California. *Geophysical Research Letters*, 44(11), 5391–5400.  
<https://doi.org/10.1002/2017GL072612>
- Heilbronner, R., & Kilian, R. (2017). The grain size (s) of Black Hills Quartzite deformed in the dislocation creep regime. *Solid Earth*, 8(6). <https://doi.org/10.5194/se-8-1071-2017>
- Heyliger, P., Ledbetter, H., & Kim, S. (2003). Elastic constants of natural quartz. *The Journal of the Acoustical Society of America*, 114(2), 644–650.  
<https://doi.org/10.1121/1.1593063>
- Hirth, G., & Tullis, J. (1992). Dislocation creep regimes in quartz aggregates. *Journal of Structural Geology*, 14(2), 145–159. [https://doi.org/10.1016/0191-8141\(92\)90053-Y](https://doi.org/10.1016/0191-8141(92)90053-Y)
- Hirth, G., Teyssier, C., & Dunlap, J. W. (2001). An evaluation of quartzite flow laws based on comparisons between experimentally and naturally deformed rocks. *International Journal of Earth Sciences*, 90(1), 77–87.  
<https://doi.org/10.1007/s005310000152>
- Holyoke, C. W., & Kronenberg, A. K. (2010). Accurate differential stress measurement using the molten salt cell and solid salt assemblies in the Griggs apparatus with applications to strength, piezometers and rheology. *Tectonophysics*, 494(1–2), 17–31. <https://doi.org/10.1016/j.tecto.2010.08.001>
- Holyoke, C. W., & Kronenberg, A. K. (2013). Reversible water weakening of quartz. *Earth and Planetary Science Letters*, 374, 185–190.  
<https://doi.org/10.1016/j.epsl.2013.05.039>
- Holyoke, C. W., & Tullis, J. (2006). Mechanisms of weak phase interconnection and the effects of phase strength contrast on fabric development. *Journal of Structural Geology*, 28(4), 621–640. <https://doi.org/10.1016/j.jsg.2006.01.008>
- Hudleston, P. J., & Treagus, S. H. (2010). Information from folds: a review. *Journal of Structural Geology*, 32(12), 2042–2071. <https://doi.org/10.1016/j.jsg.2010.08.011>

- Jackson, J. (2002). Strength of the continental lithosphere: Time to abandon the jelly sandwich? *GSA Today*, 12(9), 4. [https://doi.org/10.1130/1052-5173\(2002\)012<0004:SOTCLT>2.0.CO;2](https://doi.org/10.1130/1052-5173(2002)012<0004:SOTCLT>2.0.CO;2)
- Jamieson, R. A., Beaumont, C., Medvedev, S., & Nguyen, M. H. (2004). Crustal channel flows: 2. Numerical models with implications for metamorphism in the Himalayan-Tibetan orogen. *Journal of Geophysical Research: Solid Earth*, 109(B6), 1–24. <https://doi.org/10.1029/2003JB002811>
- Jaoul, O., Tullis, J., & Kronenberg, A. (1984). The effect of varying water contents on the creep behavior of Heavtree quartzite. *Journal of Geophysical Research: Solid Earth*, 89(B6), 4298–4312. <https://doi.org/10.1029/JB089iB06p04298>
- Ji, S., Li, L., Motra, H. B., Wuttke, F., Sun, S., Michibayashi, K., & Salisbury, M. H. (2018). Poisson's Ratio and Auxetic Properties of Natural Rocks. *Journal of Geophysical Research: Solid Earth*, 123(2), 1161–1185. <https://doi.org/10.1002/2017JB014606>
- Jiang, D. (2010). Flow and finite deformation of surface elements in three dimensional homogeneous progressive deformations. *Tectonophysics*, 487(1–4), 85–99. <https://doi.org/10.1016/j.tecto.2010.03.011>
- Jiang, D. (2014). Structural geology meets micromechanics: A self-consistent model for the multiscale deformation and fabric development in Earth's ductile lithosphere. *Journal of Structural Geology*, 68, 247-272. <https://doi.org/10.1016/j.jsg.2014.05.020>
- Jiang, D. (2016). Viscous inclusions in anisotropic materials: Theoretical development and perspective applications. *Tectonophysics*, 693, 116-142. <https://doi.org/10.1016/j.tecto.2016.10.012>
- Karato, S. I., Paterson, M. S., & FitzGerald, J. D. (1986). Rheology of synthetic olivine aggregates: Influence of grain size and water. *Journal of Geophysical Research: Solid Earth*, 91(B8), 8151-8176. <https://doi.org/10.1029/JB091iB08p08151>

- Karato, S. I., & Jung, H. (2003). Effects of pressure on high-temperature dislocation creep in olivine. *Philosophical Magazine*, 83(3), 401–414.  
<https://doi.org/10.1080/0141861021000025829>
- Karato, S. I. (2008). *Deformation of Earth Materials: an introduction to the rheology of solid earth*. Cambridge: Cambridge University Press.
- Kidder, S., Avouac, J. P., & Chan, Y. C. (2012). Constraints from rocks in the Taiwan orogen on crustal stress levels and rheology. *Journal of Geophysical Research: Solid Earth*, 117(B9). <https://doi.org/10.1029/2012JB009303>
- Kirby, S. H. (1983). Rheology of the lithosphere. *Reviews of Geophysics*, 21(6), 1458-1487. <https://doi.org/10.1029/RG021i006p01458>
- Kirby, S. H., & Kronenberg, A. K. (1984). Deformation of clinopyroxenite: Evidence for a transition in flow mechanisms and semibrittle behavior. *Journal of Geophysical Research: Solid Earth*, 89(B5), 3177-3192.  
<https://doi.org/10.1029/JB089iB05p03177>
- Kirby, S. H., & Raleigh, C. B. (1973). Mechanisms of high-temperature, solid-state flow in minerals and ceramics and their bearing on the creep behavior of the mantle. *Tectonophysics*, 19(2), 165–194. [https://doi.org/10.1016/0040-1951\(73\)90038-3](https://doi.org/10.1016/0040-1951(73)90038-3)
- Koch, P. S., Christie, J. M., Ord, A., & George, R. P. (1989). Effect of water on the rheology of experimentally deformed quartzite. *Journal of Geophysical Research: Solid Earth*, 94(B10), 13975–13996. <https://doi.org/10.1029/JB094iB10p13975>
- Kohlstedt, D. L., Evans, B., & Mackwell, S. J. (1995). Strength of the lithosphere: Constraints imposed by laboratory experiments. *Journal of Geophysical Research: Solid Earth*, 100(B9), 17587–17602. <https://doi.org/10.1029/95JB01460>
- Kreemer, C., Blewitt, G., & Klein, E. C. (2014). A geodetic plate motion and Global Strain Rate Model. *Geochemistry, Geophysics, Geosystems*, 15(10), 3849-3889.  
<https://doi.org/10.1002/2014GC005407>

- Kronenberg, A. K. (1994). Hydrogen Speciation and Chemical Weakening of quartz. *Reviews in Mineralogy and Geochemistry*, 29(1), 123–176.
- Kronenberg, A. K., Kirby, S. H., & Pinkston, J. (1990). Basal slip and mechanical anisotropy of biotite. *Journal of Geophysical Research: Solid Earth*, 95(B12), 19257–19278. <https://doi.org/10.1029/JB095iB12p19257>
- Kronenberg, A. K., & Tullis, J. (1984). Flow strengths of quartz aggregates: Grain size and pressure effects due to hydrolytic weakening. *Journal of Geophysical Research: Solid Earth*, 89(B6), 4281–4297. <https://doi.org/10.1029/JB089iB06p04281>
- Kuiper, Y. D., & Jiang, D. (2010). Kinematics of deformation constructed from deformed planar and linear elements: The method and its application. *Tectonophysics*, 492(1–4), 175–191. <https://doi.org/10.1016/j.tecto.2010.06.009>
- Levy, M., Bass, H., & Stern, R. (2000). *Handbook of Elastic Properties of Solids, Liquids, and Gases, Four Volume Set*. Academic Press.
- Luan, F. C., & Paterson, M. S. (1992). Preparation and deformation of synthetic aggregates of quartz. *Journal of Geophysical Research: Solid Earth*, 97(B1), 301–320. <https://doi.org/10.1029/91JB01748>
- Mackwell, S. J., Zimmerman, M. E., & Kohlstedt, D. L. (1998). High-temperature deformation of dry diabase with application to tectonics on Venus. *Journal of Geophysical Research: Solid Earth*, 103(B1), 975–984. <https://doi.org/10.1029/97JB02671>
- Maggi, A., Jackson, J. A., McKenzie, D., & Priestley, K. (2000). Earthquake focal depths, effective elastic thickness, and the strength of the continental lithosphere. *Geology*, 28(1990), 495–498. [https://doi.org/10.1130/0091-7613\(2000\)28<495](https://doi.org/10.1130/0091-7613(2000)28<495)
- McGill, S. F., Owen, L. A., Weldon, R. J., & Kendrick, K. J. (2013). Latest Pleistocene and Holocene slip rate for the San Bernardino strand of the San Andreas fault, Plunge Creek, Southern California: Implications for strain partitioning within the

- southern San Andreas fault system for the last ~35 k.y. *Geological Society of America Bulletin*, 125(1–2), 48–72. <https://doi.org/10.1130/B30647.1>
- Means, W.D., Hobbs, B.E., Lister, G.S., Williams, P.F. (1980). Vorticity and non-coaxiality in progressive deformation. *Journal of Structural Geology*, 2, 371–378.
- Mei, S., & Kohlstedt, D. L. (2000). Influence of water on plastic deformation of olivine aggregates: 2. Dislocation creep regime. *Journal of Geophysical Research: Solid Earth*, 105(B9), 21471–21481. <https://doi.org/10.1029/2000JB900180>
- Montési, L. G. J. (2013). Fabric development as the key for forming ductile shear zones and enabling plate tectonics. *Journal of Structural Geology*, 50, 254–266. <https://doi.org/10.1016/j.jsg.2012.12.011>
- Mercier, J. C. C., Anderson, D. A., & Carter, N. L. (1977). *Pageoph*, 115, 199–226. <https://doi.org/10.1007/BF01637104>
- Mukherjee, A. K. (1971). The rate controlling mechanism in superplasticity. *Materials Science and Engineering*, 8(2), 83–89. [https://doi.org/10.1016/0025-5416\(71\)90085-1](https://doi.org/10.1016/0025-5416(71)90085-1)
- Nicolas, A., & Poirier, J. P. (1976). *Crystalline plasticity and solid state flow in metamorphic rocks*. John Wiley & Sons.
- Norris, R. J., & Cooper, A. F. (2000). Late Quaternary slip rates and slip partitioning on the Alpine Fault, New Zealand. *Journal of Structural Geology*, 23(2–3), 507–520. [https://doi.org/10.1016/S0191-8141\(00\)00122-X](https://doi.org/10.1016/S0191-8141(00)00122-X)
- Norris, R. J., & Cooper, A. F. (2003). Very high strains recorded in mylonites along the Alpine Fault, New Zealand: implications for the deep structure of plate boundary faults. *Journal of Structural Geology*, 25(12), 2141–2157. [https://doi.org/10.1016/S0191-8141\(03\)00045-2](https://doi.org/10.1016/S0191-8141(03)00045-2)
- Ord, A., & Christie, J. M. (1984). Flow stresses from microstructures in mylonitic quartzites of the Moine Thrust zone, Assynt area, Scotland. *Journal of Structural*

- Geology*, 6(6), 639-654. [https://doi.org/10.1016/0191-8141\(84\)90002-6](https://doi.org/10.1016/0191-8141(84)90002-6)
- Ord, A., & Hobbs, B. E. (1986). Experimental Control of the Water-Weakening Effect in Quartz. *Mineral and Rock Deformation: Laboratory Studies: The Paterson Volume*, 51-72. <https://doi.org/10.1029/GM036p0051>
- Parrish, D. K., Krivz, A. L., & Carter, N. L. (1976). Finite-element folds of similar geometry. *Tectonophysics*, 32(3-4), 183-207. [https://doi.org/10.1016/0040-1951\(76\)90062-7](https://doi.org/10.1016/0040-1951(76)90062-7)
- Paterson, M. S. (1989). The interaction of water with quartz and its influence in dislocation flow-an overview. In *Rheology of Solids and of the Earth* (pp. 107-142).
- Pitzer, K. S., & Sterner, S. M. (1994). Equations of state valid continuously from zero to extreme pressures for H<sub>2</sub>O and CO<sub>2</sub>. *The Journal of Chemical Physics*, 101(4), 3111-3116. <https://doi.org/10.1063/1.467624>
- Post, A. D., Tullis, J., & Yund, R. A. (1996). Effects of chemical environment on dislocation creep of quartzite. *Journal of Geophysical Research: Solid Earth*, 101(B10), 22143-22155. <https://doi.org/10.1029/96JB01926>
- Ranalli, G. (1987). *Rheology of the Earth: Deformation and Flow Processes in Geophysics and Geodynamics*. Boston: Allen & Unwin.
- Richter, B., Stünitz, H., & Heilbronner, R. (2016). Stresses and pressures at the quartz-to-coesite phase transformation in shear deformation experiments. *Journal of Geophysical Research: Solid Earth*, 121(11), 8015-8033. <https://doi.org/10.1002/2016JB013084>
- Rutter, E. H., & Brodie, K. H. (2004). Experimental intracrystalline plastic flow in hot-pressed synthetic quartzite prepared from Brazilian quartz crystals. *Journal of Structural Geology*, 26(2), 259-270. [https://doi.org/10.1016/S0191-8141\(03\)00096-8](https://doi.org/10.1016/S0191-8141(03)00096-8)
- Rybacki, E., & Dresen, G. (2004). Deformation mechanism maps for feldspar rocks.

- Tectonophysics*, 382(3–4), 173–187. <https://doi.org/10.1016/j.tecto.2004.01.006>
- Rybacki, E., Gottschalk, M., Wirth, R., & Dresen, G. (2006). Influence of water fugacity and activation volume on the flow properties of fine-grained anorthite aggregates. *Journal of Geophysical Research: Solid Earth*, 111(B3).  
<https://doi.org/10.1029/2005JB003663>
- Schmalholz, S. M., & Fletcher, R. C. (2011). The exponential flow law applied to necking and folding of a ductile layer. *Geophysical Journal International*, 184(1), 83–89. <https://doi.org/10.1111/j.1365-246X.2010.04846.x>
- Schmalholz, S. M., & Schmid, D. W. (2012). Folding in power-law viscous multi-layers. *Phil. Trans. R. Soc. A*, 370(1965), 1798–1826. <https://doi.org/10.1098/rsta.2011.0421>
- Schulz, S. E., & Evans, J. P. (2000). Mesoscopic structure of the Punchbowl Fault, Southern California and the geologic and geophysical structure of active strike-slip faults. *Journal of Structural Geology*, 22(7), 913–930.  
[https://doi.org/10.1016/S0191-8141\(00\)00019-5](https://doi.org/10.1016/S0191-8141(00)00019-5)
- Shea, W. T., & Kronenberg, A. K. (1993). Strength and anisotropy of foliated rocks with varied mica contents. *Journal of Structural Geology*, 15(9–10), 1097–1121.  
[https://doi.org/10.1016/0191-8141\(93\)90158-7](https://doi.org/10.1016/0191-8141(93)90158-7)
- Shelton, G. L., & Tullis, J. (1981). Experimental flow laws for crustal rocks. *Eos Trans. AGU*, 62, 396.
- Sherby, O. D., & Burke, P. M. (1968). Mechanical behavior of crystalline solids at elevated temperature. *Progress in Materials Science*, 13, 323–390.  
[https://doi.org/10.1016/0079-6425\(68\)90024-8](https://doi.org/10.1016/0079-6425(68)90024-8)
- Sherby, O. D., Robbins, J. L., & Goldberg, A. (1970). Calculation of activation volumes for self-diffusion and creep at high temperature. *Journal of Applied Physics*, 41(10), 3961–3968. <https://doi.org/10.1063/1.1658396>



- Shimamoto, T., & Ikeda, Y. (1976). A simple algebraic method for strain estimation from deformed ellipsoidal objects. 1. Basic theory. *Tectonophysics*, 36(4), 315–337. [https://doi.org/10.1016/0040-1951\(76\)90107-4](https://doi.org/10.1016/0040-1951(76)90107-4)
- Shimizu, I. (2008). Theories and applicability of grain size piezometers: The role of dynamic recrystallization mechanisms. *Journal of Structural Geology*, 30(7), 899–917. <https://doi.org/10.1016/j.jsg.2008.03.004>
- Shimizu, I. (2012). Steady-state grain size in dynamic recrystallization of minerals. In *Recrystallization*. InTech.
- Sibson, R. H. (1977). Fault rocks and fault mechanisms. *Journal of the Geological Society*, 133(3), 191–213. <https://doi.org/10.1144/gsjgs.133.3.0191>
- Stipp, M., & Tullis, J. (2003). The recrystallized grain size piezometer for quartz. *Geophysical Research Letters*, 30(21). <https://doi.org/10.1029/2003GL018444>
- Stipp, M., Tullis, J., Scherwath, M., & Behrmann, J. H. (2010). A new perspective on paleopiezometry: Dynamically recrystallized grain size distributions indicate mechanism changes. *Geology*, 38(8), 759–762. <https://doi.org/10.1130/G31162.1>
- Sutherland, R., Berryman, K., & Norris, R. (2006). Quaternary slip rate and geomorphology of the Alpine fault: Implications for kinematics and seismic hazard in southwest New Zealand. *Geological Society of America Bulletin*, 118(3–4), 464–474. <https://doi.org/10.1130/B25627.1>
- Swamy, V., Saxena, S. K., Sundman, B., & Zhang, J. (1994). A thermodynamic assessment of silica phase diagram. *Journal of Geophysical Research: Solid Earth*, 99(B6), 11787–11794. <https://doi.org/10.1029/93JB02968>
- Titus, S. J., DeMets, C., & Tikoff, B. (2005). New slip rate estimates for the creeping segment of the San Andreas fault, California. *Geology*, 33(3), 205. <https://doi.org/10.1130/G21107.1>

- Tullis, J. (2002). Deformation of Granitic Rocks: Experimental Studies and Natural Examples. *Reviews in Mineralogy and Geochemistry*, 51(1), 51–95.  
<https://doi.org/10.2138/gsrng.51.1.51>
- Tullis, J., & Wenk, H. R. (1994). Effect of muscovite on the strength and lattice preferred orientations of experimentally deformed quartz aggregates. *Materials Science and Engineering: A*, 175(1-2), 209-220. [https://doi.org/10.1016/0921-5093\(94\)91060-X](https://doi.org/10.1016/0921-5093(94)91060-X)
- Tullis, J., & Yund, R. A. (1980). Hydrolytic weakening of experimentally deformed Westerly granite and Hale albite rock. *Journal of Structural Geology*, 2(4), 439–451.  
[https://doi.org/10.1016/0191-8141\(80\)90005-X](https://doi.org/10.1016/0191-8141(80)90005-X)
- Tullis, J., & Yund, R. A. (1989). Hydrolytic Weakening of Quartz Aggregates: The Effect of Water and Pressure on Recovery. *Geophysical Research Letters*, 16(11), 1343–1346.
- Twiss, R. J. (1977). Theory and applicability of a recrystallized grain size paleopiezometer. In *Stress in the Earth* (pp. 227-244). Birkhäuser, Basel.  
<https://doi.org/10.1007/BF01637105>
- Watts, A. B., & Burov, E. B. (2003). Lithospheric strength and its relationship to the elastic and seismogenic layer thickness. *Earth and Planetary Science Letters*, 213(1–2), 113–131. [https://doi.org/10.1016/S0012-821X\(03\)00289-9](https://doi.org/10.1016/S0012-821X(03)00289-9)
- White, S. H. (1979). Difficulties associated with paleostress estimates. *Bull. Mineral.*, 102, 210-215.
- White, J. C., & Mawer, C. K. (1991). Deep-crustal deformation textures along megathrusts from Newfoundland and Ontario: implications for microstructural preservation, strain rates, and the strength of the lithosphere. *Can. J. Earth Sci.*, 29, 328–337. <https://doi.org/10.1139/e92-029>
- Wightman, R. H., Prior, D. J., & Little, T. A. (2006). Quartz veins deformed by diffusion creep-accommodated grain boundary sliding during a transient, high strain-rate

event in the Southern Alps, New Zealand. *Journal of Structural Geology*, 28(5), 902–918. <https://doi.org/10.1016/j.jsg.2006.02.008>

Wilks, K. R., & Carter, N. L. (1990). Rheology of some continental lower crustal rocks. *Tectonophysics*, 182(1–2), 57–77. [https://doi.org/10.1016/0040-1951\(90\)90342-6](https://doi.org/10.1016/0040-1951(90)90342-6)

van Der Woerd, J., Klinger, Y., Sieh, K., Tapponnier, P., Ryerson, F. J., & Mériaux, A. S. (2006). Long-term slip rate of the southern San Andreas fault from <sup>10</sup>Be-<sup>26</sup>Al surface exposure dating of an offset alluvial fan. *Journal of Geophysical Research: Solid Earth*, 111(B4). <https://doi.org/10.1029/2004JB003559>

Zulauf, G. (2001). Structural style, deformation mechanisms and paleodifferential stress along an exposed crustal section: constraints on the rheology of quartzofeldspathic rocks at supra-and infrastructural levels (Bohemian Massif). *Tectonophysics*, 332(1–2), 211–237. [https://doi.org/10.1016/S0040-1951\(00\)00258-4](https://doi.org/10.1016/S0040-1951(00)00258-4)

## Chapter 5

### 5 Dislocation Creep Flow Laws of Wet Quartzite: The Significance of Pressure and Slip Systems

#### 5.1 Introduction

The creep behavior of quartzites is critical for the understanding of continental rheology (e.g., Kohlstedt et al., 1995; Ranalli, 1987). The dislocation creep of wet quartzites has been described by a flow law of the form  $\dot{\epsilon} = Af_w^m \exp\left(-\frac{Q}{RT}\right)\sigma^n$ , where  $\dot{\epsilon}$  is the strain rate,  $A$  the pre-exponential parameter,  $f_w$  the water fugacity,  $m$  the water fugacity exponent,  $Q$  the activation energy,  $R$  the universal gas constant,  $T$  the absolute temperature,  $\sigma$  the differential stress, and  $n$  the stress exponent. A large number of creep experiments on quartz samples have been conducted to determine the values of  $Q$ ,  $n$ ,  $m$ , and  $A$  (called flow law parameters hereafter). However, very different results are obtained with variations between 2 and 4 for  $n$ , 130 kJ/mol and 240 kJ/mol for  $Q$ , and 0.372 and 2.8 for  $m$  (e.g., Kronenberg and Tullis, 1984; Koch et al., 1989; Gleason and Tullis, 1995; Luan and Paterson, 1992; Post et al., 1996; Rutter and Brodie, 2004; Chernak et al., 2009; Holyoke and Kronenberg, 2013). The pre-exponential parameter  $A$  varies accordingly. The large variations in flow law parameters lead to very different predictions on the strength of the continent.

We have suggested recently that the large difference in  $Q$  from experiments may be explained by considering the pressure dependence of the activation enthalpy (Lu and Jiang 2019). Although the pressure range in the continental lithosphere is relatively small, the creep experiments on wet quartzite were conducted in very different confining pressures from 0.3GPa (Luan and Paterson, 1992; Rutter and Brodie 2004) to more than 1.5GPa (e.g., Gleason and Tullis, 1995). In order to account for this pressure effect, we used the following flow law (e.g., Karato and Jung, 2003):

$$\dot{\epsilon} = Af_w^m \exp\left(-\frac{Q+PV}{RT}\right) \sigma^n = Af_w^m \exp\left(-\frac{H}{RT}\right) \sigma^n \quad (5.1)$$

where  $P$  is the pressure,  $V$  the activation volume, and  $H = Q + PV$  the activation enthalpy. We used the flow law in Eq.5.1 to refit the experiments of Gleason and Tullis (1995) and Luan and Paterson (1992) that are thought to have undergone dominantly steady-state regimes 2 and 3 dislocation creep. The use of this flow law also implies that  $n$ ,  $m$ , and  $V$  are no longer independent parameters, because (see Eq. 4, in Lu and Jiang, 2019):

$$m = -n \left( \frac{\partial \ln \sigma}{\partial \ln f_w} \right)_{T, \dot{\epsilon}} + \frac{V}{RT} \left( \frac{\partial P}{\partial \ln f_w} \right)_{T, \dot{\epsilon}} \quad (5.2)$$

Using  $n = 4$  for regimes 2 and 3 dislocation creep, based on Gleason and Tullis (1995) and Luan and Paterson (1992), and a set of 3 selected experimental data from Kronenberg and Tullis (1984), Lu and Jiang (2019) obtained  $V = 35.3 \text{ cm}^3/\text{mol}$  and  $m = 2.7$  which in turn yielded  $Q = 132 \pm 5 \text{ kJ/mol}$  for the experimental results of Gleason and Tullis (1995) and Luan and Paterson (1992).

The flow law presented in Lu and Jiang (2019) is based on  $n = 4$ . However, other experiments (e.g., Kronenberg and Tullis, 1984; Koch et al., 1989; Gleason and Tullis, 1995; Luan and Paterson, 1992; Rutter and Brodie, 2004) suggested that  $n$  varies between 2 and 4. Goldsby and Kohlstedt (2001) and Hirth and Kohlstedt (2003) have suggested, for ice I and olivine respectively, that  $n$  may depend on the dominant slip system. Togle et al. (2019) have shown that the value of  $n$  and quartz c-axis fabrics are correlated in the following manner: At higher temperatures and lower stresses where the experimental data yield  $n = 4$ , the deformed quartz samples show Y-max c-axis fabrics suggesting that the dominant slip system was prism  $\langle a \rangle$  (Nachlas and Hirth, 2015; Richter et al., 2018). At lower temperatures and higher stresses where the experimental data yield  $n = 2.7$ , the samples exhibit c-axis fabrics suggesting the dominant basal  $\langle a \rangle$  slip system (Togle et al., 2013; Richter et al., 2018).

In this chapter, we examine the current database on quartz creep experiments by considering both the pressure effect on the activation enthalpy as in Lu and Jiang (2019) and the slip system dependence of the stress exponent as in Tokle et al. (2019). We demonstrate that the current experimental dataset is consistent with two dislocation creep flow laws, corresponding respectively to dominant prism  $\langle a \rangle$  slip and dominant basal  $\langle a \rangle$  slip, and transitional flow behaviors in between. Transitional flow behaviors are also common in nature. We regard the flow law in the transitional flow as a superposition of the two dislocation creep flow laws and discuss the significance and implications of multiple flow behaviors for continental strength.

## 5.2 Selection of experimental data

As in Lu and Jiang (2019), we select quartz experimental data corresponding to steady-state regimes 2 and 3 dislocation creep. A total of 20 creep experiments on quartz samples are analyzed in this paper, and they were deformed from 700 °C to 1200 °C (Appendix C). We have excluded experimental runs that involved semi-brittle deformation or exhibited microstructures indicating regime 1 dislocation creep. To minimize complications from the effect of water on quartz, we only include data from samples with 0.1-0.4 wt.% H<sub>2</sub>O added, following Tokle et al. (2019). With the exception of the ultrafine-grained quartzites of Rutter and Brodie (2004; 12-20 μm) and one sieved sample of Richter et al. (2018; 7-11 μm), all experiments we used in this paper were on samples with grain size between 20-200 μm. The creep experiments were performed in either uniaxial compression or general shear experiments. For the general shear experiments, the shear stresses ( $\tau$ ) and the shear strain rates ( $\dot{\gamma}$ ) were converted to von Mises equivalent stresses ( $\sigma_{eqv} = \sqrt{3}\tau$ ) and equivalent strain rates ( $\dot{\epsilon}_{eqv} = \frac{\dot{\gamma}}{\sqrt{3}}$ ) so that the results could be directly compared with those from uniaxial compression experiments where the differential stresses and axial strain rates were used (Paterson and Olgaard, 2000). Tokle et al. (2019) have shown that converting the shear stresses and shear strain rates to von Mises equivalent stresses and equivalent strain rates causes no systematic difference between the uniaxial compression experiments and general shear experiments.

The experiments we used in this paper were conducted in the Griggs-type apparatus with solid salt assemblies, molten salt, or gas confining media. The stress calibration of Holyoke and Kronenberg (2010) for Griggs apparatus with solid medium or molten-salt medium was not applied for the following 3 reasons: First, it is not clear yet if such stress calibration, which was determined under uniaxial compression experiments, is applicable to general shear experiments (Tokle et al., 2019). Second, Holyoke and Kronenberg (2010) pointed out that applying their calibration for molten-salt medium to the data of Gleason and Tullis (1995) only changed the fitting term  $A$  (from  $1.1 \times 10^{-4} \text{MPa}^{-n} \text{s}^{-1}$  to  $5.1 \times 10^{-4} \text{MPa}^{-n} \text{s}^{-1}$ ) but not the values of  $n$  or  $Q$  substantially. Third, some experimental studies suggested that this stress calibration might be overdone (Kidder et al., 2016; Richter et al., 2016), an observation consistent with our recent results (Lu and Jiang, 2019).

### 5.3 Two dislocation creep flow laws

To determine the flow law parameters in Eq.5.1 ( $n$ ,  $m$ ,  $V$ ,  $Q$ , and  $A$ ) we use the following iterative approach: Starting with an initial input of  $n$ , we solve for the values of  $m$  and  $V$  using Eq.5.2 based on a minimum of three sets of  $P$  and  $f_w$  stepping experimental data at constant  $\dot{\epsilon}$  and  $T$  (Lu and Jiang, 2019). Once the values of  $n$ ,  $m$  and  $V$  are determined, the activation energy  $Q$  can be obtained from  $T$  stepping experimental data using the following equation:  $\ln(\dot{\epsilon}) - m \ln(f_w) - n \ln(\sigma) + \frac{PV}{RT} = \frac{Q}{RT} + \ln(A)$ . From each  $T$  stepping run, the  $T$ ,  $P$ ,  $\dot{\epsilon}$ , and  $\sigma$  are known. The water fugacity  $f_w$  is determined using the state equation of water (Pitzer and Sterner, 1994), assuming the partial pressure of water is equal to the confining pressure. Plotting  $\ln(\dot{\epsilon}) - m \ln(f_w) - n \ln(\sigma) + \frac{PV}{RT}$  versus  $\frac{1}{RT}$ , the value of  $Q$  is obtained by linear regression. With the obtained parameters ( $m$ ,  $V$ , and  $Q$ ), we normalize all data in Appendix C to a chosen reference P-T condition. To determine  $n$ , constant  $T$ ,  $P$ , and  $f_w$  tests are required because  $n = \left( \frac{\partial \ln \dot{\epsilon}}{\partial \ln \sigma} \right)_{T,P,f}$ . As creep

experiments (Appendix C) were performed under different P-T conditions, we need to normalize the data to a chosen reference P-T condition and then plot the normalized strain rates versus normalized stresses. This, in turn, allows us to determine a new value of  $n$  by linear regression. A new round of iteration is initiated with the new  $n$ . The iteration continues until the output  $n$  is equal to the input  $n$  within a specific tolerance. The pre-exponential term  $A$  is a fitting parameter, which can be obtained once  $n$ ,  $m$ ,  $V$ ,  $Q$  are determined. The final set of  $n$ ,  $m$ ,  $V$ ,  $Q$  and  $A$  is then the best-fit flow law parameters for the data.

As Tokle et al. (2019) have pointed out in their stress and strain rate plots (their Fig.1a), the high-temperature data and the low-temperature data follow two distinct trends. We consider the high-temperature data and low-temperature data separately to determine the flow law parameters. First, we consider the samples with large grainsize (20-200  $\mu\text{m}$ ) deformed at higher temperatures (900-1200 $^{\circ}\text{C}$ ) and lower stresses (Luan and Paterson, 1992; Gleason and Tullis, 1995; Stipp and Tullis, 2003; Heilbronner and Tullis, 2006; Nachlas and Hirth, 2015; Kidder et al., 2016; Richter et al., 2018). Using the three sets of  $P$  and  $f_w$  stepping experimental data from 820 MPa to 1590 MPa (Kronenberg and Tullis, 1984) and the  $T$  stepping experimental data from 827  $^{\circ}\text{C}$  to 1050  $^{\circ}\text{C}$  (Luan and Paterson, 1992; Gleason and Tullis, 1995), the application of the iterative method described above yields a final set of  $n = 3.9 \pm 0.2$ ,  $m = 2.6$ ,  $V = 35.8 \text{ cm}^3/\text{mol}$ ,  $Q = 132 \pm 19 \text{ kJ/mol}$ , and  $A = 2.5 \times 10^{-(14 \pm 0.4)} \text{ MPa}^{-n-m} \text{ s}^{-1}$ . The strain rate versus differential stress plot for all data in Appendix C at a reference P-T condition ( $T = 900 \text{ }^{\circ}\text{C}$  and  $P = 1500 \text{ MPa}$ ) using the final set of flow law parameters is shown in Fig.5.1a. Fig.5.2a shows how  $Q$  is determined based on the  $T$  stepping experimental data of Luan and Paterson (1992) and Gleason and Tullis (1995). If the data from Rutter and Brodie (2004) on ultrafine-grained quartzites are also included in the calculation, we got  $n = 3.7 \pm 0.2$  and  $A = 5.0 \times 10^{-(14 \pm 0.4)} \text{ MPa}^{-n-m} \text{ s}^{-1}$ . Therefore, the following flow law is applicable to these high-temperature data:



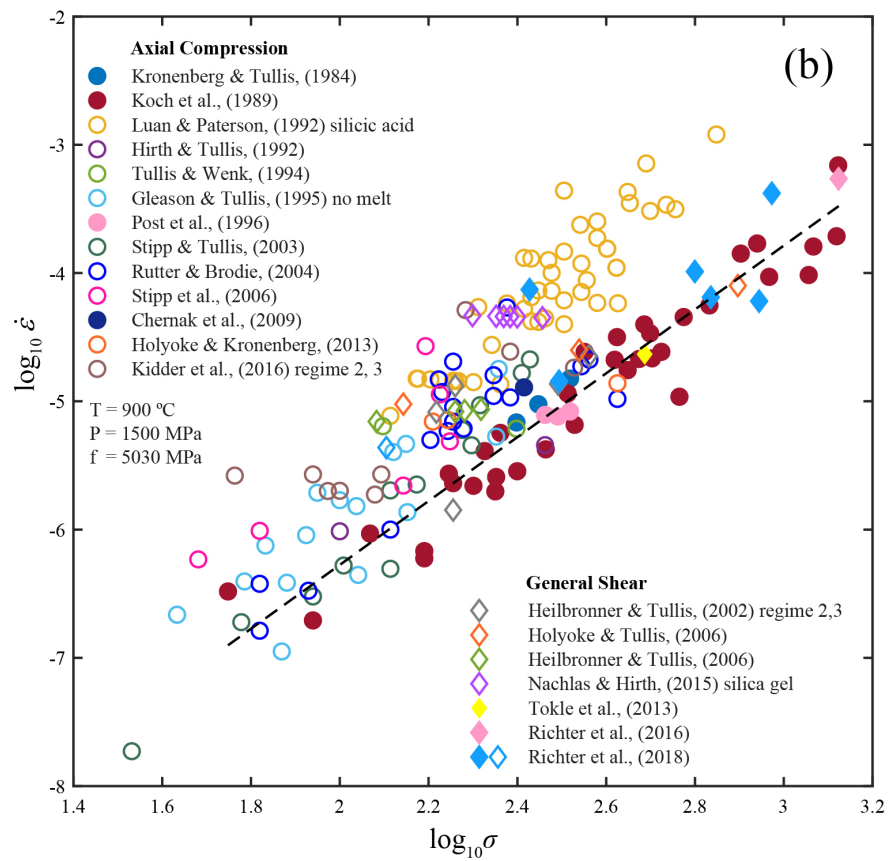
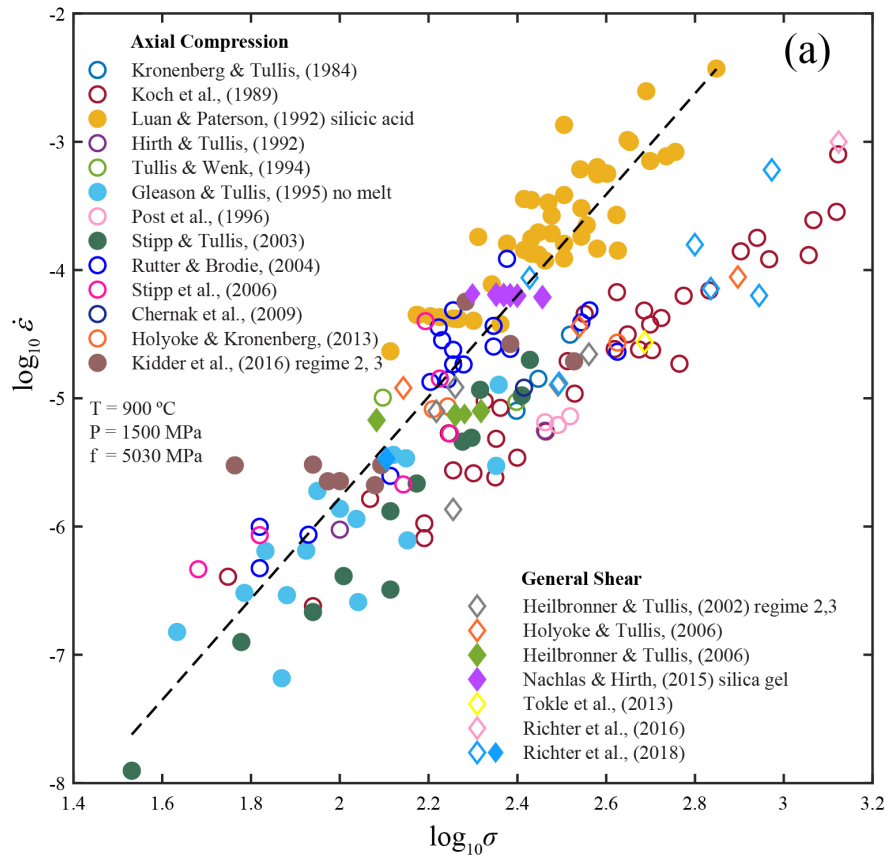


**Figure 5.1 Plots of normalized strain rate versus normalized stress for quartz creep experiments and the dislocation creep flow laws**

The data in (a) and (b) are from the following 20 studies: Kronenberg and Tullis (1984), Koch et al. (1989), Luan and Paterson (1992), Hirth and Tullis (1992), Tullis and Wenk (1994), Gleason and Tullis (1995), Post et al. (1996), Heilbronner and Tullis (2002), Stipp and Tullis (2003), Rutter and Brodie (2004), Holyoke and Tullis (2006), Heilbronner and Tullis (2006), Stipp et al. (2006), Chernak et al. (2009), Holyoke and Kronenberg (2013), Kidder et al. (2016), Nachlas and Hirth (2015), Tokle et al. (2013), Richter et al. (2016), and Richter et al. (2018). The circles represent data collected from the axial compression experiments, and the diamonds represent data collected from the general shear experiments. All mechanical data are normalized to a reference condition of  $T = 900 \text{ }^\circ\text{C}$ ,  $P = 1500 \text{ MPa}$ , and  $f_w = 5030 \text{ MPa}$ . The water fugacity is determined using the state equation of water (Pitzer and Sterner, 1994). (a) All data are normalized using the flow law parameters  $m = 2.6$ ,  $V = 35.8 \text{ cm}^3/\text{mol}$ , and  $Q = 132 \text{ kJ/mol}$ . The dashed line represents the best fit line of the high-temperature experimental data (the solid circles and diamonds).  $n = 3.9 \pm 0.2$  and  $A = 2.5 \times 10^{-14 \pm 0.4} \text{ MPa}^{-n} \text{ s}^{-1}$  are obtained by linear regression. (b) All data are normalized using  $m = 1.7$ ,  $V = 23.1 \text{ cm}^3/\text{mol}$  and  $Q = 126 \text{ kJ/mol}$ . The dashed line represents the best fit line of the low-temperature experimental data (the solid circles and diamonds).  $n = 2.5 \pm 0.1$  and  $A = 6.3 \times 10^{-12 \pm 0.3} \text{ MPa}^{-n} \text{ s}^{-1}$  are obtained by linear regression.

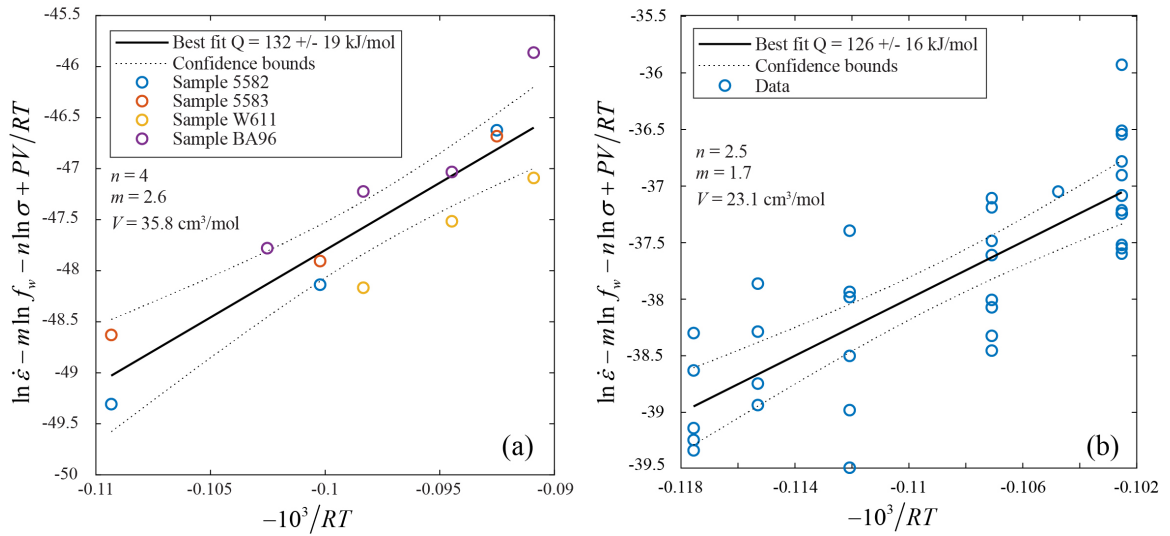


**Figure 5.2 Determination of the activation energy**

(a). The plot of  $\ln(\dot{\epsilon}) - m \ln(f_w) - n \ln(\sigma) + \frac{PV}{RT}$  versus  $-\frac{1}{RT}$  for the  $T$  stepping data of Luan and Paterson (1992; sample 5582 and sample 5583) and Gleason and Tullis (1995; sample W611 and sample BA96) using  $n = 4$ ,  $m = 2.6$ , and  $V = 35.8$  cm<sup>3</sup>/mol, which yields  $Q = 132 \pm 19$  kJ/mol by linear regression. (b) The plot of  $\ln(\dot{\epsilon}) - m \ln(f_w) - n \ln(\sigma) + \frac{PV}{RT}$  versus  $-\frac{1}{RT}$  for the  $T$  stepping data of Koch et al. (1989) using  $n = 2.5$ ,  $m = 1.7$ , and  $V = 23.1$  cm<sup>3</sup>/mol, which yields  $Q = 126 \pm 16$  kJ/mol by linear regression.

$$\dot{\epsilon} = 2.5 \times 10^{-14} f_w^{2.6} \exp\left(-\frac{132000 + 35.8P}{RT}\right) \sigma^4 \quad (5.3)$$

where  $\sigma$  and  $P$  are in MPa.

This flow law differs slightly from that in Lu and Jiang (2019) in  $m$  and  $V$  ( $m = 2.7$ ,  $V = 35.3 \text{ cm}^3/\text{mol}$  in Lu and Jiang, 2019) and more in  $A$  ( $A = 6.0 \times 10^{-15}$  in Lu and Jiang 2019). The difference is due to the fact that stress calibration based on Holyoke and Kronenberg (2010) was applied in Lu and Jiang (2019) but not here. This flow law is for wet quartzites deforming predominantly by prism  $\langle a \rangle$  slip producing characteristic Y-max c-axis fabrics (Fig.5.3).

To consider the samples deformed at lower temperatures (700-900 °C) and higher stresses (Kronenberg and Tullis, 1984; Koch et al., 1989; Post et al., 1996; Chernak et al., 2009; Togle et al., 2013; Richter et al., 2016; Richter et al., 2018), we used the three sets of  $P$  and  $f_w$  stepping experimental data from 820 MPa to 1590 MPa (Kronenberg and Tullis, 1984) and the  $T$  stepping experimental data of Koch et al. (1989) ranging from 750 °C to 900 °C. Application of the above iterative method, starting with an initial value of  $n = 2$ , yields a final set of  $n = 2.5$ ,  $m = 1.7$ ,  $V = 23.1 \text{ cm}^3/\text{mol}$ ,  $Q = 126 \pm 16 \text{ kJ/mol}$ , and  $A = 6.3 \times 10^{-(12 \pm 0.4)} \text{ MPa}^{-n-m} \text{ s}^{-1}$ . The strain rate versus differential stress plot at the reference P-T condition ( $T = 900 \text{ °C}$  and  $P = 1500 \text{ MPa}$ ) using the above flow law parameters is shown in Fig.5.1b. The plots of  $T$  stepping experimental data of Koch et al. (1989) to determine  $Q$  is shown in Fig.5.2b. The following flow law is applicable to the low-temperature data:

$$\dot{\epsilon} = 6.3 \times 10^{-12} f_w^{1.7} \exp\left(-\frac{126000 + 23.1P}{RT}\right) \sigma^{2.5} \quad (5.4)$$

This flow law is for wet quartzites deforming predominantly by basal  $\langle a \rangle$  slip and producing a strong cluster of c-axes in the periphery (Fig.5.3). The parameters of the two dislocation creep flow laws determined in this paper are listed in Table 5.1.

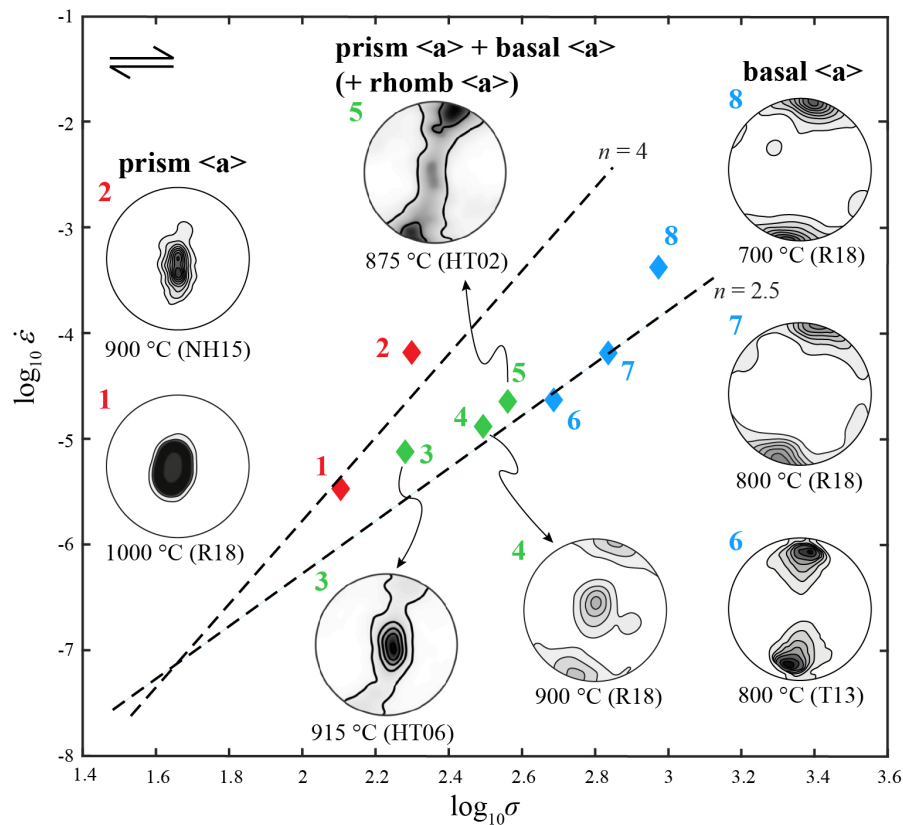


**Figure 5.3 Quartz c-axis fabrics and stress and strain rate data of eight general shear experimental runs**

The quartz c-axis patterns and experimental data are from the following five studies: Heilbronner and Tullis (2002, 875 °C), Nachlas and Hirth (2015, 900 °C), Heilbronner and Tullis (2006, 915 °C), Tokle et al. (2013, 800 °C), and Richter et al. (2018, 700 °C, 800 °C, 900 °C, 1000 °C). Two dislocation creep flow laws are also plotted. The strain rate and stress data are normalized to a reference condition  $T = 900 \text{ °C}$ ,  $P = 1500 \text{ MPa}$ , and  $f_w = 5030 \text{ MPa}$  using the flow law in Eq.5.3 (for data  $\geq 900 \text{ °C}$ ) and the flow law in Eq.5.4 (for data  $< 900 \text{ °C}$ ). Transitional quartz c-axis fabrics are evident, from Y-max pattern indicating dominant prism  $\langle a \rangle$  slip system at 1000 °C and 900 °C, through a mixture of basal  $\langle a \rangle$ , prism  $\langle a \rangle$ , and rhomb  $\langle a \rangle$  c-axis fabric pattern at 915 ~ 875 °C, to a strong cluster of c-axes in the periphery reflecting dominant basal  $\langle a \rangle$  slip system at 800 °C and 700 °C.

**Table 5.1 Parameters of two distinct dislocation creep flow laws for wet quartzites**

	$n$	$Q$ (kJ/mol)	$V$ (cm <sup>3</sup> /mol)	$M$	$A$ (MPa <sup>-n-m</sup> s <sup>-1</sup> )
dominant prism <a> slip (Eq.5.3)	3.9±0.2	132±19	35.8	2.6	2.5×10 <sup>-(14±0.4)</sup>
dominant basal <a> slip (Eq.5.4)	2.5±0.1	126±16	23.1	1.7	6.3×10 <sup>-(12±0.4)</sup>

One notes that the values of  $Q$  in two dislocation creep flow laws are similar ( $Q = 132 \pm 19$  kJ/mol for flow law in Eq. 3 and  $Q = 126 \pm 16$  kJ/mol for flow law in Eq. 4). This can be understood by the fact that dislocation creeps, regardless of the dominant slip system, are ultimately accommodated by solid-state self-diffusion of vacancy defects (Dorn 1954; Sherby and Burke 1968; Freer, 1981). Different dominant slip systems correspond to distinct activation volumes and water fugacity exponents. As the activation volume is the sum of  $V_f$  for point defect formation and  $V_m$  for point defect migration (Béjina et al., 2003), we suspect that point defect migration associated with different dominant slip systems must be distinct, leading to distinct  $V$  in flow laws. The  $V$  values are reasonable both from a theoretical consideration (Lu and Jiang, 2019) and in comparison with the activation volumes of other silicates ( $V = 14 \sim 24$  cm<sup>3</sup>/mol for olivine, Karato and Jung, 2003, and  $V = 24 \sim 38$  cm<sup>3</sup>/mol for anorthite, Rybacki et al., 2006). The variation in the water fugacity exponent remains poorly understood. The original introduction of the water fugacity term into the flow law expression was essentially phenomenological (e.g., Kohlstedt et al., 1995). As Eq.5.2 shows explicitly, the value of  $m$  increases with  $V$  as  $\frac{\partial P}{\partial \ln f_w}$  is always positive in both crustal and experimental P-T conditions.

## 5.4 Homogenized creep behavior in the transitional regime

We notice that the experimental data from the intermediate-temperature runs (~900-800 °C; Hirth and Tullis, 1992; Tullis and Wenk, 1994; Holyoke and Tullis, 2006; Heilbronner and Tullis, 2002, 2006; Stipp et al., 2006; Holyoke and Kronenberg, 2013; Richter et al., 2018) do not perfectly follow either of the flow laws (Figs.5.1a and b). The corresponding quartz c-axis fabrics (Fig.5.3; Heilbronner and Tullis, 2002, 2006; Richter et al., 2018) also suggest that both prism  $\langle a \rangle$  and basal  $\langle a \rangle$  slip systems are significant. The data of Rutter and Brodie (2004) do not perfectly follow flow law in Eq.5.3 either. But because of the ultrafine grain size (12-20  $\mu\text{m}$ ) of their samples, it is not clear whether that is due to some contribution of grain boundary sliding mechanism (as discussed in Lu and Jiang, 2019) or activation of multiple slip systems or both. Mylonites from natural shear zones also have quartz c-axis fabrics suggesting a mixture of basal  $\langle a \rangle$ , prism  $\langle a \rangle$ , and rhomb  $\langle a \rangle$  slip systems (Stipp et al., 2002; Law et al., 2010; Toy et al., 2010; Behr and Platt, 2011; Whitney et al., 2014).

Although many mechanisms, including the contribution of grain boundary sliding, may lead to transitional flow behaviors of wet quartzites, we consider the simple situation of transitional flow behaviors as a result of the activation of prism  $\langle a \rangle$  and basal  $\langle a \rangle$  slip systems in this work. A significant concern in studies of multiple deformation mechanisms (or multiple slip systems) is to identify the dominant one in a specific condition. The dominant mechanism under a selected condition depends critically on the state variables, such as temperature, stress, strain rate, etc. A deformation mechanism map, which plots two of the state variables when the other variables remain constant, could help to determine distinct fields in each of which one mechanism (the fastest) dominates. Since Ashby (1972), the concept of deformation mechanism mapping has been applied to a large number of polycrystalline solids (e.g., Stocker and Ashby, 1973; Langdon and Mohamed, 1976; Frost and Ashby, 1982). Previous deformation mechanism maps generally include the following potential creep mechanisms: dislocation creep, Nabarro-Herring and Coble diffusion creep, as well as grain boundary sliding. These creep mechanisms may operate at the same time in adjacent grains or a single grain. The

total strain rate of a polycrystalline is given by the sum of all operating creep mechanisms:  $\dot{\epsilon}^{total} = \dot{\epsilon}^{creep} + \dot{\epsilon}^{GBS} + \dot{\epsilon}^{Coble} + \dot{\epsilon}^{Nabarro-Herring}$ . At a given condition, one mechanism is commonly much faster (more than one order of magnitude faster) than the others according to deformation mechanism maps; therefore, the fastest strain rate can approximately represent the total strain rate.

In the event two dislocation creeps (flow laws in Eq.5.3 and Eq.5.4) operate simultaneously in a quartzite, the two mechanisms are associated with different grains, leading to the partitioning of the deformation, and the combined flow law is a volumetrically homogenized flow that differs from the above relation. In this situation, quartzite can be represented by a two-phase composite material where both phases are uniformly mixed, randomly orientated, and rheologically isotropic. Phase 1 follows the flow law in Eq.5.3, and phase 2 follows the flow law in Eq.5.4. The bulk strain rate of quartzite is expressed as a volumetric average of strain rates of two phases:

$\bar{\epsilon} = \alpha \dot{\epsilon}_1 + (1 - \alpha) \dot{\epsilon}_2$ , where  $\dot{\epsilon}_1$  is the strain rate of phase 1 and  $\dot{\epsilon}_2$  the strain rate of phase 2,  $\alpha$  and  $1 - \alpha$  the relative molar proportions of phase 1 and phase 2. For mono-phase quartzites considered here,  $\alpha$  and  $1 - \alpha$  are simply the volume fractions of the two phases. The bulk stress is a volumetric average of stresses of two phases:

$\bar{\sigma} = \alpha \sigma_1 + (1 - \alpha) \sigma_2$ , where the  $\sigma_1$  is the stress of phase 1 and  $\sigma_2$  the stress of phase 2.

To get the volumetrically homogenized flow law of a quartzite, one requires the knowledge of the strain rate and stress in each phase.

Assuming the strain rate is uniform throughout a quartzite and combining two dislocation creep flow laws (Eqs.5.3 and 5.4) and the expression of bulk stress, we get the homogenized flow law under a uniform-strain-rate assumption:

$$\bar{\sigma} = \alpha A \frac{1}{n_1} f_w^{\frac{m_1}{n_1}} \exp\left(\frac{Q_1 + PV_1}{n_1 RT}\right) \bar{\epsilon}^{-\frac{1}{n_1}} + (1 - \alpha) A \frac{1}{n_2} f_w^{\frac{m_2}{n_2}} \exp\left(\frac{Q_2 + PV_2}{n_2 RT}\right) \bar{\epsilon}^{-\frac{1}{n_2}} \quad (5.5)$$



Similarly, assuming the stress is uniform throughout a quartzite and combining two dislocation creep flow laws (Eqs.5.3 and 5.4) and the expression of bulk strain rate, we obtain the homogenized flow law under a uniform-stress assumption:

$$\bar{\dot{\epsilon}} = \alpha A f_w^{m_1} \exp\left(-\frac{Q_1 + PV_1}{RT}\right) \bar{\sigma}^{n_1} + (1 - \alpha) A f_w^{m_2} \exp\left(-\frac{Q_2 + PV_2}{RT}\right) \bar{\sigma}^{n_2} \quad (5.6)$$

Eq.5.5 and Eq.5.6 are the Voigt (887) average and the Reuss (1929) average, respectively. They are commonly regarded as the upper and lower limits (Nemat-Nasser & Hori, 1999). Under the uniform-stress assumption, we can construct a deformation mechanism map for wet quartzites using two dislocation creep flow laws (Eqs.5.3 and 5.4) as a plot of differential stress versus temperature at constant pressure (Fig.5.4a). Fig.5.4a allows us to determine the strain rate of prism <a> slip ( $\dot{\epsilon}_1$ ) and the strain rate of basal <a> slip ( $\dot{\epsilon}_2$ ) at a temperature and stress. Similarly, we construct a deformation mechanism map for wet quartzites as a plot of strain rate against temperature at constant pressure (Fig.5.4b), assuming the strain rate is uniform. We can obtain the differential stress of prism <a> slip ( $\sigma_1$ ) and the differential stress of basal <a> slip ( $\sigma_2$ ) in Fig.5.4b at a temperature and strain rate. According to the deformation mechanism maps of quartzites (Fig.5.4), the strain rates/stresses of two slip systems are comparable (differ less than one order of magnitude), in most of the natural deformation conditions ( $t = 300^\circ\text{C} \sim 700^\circ\text{C}$ ,  $\sigma = 10\text{MPa} \sim 200\text{MPa}$ ,  $\dot{\epsilon} = 10^{-13}\text{s}^{-1} \sim 10^{-11}\text{s}^{-1}$ ), which is consistent with the quartz c-axis from both natural mylonites or experimental samples.

However, the Voigt average and Reuss average are too far away to allow accurate evaluations of bulk rheological properties. Furthermore, neither uniform-stress assumption nor uniform-strain-rate assumption is realistic. The partitioned strain rates and stresses in individual quartz grains depend on their shapes, orientations, rheological properties as well as preferred orientation development. Therefore, a more rigorous micromechanics-based self-consistent homogenization method (e.g., Jiang, 2014, 2016, and references therein) is required to evaluate the bulk rheology. In such a case, the

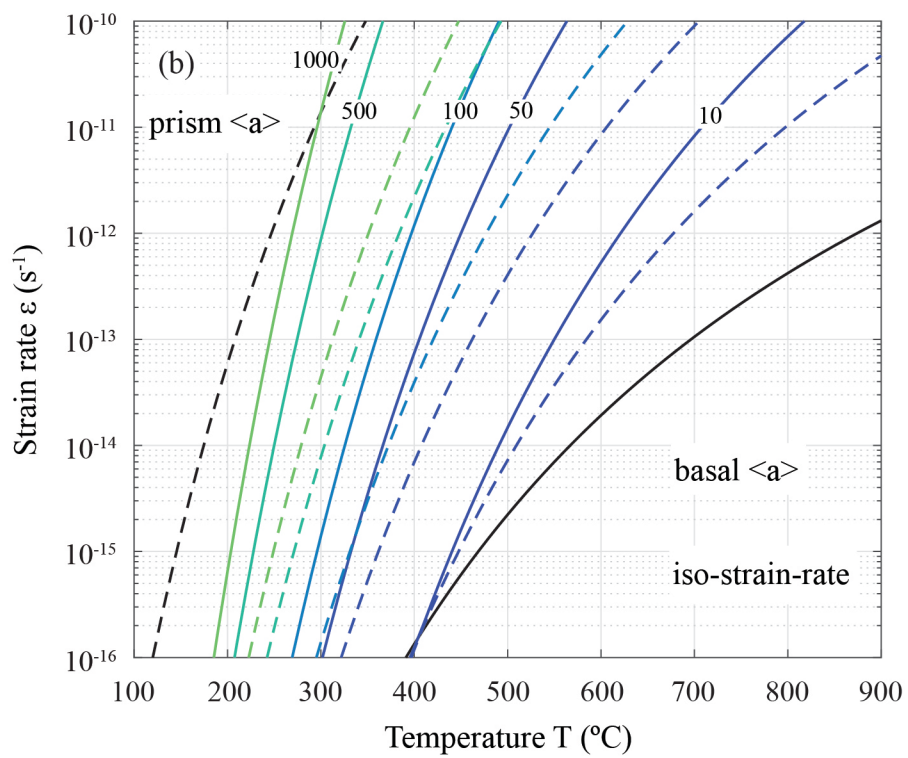
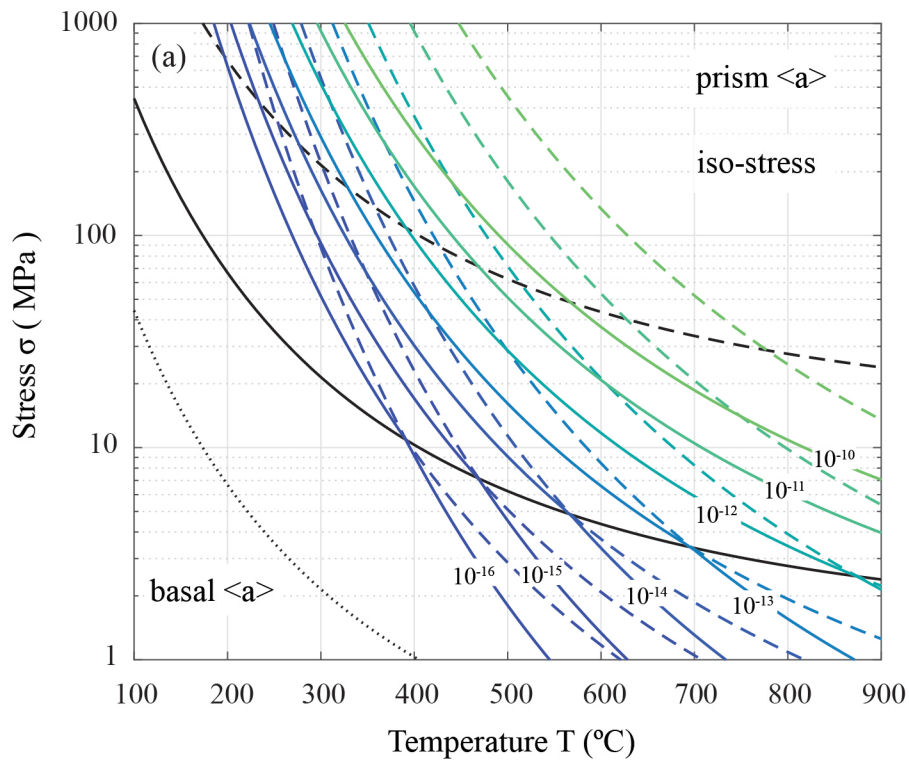


**Figure 5.4 Deformation mechanism maps for quartzite**

**(a) A plot of differential stress versus temperature at 400MPa. Two distinct fields are separated by a solid black line. On the solid black line, the strain rates of prism <a> and basal <a> slip systems are equal. The solid colored lines are the strain-rate contour lines ( $10^{-10} \text{ s}^{-1}$ ,  $10^{-11} \text{ s}^{-1}$ ,  $10^{-10} \text{ s}^{-1}$ ,  $10^{-10} \text{ s}^{-1}$ , and  $10^{-10} \text{ s}^{-1}$ ) of the dominant slip system; the dashed colored lines represent the strain-rate contour lines of the other slip system. On the dashed black line, prism <a> slip system is ten times faster than basal <a> slip system. On the dotted black line, basal <a> slip system is ten times faster than prism <a> slip system. (b) A plot of strain rate versus temperature at 400MPa. Two distinct fields are separated by a solid black line. On the solid black line, the differential stresses of prism <a> and basal <a> slip systems are equal. The solid colored lines are the stress contour lines (10 MPa, 50 MPa, 100 MPa, 500 MPa, and 1000 MPa) of the dominant slip system; the dashed colored lines represent the stress contour lines of the other slip system. On the dashed black line, the differential stress of prism <a> slip system is ten times smaller than that of basal <a> slip system.**

actual rheology of a polycrystalline aggregate is anisotropic and evolves with time. It cannot be expressed in a simple scalar equation like Eqs.5.5. Numerical calculations (e.g., Jiang, 2014) are required to obtain actual time-dependent rheological behaviors.

In Micromechanics, the overall rheological property of a polyphase material is defined as the average property over a Representative Volume Element (RVE) (Fig.5.5), which contains a large number of constituent elements. Consider a quartzite made of  $N$  constituent elements, which are quartz grains, denoted by  $k = 1, 2, \dots, N$ . Applying the concept of the Homogenous Equivalent Medium (HEM) (e.g., Lebensohn and Tomé, 1993; Jiang, 2014), each quartz grain is regarded as an ellipsoidal inclusion embedded in HEM (Fig.5.5), whose rheological properties are obtained from the overall rheological properties of the RVE. Known the shapes, orientations, and the rheological properties of all grains, the general Eshelby's formalism (Jiang, 2014) allows the determination of partitioned strain rates and stresses in individual grains:

$$\boldsymbol{\varepsilon}^{(k)} = \mathbf{A}^{(k)} : \mathbf{E} ; \boldsymbol{\sigma}^{(k)} = \mathbf{B}^{(k)} : \boldsymbol{\Sigma} \quad (5.7)$$

In Eq.5.7, the sign “:” stands for the double-index contraction of two tensors.  $\boldsymbol{\varepsilon}^{(k)}$  and  $\boldsymbol{\sigma}^{(k)}$  are the partitioned strain rate and deviatoric stress tensors. The uppercase symbols  $\mathbf{E}$  and  $\boldsymbol{\Sigma}$  are the corresponding quantities at infinity.  $\mathbf{A}^{(k)}$  and  $\mathbf{B}^{(k)}$  are 4<sup>th</sup> order strain rate partitioning and stress partitioning tensors for each inclusion, and they are related to the inclusion shape and orientation and viscous stiffness (viscosity) of the matrix (HEM). The partitioned strain rates and deviatoric stresses, in turn, are used to evaluate the bulk rheology of the composite material (Lebensohn and Tomé, 1993; Jiang, 2014). These two opposite processes relied on the same equation (Eq.5.7), and they must be solved simultaneously, which is called self-consistent. Numerical calculations in this paper using Eq.5.7 are realized using MATLAB scripts, the algorithms for which are in the literature (Jiang, 2014, 2016; Qu et al., 2016) and Chapter 2.

Here we consider a two-phase quartzite made of 500 ellipsoidal quartz grains with their shapes (long axis: intermediate axis: short axis): 1-10: 1-10: 1. We assume that all quartz

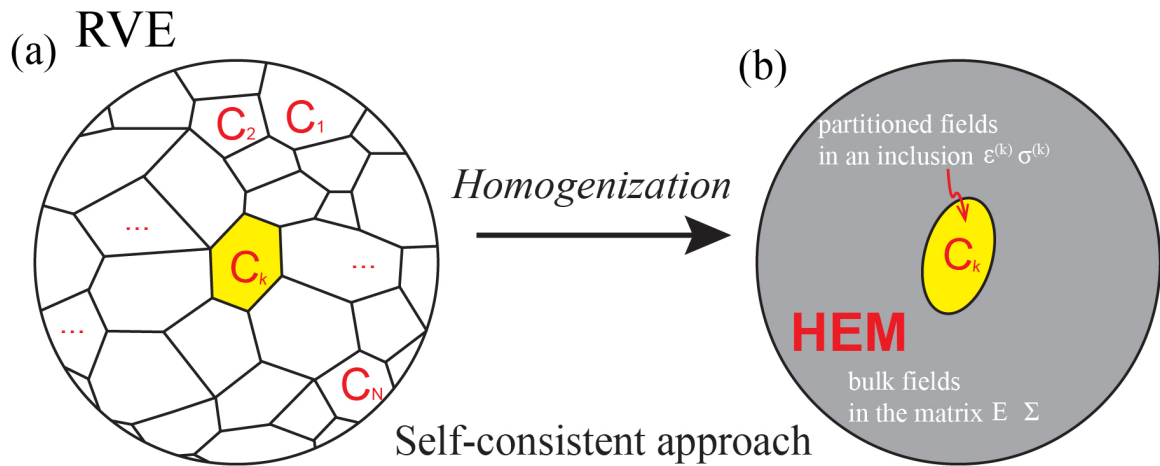


**Figure 5.5** A conceptual diagram of the self-consistent homogenization approach

A quartzite made of  $N$  constituent quartz grains, denoted by  $k = 1, 2, \dots, N$ . The overall rheological property of the quartzite is defined as the average property over a Representative Volume Element (RVE) (a), which contains a large number of quartz grains. Each quartz grain is regarded as an ellipsoidal inclusion embedded in the Homogenous Effective Medium (HEM) (b), whose rheological properties are obtained from the overall rheological properties of the RVE. To get the overall rheology from the constituents' properties is called homogenization.  $\epsilon^{(k)}$  and  $\sigma^{(k)}$  are the partitioned strain rate and deviatoric stress in a constituent grain. The uppercase symbols  $E$  and  $\Sigma$  are the corresponding bulk quantities in the matrix.

grains are isotropic and randomly distributed; therefore, the whole quartz aggregates is also isotropic. As the self-consistent homogenization method involves tensor calculations, like Eq.5.7, the tensor-form flow law of quartzite is required. In order to generalize the tensor-form equation, one needs to rewrite the flow laws in the form of Eq.5.1 in terms of second invariants of the deviatoric stress ( $\sigma_E$ ) and strain rate ( $\dot{\epsilon}_E$ ) as

$$\dot{\epsilon}_E = A_i f_w^m \exp\left(-\frac{Q+PV}{RT}\right) \sigma_E^n, \text{ where } A_i = \frac{3^{(n+1)/2}}{2} A \text{ (Ranalli, 1987, p.70). Then the}$$

tensor-form constitutive equation of isotropic materials is expressed as (Ranalli, 1987, p.70):

$$\sigma_{ij} = 2\eta_{eff} \epsilon_{ij} \quad (5.8a)$$

$$\eta_{eff} = \frac{1}{2} A_i^{-1} f_w^{-m} \exp\left(\frac{Q+PV}{RT}\right) \sigma_E^{1-n} \text{ or} \quad (5.8b)$$

$$\eta_{eff} = \frac{1}{2} A_i^{\frac{1}{n}} f_w^{-\frac{m}{n}} \exp\left(\frac{Q+PV}{nRT}\right) \dot{\epsilon}_E^{\left(\frac{1}{n}-1\right)} \quad (5.8c)$$

where  $\sigma_{ij}$  and  $\epsilon_{ij}$  are the components of the deviatoric stress and strain rate tensors;  $\eta_{eff}$  is the effective viscosity defined at a given state of stress or strain rate. The effective viscosities of all quartz grains at a given state of stress or strain rate can be obtained using the parameters in Table 5.1. Then numerical simulations allow us to evaluate the bulk rheological properties of two-phase quartzite with varying contributions of dominant slip systems.

In order to show the variation of strength predictions based on different quartz flow laws, we construct the strength profiles using two dislocation creep flow laws (Eqs.5.3 and 5.4) and the calculated bulk strengths with varying contributions of the prism <a> slip system in Fig.5.6. We used homogenized flow laws under uniform-strain-rates (Eq.5.5) and uniform-stress (Eq.5.6) conditions and the self-consistent homogenization approach to evaluate the bulk strengths. Note, we have converted Eq.5.5 and Eq.5.6 in terms of  $\sigma_E$

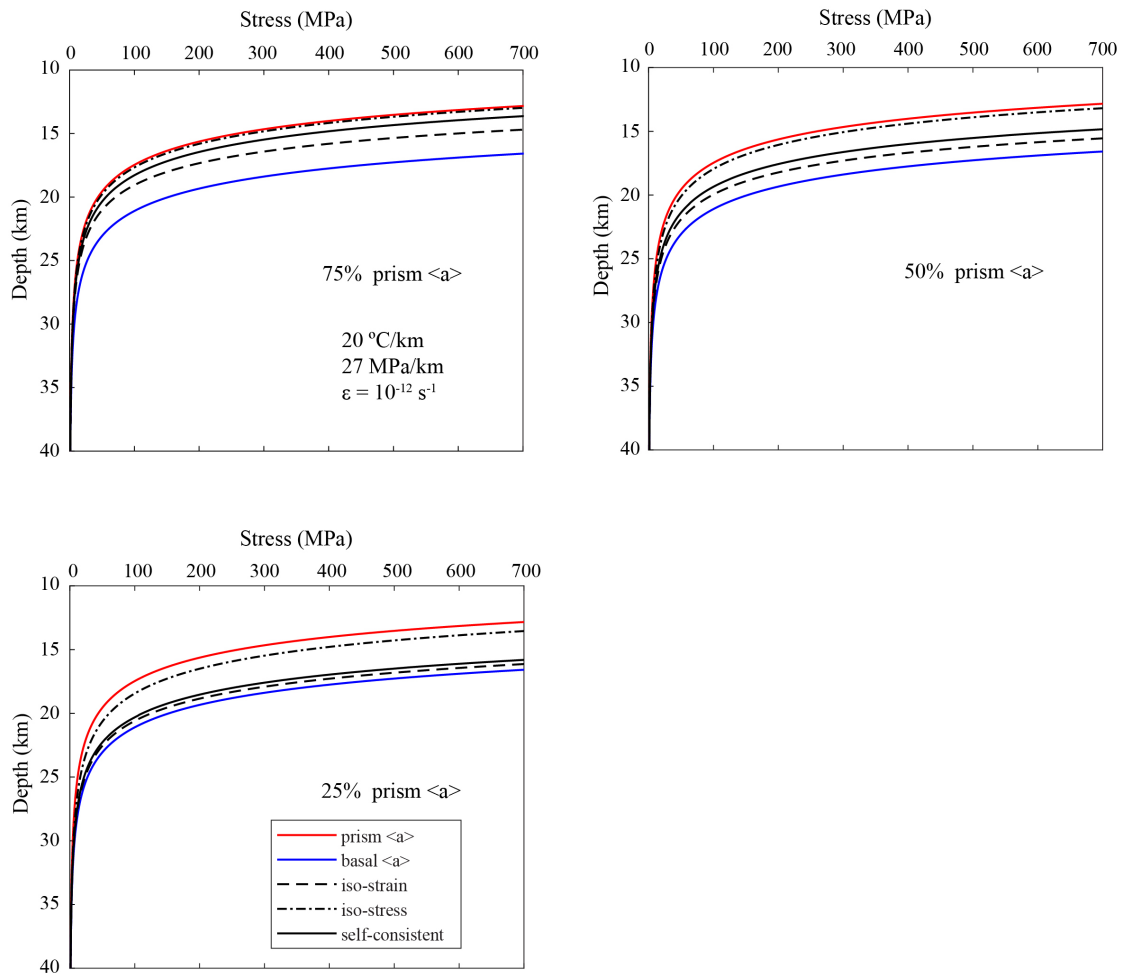


**Figure 5.6** The strength profiles of the continental lithosphere using the two dislocation creep flow laws and the calculated bulk strengths of quartzite with varying contributions of prism <a> slip system

The bulk strengths of quartzite are evaluated using homogenized flow laws assuming uniform-strain-rate (dashed line) and uniform-stress (dashed-dotted line) and a self-consistent approach (solid line). The red line represents flow law in Eq.3, and the blue line represents flow law in Eq.4. A reference strain rate  $\dot{\epsilon}_E = 10^{-12} \text{ s}^{-1}$  and a geothermal gradient of 20°C/km are used. The water partial pressure is assumed to equal to the lithostatic pressure. The contributions of prism <a> slip system are (a) 25%, (b) 50%, and (c) 75%.

and  $\dot{\epsilon}_E$  in Fig.5.6 to keep consistency in all three calculations. A reference strain rate  $\dot{\epsilon}_E = 10^{-12} \text{ s}^{-1}$  and a geothermal gradient of  $20^\circ\text{C}/\text{km}$  are used. The water partial pressure is assumed to equal to the lithostatic pressure. The strength of the wet quartzites deformed by creep in the transitional regime depends on the relative contribution of dominant slip systems. As the contribution of prism  $\langle a \rangle$  slip decreases, the bulk strength of wet quartzites increases. Therefore, evaluating the relative significance of dominant slip systems using quartz c-axis fabrics is crucial to understand the rheology and strength information that mylonites may provide. Furthermore, the bulk strength of wet quartzites highly depends on the mixing models used for homogenization. The homogenized flow law under the iso-strain-rate assumption gives the highest estimation of bulk strength, followed by the self-consistent approach and then the homogenized flow law under the iso-stress assumption.

## 5.5 Discussions

We have shown that existing experimental data as collected in Appendix C are consistent with the following creep behaviors for wet quartzites: When prism  $\langle a \rangle$  is the dominant slip system with characteristic Y-max c-axis fabrics, wet quartzites flow according to Eq.5.3. When basal  $\langle a \rangle$  is the dominant slip system with diagnostic strong clusters of c-axes in the periphery, the dislocation creep of wet quartzites follows Eq.5.4. When both slip systems are significant, the transitional creep behavior can be approximated by the superposition of two dislocation creep behaviors. Our results are derived from fitting experimental data from well-controlled experiments iteratively into a flow law (Eq.5.1) that includes the dependence of the activation enthalpy on pressure (Lu and Jiang, 2019).

Tokle et al. (2019) took a different approach. They also obtained two dislocation creep flow laws corresponding to dominant prism  $\langle a \rangle$  and basal  $\langle a \rangle$  slip systems respectively. First, they regarded the difference in flow law parameters from existing experiments as solely due to  $f_w$  variations as in Kohlstedt et al. (1995). Second, they used experimental data (their Appendix A) to obtain two “laboratory fit flow laws” and estimations of stress,



strain rate, and temperature from natural mylonite samples to determine two “extrapolated fit flow laws”. In the former, they obtained  $n = 4$ ,  $m = 1$ , and  $Q = 140 \pm 15$  kJ/mol for prism  $\langle a \rangle$  slip system and  $n = 2.7$ ,  $m = 1.1$ , and  $Q = 105 \pm 15$  kJ/mol for basal  $\langle a \rangle$  slip system. In the latter, they got  $n = 4$ ,  $m = 1$ , and  $Q = 125 \pm 15$  kJ/mol for prism  $\langle a \rangle$  slip system and  $n = 3$ ,  $m = 1.2$ , and  $Q = 115 \pm 15$  kJ/mol for basal  $\langle a \rangle$  slip system.

We believe the pressure dependence of the activation enthalpy is significant, and considering  $f_w$  variation alone using the flow law  $\dot{\epsilon} = Af_w^m \exp\left(-\frac{Q}{RT}\right)\sigma^n$  cannot explain the difference between Luan and Paterson (1994) and Gleason and Tullis (1994) as we explained in Lu and Jiang (2019). When the effect of  $PV$  term is considered, the water fugacity exponent  $m$  is no longer an independent parameter (Eq.5.2) but must be determined self-consistently through an iterative approach. The effort of Tokle et al. (2019) to fit natural stress, strain rate, and temperature estimates is essential to determine the  $Q$  value. In doing so, they slightly adjusted the values of  $n$  and  $m$  determined for the “laboratory fit flow law” for basal  $\langle a \rangle$  slip system to better fit the natural data. The new  $Q$  values are calculated by fitting stress and strain rate estimations from natural mylonite samples, disregarding  $Q$  values determined from experimental data. We have pointed out that stress and strain rate estimates from natural mylonite samples have uncertainties too great to allow reasonably accurate flow laws to be determined (Lu and Jiang, 2019).

In the transitional flow regime, Tokle et al. (2019) attributed the creep qualitatively to the contribution of grain boundary sliding mechanism. Whereas grain boundary sliding may be more significant in the creep experiment dataset considered by Tokle et al. (2019) as they included ultrafine-grained samples (1.7-12 $\mu\text{m}$ ; Fukuda et al., 2018; Richter et al., 2018), the dataset we used this work (Appendix C) is mainly from samples with grain size between 20-200  $\mu\text{m}$ , where dislocation creep is likely the dominant deformation mechanism. This is supported by quartz c-axis fabrics suggesting the mixture of basal  $\langle a \rangle$ , prism  $\langle a \rangle$ , and rhomb  $\langle a \rangle$  slips in both experiments (Fig.5.3) and nature. Grain

boundary sliding mechanism can only weaken preferred quartz c-axis fabrics produced by dislocation creeps and cannot produce new c-axis fabric patterns. We believe the creep of wet quartzites in such transitional regime may be caused by the activation of prism  $\langle a \rangle$  and basal  $\langle a \rangle$  slip systems. The bulk rheological properties of wet quartzites can be obtained using homogenized flow laws under uniform-strain-rate (Eqs.5.5) and uniform-stress assumptions (Eqs.5.6), as well as a self-consistent approach.

We wish to point out that a dislocation creep always requires activation of multiple slip systems, although one slip system may be dominant. The division of the flow behavior into end members and transitional behaviors are somewhat subjective. There is a continuous spectrum from dominant prism  $\langle a \rangle$  slip to a mixture of prism  $\langle a \rangle$  and basal  $\langle a \rangle$  slip to dominant basal  $\langle a \rangle$  slip. For convenience of description, we have regarded the flow behaviors where both prism  $\langle a \rangle$  and basal  $\langle a \rangle$  slip are significant as transitional flow. However, no clear boundaries are expected between them. This point is clear both from the observed quartz c-axis fabric patterns as well as the plots of stress versus strain rate of some experiments (Fig.5.3).

## 5.6 Conclusions

We have determined wet quartzite flow laws based on carefully selected creep experiments believed to be in regimes 2 and 3 dislocation creep by considering both the pressure dependence of the activation enthalpy and slip system dependence of the stress exponent. Our approach to determine the flow law parameters is self-consistent and iterative, solely based on experimental data.

The creep behavior of wet quartzites can be summarized as follows: At higher temperatures and lower stresses, they deform predominantly by prism  $\langle a \rangle$  slip, producing characteristic Y-max c-axis fabrics, and follow Eq.5.3. At lower temperatures and higher stresses, where basal  $\langle a \rangle$  is the dominant slip system with diagnostic strong clusters of c-axes in the periphery, the dislocation creep of wet quartzites follows Eq.5.4. Quartz c-axis fabrics from natural and experimental samples, and the study of the deformation mechanism map suggested that the activation of multiple slip systems is common. Where

dislocation creep through multiple slip systems is the main mechanism, the transitional flow behavior may be approximated by homogenized flow laws (Eq.5.5 and Eq.5.6) or a self-consistent approach.

## 5.7 References

- Ashby, M. F. (1972). A first report on deformation-mechanism maps. *Acta Metallurgica*, 20(7), 887-897. [https://doi.org/10.1016/0001-6160\(72\)90082-X](https://doi.org/10.1016/0001-6160(72)90082-X)
- Behr, W. M., & Platt, J. P. (2011). A naturally constrained stress profile through the middle crust in an extensional terrane. *Earth and Planetary Science Letters*, 303(3-4), 181-192. <https://doi.org/10.1016/j.epsl.2010.11.044>
- Béjina, F., Jaoul, O., & Liebermann, R. C. (2003). Diffusion in minerals at high pressure: a review. *Physics of the Earth and Planetary Interiors*, 139(1-2), 3-20. [https://doi.org/10.1016/S0031-9201\(03\)00140-7](https://doi.org/10.1016/S0031-9201(03)00140-7)
- Chernak, L. J., Hirth, G., Selverstone, J., & Tullis, J. (2009). Effect of aqueous and carbonic fluids on the dislocation creep strength of quartz. *Journal of Geophysical Research: Solid Earth*, 114(B4). <https://doi.org/10.1029/2008JB005884>.
- Dorn, J. E. (1955). Some fundamental experiments on high temperature creep. *Journal of the Mechanics and Physics of Solids*, 3(2), 85-116. [https://doi.org/10.1016/0022-5096\(55\)90054-5](https://doi.org/10.1016/0022-5096(55)90054-5)
- Freer, R. (1981). Diffusion in silicate minerals and glasses: a data digest and guide to the literature. *Contributions to Mineralogy and Petrology*, 76(4), 440-454.
- Frost, H. J., & Ashby, M. F. (1982). *Deformation mechanism maps: the plasticity and creep of metals and ceramics*. Pergamon Press.
- Fukuda, J. I., Holyoke III, C. W., & Kronenberg, A. K. (2018). Deformation of Fine-Grained Quartz Aggregates by Mixed Diffusion and Dislocation Creep. *Journal of Geophysical Research: Solid Earth*, 123(6), 4676-4696. <https://doi.org/10.1029/2017JB015133>

- Gleason, G. C., & Tullis, J. (1995). A flow law for dislocation creep of quartz aggregates determined with the molten salt cell. *Tectonophysics*, 247(1-4), 1-23. [https://doi.org/10.1016/00401951\(95\)00011-B](https://doi.org/10.1016/00401951(95)00011-B).
- Goldsby, D. L., & Kohlstedt, D. L. (2001). Superplastic deformation of ice: Experimental observations. *Journal of Geophysical Research: Solid Earth*, 106(B6), 11017-11030. <https://doi.org/10.1029/2000JB900336>
- Heilbronner, R., & Tullis, J. (2002). The effect of static annealing on microstructures and crystallographic preferred orientations of quartzites experimentally deformed in axial compression and shear. *Geological Society, London, Special Publications*, 200(1), 191-218. <https://doi.org/10.1144/GSL.SP.2001.200.01.12>.
- Heilbronner, R., & Tullis, J. (2006). Evolution of c axis pole figures and grain size during dynamic recrystallization: Results from experimentally sheared quartzite. *Journal of Geophysical Research: Solid Earth*, 111(B10). <https://doi.org/10.1029/2005JB004194>.
- Hirth, G., & Tullis, J. (1992). Dislocation creep regimes in quartz aggregates. *Journal of structural geology*, 14(2), 145-159. [https://doi.org/10.1016//0191-8141\(92\)90053-Y](https://doi.org/10.1016//0191-8141(92)90053-Y).
- Hirth, G., & Kohlstedt, D. (2004). Rheology of the upper mantle and the mantle wedge: A view from the experimentalists. *Inside the subduction Factory*, 138, 83-105. <https://doi.org/10.1029/138GM06>
- Hobbs, B. E., Ord, A., Ulrich, S., & Schulmann, K. (2019). Rheology of mixed deformation mechanisms and mineral phase assemblages. *Journal of Structural Geology*, 103891. <https://doi.org/10.1016/j.jsg.2019.103891>
- Holyoke, C. W., & Kronenberg, A. K. (2010). Accurate differential stress measurement using the molten salt cell and solid salt assemblies in the Griggs apparatus with

- applications to strength, piezometers and rheology. *Tectonophysics*, 494(1-2), 17-31. <https://doi.org/10.1016/j.tecto.2010.08.001>
- Holyoke, C. W., & Kronenberg, A. K. (2013). Reversible water weakening of quartz. *Earth and Planetary Science Letters*, 374, 185-190. <https://doi.org/10.1016/j.epsl.2013.05.039>.
- Holyoke, C. W., & Tullis, J. (2006). Mechanisms of weak phase interconnection and the effects of phase strength contrast on fabric development. *Journal of Structural Geology*, 28(4), 621-640. <https://doi.org/10.1016/j.jsg.2006.01.008>.
- Hutchinson, J. W. (1976). Bounds and self-consistent estimates for creep of polycrystalline materials. *Proceedings of the Royal Society of London. A. Mathematical and Physical Sciences*, 348(1652), 101-127. <https://doi.org/10.1098/rspa.1976.0027>
- Jiang, D., & Bentley, C. (2012). A micromechanical approach for simulating multiscale fabrics in large-scale high-strain zones: Theory and application. *Journal of Geophysical Research: Solid Earth*, 117(B12). <https://doi.org/10.1029/2012JB009327>
- Jiang, D. (2014). Structural geology meets micromechanics: A self-consistent model for the multiscale deformation and fabric development in Earth's ductile lithosphere. *Journal of Structural Geology*, 68, 247-272. <https://doi.org/10.1016/j.jsg.2014.05.020>
- Jiang, D. (2016). Viscous inclusions in anisotropic materials: Theoretical development and perspective applications. *Tectonophysics*, 693, 116-142. <https://doi.org/10.1016/j.tecto.2016.10.012>
- Karato, S. I., & Jung, H. (2003). Effects of pressure on high-temperature dislocation creep in olivine. *Philosophical Magazine*, 83(3), 401-414. <https://doi.org/10.1080/0141861021000025829>.

- Kidder, S., Hirth, G., Avouac, J. P., & Behr, W. (2016). The influence of stress history on the grain size and microstructure of experimentally deformed quartzite. *Journal of Structural Geology*, 83, 194-206. <https://doi.org/10.1016/j.jsg.2015.12.004>.
- Koch, P. S., Christie, J. M., Ord, A., & George Jr, R. P. (1989). Effect of water on the rheology of experimentally deformed quartzite. *Journal of Geophysical Research: Solid Earth*, 94(B10), 13975-13996. <https://doi.org/10.1029/JB094iB10p13975>
- Kohlstedt, D. L., Evans, B., & Mackwell, S. J. (1995). Strength of the lithosphere: Constraints imposed by laboratory experiments. *Journal of Geophysical Research: Solid Earth*, 100(B9), 17587–17602. <https://doi.org/10.1029/95JB01460>
- Kronenberg, A. K., & Tullis, J. (1984). Flow strengths of quartz aggregates: grain size and pressure effects due to hydrolytic weakening. *Journal of Geophysical Research: Solid Earth*, 89(B6), 4281-4297. <https://doi.org/10.1029/JB089iB06p04281>
- Langdon, T. G., & Mohamed, F. A. (1976). Deformation mechanism maps for ceramics. *Journal of Materials Science*, 11(2), 317-327. <https://doi.org/10.1007/BF00551443>
- Lebensohn, R. A., & Tomé, C. N. (1993). A self-consistent anisotropic approach for the simulation of plastic deformation and texture development of polycrystals: application to zirconium alloys. *Acta metallurgica et materialia*, 41(9), 2611-2624. [https://doi.org/10.1016/0956-7151\(93\)90130-K](https://doi.org/10.1016/0956-7151(93)90130-K).
- Lu, L. X., & Jiang, D. (2019). Quartz Flow Law Revisited: The Significance of Pressure Dependence of the Activation Enthalpy. *Journal of Geophysical Research: Solid Earth*, 124(1), 241-256. <https://doi.org/10.1029/2018JB016226>

- Luan, F. C., & Paterson, M. S. (1992). Preparation and deformation of synthetic aggregates of quartz. *Journal of Geophysical Research: Solid Earth*, 97(B1), 301-320. <https://doi.org/10.1029/91JB01748>.
- Nachlas, W. O., & Hirth, G. (2015). Experimental constraints on the role of dynamic recrystallization on resetting the Ti-in-quartz thermobarometer. *Journal of Geophysical Research: Solid Earth*, 120(12), 8120-8137. <https://doi.org/10.1002/2015JB012274>.
- Nemat-Nasser, S., Hori, M., 1999. *Micromechanics: Overall Properties of Heterogeneous Materials*. Second revised edition. Elsevier.
- Paterson, M. S., & Olgaard, D. L. (2000). Rock deformation tests to large shear strains in torsion. *Journal of structural Geology*, 22(9), 1341-1358. [https://doi.org/10.1016/S0191-8141\(00\)00042-0](https://doi.org/10.1016/S0191-8141(00)00042-0).
- Pitzer, K. S., & Sterner, S. M. (1994). Equations of state valid continuously from zero to extreme pressures for H<sub>2</sub>O and CO<sub>2</sub>. *The Journal of Chemical Physics*, 101(4), 3111–3116. <https://doi.org/10.1063/1.467624>
- Post, A. D., Tullis, J., & Yund, R. A. (1996). Effects of chemical environment on dislocation creep of quartzite. *Journal of Geophysical Research: Solid Earth*, 101(B10), 22143-22155. <https://doi.org/10.1029/96JB01926>.
- Qu, M., Jiang, D., & Lu, L. X. (2016). An optimal scheme for numerical evaluation of Eshelby tensors and its implementation in a MATLAB package for simulating the motion of viscous ellipsoids in slow flows. *Computers & geosciences*, 96, 98-108. <https://doi.org/10.1016/j.cageo.2016.08.005>
- Ranalli, G. (1987). *Rheology of the Earth: Deformation and Flow Processes in Geophysics and Geodynamics*. Boston: Allen & Unwin.



- Reuss, A. (1929). Berechnung der fließgrenze von mischkristallen auf grund der plastizitätsbedingung für einkristalle. *ZAMM-Journal of Applied Mathematics and Mechanics/Zeitschrift für Angewandte Mathematik und Mechanik*, 9(1), 49-58.
- Richter, B., Stünitz, H., & Heilbronner, R. (2016). Stresses and pressures at the quartz-to-coesite phase transformation in shear deformation experiments. *Journal of Geophysical Research: Solid Earth*, 121(11), 8015-8033. <https://doi.org/10.1002/2016JB013084>.
- Richter, B., Stünitz, H., & Heilbronner, R. (2018). The brittle-to-viscous transition in polycrystalline quartz: An experimental study. *Journal of Structural Geology*, 114, 1-21. <https://doi.org/10.1016/j.jsg.2018.06.005>.
- Rutter, E. H., & Brodie, K. H. (2004). Experimental intracrystalline plastic flow in hot-pressed synthetic quartzite prepared from Brazilian quartz crystals. *Journal of Structural Geology*, 26(2), 259-270. [https://doi.org/10.1016/S0191-8141\(03\)00096-8](https://doi.org/10.1016/S0191-8141(03)00096-8).
- Rybacki, E., Gottschalk, M., Wirth, R., & Dresen, G. (2006). Influence of water fugacity and activation volume on the flow properties of fine-grained anorthite aggregates. *Journal of Geophysical Research: Solid Earth*, 111(B3). <https://doi.org/10.1029/2005JB003663>
- Sherby, O. D., & Burke, P. M. (1968). Mechanical behavior of crystalline solids at elevated temperature. *Progress in Materials Science*, 13, 323–390. [https://doi.org/10.1016/0079-6425\(68\)90024-8](https://doi.org/10.1016/0079-6425(68)90024-8)
- Stipp, M., Stünitz, H., Heilbronner, R., & Schmid, S. M. (2002). The eastern Tonale fault zone: a ‘natural laboratory’ for crystal plastic deformation of quartz over a temperature range from 250 to 700 C. *Journal of structural geology*, 24(12), 1861-1884. [https://doi.org/10.1016/S01918141\(02\)00035-4](https://doi.org/10.1016/S01918141(02)00035-4).

- Stipp, M., & Tullis, J. (2003). The recrystallized grain size piezometer for quartz. *Geophysical Research Letters*, 30(21).  
<https://doi.org/10.1029/2003GL018444>.
- Stipp, M., Tullis, J., & Behrens, H. (2006). Effect of water on the dislocation creep microstructure and flow stress of quartz and implications for the recrystallized grain size piezometer. *Journal of Geophysical Research: Solid Earth*, 111(B4).<https://doi.org/10.1029/2005JB003852>.
- Stocker, R. L., & Ashby, M. F. (1973). On the rheology of the upper mantle. *Reviews of Geophysics*, 11(2), 391-426. <https://doi.org/10.1029/RG011i002p00391>
- Tokle, L., Stunitz, H., & Hirth, G., (2013). The effect of muscovite on the fabric evolution of quartz under general shear. In: American Geophysical Union Fall Meeting. Abstract T53A-2559.
- Tokle, L., Hirth, G., & Behr, W. M. (2019). Flow laws and fabric transitions in wet quartzite. *Earth and Planetary Science Letters*, 505, 152-161.  
<https://doi.org/10.1016/j.epsl.2018.10.017>
- Tóth, L. S., Molinari, A., & Bouaziz, O. (2009). Effective strain rate sensitivity of two-phase materials. *Materials Science and Engineering: A*, 524(1-2), 186-192.  
<https://doi.org/10.1016/j.msea.2009.06.041>
- Tullis, J., & Wenk, H. R. (1994). Effect of muscovite on the strength and lattice preferred orientations of experimentally deformed quartz aggregates. *Materials Science and Engineering: A*, 175(1-2), 209-220. [https://doi.org/10.1016/0921-5093\(94\)91060-X](https://doi.org/10.1016/0921-5093(94)91060-X).
- Whitney, D. L., Teyssier, C., Seaton, N. C., & Fornash, K. F. (2014). Petrofabrics of high-pressure rocks exhumed at the slab-mantle interface from the “point of no return” in a subduction zone (Sivrihisar, Turkey). *Tectonics*, 33 (12), 2315-2341.  
<https://doi.org/10.1002/2014TC003677>.

Voigt, W. (1887). *Theoretische studien über die elasticitätsverhältnisse der krystalle.* in der Dieterichschen Buchhandlung.

## Chapter 6

### 6 Conclusions and Future Work

#### 6.1 Conclusions

This thesis makes contributions to the understanding of the continental rheology and how the variations in the continental rheology control the multiscale deformation patterns in Earth's lithosphere by applying the micromechanics-based MultiOrder Power Law Approach together with high-quality experimental data of wet quartzites and geological records in natural rocks.

The main contributions are summarized below:

- (1) This thesis briefly summarizes the backbone theory and the important equations of MOPLA for better reference and refines the algorithm of MOPLA in Jiang, (2014). Then, in order for the high-performance computing, the refined algorithm of MOPLA has been implemented in MATLAB, a powerful and popular software, incorporating the optimal scheme of Qu et al. (2016) to evaluate the Eshelby tensors efficiently and using the MATLAB built-in Parallel Computing Toolbox as well. The MATLAB package of MOPLA has been validated by applying it to the fabric development in Cascade Lake shear zone (Jiang, 2014). This work also provides a manual for the MOPLA MATLAB package and gives an example showing how to use it to investigate the multiscale lithospheric deformation.
- (2) A new micromechanics-based shear zone model has been proposed by considering the large-scale shear zone as a planar heterogeneous inclusion embedded in the ductile lithosphere subjected to the remote plate motion. The extended Eshelby's solutions on inclusions for interior and exterior fields are used to investigate the partitioned kinematic and mechanical fields inside and outside the shear zone from the tectonic scale deformation due to the remote plate motion. The kinematic fields inside the shear zone govern the finite strain accumulation

there. This complete mechanical approach also allows the investigation of the stress distribution and the rheology of the shear zone. The overall strength of the heterogeneous poly-element shear zone can be obtained by means of a self-consistent homogenization scheme from the properties of its constituent elements.

- (3) The geometric results deduced from this model are compared with the fabric data collected from Shangdan Tectonic Zone in Qinling Orogenic belt, which helps us to validate this model and constrain the convergence angle during the deformation time in this field area to  $5^{\circ} \sim 20^{\circ}$ .
- (4) This model has been applied to the San Andreas Fault (SAF) in Central California to validate it and understand the stress distribution within and in the vicinity of SAF in the ductile region. The plate motion between the North America and Pacific Plates ultimately determines the stress field in this area. The presence of the weak SAF in the ductile region can account for a narrow band of stress rotation; however, it cannot explain the widespread thrust faults and upright folds perpendicular to the SAF.
- (5) The rheology of the large-scale shear zone is crucial to understand the continental rheology. This thesis discusses the strength of the large-scale shear zone by applying the self-consistent homogenization scheme to the mylonite zone in the Grenville Front Tectonic Zone. This work quantitatively demonstrates that the presence of weak minerals, like mica and the rheological anisotropy due to the development of fabrics in the shear zone significantly weaken the shear zone with respect to shearing along the foliation plane. It is oversimplified to use the strength of the quartz aggregates to represent the shear zone strength or even to constrain the continental strength. To understand the continental rheology, a more rigorous homogenization approach, like the self-consistent homogenization scheme, is necessary to account for the distinct rheological properties, shapes, and orientations of the constituents as well as the continental rheology evolution with time during the progressive deformation.

- (6) This thesis has demonstrated that both the pressure dependence of the activation enthalpy through the activation volume and the slip system dependence of the stress exponent is the key to reconcile the great difference in quartz flow laws derived from existing experiments. By critically evaluating existing high-quality experimental data on quartz creep corresponding to steady-state regimes 2 and 3 dislocation creep together with related quartz c-axis fabrics, the creep behaviors of wet quartzite are summarized as follows: At higher temperatures and lower stresses, wet quartzite deforms predominantly by prism  $\langle a \rangle$  slip, producing characteristic Y-max c-axis fabrics, and follows

$$\dot{\epsilon} = 2.5 \times 10^{-14} f_w^{2.6} \exp\left(-\frac{132000 + 35.8P}{RT}\right) \sigma^4.$$

At lower temperatures and higher stresses, where basal  $\langle a \rangle$  is the dominant slip system with diagnostic strong clusters of c-axes in the periphery, the dislocation creep of wet quartzite follows

$$\dot{\epsilon} = 6.3 \times 10^{-12} f_w^{1.7} \exp\left(-\frac{126000 + 23.1P}{RT}\right) \sigma^{2.5}.$$

- (7) Transitional flow behaviors are common in nature and experiments. In the transitional flow regime where both slip systems are significant, the quartzites can be regarded as a two-phase composite material. Each phase follows one dislocation creep flow law. This work proposed two simple homogenized flow laws for wet quartzites using uniform stress and uniform strain, respectively. These two homogenized flow laws are the upper and lower bounds. The actual bulk strength is between the two bounds and must be obtained through a self-consistent approach. A strength profile using the two homogenized flow laws and the bulk strength obtained through a self-consistent homogenization scheme is constructed for the wet quartzites in a transitional flow regime.

## 6.2 Future Work

Understanding the variations in rheology throughout the lithosphere is my main interest and the ultimate goal of my reach. This thesis provided a MOPLA MATLAB package, refined dislocation creep flow laws for wet quartzite, and a new micromechanics-based

shear zone model with a few field applications, giving a preliminary understanding of continental rheology. I believe that combining the theoretical works, the numerical modeling together with the abundant and valuable field data and mylonite samples from Grenville Front Tectonic Zone will give more insights into the variation and evolution of the continental rheology during the progressive lithospheric deformation process in my future work.

In addition, the rheology of Earth's lithosphere is highly sensitive to the rates and timescales of the deformation (Huntington and Klepeis, 2018). How the continental lithosphere responds to the relatively short-lived process, like earthquakes, the longer-lived tectonic process or the transient process is the key to explore the variations in rheology throughout the lithosphere. In the future, I would like to focus on these interesting works associated with the continental rheology problem.

### 6.3 References

Huntington, K. W., & Klepeis, K. A. (2018). Challenges and opportunities for research in tectonics: Understanding deformation and the processes that link Earth systems, from geologic time to human time. A community vision document submitted to the US National Science Foundation.

Jiang, D. (2014). Structural geology meets micromechanics: A self-consistent model for the multiscale deformation and fabric development in Earth's ductile lithosphere. *Journal of Structural Geology*, 68, 247-272.

<https://doi.org/10.1016/j.jsg.2014.05.020>



## Appendices

### Appendix A The description of the functions in “*Routines*” in the MATLAB package of MOPLA

#### Common Tensor Operations

*Contract.m* is for the Double-index contraction between two 4<sup>th</sup> order tensors. The inputs are two 4<sup>th</sup> order tensors  $A_{ijmn}$  and  $B_{mnkl}$  and the output is a 4<sup>th</sup> order tensor  $C_{ijkl}$  :

$$C_{ijkl} = A_{ijmn} B_{mnkl}.$$

*contract1.m* is for the Double-index contraction between two 2<sup>nd</sup> order tensors. The inputs are two 2<sup>nd</sup> order tensors  $a_{ij}$  and  $b_{ij}$  and the output is a scalar  $\alpha$  :  $\alpha = a_{ij} b_{ij}$ .

*Multiply.m* is for Double-index contraction of a 4<sup>th</sup> order tensor and a 2<sup>nd</sup> order tensor. The inputs are a 4<sup>th</sup> order tensor  $C_{ijkl}$  and a 2<sup>nd</sup> order tensor  $\varepsilon_{kl}$  and the output is a 2<sup>nd</sup> order tensor  $\sigma_{ij}$  :  $\sigma_{ij} = C_{ijkl} \varepsilon_{kl}$ . The generalized Hook’s law is an example.

*FourIdentity.m* is to generate the 4<sup>th</sup> order identities:  $\mathbf{J}^d, \mathbf{J}^s, \mathbf{J}^a, \mathbf{J}^m$  according to Eq.2.6.

*Norm.m* is for the norm of 4<sup>th</sup> order tensors. The input is a 4<sup>th</sup> order tensor  $C_{ijkl}$  and the output is a scalar indicating the magnitude of the 4<sup>th</sup> order tensor:

$$\|\mathbf{C}\| = \sqrt{\sum_{i=1}^3 \sum_{j=1}^3 \sum_{k=1}^3 \sum_{l=1}^3 |C_{ijkl}|^2}. \text{ Note this function is different from the MATLAB built-in}$$

function “norm”. It is equivalent to the Frobenius norm for a 2<sup>nd</sup> order matrix.

*Transform.m* is for coordinate transformation of 4<sup>th</sup> order tensors. The inputs are a 4<sup>th</sup> order tensor  $C_{mhrs}$  and a 2<sup>nd</sup> order transformation matrix Q between two coordinates,

and the output is a 4<sup>th</sup> order tensor  $C'_{ijkl}$  : 
$$C'_{ijkl} = \sum_{m=1}^3 \sum_{n=1}^3 \sum_{r=1}^3 \sum_{s=1}^3 Q_{im} Q_{jn} Q_{kr} Q_{ls} C_{mhrs} .$$

*FourTensorInv.m* is for the inversion of 4<sup>th</sup> order symmetry tensors for an incompressible material. The input is a 4<sup>th</sup> order symmetry tensor  $\mathbf{C}$ . To calculate the inversion of  $\mathbf{C}$ , we first express  $\mathbf{C}$  as a 2<sup>nd</sup> order tensor in an orthonormal basis of 2<sup>nd</sup> order symmetric tensors  $\{\mathbf{b}^{(\lambda)}\}, \lambda = 1, \dots, 6$  (Lebensohn et al., 1998). Then calculate the inversion of the 2<sup>nd</sup> order tensors and convert it back to a 4<sup>th</sup> order tensor  $\mathbf{M}$  ( $\mathbf{M} = \mathbf{C}^{-1}$ ). For an incompressible material,  $\lambda = 5$ .

For a compressible material, please run *FourTensorInv\_el.m*, where  $\lambda = 6$ .

*Inva.m* is for the second invariant of the 2<sup>nd</sup> deviatoric stress tensor or the strain-rate tensor. The input is the deviatoric stress  $\sigma'_{ij}$  or strain rate  $\varepsilon_{ij}$ , and the output is the

second invariant  $\sigma_E$  or  $\varepsilon_E$  : 
$$\sigma_E = \sqrt{\frac{1}{2} \sigma'_{ij} \sigma'_{ij}} ; \varepsilon_E = \sqrt{\frac{1}{2} \varepsilon_{ij} \varepsilon_{ij}} .$$

### Eshelby Tensors and Green Interaction Tensor

*SnPI\_poisson.m* is for the evaluation of Eshelby tensors  $\mathbf{S}$  and  $\mathbf{\Pi}$  for isotropic elastic (compressible) materials according to the expressions of Mura (1987, P.77-84).

The inputs are the three semi-axes (a) of an RDE and the Poisson ratio (v), and the outputs are  $\mathbf{S}$  and  $\mathbf{\Pi}$ .

*SnPI\_vis.m* is for the evaluation of Eshelby tensors  $\mathbf{S}^\nu$  and  $\mathbf{\Pi}^\nu$  for isotropic incompressible materials by setting the Poisson ratio  $\nu = 0.5$  in the expressions of  $\mathbf{S}$  and  $\mathbf{\Pi}$  for isotropic elastic materials and using Eq.2.4. The input is the three semi-axes (a) of an RDE and the outputs are  $\mathbf{S}^\nu$  and  $\mathbf{\Pi}^\nu$ .

*Tfunction.m* and *Tfunction\_AGLQ.m* are for the calculation of Green interaction tensor ( $\mathbf{T}$  or  $\mathbf{T}^\nu$ ) for general compressible/incompressible materials according to Eq.2.7, which is required in the evaluation of Eshelby tensors. *Tfunction.m* is using a combination of Gauss-Legendre Quadrature and Lebedev Quadrature (Qu et al., 2016) to evaluation  $\mathbf{T}$  or  $\mathbf{T}^\nu$ . *Tfunction\_AGLQ.m* is using adaptive Gauss-Legendre Quadrature, in which the numerical integration will continue until a prescribing tolerance is reached. The default tolerance is  $10^{-4}$ . These two functions are modified from the “TGreen.m” in Qu et al. (2016). The inputs of the two functions are the three semi-axes of an RDE (a), the stiffness tensors of the matrix (Cm), the nodes and weights (Alp#, Bet#, ww#, p and ww) for the integration, and a variable “type”, indicating the material type. For compressible material set “type” to “1”; for incompressible material set “type” to “2”. The output of the two functions is  $\mathbf{T}$  or  $\mathbf{T}^\nu$ . In two main functions “MOPLA1.m” and “MOPLA2.m”, the default setting of “type” is “2”, the nodes and weights are automatically generated before the loops. Note, part of the two functions are written in C language and compiled in MATLAB. Before running the two functions, please read the txt file “readme.txt”

### **Evolution of the Inhomogeneities**

*RandaANG.m* is to generate  $n$  uniformly distributed RDEs with random shapes. The inputs are the maximum length of the RDEs ( $a1$ ) and the number of RDEs ( $n$ ). The outputs are the semi-axes of  $n$  RDEs ( $a$ ), which is a 3-by- $n$  matrix, and the spherical angles of  $n$  RDEs ( $ang$ ) which is a 3-by- $n$  matrix.

*Q.m* is for the calculation of the transformation matrix of an RDE between the coordinate fixed with the RDE's three semi-axes and the global coordinate from the three spherical angles of the RDE. The input is  $ang$  (3-by-1 matrix), three spherical angles of an RDE. The output is  $Q$  (3-by-1 matrix), the transformation matrix of the RDE. *Qvec.m* is for the vectorized version of *Q.m*. *Qvec.m* could handle the calculation of the transformation matrixes for  $n$  RDEs from their spherical angles. The input is the  $ang$  (3-by- $n$  matrix), the spherical angles of  $n$  RDEs. The output is  $Q$  (3-by- $n$  matrix), the transformation matrixes of  $n$  RDEs.

*Ed.m* is for the Calculation of the strain rate inside an RDE. The inputs are power-law stress exponent of the matrix ( $Nm$ ) and that of RDE ( $Ne$ ), the viscous stiffness tensors of the matrix ( $Cm$ ) and that of RDE ( $Ce$ ) at matrix strain rate, the viscosity ratio between the RDE and the matrix ( $r$ ) at matrix strain rate, the Eshelby tensor ( $S$ ) of RDE, the imposed strain rate in the matrix ( $E$ ) expressed in RDE's coordinate, the strain rate invariant at which the viscosity of RDE is defined ( $\epsilon_{II}$ ) and the deviatoric identity tensor ( $J^d$ ). The outputs are the strain rate inside the RDE ( $e$ ) and the viscous stiffness tensors of RDE ( $C\_clst$ ) at the state of RDE's strain rate.

*Wd.m* is for the Calculation of the vorticity inside an RDE referred to the frame tracking its semi-axes. The inputs are the three semi-axes of RDE ( $a$ ), the vorticity ( $w$ ) and the strain rate ( $e$ ) inside an RDE. The output is the vorticity inside an RDE referred to the frame tracking its semi-axes ( $w_p$ ).

*RodrgRot.m* for the Rodrigues' rotation approximation. The input is a 3-by-3 matrix  $A$ , and the output is a matrix after the rotation  $A'$ . In the calculation of MOPLA, this function is used to update the orientation of an RDE defined by  $Q$  for a time increment (Eq.2.21b).

## Visualization

*Stereonet.m* is for plotting the orientations of semi-axes of  $n$  RDEs in equal-area lower hemisphere stereonet projection. The input is  $Q$  (3-by-3-by- $n$  matrix), the orientations of semi-axes of  $n$  RDEs. The outputs are three stereonet projections plotting respectively the orientations of the longest axes ( $a_1$ ) of  $n$  RDEs, the orientations of the intermediate axes ( $a_2$ ) of  $n$  RDEs and the orientations of the shortest axes ( $a_3$ ) of  $n$  RDEs.

*ConvertQ2Angs.m* is for Converting the transformation matrix  $Q$  of RDEs to the spherical angles. This function is called in *Stereonet.m*.

*Flinn.m* is Plotting the lengths of the semi-axes of  $n$  RDEs in a Flinn diagram. The input is a (3-by- $n$  matrix), the lengths of semi-axes of  $n$  RDEs. The output is a Flinn diagram showing the shapes of  $n$  RDEs.

**Appendix B Download link for the MATLAB package in Chapter 2.**

The MATLAB package can be download here:

[https://github.com/MOPLA/MOPLA/tree/master/MOPLA\\_MATLAB\\_package](https://github.com/MOPLA/MOPLA/tree/master/MOPLA_MATLAB_package)

### Appendix C Dataset of 20 creep experiments on quartz samples

Dislocation creep flow laws of quartzite: the significance of pressure and slip systems								
Below is a dataset of 20 creep experiments on quartz samples used in this paper.								
We list the sample description, sample ID, stress, strain rate, deformation temperature and confining pressure in the table.								
	Sample	Sample ID	Stress (MPa)	Strain Rate (s <sup>-1</sup> )	Temperature (°C)	Confining Pressure (GPa)	Notes	Apparatus
Kronenberg & Tullis (1984)	Arkansas Novaculite 1-60µm	NV-16	250	1.60E-06	800	1.59	0.4wt% water added, stress determined at 20% strain	Griggs-type solid medium apparatus (NaCl, CaCO <sub>3</sub> )
		NV-46	280	1.60E-06	800	1.22		
		NV-36	330	1.60E-06	800	0.82		
Koch et al. (1989)	Simpson Orthoquartzite 0.21±0.01mm	K874	582	1.52E-06	800	0.95		Griggs-type solid medium apparatus
		K875a	445	1.52E-06	770	1.05		
		K875b	1166	1.75E-05	770	1.03		
		K875c	176	2.11E-07	770	1.04		
		K875d	356	1.99E-06	770	1.03		
		K903	338	1.81E-06	850	0.91		
		K904a	595	1.61E-05	850	1.03		
		K904b	155	2.05E-07	850	1.04		
		K905	230	1.83E-06	850	1.07		
		K908	500	2.20E-05	875	1.27		
	K909	224	1.51E-06	900	1.16			

		K910	251	2.19E-06	900	1.16		
		K911	871	1.59E-04	900	1.14		
		K912a	87	1.48E-07	900	1.2		
		K912c	291	1.63E-06	850	1.21		
		K912d	155	2.17E-07	850	1.2		
		K919a	421	1.64E-06	750	0.94		
		K919b	212	1.87E-07	750	0.91		
		K922a	326	1.64E-06	800	1.05		
		K922b	117	1.25E-07	800	1.07		
		K922C	1138	1.86E-05	800	1.07		
		K923	472	1.82E-05	900	1.18		
		K924	927	1.90E-05	800	1.2		
		K929a	200	1.73E-06	900	1.2		
		K929b	56	2.46E-07	900	1.2		
		K929c	505	1.90E-05	900	1.2		
		K932a	800	1.44E-04	900	1.25		
		K932b	1326	1.64E-04	800	1.25		
		K933a	530	1.65E-06	750	1.15		
		K933b	225	1.57E-07	750	1.15		
		K933c	1315	1.64E-05	750	1.13		
		K934	180	1.80E-06	900	1.2		
		K936	485	1.69E-05	850	1.24		
		K938	416	1.74E-05	900	1.17		
		K939	680	2.32E-05	850	1.15		
Luan & Paterson (1992)	Silicic acid 20- 30µm	5417a	350	6.00E-05	1027	0.3		Griggs-type gas medium apparatus
		5417b	500	3.00E-04	1027	0.3		
		5424	300	5.80E-05	1027	0.3		



		5433a	360	7.50E-05	1027	0.3		
		5433b	290	3.50E-05	1027	0.3		
		5433c	544	3.50E-04	1027	0.3		
		5485a	380	5.10E-05	1027	0.3		
		5485b	182	1.00E-05	1027	0.3		
		5485c	350	1.00E-04	1027	0.3		
		5490a	423	5.30E-05	1027	0.3		
		5490b	130	5.00E-06	1027	0.3		
		5490c	180	1.00E-05	1027	0.3		
		5490d	220	2.00E-05	1027	0.3		
		5490e	260	4.00E-05	1027	0.3		
		5490f	300	8.00E-05	1027	0.3		
		5490g	380	2.20E-04	1027	0.3		
		5490h	445	4.00E-04	1027	0.3		
		5493	280	5.70E-05	1027	0.3		
		5568a	160	1.00E-05	1027	0.3		
		5568b	260	1.00E-04	1027	0.3		
		5568c	205	1.20E-05	927	0.3		
		5568d	320	1.10E-04	927	0.3		
		5574a	149	1.00E-05	1027	0.3		
		5574b	238	4.30E-05	1027	0.3		
		5574c	320	1.20E-04	1027	0.3		
		5575a	270	1.00E-05	927	0.3		
		5575b	150	1.00E-05	1027	0.3		
		5575c	450	1.00E-04	927	0.3		
		5575d	295	1.00E-04	1027	0.3		
		5577a	230	1.00E-05	1027	0.3		

		5577b	420	1.00E-04	1027	0.3		
		5577c	320	5.00E-05	1027	0.3		
		5578a	168	1.00E-05	1027	0.3		
		5578b	270	1.00E-04	1027	0.3		
		5578c	348	2.00E-04	1027	0.3		
		5579a	200	1.00E-05	1027	0.3		
		5579b	420	1.00E-04	1027	0.3		
		5580a	320	1.00E-05	927	0.3		
		5580b	570	1.00E-04	927	0.3		
		5581a	400	1.00E-05	827	0.3		
		5581b	705	1.00E-04	827	0.3		
		5582a	185	1.00E-05	1027	0.3		
		5582b	280	1.00E-05	927	0.3		
		5582c	400	1.00E-05	827	0.3		
		5583a	270	5.00E-05	1027	0.3		
		5583b	380	5.00E-05	927	0.3		
		5583c	490	5.00E-05	827	0.3		
Hirth & Tullis (1992)	Black Hills Quartzite 100 $\mu$ m	CQ-82	100	1.00E-06	900	1.5		Griggs-type solid medium apparatus
	Heavitree Quartzite 210 $\mu$ m	W339	290	1.00E-06	800	1.5		Griggs-type molten salt apparatus
Tullis & Wenk (1994)	Heavitree Quartzite 180- 200 $\mu$ m	W-370	250	1.00E-06	800	1.2		Griggs-type solid medium apparatus

	Black Hills Quartzite 100- 120 $\mu$ m	W-502	125	1.00E-06	800	1.2		Griggs-type molten salt apparatus
Gleason & Tullis (1995)	Black Hills Quartzite 100 $\mu$ m	W611a	84	6.31E-06	1050	1.5	samples with no melt	Griggs-type molten salt apparatus
		W611b	100	6.31E-06	1000	1.45		
		W611c	132	7.94E-06	950	1.44		
		BA96a	43	1.58E-06	1050	1.56		
		BA96b	61	1.58E-06	1000	1.54		
		BA96c	68	1.58E-06	950	1.53		
		BA96d	89	1.99E-06	900	1.5		
		BA94a	76	1.58E-06	1000	1.56		
		BA94b	109	6.31E-06	1000	1.56		
		BA94c	141	2.00E-05	1000	1.59		
		BA94d	228	7.94E-05	1000	1.6		
		BA95a	74	1.58E-06	1100	1.68		
		BA95b	110	6.31E-06	1100	1.68		
		BA95c	142	2.00E-05	1100	1.7		
		BA95d	225	7.94E-05	1100	1.7		
Post et al. (1996)	Black Hills Quartzite 100 $\mu$ m	W614	290	1.00E-05	900	1.69		Tullis-modified Griggs Apparatus
		W625	310	1.00E-05	900	1.72		
		W728	330	1.00E-05	900	1.6		
Stipp & Tullis (2003)	Black Hills Quartzite 100 $\mu$ m	W1030	207	2.00E-06	800	1.5		

		W1085	198	2.25E-06	850	1.5		
		W1049	268	2.30E-05	900	1.5		
		W1099	149	2.35E-06	900	1.5		
		W1051	189	2.40E-05	1000	1.5		
		W1024	102	2.05E-06	1000	1.5		
		W1025	87	2.10E-06	1050	1.5		
		W1119	257	2.10E-04	1100	1.5		
		W1029	130	2.45E-05	1100	1.5		
		W1022	130	6.00E-06	1100	1.5		
		W1066	60	2.25E-06	1100	1.5		
		W1126	34	2.20E-07	1100	1.5		
Rutter & Brodie (2004)	Ultrafine- graind quartzite 12- 20µm	Q7a	167	5.00E-05	1200	0.3		Griggs-type gas medium apparatus
		Q7b	238	2.00E-04	1200	0.3		
		Q14a	365	3.80E-05	1100	0.3		
		Q16a	170	4.00E-05	1200	0.3		
		Q16b	160	7.00E-06	1100	0.3		
		Q16c	175	2.00E-05	1200	0.3		
		Q18	350	8.00E-05	1200	0.3		
		Q19	242	4.00E-05	1200	0.3		
		Q20	222	4.00E-05	1200	0.3		
		Q21a	180	7.00E-05	1200	0.3		
		Q21b	180	1.30E-05	1100	0.3		
		Q21c	180	1.00E-05	1100	0.3		
		Q21d	190	3.20E-06	1000	0.3		
		Q21e	130	3.20E-06	1200	0.3		
		Q30a	222	5.80E-05	1200	0.3		

		Q30b	85	1.00E-06	1200	0.3		
		Q30c	66	1.10E-06	1200	0.3		
		Q30d	66	2.00E-07	1100	0.3		
		Q30e	422	2.00E-05	1100	0.3		
Stipp et al. (2006)	Black Hills Quartzite 100 $\mu$ m	W1172	48	2.25E-06	1000	1.5		Griggs-type molten salt apparatus
		W1142	66	2.00E-06	950	1.5		
		W1081	139	2.30E-06	900	1.5		
		W1089	177	2.40E-06	850	1.5		
		W1082	168	2.40E-06	800	1.5		
		W1140	156	2.25E-06	750	1.5		
Chernak et al. (2009)	Black Hills Quartzite	W1341	260	1.39E-05	900	1.5		Griggs-type solid medium apparatus
Holyoke & Kronenberg (2013)	Black Hills Quartzite 100 $\mu$ m	TMQ - 7	162	1.60E-06	800	1.6		Griggs-type solid medium apparatus
			422	1.60E-06	800	0.85		
			175	1.60E-06	800	1.56		
Kidder et al. (2016)	Black Hills Quartzite 70 $\mu$ m	W1341	242	2.17E-05	900	1.3		Griggs-type solid medium apparatus
		W1505	100	1.70E-06	900	1.3		
		W1509a	120	1.60E-06	900	1.3		
		W1510	87	2.27E-06	900	1.3		
		W1525a	94	1.69E-06	900	1.3		
		W1525b	192	4.50E-05	900	1.3		
		W1526a	337	1.68E-05	900	1.3		

		W1526b	124	2.30E-06	900	1.3		
		W1518b	58	2.20E-06	900	1.3		
Heilbronner & Tullis (2002)	Black Hills Quartzite 100µm	W872	310	1.50E-05	900	1.5		Griggs-type solid medium apparatus
		W858	180	1.50E-06	900	1.5		
		W946	364	1.73E-05	875	1.5		
		W920	165	8.66E-06	900	1.5		
		W935	182	1.73E-05	915	1.5		
Holyoke & Tullis (2006)	Black Hills Quartzite 100µm	W1105	788	2.00E-05	800	1.5	minimum strength after yield	Griggs-type solid medium apparatus
		W1106	139	2.00E-06	800	1.5		
		W1153	346	2.00E-06	745	1.5		
Heilbronner & Tullis (2006)	Black Hills Quartzite 100µm	W920	121	7.22E-06	900	1.5		Griggs-type solid medium apparatus
		W1010	182	1.14E-05	915	1.55		
		W935	208	1.14E-05	915	1.5		
		W965	191	1.16E-05	915	1.55		
Nachlas & Hirth (2015)	Silica gel (20-40µm)	W1674	242	2.89E-05	900	1		Griggs-type solid medium apparatus
		W1678	286	2.89E-05	900	1		
		W1680	251	2.89E-05	900	1		
		W1699	234	2.89E-05	900	1		
		W1700	225	2.89E-05	900	1		
		W1701	199	2.89E-05	900	1		

Tokle et al. (2013)		LT379	486	5.40E-06	800	1.5		
Richter et al. (2016)	Crushed quartz crystal <100 $\mu$ m	BR452	1329	1.56E-05	700	1.064		Griggs-type solid medium apparatus
Richter et al. (2018)	Crushed quartz crystal <100 $\mu$ m	BR383	940	1.62E-05	700	1.59	viscous regime	Griggs-type solid medium apparatus
		Br388	685	1.62E-05	800	1.53		
		Br445	268	1.73E-05	800	1.58	"sieved" 7-11 $\mu$ m	
		Br419	880	1.62E-05	800	1.56		
		Br448	630	1.67E-05	800	1.07		
		Br412	312	1.62E-05	900	1.53		
		Br337	127	1.73E-05	1000	1.51		

## Curriculum Vitae

**Name:** Lucy (Xi) Lu

### **Post-secondary Education and Degrees:**

- 2010-2012: BSc China University of Geosciences (Beijing), Beijing, China
- 2012-2014: BSc University of Waterloo, Waterloo, Ontario, Canada
- 2014-2019: PhD student Western University, London, Ontario, Canada

### **Related Work Experience:**

- 2014-2019: Teaching Assistant/Research Assistant, Western University

### **Publications:**

Qu, M., Jiang, D., & Lu, L. X. (2016). An optimal scheme for numerical evaluation of Eshelby tensors and its implementation in a MATLAB package for simulating the motion of viscous ellipsoids in slow flows. *Computers & geosciences*, 96, 98-108.

Lu, L. X., & Jiang, D. (2019). Quartz Flow Law Revisited: The Significance of Pressure Dependence of the Activation Enthalpy. *Journal of Geophysical Research: Solid Earth*, 124(1), 241-256.

Yang, R., Jiang, D., & Lu, L. X. (2019). Constrictional strain and linear fabrics as a result of deformation partitioning: a multiscale modeling investigation and tectonic significance. *Tectonics*.



Lu, L. X., & Jiang, D. (2019). Dislocation creep flow laws of quartzite: the significance of pressure and slip systems. Manuscript submitted.

**Conferences:**

Lu, L.X. and Jiang, D., 2016. Mechanics of Oblique Convergence of Plates and Continental Tectonics (POSTER). In Canadian Tectonic Group Meeting at Muskoka.

Qu, M., Jiang, D., Lu, L.X., Baker, I.R., Moser, D.E., 2016. A comparison between multiscale simulation results of quartz lattice preferred orientations and EBSD data from the Shangdan tectonic zone of the Qinling orogenic belt, China (POSTER). In Canadian Tectonic Group Meeting at Muskoka.

Lu, L.X. and Jiang, D., 2018. The strength of polyphase rocks and the rheology of continental lithosphere. (ORAL PRESENTATION) In Canadian Tectonic Group Meeting at Saints-Martyrs-Canadiens.

Lu, L.X., Jiang, D., 2019. Ductile shear zones as flat heterogeneous inclusions in the continental lithosphere: a numerical investigation based on the Eshelby Formalism. (ORAL PRESENTATION) In GACMAC annual meeting at Quebec City.

Yang, R., Jiang, D., Lu, L.X., 2019. (POSTER) Development of L-tectonites in isolated rock volumes: a numerical investigation. In GACMAC annual meeting at Quebec City.